

RADIATION DAMAGE STUDIES IN THE LHCB  
VELO DETECTOR AND MEASUREMENT OF THE  
FLAVOUR-SPECIFIC ASYMMETRY IN  
SEMILEPTONIC B-DECAYS

A THESIS SUBMITTED TO  
THE UNIVERSITY OF MANCHESTER  
FOR THE DEGREE OF DOCTOR OF PHILOSOPHY  
IN THE FACULTY OF  
ENGINEERING AND PHYSICAL SCIENCES

**ADAM D. WEBBER**  
MPHYS, UNIVERSITY OF MANCHESTER, 2009

CERN-THESIS-2013-117  
21/02/2013  


PARTICLE PHYSICS GROUP  
SCHOOL OF PHYSICS AND ASTRONOMY  
2013



# CONTENTS

<b>Abstract</b>	<b>vii</b>
<b>Declaration</b>	<b>ix</b>
<b>Copyright</b>	<b>xi</b>
<b>Acknowledgements</b>	<b>xiii</b>
<b>1 Introduction</b>	<b>1</b>
<b>2 Theoretical Review</b>	<b>3</b>
2.1 The Standard Model . . . . .	3
2.1.1 The Standard Model particles . . . . .	4
2.1.2 Particle interactions . . . . .	7
2.2 Charge-Parity violation . . . . .	10
2.3 <i>B</i> -meson mixing . . . . .	17
<b>3 Particle Acceleration and Detection at LHCb</b>	<b>21</b>
3.1 Particle acceleration . . . . .	21
3.1.1 Injector chain . . . . .	22
3.1.2 The Large Hadron Collider . . . . .	22
3.1.3 LHC performance . . . . .	24
3.2 The LHCb detector . . . . .	25
3.2.1 The LHCb coordinate system . . . . .	26
3.2.2 Dipole magnet . . . . .	27
3.2.3 Tracking system . . . . .	28
3.2.4 Particle identification . . . . .	35
3.3 Event triggers . . . . .	39
3.3.1 Level-0 trigger . . . . .	40
3.3.2 Higher level trigger . . . . .	41
3.4 LHCb software . . . . .	42

3.4.1	Simulation . . . . .	42
3.4.2	Reconstruction . . . . .	43
<b>4</b>	<b>LHCb Detector Upgrade Studies</b>	<b>45</b>
4.1	Tracker Turicensis . . . . .	45
4.2	The role of the TT in the upgrade . . . . .	47
4.3	Event simulation . . . . .	48
4.4	Spillover subtraction . . . . .	48
4.5	PatVeloTT . . . . .	51
4.6	VeloTT multiplicity . . . . .	52
4.7	“Best” track selection . . . . .	53
4.8	Efficiency and fake rate . . . . .	54
4.9	Efficiency losses . . . . .	56
4.10	Minimum bias . . . . .	58
4.11	Conclusions and upgrade status . . . . .	59
<b>5</b>	<b>Radiation Damage Studies of the LHCb VELO</b>	<b>61</b>
5.1	Particle detection using silicon . . . . .	61
5.1.1	Silicon diodes . . . . .	63
5.1.2	Particle energy loss . . . . .	65
5.1.3	Radiation damage in silicon . . . . .	65
5.1.4	Annealing . . . . .	69
5.2	VELO hardware . . . . .	69
5.2.1	Strip layout . . . . .	71
5.2.2	Electronics . . . . .	73
5.2.3	Radiation hardness . . . . .	73
5.3	Charge Collection Efficiency scans . . . . .	74
5.4	Tracking resolution . . . . .	76
5.4.1	Cluster inclusion thresholds . . . . .	78
5.4.2	Overdepletion . . . . .	79
5.5	Charge Collection Efficiency . . . . .	80
5.5.1	Effective Depletion Voltages . . . . .	80
5.5.2	Effective Depletion Voltage with fluence . . . . .	81
5.5.3	Noise scans . . . . .	89
5.6	Cluster Finding Efficiency . . . . .	91
5.6.1	Second metal layer . . . . .	93
5.7	Summary . . . . .	98

<b>6</b>	<b>Flavour-specific Asymmetries using Semileptonic <math>B</math> Decays: Method and Efficiency Corrections</b>	<b>101</b>
6.1	An untagged time-integrated approach . . . . .	102
6.1.1	Production asymmetry . . . . .	104
6.2	Experimental status . . . . .	106
6.2.1	Evidence for an anomalous like-sign dimuon asymmetry from the $D\bar{0}$ experiment . . . . .	107
6.3	Analysis method . . . . .	108
6.3.1	Data selection . . . . .	109
6.3.2	The master formula . . . . .	113
6.4	Muon efficiencies . . . . .	114
6.4.1	The muon system . . . . .	114
6.4.2	Calibration samples . . . . .	115
6.4.3	Muon distributions . . . . .	117
6.4.4	Efficiency finding method . . . . .	121
6.4.5	Offline muon identification efficiency . . . . .	123
6.4.6	The HLT1 trigger . . . . .	126
6.4.7	The L0 muon trigger . . . . .	127
6.4.8	The total muon efficiency . . . . .	132
6.5	The HLT2 trigger . . . . .	133
<b>7</b>	<b>Flavour-specific Asymmetries using Semileptonic <math>B</math> Decays: Results</b>	<b>135</b>
7.1	Signal yield determination . . . . .	135
7.1.1	Raw yields and charge asymmetries . . . . .	137
7.1.2	Prompt component . . . . .	140
7.1.3	Fitting consistency . . . . .	141
7.1.4	Kinematic binning . . . . .	144
7.2	The measured asymmetry . . . . .	149
7.3	Systematic studies and further corrections . . . . .	153
7.3.1	Data fitting models . . . . .	154
7.3.2	Fiducial selection . . . . .	155
7.3.3	HLT2 trigger categories . . . . .	155
7.3.4	Stability over time . . . . .	156
7.3.5	Raw asymmetries . . . . .	157
7.3.6	Background correction . . . . .	159
7.3.7	Tracking efficiencies . . . . .	161
7.3.8	Systematic uncertainties . . . . .	162
7.4	Summary and conclusions . . . . .	163

*CONTENTS*

---

**A Projected Angle** 167

**Bibliography** 177

**Approximate word count: 37,372**

## ABSTRACT

This thesis presents several studies of data collected at the LHCb detector during its first two years of operation. A detector upgrade study is first presented, using simulated events at an increased luminosity. A second study involves radiation damage to the silicon sensors of the LHCb Vertex Locator. During 2010 and 2011 the silicon sensors were exposed to a range of fluences, with sensors in the most active regions exposed to fluences of up to approximately  $45 \times 10^{12}$  1 MeV neutron equivalent ( $1 \text{ MeV n}_{\text{eq}}$ ). The first observation of  $n^+$ -on- $n$  sensor type inversion at the Large Hadron Collider is reported, occurring at a fluence of around  $(10-15) \times 10^{12}$  of  $1 \text{ MeV n}_{\text{eq}}$ . The effective depletion voltages of the only  $n^+$ -on- $p$  sensors in use at the Large Hadron Collider have also been studied, with decreases of around 25 V observed after initial irradiation. Following this, the effective depletion voltage in  $n^+$ -on- $p$  type sensors is observed to increase at a comparable rate to type inverted  $n^+$ -on- $n$  type sensors. A reduction in the charge collection efficiency due to an unexpected effect involving the sensor readout lines is also observed.

A third study relates to  $CP$  violation in neutral  $B$ -meson mixing, by the measurement of the *flavour-specific asymmetry*. In the Standard Model,  $CP$  violation from this source is expected to be of order  $10^{-4}$ . Any measured enhancement of this would be a strong indication of new physics. The DØ collaboration has measured the flavour specific asymmetry from  $B^0$  and  $B_s^0$  mixing, and found it to be inconsistent with the Standard Model at a confidence level of 3.9 standard deviations, thus motivating an independent measurement from the LHCb experiment. Using the full 2011 LHCb dataset, corresponding to  $1.0 \text{ fb}^{-1}$  of recorded luminosity, the  $B_s^0$ -meson component of the flavour-specific asymmetry is measured to be  $a_{\text{fs}}^s = (-0.12 \pm 0.48 \pm 0.34)\%$ , where the first uncertainty is statistical and the second is systematic. This is the single most accurate measurement of  $a_{\text{fs}}^s$ , and is consistent with both the DØ measurement and the Standard Model prediction.



## DECLARATION

This work represents the combined efforts of the LHCb collaboration. Some of the content has been published elsewhere and/or presented to several audiences. No portion of the work referred to in this thesis has been submitted in support of an application for another degree or qualification of this or any other university or other institute of learning.

Signed:

Date: February 27, 2013

Adam D. Webber  
School of Physics and Astronomy  
University of Manchester  
Oxford Road  
Manchester  
M13 9PL  
United Kingdom



## COPYRIGHT

1. The author of this thesis (including any appendices and/or schedules to this thesis) owns certain copyright or related rights in it (the “Copyright”) and he has given The University of Manchester certain rights to use such Copyright, including for administrative purposes.
2. Copies of this thesis, either in full or in extracts and whether in hard or electronic copy, may be made only in accordance with the Copyright, Designs and Patents Act 1988 (as amended) and regulations issued under it or, where appropriate, in accordance with licensing agreements which the University has from time to time. This page must form part of any such copies made.
3. The ownership of certain Copyright, patents, designs, trade marks and other intellectual property (the “Intellectual Property”) and any reproductions of copyright works in the thesis, for example graphs and tables (“Reproductions”), which may be described in this thesis, may not be owned by the author and may be owned by third parties. Such Intellectual Property and Reproductions cannot and must not be made available for use without the prior written permission of the owner(s) of the relevant Intellectual Property and/or Reproductions.
4. Further information on the conditions under which disclosure, publication and exploitation of this thesis, the Copyright and any Intellectual Property Rights and/or Reproductions described in it may take place is available from the Head of School of Physics and Astronomy (or the Vice-President) and the Dean of the Faculty of Engineering and Physical Sciences.



## ACKNOWLEDGEMENTS

First of all, thanks to everyone who has helped me during my PhD, and apologies to those I may have forgotten to mention below. More specifically, thanks to my supervisor, George Lafferty, who has always been friendly and helpful when approached (which in the last year has been often), whilst allowing me the freedom to pursue my research in a manner of my own choosing. There are many others who have acted in supervisory roles. Thanks to all of you, who I unceremoniously list (chronologically): Fred Loebinger, Dave Bailey, Steven Blusk, Tomasz Skwarnicki, Rob Lambert, Ulrich Kerzel, Chris Parkes, Paula Collins, Marina Artuso, Sheldon Stone and Mika Vesterinen. You have all aided the research shown in this thesis, and it has been a pleasure working with all of you. Thanks also to Anne Morrow for providing invaluable administrative support, whilst I have been both in Manchester and abroad.

Next, my work colleagues, who whilst having not supervised me in the same way as those listed above, have been equally helpful to my studies. The computing gurus: Marius Björnstad and Thomas Bird. My PhD “older brothers”: Grant McGregor, Dermot Moran and Stephen Farry. My fellow PhD students: Hamish Gordon, Sam Gregson, Alex Shires, Alessandra Borgia, Zhou Xing and Joel Klinger. I felt I could ask you questions without fear of ridicule, which is an important thing in particle physics. Thanks also to Jon Harrison, the once timid young man who I took under my radiative wing; helping you has helped me.

Finally, the people who didn’t actually do anything related to my studies other than be around. In a particular order: Fred, Kathy, Tom, Josh, Joe, family and peripheral (Gareth, Vik, John, etc...). You are all important, for without you I would have been lonely. And lonely physicists work too hard and make mistakes. Cheers.



## INTRODUCTION

Particle physics is the study of the fundamental constituents of matter and their interactions. Such interactions are described within the theoretical framework of the Standard Model (SM), which is a quantum field theory in which particles are treated as excitations of relativistic fields. The theory has been developed over the course of many decades, sometimes evolving due to theoretical advances and sometimes due to experimental discovery. Three of the four fundamental forces of nature are described by the model, corresponding to electromagnetic, weak and strong interactions. The SM has been successful at both predicting and describing the majority of experimental data. It is not however without its limitations, as it does not explain gravity, the presence of dark matter or dark energy, or the observed baryon-asymmetry of the universe. It is the last of these phenomena that is the main subject of this thesis.

The predictions of the SM can be tested in a variety of experimental environments. For example, particles are naturally produced by cosmological, solar and radioactive sources, all of which require different detection systems to extract parameters of interest. Another approach is pursued at particle colliders such as the Large Hadron Collider (LHC), where particles are accelerated to specific energies with man-made machinery. The LHC is the final component of an accelerating complex at the CERN research facility, which was built to provide high energy proton collisions for particle detectors. The large proton-beam energies can produce exotic particles with masses much greater than those of the incident protons, in accordance with the famous energy-mass relation,  $E = mc^2$ .

The LHCb experiment is one of the four major particle physics experiments located at the LHC. It is a dedicated heavy-flavour experiment with the primary aim of measuring processes involving rare decays and  $CP$  violation, the latter of which is a requirement for producing a matter-antimatter asymmetric universe. An aim of modern particle physics is to find inconsistencies in the SM, by making increasingly

precise measurements of its parameters. It is hoped that in first proving that it is wrong, a hint of the true underlying processes will be revealed and a more complete theory may be formulated.

This thesis presents several studies of data collected with the LHCb detector during its first two years of operation. The theory of the SM is first reviewed in Chapter 2, with particular emphasis given to  $CP$  violation. The apparatus used for particle acceleration and detection are then described in Chapter 3. Preparations are underway for the LHCb detector upgrade, which involves detector improvements and replacements to allow for a significantly increased data collection rate. A study of the particle tracking performance at increased proton interaction rates is presented in Chapter 4, for which simulation data have been used to estimate the detector occupancy in an upgraded environment.

Particle decay vertices are reconstructed at LHCb with a silicon microstrip detector called the Vertex Locator (VELO). The VELO surrounds the proton interaction region, and is therefore subject to high particle flux. A study of the effects of radiation damage to the VELO sensors is presented in Chapter 5. Finally, a study of  $CP$  violation in neutral  $B$ -meson mixing is presented in Chapters 6 and 7, in which the flavour-specific asymmetry of  $B_s^0$  and  $\bar{B}_s^0$  mesons is determined using semileptonic decays.

## THEORETICAL REVIEW

The research described in this thesis is related to charge-parity ( $CP$ ) violation in particle-antiparticle mixing in the neutral  $B$ -meson system<sup>1</sup>. To discuss the interactions of  $B$  mesons it is first useful to review the components of the Standard Model, as is done in Section 2.1. The subject of  $CP$  violation is central to the physics goals of the LHCb experiment. It is shown in Section 2.2 how this phenomenon can be incorporated into the framework of the SM. Finally, neutral meson mixing, a process in which a particle oscillates between its particle and anti-particle states, is discussed in Section 2.3. The following is far from a complete theoretical review, with mathematical formalism largely abandoned for qualitative descriptions of the underlying concepts. A more thorough treatment can be found in the referenced literature at the start of each section.

### 2.1 The Standard Model

The Standard Model (SM) is a quantum field theory used to describe the interactions of elementary particles due to the electromagnetic, weak and strong forces<sup>2</sup>. A notable absentee is gravity, which is yet to be incorporated into the model. However, as the interaction strength of gravity is many orders of magnitude lower than that of the other forces, it is reasonable to assume that it can be neglected when discussing high energy particle interactions. In the following section the SM particles are introduced. The mechanisms by which these particles interact are then discussed.

---

<sup>1</sup>A study of radiation damage in silicon is also presented in Chapter 5, together with the theory of silicon strip detectors.

<sup>2</sup>The material summarised in this section has been sourced from, and is described in far greater detail, in Refs. [1–4].

### 2.1.1 The Standard Model particles

#### Leptons

In the SM, matter is composed of elementary spin- $\frac{1}{2}$  particles known as *leptons* and *quarks*. In total there are 6 leptons that have been identified by experiment, of which 3 carry electric charge and three are electrically neutral. The total number of leptons is not theoretically constrained by the SM; however, there is strong experimental support for the existence of only 6 leptons. The most familiar of the charged leptons is the electron, which binds to nuclei through the electromagnetic force. The other two charged leptons, known as *muons* and *taus*, each carry the same electric charge as the electron,  $Q = -|e|$ , where  $|e|$  is the magnitude of the electron charge. The three neutral leptons are known as *neutrinos*, each of which is paired with one of the charged leptons, thus forming three generations of lepton doublet,

$$\begin{pmatrix} \nu_e \\ e^- \end{pmatrix}, \quad \begin{pmatrix} \nu_\mu \\ \mu^- \end{pmatrix}, \quad \begin{pmatrix} \nu_\tau \\ \tau^- \end{pmatrix}. \quad (2.1)$$

The leptons in each generation conserve the additive lepton-flavour quantum numbers,  $L_l(l^-) = L_l(\nu_l) = 1$ , with  $l = e, \mu, \tau$ . The charged leptons interact both electromagnetically and via the weak interaction, whereas the neutrinos carry no electric charge and so interact by the weak force only. The properties of the leptons are summarised in Table 2.1.

Until recently it was thought that neutrinos were massless. However, the observation of neutrino oscillations, the process in which a neutrino changes its flavour, implies that the neutrinos are in fact massive particles. Such oscillations are direct evidence of lepton flavour violation. The experimental limit on the summed mass of the three neutrino flavours is found to be less than 0.28 eV [5].

Table 2.1: Some properties of the SM leptons. The upper limits on the neutrino masses are given to the 95% confidence level. The masses are determined by experiment, with values taken from Ref. [6].

particle	$Q$	selected quantum numbers	mass [ MeV/ $c^2$ ]
$\nu_e$	0	$L_e = 1, L_\mu = 0, L_\tau = 0$	$< 2 \times 10^{-6}$
$e^-$	-1	$L_e = 1, L_\mu = 0, L_\tau = 0$	0.510998928(11)
$\nu_\mu$	0	$L_e = 0, L_\mu = 1, L_\tau = 0$	$< 0.19$
$\mu^-$	-1	$L_e = 0, L_\mu = 1, L_\tau = 0$	105.6583715(35)
$\nu_\tau$	0	$L_e = 0, L_\mu = 0, L_\tau = 1$	$< 18.2$
$\tau^-$	-1	$L_e = 0, L_\mu = 0, L_\tau = 1$	1776.82(16)

## Quarks

The quark sector shares a similar structure to the leptons, with a total of 6 quarks forming three generations of quark doublet,

$$\begin{pmatrix} u \\ d \end{pmatrix}, \quad \begin{pmatrix} c \\ s \end{pmatrix}, \quad \begin{pmatrix} t \\ b \end{pmatrix}. \quad (2.2)$$

The  $u$ ,  $d$ ,  $c$ ,  $s$ ,  $t$  and  $b$  are shorthand for *up*, *down*, *charm*, *strange*, *top* and *bottom* quarks. A particle's *internal* quantum numbers are those that are not associated with space-time symmetries (e.g. the electric charge). Just as the leptons have lepton-flavour quantum numbers, the quarks possess analogous internal quantum numbers known as baryon number,  $B$  (equal to  $+1/3$  for each quark), strangeness,  $S$ , charm,  $C$ , bottomness,  $\tilde{B}$ , and topness,  $T$ . The latter of these are non-zero for the strange, charm, bottom and top quarks, respectively. The quantum numbers that are specific to a quark's flavour are conserved in electromagnetic and strong interactions, but are violated by the weak force. Some selected quark properties are summarised in Table 2.2.

Table 2.2: Some properties of the SM quarks. The quantum numbers that are specific to each quark flavour are shown (those of the  $u$  and  $d$  quarks are described in the following text). The particle masses are taken from Ref. [6].

particle	$Q$	selected quantum numbers	mass [ MeV/ $c^2$ ]
$u$	$+2/3$	$I = 1/2, \quad I_3 = +1/2$	$2.3_{-0.5}^{+0.7}$
$d$	$-1/3$	$I = 1/2, \quad I_3 = -1/2$	$4.8_{-0.3}^{+0.7}$
$c$	$+2/3$	$C = +1$	1275(25)
$s$	$-1/3$	$S = -1$	95(5)
$t$	$+2/3$	$T = +1$	$173.5_{-0.6}^{+0.7} \times 10^3$
$b$	$-1/3$	$\tilde{B} = -1$	4180(30)

Unlike the heavier quarks, the  $u$  and  $d$  are not assigned unique, “self-named”, flavour quantum numbers. Because of their relatively small, and comparably sized masses, they are assigned values of *isospin* instead. Isospin was initially introduced to describe similarities between strongly interacting protons and neutrons, which are themselves composed of  $u$  and  $d$  quarks. It was suggested that the proton and neutron could be treated as the same particle, which is observed in two differently charged isospin substates. The third component of isospin is defined as  $I_3 \equiv Q - Y/2$ , where  $Q$  is the electric charge and  $Y = B + S + C + \tilde{B} + T$  is the *hypercharge*. The  $u$  and  $d$  quarks have  $I_3$  values of  $+1/2$  and  $-1/2$ , thus forming an isospin doublet with isospin quantum number  $I \equiv (I_3)_{\max} = 1/2$ . The formalism of an  $I = 1/2$  doublet with two  $I_3 = \pm 1/2$  substates is mathematically analogous to that of a spin- $1/2$  system,

with spin-up and spin-down substates. This analogy extends to systems with greater than two components, such that the well established quantum mechanical formalism developed for the addition of angular momentum can be used to describe isospin multiplets of various size.

Isospin is conserved to a good approximation by the strong force. The small difference in mass between  $u$  and  $d$  quarks prevents this from being an exact symmetry; however, this is small compared to the typical mass of the composite hadrons and so the isospin symmetry is still a useful calculative tool.

For each of the particles introduced so far (both leptons and quarks), there exists an antiparticle with identical mass and lifetime, but with opposite internal quantum numbers. Matter and antimatter are found to behave almost identically; however, small differences have been observed in interactions involving the weak force. The SM interpretation of these differences is discussed in Section 2.2.

### Composite particles

An interesting characteristic of the quarks is that they carry non-integer electric charge; the three *up-type* quarks have  $Q(u/c/t) = +2/3|e|$  and the three *down-type* quarks have  $Q(d/s/b) = -1/3|e|$ . At first this may appear inconsistent with what is seen in nature, where charges are found to be either zero or integer multiples of  $|e|$ . This is resolved by the assertion that quarks cannot exist in isolation, but instead must combine to form composite *hadrons* due to the strong force. The conserved “charge” of the strong force is referred to as *colour*, which can be viewed as the analogue of electric charge in electromagnetism. Colour takes one of three states, described as red, blue and green. Hadrons are colour neutral particles known as *mesons* and *baryons*. The mesons have integer spin and are composed of a quark,  $q$ , of colour,  $c_i$ , and an antiquark,  $\bar{q}$ , of anticolour,  $\bar{c}_i$ , where  $i$  represents a specific colour charge. Baryons and antibaryons are half-integer spin particles composed of three quark combinations  $qqq$  and  $\bar{q}\bar{q}\bar{q}$ . For the composite particle to be colour neutral, each of the baryon quarks must have different colour charge. The properties of a selection of hadrons (most of which are studied in the latter parts of this thesis) are shown in Table 2.3.

### Gauge bosons and the Higgs

In addition to the quarks and leptons, there is a third SM particle group comprising the *gauge bosons*. These are the “force carriers” of the electromagnetic, strong and weak forces. The electromagnetic force is mediated by the exchange of *photons*,  $\gamma$ , the weak force by the  $W^\pm$  and  $Z$  bosons, and the strong force by *gluons*,  $g$ . The final particle predicted by the SM is the Higgs boson. This is introduced to allow

the massive leptons, quarks,  $W^\pm$  and  $Z$  to obtain mass parameters within the theoretical framework of the model. Some parameters of the SM bosons are summarised in Table 2.4.

Table 2.3: Properties of a selection of hadrons. The particle masses are taken from Ref. [6].

particle	quark content	mass [ MeV/ $c^2$ ]	$Q$	$B$	$S$	$C$	$\tilde{B}$
p	$uud$	938	1	1	0	0	0
n	$udd$	940	0	1	0	0	0
$\pi^+$	$u\bar{d}$	140	1	0	0	0	0
$K^-$	$s\bar{u}$	494	-1	0	-1	0	0
$D^+$	$\bar{d}c$	1870	1	0	0	1	0
$B^+$	$u\bar{b}$	5279	1	0	0	0	1
$B_s^0$	$\bar{b}s$	5367	0	0	-1	0	1

Table 2.4: Some properties of the gauge bosons and Higgs boson. The  $W^\pm$  and  $Z$  masses are taken from Ref. [6] and the Higgs mass from Refs. [7, 8].

sector	particle	$Q$	mass [ GeV/ $c^2$ ]
electromagnetic	$\gamma$	0	0
weak	$Z$	0	91.188(2)
	$W^\pm$	$\pm 1$	80.385(15)
strong	$g$	0	0
Higgs	$H$	0	$\sim 125$

### 2.1.2 Particle interactions

Approximately half of the SM particles discussed in the previous section were first identified by experiment, and incorporated into the theory later (e.g.  $e^-$ ,  $u$ ,  $\gamma$ ). However, many of the particles were first postulated by the theory through symmetry based arguments and later discovered by the experiments (e.g.  $e^+$ ,  $c$ ,  $H$ ). At the heart of the ‘‘symmetry approach’’ of the SM is Noether’s theorem, which states that for each continuous symmetry of a system there is an associated conserved quantity. A system is said to be symmetric if the dynamics of the system remain unchanged following some transformation. The transformations can be *global*, for which the transformation is carried out at all space-time points, or *local*, for which the transformation is a function of the space-time coordinates. Particle interactions are introduced in the SM by a particular type of symmetry known as *gauge invariance*. These concepts are most simply introduced in the context of quantum electrodynamics, the gauge theory of the electromagnetic force.

### Quantum electrodynamics

Quantum electrodynamics (QED) describes the electromagnetic interactions of the charged spin-1/2 fermions. In the SM, a relativistic particle of mass,  $m$ , electric charge,  $Q$ , and spin-half is described by the free Dirac fermion field  $\psi(x)$ . The Lagrangian density,  $\mathcal{L}$ , of such a particle is expressed as,

$$\mathcal{L} = \bar{\psi}(i\gamma^\mu\partial_\mu - m)\psi, \quad (2.3)$$

where  $\mathcal{L}$  can simply be thought of as a mathematical object that contains the dynamical information of the fermion system. It can be combined with the Euler-Lagrange equation to obtain the relativistic Dirac equation,

$$(i\gamma^\mu\partial_\mu - m)\psi = 0. \quad (2.4)$$

It is easily shown that the Lagrangian density from Equation 2.3 is invariant under a global transformation of the fermion field,

$$\psi \rightarrow e^{-i\omega}\psi, \quad \bar{\psi} \rightarrow e^{i\omega}\bar{\psi}, \quad (2.5)$$

where  $\omega$  is a real constant. By Noether's theorem, the invariance of  $\mathcal{L}$  corresponds to the conservation of a quantity, which in this case is the conservation of electric charge. If the global transformation is promoted to a local one,  $\omega \rightarrow \omega(x)$ ,  $\mathcal{L}$  is no longer invariant, due to an additional term involving the derivative of  $\omega(x)$ . To restore gauge invariance, the additional term can be compensated for by making the simultaneous transformations,

$$\partial_\mu \rightarrow \partial_\mu - ieA_\mu \equiv D_\mu, \quad A_\mu \rightarrow A_\mu + \frac{1}{e}\partial_\mu\omega(x), \quad (2.6)$$

where  $D_\mu$  is known as the covariant derivative and  $A_\mu$  is the gauge vector boson field. Thus by requiring that the dynamics of the fermion field are invariant under a local gauge transformation, the QED interactions are quite elegantly introduced to the theory. The vector field,  $A_\mu$ , is interpreted as the photon field, which interacts with the charged fermion fields due to terms in  $\mathcal{L}$  of the form  $-e\bar{\psi}\gamma^\mu A_\mu\psi$ . The photon is required to have zero mass to maintain gauge invariance, in agreement with observation.

### Quantum chromodynamics and electroweak unification

The theory describing the strong force is known as quantum chromodynamics (QCD). The gauge bosons of QCD are the massless gluons, which interact with

particles of non-zero colour-charge. Unlike the electrically neutral photons from QED, the gluons carry colour-charge themselves. This allows gluons to interact with one another, which influences the strength of the strong interaction in such a way as to decrease it at small distances and increase it towards infinity at large distances. The weakening of the strong force at low distances is known as *asymptotic freedom*, while the behaviour at large distances prevents quarks from being observed in isolation, a phenomenon known as *confinement*.

The local transformations in QED are generated by the  $U(1)$  gauge group. This is described by a single parameter,  $\omega(x)$ , resulting in the introduction of a single gauge boson, the photon. The QCD interactions are introduced with an analogous approach, by requiring invariance under local transformations of the  $SU(3)$  group<sup>1</sup>. The theory does not predict which specific transformation group will generate the interactions of QCD; the  $SU(3)$  group is chosen as it agrees well with experimental data. A general  $SU(N)$  group has  $N^2 - 1$  independent generators, thus the  $SU(3)$  group has 8 generators, each of which corresponds to one of 8 gluon colour states.

The successful formulation of QED and QCD through gauge invariance suggests that the third force of the SM, the weak interaction, may also be formulated as a gauge theory. Weak interactions are mediated by three force carriers, suggesting that its gauge group will have three generators, as is the case for the  $SU(2)$  group. However, the reality is not so simple, and to obtain agreement with experiment the weak and electromagnetic forces must be unified by a single gauge theory. The *electroweak* force is defined by gauge invariance under  $SU(2) \otimes U(1)$  transformations, in a process known as electroweak unification. The SM is therefore a gauge theory based on the invariance of the combined gauge group,

$$SU(3) \otimes SU(2) \otimes U(1). \quad (2.7)$$

### The Higgs mechanism

To maintain invariance in a simple gauge theory, the gauge bosons are required to be massless. For the photons and gluons of QED and QCD this is in agreement with experiment. However, the weak  $W^\pm$  ( $80 \text{ GeV}/c^2$ ) and  $Z$  ( $91 \text{ GeV}/c^2$ ) bosons are far from massless. Mass terms for these particles cannot simply be added to the SM Lagrangian “by hand”, as this would break the fundamental gauge invariance of the theory.

The solution comes in the form of the the Higgs field. When added to the theory, gauge invariance is spontaneously broken by the ground state of the Higgs field, due to its non-zero vacuum expectation value. Although broken by the Higgs ground

---

<sup>1</sup>The special unitarity groups,  $SU(N)$ , are the group of  $n \times n$  unitary matrices of determinant equal to 1.

state, the gauge invariance of the theory as a whole is maintained. The subtlety of this mechanism cannot be appreciated from this brief description; however, it can be shown that the SM Lagrangian density acquires additional Higgs field induced terms corresponding to the weak gauge bosons masses. A similar Higgs mechanism is also required to generate the fermion mass terms, due to electroweak parity violation (see Section 2.2).

The final particle that is predicted by the SM is the massive scalar boson associated to the Higgs field. Until recently the Higgs mechanism remained theoretically attractive, but experimentally unproven, despite many years of experimental attention. Last year the ATLAS and CMS collaborations reported the discovery of a particle with a mass of approximately  $125 \text{ GeV}/c^2$ , consistent with the Higgs boson [7, 8]. If this discovery is confirmed, the final particle that is predicted by the SM will have been found.

### SM as a perturbation theory

The SM has been enormously successful at both predicting and describing experimental data. Observables can be calculated from first principles; however, in practice such calculations are complicated by the infinite number of higher order corrections which contribute to the process. Predictions are therefore obtained by a perturbative approach, in which the process is expanded in powers of the coupling constant of the mediating force. For small coupling constants, a good approximation can be made by considering lowest order interactions only.

A great convenience of the SM is that the mathematically complicated calculations can be summarised in the form of Feynman diagrams, such as those shown for a simple QED process in Figure 2.1. These encapsulate all the relevant information of the process, and can be translated into mathematical form using the “Feynman rules”. Each element of the diagram (i.e. each line and vertex) is assigned an algebraic factor related to the rate of the process. Higher order processes involving loops correspond to higher orders in the perturbation theory, as each vertex contributes a factor of the coupling constant.

## 2.2 Charge-Parity violation

The importance of symmetries in particle physics was discussed in the previous section, with the SM forces generated by local  $SU(3) \otimes SU(2) \otimes U(1)$  gauge symmetry. Attention is now turned to the discrete symmetries of parity, time reversal and charge conjugation<sup>1</sup>. The parity transformation,  $P$ , consists of the simultaneous reflection

---

<sup>1</sup>For a more comprehensive description of the material reviewed in this section, see Refs. [9–11]

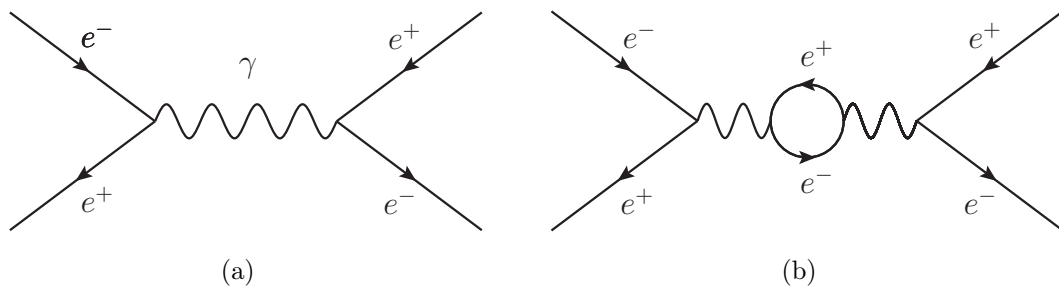


Figure 2.1: A Feynman diagram for electron-positron scattering at **a**) “tree level” (i.e. there are a minimum number of vertices) and **b**) at the higher order, one-loop level.

of the three Cartesian space coordinates,  $x \rightarrow -x$ ,  $y \rightarrow -y$  and  $z \rightarrow -z$ . Similarly, the time-reversal transformation,  $T$ , changes the sign of the time coordinate  $t \rightarrow -t$ . These operations are simple to interpret in a classical setting. For example, consider the velocity,  $\vec{v}$ , of a particle,

$$\vec{v} = \frac{d\vec{r}}{dt}. \quad (2.8)$$

Under  $P$  the position vector  $\vec{r} \rightarrow -\vec{r}$ , and under  $T$  the time coordinate  $t \rightarrow -t$ . Therefore individually both  $P$  and  $T$  invert the sign of  $\vec{v}$ , whilst the simultaneous transformation of  $PT$  leaves  $\vec{v}$  unchanged. The charge conjugation transformation,  $C$ , corresponds to the transformation of any particle into its antiparticle, and has no classical analogue. While the combined  $CPT$  symmetry is thought to be perfectly conserved in quantum field theories such as the SM, the individual  $C$ ,  $P$ ,  $T$  and  $CP$  transformations are all found to be violated by the weak force.

Despite the great success of the standard model, there are still many unexplained phenomena in the observed universe. One such phenomenon is the excess of baryons over antibaryons, without which the matter-based planets, stars and galaxies could not have formed. A particle and antiparticle brought into contact can participate in a process known as *annihilation*, in which the incident particles are converted into particle-antiparticle pairs or energetic photons. It is thought that at some early time in the history of the universe, the majority of matter and antimatter annihilated, and that a small fraction of matter remains due to residual effects. Measurements of the cosmic background radiation show that the density of photons in the universe is a factor of approximately  $10^{10}$  greater than that of baryonic matter. The universe is therefore mostly empty, with only a small fraction occupied by the residual baryonic matter. The necessary ingredients to induce a baryon asymmetry were first described by A. Sakharov [12]:

1. There has to be a baryon-number violating transition.
2.  $CP$  invariance must be violated (otherwise the baryon number violating process,  $i \rightarrow f$ , would be cancelled by the  $CP$  conjugate process,  $\bar{i} \rightarrow \bar{f}$ , and no

net baryon number would be generated).

3. The process satisfying conditions 1 and 2 must occur out of thermal equilibrium. In thermal equilibrium, an interaction and the time-reversed process are equally likely, hence a  $CP$  and baryon number violating process cannot generate an asymmetry.

Baryon number violating processes have not yet been observed by experiment. However, there are various theories of how baryon number could be violated, both within the existing framework of the SM, and in extended models beyond the SM<sup>1</sup>. It is thought that the condition related to thermal equilibrium could have been satisfied during an early “inflationary” period, suggesting that it was around this time that the baryon asymmetry was generated. The condition related to  $CP$ -violation is discussed in the remainder of this section.

The “handedness” of a particle is defined by the orientation of the particle’s spin with respect to its flight direction. The spin of a right-handed particle is orientated along its trajectory, while a left-handed particle has spin with opposite orientation. The parity transformation does not change the spin of a particle, hence  $P$  transforms a left-handed particle into a right-handed one. In the SM, parity is found to be violated in charged-current weak interactions (i.e. processes mediated by  $W^\pm$ ), which interact only with left-handed fermions. Parity violation is incorporated into the formalism by arranging fermion fields into left-handed doublets with weak-isospin quantum number  $T = 1/2$ , and third component of weak-isospin number  $T_3 = \pm 1/2$ ,

$$\begin{pmatrix} \nu_l \\ l^- \end{pmatrix}_L, \quad \begin{pmatrix} u_g \\ d'_g \end{pmatrix}_L, \quad (2.9)$$

where  $l = e, \mu, \tau$  and the quark generation number  $g = 1, 2, 3$ . Weak-isospin is the conserved “charge” of the weak interaction, in analogy to electric and colour charge in QED and QCD. Left-handed fermions are “rotated” within a weak-isospin doublet by the emission of a  $W^\pm$ , thus coupling the components of a doublet. The down-type weak eigenstates that form the lower part of the weak-isospin doublets,  $d'_g$ , are not the same as the down-type mass eigenstates that participate in the strong interaction,  $d_g$ . Intergenerational quark mixing is observed in experiment, hence the  $d'_g$  are superpositions of the three down-type mass eigenstates,  $d, s, b$ . This allows each  $u_g$  to couple to each of the down-type quarks in charged current weak interactions (e.g.  $u \rightarrow W^+d$ ,  $W^- \rightarrow \bar{u}s$ ,  $\bar{b} \rightarrow W^+\bar{c}$ , etc). The right-handed fermions do not participate in charged current weak interactions, and are therefore arranged

---

<sup>1</sup>Baryon number violation is not discussed further here. See, for example, Ref. [9] p.448-53 for further discussion of baryon number violation.

into weak-isospin singlets with  $T = 0 = T_3$ ,

$$(\nu_l)_R, \quad (l^-)_R, \quad (u_g)_R, \quad (d_g)_R. \quad (2.10)$$

Theoretically,  $CP$  violation can be incorporated into both the strong and weak sectors of the SM. However,  $CP$ -violation due to the strong force has not been observed, giving rise to what is known as the “strong  $CP$  problem”.  $CP$  violation has been measured in charged-current weak interactions. This is incorporated by the SM in couplings between the fermions and the Higgs field. A fermion mass term in the standard model Lagrangian density contains both left and right-handed field components,  $m\bar{\psi}\psi = m(\bar{\psi}_L\psi_R + \bar{\psi}_R\psi_L)$ , where the subscripts  $L,R$  refer to the handedness of the particle. To obtain such a term in electroweak theory requires mixing between the left-handed weak-isospin doublets and right-handed singlets. This is achieved by introducing an  $SU(2)$  Higgs doublet which mixes the left and right components of the fermion fields. Electroweak gauge invariance is maintained using the principle of spontaneous symmetry breaking in an analogous approach to that used for the massive weak gauge bosons (see Section 2.1.2). The values of the fermion masses are proportional to the “Yukawa coupling” constants, which must be experimentally determined.

The form of the Yukawa couplings are quite arbitrary. With three generations of quarks they take the general form of  $3 \times 3$  complex matrices which mix the mass eigenstates<sup>1</sup>. To obtain quark masses in terms of the mass eigenstates, the Yukawa couplings can be diagonalised with four independent unitary transformation matrices (i.e. one for each of the weak eigenstates:  $(u_g)_L, (u_g)_R, (d'_g)_L, (d_g)_R$ ). This change of basis does not influence the strong, electromagnetic or neutral-current weak forces, as these treat left and right-handed states identically. However, for the charged-current weak force, the unitary matrices combine to form a  $3 \times 3$  unitary matrix known as the Cabibbo-Kobayashi-Maskawa (CKM) matrix,  $\mathbf{V}_{CKM}$ ,

$$\begin{pmatrix} d' \\ s' \\ b' \end{pmatrix} = \begin{pmatrix} V_{ud} & V_{us} & V_{ub} \\ V_{cd} & V_{cs} & V_{cb} \\ V_{td} & V_{ts} & V_{tb} \end{pmatrix} \begin{pmatrix} d \\ s \\ b \end{pmatrix} = \mathbf{V}_{CKM} \begin{pmatrix} d \\ s \\ b \end{pmatrix}. \quad (2.11)$$

This matrix relates the mass eigenstates,  $d, s, b$ , to the weak eigenstates,  $d', s', b'$ . Each element,  $V_{ij}$ , represents the coupling strength between quarks  $q_i$  and  $q_j$  at a  $W^\pm$  vertex. For example, the decay rate of a  $b$  quark to a  $c$  quark by the emission of a  $W^-$  is proportional to  $|V_{cb}|^2$ .

As the Yukawa couplings are quite arbitrary, so too are the corresponding mass matrices from which  $\mathbf{V}_{CKM}$  is derived. An arbitrary  $3 \times 3$  complex matrix

<sup>1</sup>The mass eigenstates are defined as the flavour-conserving eigenstates of the strong force.

has  $3 \times 3 \times 2 = 18$  free parameters. The unitarity of  $\mathbf{V}_{CKM}$  applies 9 constraints, leaving 9 free parameters. Six of these can be attributed to the phases of the fermion fields. However, it is the relative phase of the various quark fields that is of physical relevance, hence 5 of the 6 quark phases can be absorbed. This leaves a total of 4 free parameters, which are attributed to 3 Euler mixing angles and a single complex phase. A complex phase,  $\delta$ , will enter a general wavefunction as  $\exp[i(\omega t + \delta)]$ , which is clearly not invariant under the  $T$  transformation (i.e.  $t \rightarrow -t$ ). Assuming  $CPT$  invariance, the breaking of  $T$  implies that  $CP$  is also violated.

There are an infinite number of ways of expressing the elements of  $\mathbf{V}_{CKM}$  in terms of three angles and a complex phase. The commonly used Wolfenstein parameterisation expresses the elements in powers of the real parameter  $\lambda$ ,

$$\mathbf{V}_{CKM} = \begin{pmatrix} 1 - \lambda^2/2 & \lambda & A\lambda^3(\rho - i\eta) \\ -\lambda & 1 - \lambda^2/2 & A\lambda^2 \\ A\lambda^3(1 - \rho - i\eta) & -A\lambda^2 & 1 \end{pmatrix} + \mathcal{O}(\lambda^4) + \dots, \quad (2.12)$$

where by experiment  $\lambda \approx 0.23$ . This parameterisation shows the hierarchical nature of charged-current weak interactions, with diagonal elements of order 1, and off-diagonal elements of order  $\lambda$  or smaller. This scheme was suggested due to measurements showing  $|V_{ub}|^2 \ll |V_{cb}|^2 \ll |V_{us}|^2 \ll 1$ . The relative coupling strength between quarks is found to be approximately 1 within a generation, of order  $\lambda$  between generations  $1 \leftrightarrow 2$ , of order  $\lambda^2$  between generations  $2 \leftrightarrow 3$ , and of order  $\lambda^3$  between generations  $1 \leftrightarrow 3$ .

The unitarity of the  $\mathbf{V}_{CKM}$  matrix is used to establish some useful relations between the matrix elements. Nine such relations exist, three of which correspond to *weak universality*:

$$\sum_{i=1}^3 |V_{ij}|^2 = 1; \quad j = 1, 2, 3. \quad (2.13)$$

This is equivalent to the statement that the charged coupling of each up-type quark to all of the down-type quarks mass-eigenstates is of universal strength (i.e. each of the  $SU(2)$  doublets  $\begin{pmatrix} u \\ d' \end{pmatrix}, \begin{pmatrix} c \\ s' \end{pmatrix}, \begin{pmatrix} t \\ b' \end{pmatrix}$  have third components of weak-isospin  $\begin{pmatrix} +1/2 \\ -1/2 \end{pmatrix}$ ). The other unitarity relations involve the  $CP$ -violating complex phase,

$$\sum_{i=1}^3 V_{ji} V_{ki}^* = 0 = \sum_{i=1}^3 V_{ij} V_{ik}^*; \quad j, k = 1, 2, 3; \quad j \neq k. \quad (2.14)$$

Each of these relations can be drawn as a triangle in the complex plane. In expanded

form, the 6 triangles are defined by,

$$V_{ud}V_{us}^* + V_{cd}V_{cs}^* + V_{td}V_{ts}^* = 0 \quad (jk) \quad (2.15a)$$

$$V_{ud}V_{cd}^* + V_{us}V_{cs}^* + V_{ub}V_{cb}^* = 0 \quad (uc) \quad (2.15b)$$

$$V_{us}V_{ub}^* + V_{cs}V_{cb}^* + V_{ts}V_{tb}^* = 0 \quad (sb) \quad (2.15c)$$

$$V_{td}V_{cd}^* + V_{ts}V_{cs}^* + V_{tb}V_{cb}^* = 0 \quad (tc) \quad (2.15d)$$

$$V_{td}V_{ud}^* + V_{ts}V_{us}^* + V_{tb}V_{ub}^* = 0 \quad (tu) \quad (2.15e)$$

$$V_{ud}V_{ub}^* + V_{cd}V_{cb}^* + V_{td}V_{tb}^* = 0 \quad (db). \quad (2.15f)$$

By inspection of the Wolfenstein parameterisation (Equation 2.12), the first, second and third components of Equations 2.15a and 2.15b are found to be of order  $\lambda$ ,  $\lambda$  and  $\lambda^5$ . These relations represent “squashed” triangles in the complex plane, as one of the lengths is significantly smaller than the other two (i.e.  $\lambda \gg \lambda^5$ ). Similarly, the lengths of the triangles defined by Equations 2.15c and 2.15d are of order  $\lambda^4$ ,  $\lambda^2$  and  $\lambda^2$ , resulting in two further squashed triangles, albeit less so. The remaining two triangles, defined by Equations 2.15e and 2.15f, have lengths of order  $\lambda^3$ ,  $\lambda^3$  and  $\lambda^3$ , and therefore represent a triangle with sides of approximately equal length. The triangle defined by Equation 2.15f is shown in Figure 2.2.

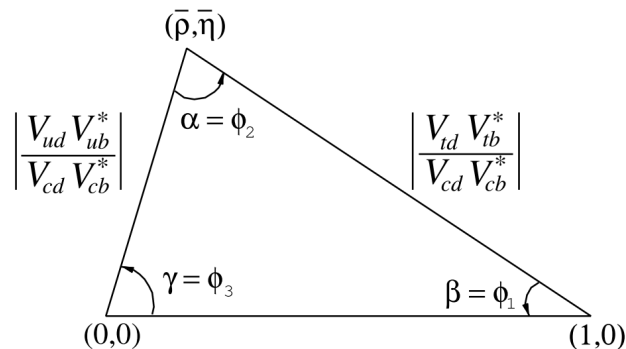


Figure 2.2: The unitary triangle defined by the relation,  $V_{ud}V_{ub}^* + V_{cd}V_{cb}^* + V_{td}V_{tb}^* = 0$ , where  $\bar{\rho} = \rho\bar{c}$  and  $\bar{\eta} = \eta\bar{c}$  with  $\bar{c} = \sqrt{1 - \lambda^2} = (1 - \frac{\lambda^2}{2} - \frac{\lambda^4}{8} + \dots)$ . Figure from Ref. [11].

The side-lengths and angles of the unitary triangles can be determined by measuring decay rates and asymmetries of interactions involving the flavour-violating  $W^\pm$  bosons. The parameters of the unitarity triangle shown in Figure 2.2 have been put under the greatest experimental scrutiny, as the large angles of this triangle lend themselves to experimental study. In addition, many of the parameters in this triangle are measurable with  $B$  and  $D$  meson decays, which are copiously produced at  $\Upsilon(4S)$  resonance colliders, and high energy hadron colliders such as the Tevatron and the LHC. Particle events can be reconstructed with great precision due to the

relatively long lifetimes of  $B$  and  $D$  mesons, which result in large flight distances in the laboratory frame.

It is generally accepted that the magnitude of  $CP$  violation in the SM is not large enough (by several orders of magnitude) to account for the observed baryon number asymmetry. The experimental constraints on the unitarity triangle of Figure 2.2 are shown in Figure 2.3, with all  $CP$  violating measurements consistent with having been induced by a single complex phase. The primary aim of modern flavour physics experiments is to measure  $CP$  violating processes to high levels of precision, in the hope that deviations from the SM will be observed which are indicative of physics beyond the SM. Measurements are generally said to belong to one of three categories:

- **Direct:** The decay amplitude of a particular interaction is different to that of the conjugate process (i.e.  $\Gamma[M \rightarrow f] \neq \Gamma[\bar{M} \rightarrow \bar{f}]$ ).
- **Mixing:**  $CP$  violation in the mixing between neutral particle and antiparticle states (i.e. the probability of  $M^0 \rightarrow \bar{M}^0$  is different to that of  $\bar{M}^0 \rightarrow M^0$ ).
- **Interference:** The mixing and decay amplitudes interfere to cause  $CP$ -violation.

The analysis presented in the latter parts of this thesis falls into the second of these categories.

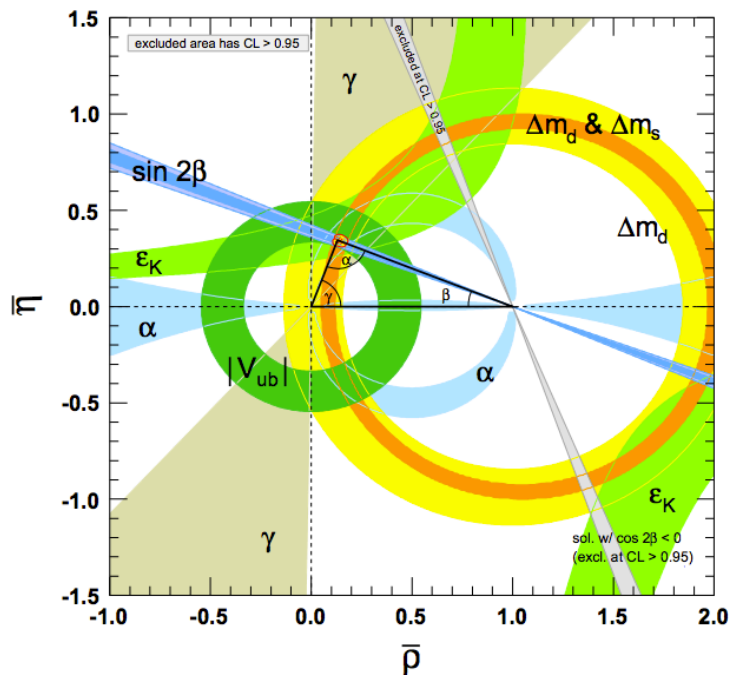


Figure 2.3: Various measurements related to  $CP$  violation are shown in the complex plane. The particular unitarity triangle constrained by these measurements is overlaid (i.e. that from Figure 2.2). Figure from Ref. [11].

## 2.3 *B*-meson mixing

Neutral *B* mesons are one of only a few particles that have the interesting characteristic of oscillating between particle and antiparticle states<sup>1</sup>. Oscillations are described by the exchange of two *W* bosons in an internal loop, as shown by the Feynman “box” diagrams in Figure 2.4. The masses of the particles produced at an experiment are limited by the energy of the experiment’s collider. In mixing-type interactions, energy scales several orders of magnitude higher than the collider energy can be probed by virtual particles within box diagram loops. Accurate measurements of the parameters associated with these oscillations are therefore a stern test of the standard model and a sensitive probe of new physics. The mixing formalism is similar for neutral *K*, *D*, *B* and *B<sub>s</sub>* mesons, with conventional differences arising due to the particular masses, lifetimes and oscillation rates of the particles in each system. The remainder of this section focuses on the case of *B<sup>0</sup>* and *B<sub>s</sub><sup>0</sup>* mixing. For brevity, *B<sub>q</sub>* will often be used to refer to both, where *q* represents the *d* or *s* partners of the *b* quark.

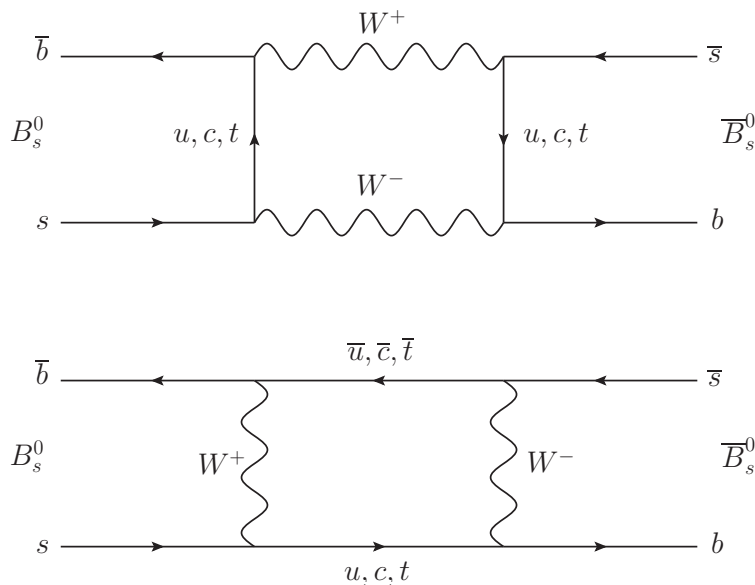


Figure 2.4: The Feynman diagrams for  $B_s^0$  mixing. The equivalent  $B^0$  mixing diagrams are obtained by replacing  $s \rightarrow d$  and  $\bar{s} \rightarrow \bar{d}$ .

The time evolution of the *B*-meson system is governed by the Schrödinger equation,

$$i \frac{d}{dt} \begin{pmatrix} |B_q^0(t)\rangle \\ |\bar{B}_q^0(t)\rangle \end{pmatrix} = \left( M^q - \frac{i}{2} \Gamma^q \right) \begin{pmatrix} |B_q^0(t)\rangle \\ |\bar{B}_q^0(t)\rangle \end{pmatrix}, \quad (2.16)$$

where  $|B_q^0(t)\rangle$  and  $|\bar{B}_q^0(t)\rangle$  are the flavour (i.e. strong) eigenstates, and  $M^q$  and  $\Gamma^q$  are

<sup>1</sup>Only a brief introduction to the mixing formalism is given. For a more comprehensive treatment see Ref. [13].

the Hermitian  $2 \times 2$  mass and decay mixing matrices. In the absence of mixing,  $M^q$  and  $\Gamma^q$  are diagonal matrices, with elements  $M_{11}$  and  $M_{22}$  representing the masses of the  $B_q^0$  and  $\bar{B}_q^0$ . Particle-antiparticle mixing implies that the off-diagonal elements are non-zero, and potentially complex due to their dependence on  $\mathbf{V}_{CKM}$ . The off-diagonal elements of  $M_{12}^q$  correspond to off-shell quark lines in the box diagrams (e.g. the  $t$  quark), whereas  $\Gamma_{12}^q$  corresponds to on-shell internal quark lines (e.g. the  $u$  or  $c$  quarks). It can be seen by expanding Equation 2.16 that the flavour states are not pure eigenstates of the weak interaction. The physical eigenstates are interpreted as a superposition of the well defined flavour eigenstates. By diagonalising  $M^q - i\Gamma^q/2$ , the light and heavy physical mass eigenstates,  $B_L^q$  and  $B_H^q$ , are obtained,

$$|B_L^q(t)\rangle = p|B_q^0(t)\rangle + q|\bar{B}_q^0(t)\rangle, \quad |B_H^q(t)\rangle = p|B_q^0(t)\rangle - q|\bar{B}_q^0(t)\rangle, \quad (2.17)$$

with the complex numbers  $p$  and  $q$  satisfying  $|p|^2 + |q|^2 = 1$ . In the absence of  $CP$  violation,  $|p/q| = 1$  and the physical eigenstates are  $CP$  eigenstates with eigenvalues  $\pm 1$  (i.e.  $CP|B_L^q(t)\rangle = +1|B_L^q(t)\rangle$ ,  $CP|B_H^q(t)\rangle = -1|B_H^q(t)\rangle$ ).

Theoretical calculations involving neutral meson mixing are often related to the three physical quantities:  $|M_{12}^q|$ ,  $|\Gamma_{12}^q|$  and the relative phase  $\phi_q = \arg(-M_{12}^q/\Gamma_{12}^q)$ . These can be related to the experimentally measured properties of the physical eigenstates,  $B_L^q$  and  $B_H^q$ . The mass difference,  $\Delta m_q$ , is defined as,

$$\Delta m_q \equiv M_H^q - M_L^q = 2|M_{12}^q| \left( 1 - \frac{1}{8} \frac{|\Gamma_{12}^q|^2}{|M_{12}^q|^2} \sin^2 \phi_q + \dots \right). \quad (2.18)$$

For  $B$  mesons the ratio  $|\Gamma_{12}^q|/|M_{12}^q|$  is approximately  $5 \times 10^{-3}$ , reducing Equation 2.18 to  $\Delta m_q \approx 2|M_{12}^q|$ . Since  $M_{12}^q$  corresponds to the virtual part of the box diagrams, it is thought that measurements of  $\Delta m_q$  are a sensitive probe of new physics. Similarly, the decay rate difference,  $\Delta \Gamma_q$ ,

$$\Delta \Gamma_q \equiv \Gamma_L^q - \Gamma_H^q = 2|\Gamma_{12}^q| \cos \phi \left( 1 + \frac{1}{8} \frac{|\Gamma_{12}^q|^2}{|M_{12}^q|^2} \sin^2 \phi_q + \dots \right), \quad (2.19)$$

reduces to approximately  $\Delta \Gamma_q \approx 2|\Gamma_{12}^q| \cos \phi$ .  $\Delta \Gamma_q$  is related to the on-shell parts of the box diagrams and is thought to be less sensitive to the effects of new physics than  $\Delta m_q$ . It can be shown that a system that is an initially pure flavour state of  $B_q^0$  or  $\bar{B}_q^0$  will evolve in time according to,

$$|B_q^0(t)\rangle = g_+|B_q^0(t)\rangle + \frac{q}{p}g_-|\bar{B}_q^0(t)\rangle, \quad (2.20a)$$

$$|\bar{B}_q^0(t)\rangle = g_+|\bar{B}_q^0(t)\rangle + \frac{p}{q}g_-|B_q^0(t)\rangle, \quad (2.20b)$$

where  $g_{\pm}$  are defined in terms of the mass and decay width differences,

$$|g_{\pm}(t)|^2 = \frac{e^{-\Gamma_q t}}{2} \left[ \cosh\left(\frac{\Delta\Gamma_q t}{2}\right) \pm \cos(\Delta m_q t) \right]. \quad (2.21)$$

A third mixing quantity that provides independent information about  $B$  mixing is the *flavour-specific* asymmetry,  $a_{\text{fs}}$ , which is a measure of the difference between the mass and the  $CP$  eigenstates,

$$a_{\text{fs}} = \frac{|\Gamma_{12}^q|}{|M_{12}^q|} \sin\phi = -2 \left( \left| \frac{q}{p} \right| - 1 \right). \quad (2.22)$$

The term flavour-specific refers to processes in which  $B_q^0 \rightarrow f$  is allowed at tree level, but the decay to the conjugate final state,  $B_q^0 \rightarrow \bar{f}$ , is not. In terms of the observable particle decay widths,  $a_{\text{fs}}$  is defined as the asymmetry of  $B$ -mesons that oscillate prior to decay,

$$a_{\text{fs}}^q = \frac{\Gamma(\bar{B}_q^0 \rightarrow B_q^0 \rightarrow f) - \Gamma(B_q^0 \rightarrow \bar{B}_q^0 \rightarrow \bar{f})}{\Gamma(\bar{B}_q^0 \rightarrow B_q^0 \rightarrow f) + \Gamma(B_q^0 \rightarrow \bar{B}_q^0 \rightarrow \bar{f})} \quad (2.23)$$

In the SM the flavour-specific asymmetry is predicted to be small for both  $B^0$  and  $B_s^0$  mixing [14],

$$a_{\text{fs}}^d = (-4.1 \pm 0.6) \times 10^{-4}, \quad a_{\text{fs}}^s = (1.9 \pm 0.3) \times 10^{-5}. \quad (2.24)$$

New physics entering as a change in the magnitude or phase of  $M_{12}$  could enhance  $a_{\text{fs}}$  by as much as a factor of  $\sim 250$  [15]. Recent measurements from the DØ experiment [16, 17] disagree with the SM predictions at approximately the  $4\sigma$  confidence level, hinting that physics beyond the SM may be manifest through this parameter. In the latter parts of this thesis an independent measurement of the  $a_{\text{fs}}^s$  is presented, using data collected at the LHCb experiment. Further details regarding the extraction of  $a_{\text{fs}}^s$  from experimental data are reserved for Section 6.1.



## PARTICLE ACCELERATION AND DETECTION AT LHCb

The Large Hadron Collider (LHC) [18–20] is the most recent addition to the system of particle accelerators located at the European Organisation for Nuclear Research (CERN), the world’s largest particle physics research laboratory. It is located below the Swiss-French border in the Geneva region, as shown in Figure 3.1. Constructed between 1998 and 2008, the LHC was built to supply the various experiments located around the ring with high energy particle interactions. Although the accelerator is used to collide both protons and heavy ions, the following discussion refers to proton collisions alone as these are the subject of this thesis. The data collected from these interactions are analysed in the hope of discovering new physics processes beyond those predicted by the Standard Model (SM).

This chapter describes the various hardware and computing systems that facilitate the production, detection and analysis of proton-proton collisions. The particle accelerating system is first described in Section 3.1. The LHCb experiment sub-detectors, triggering system and computing strategy are then described in Sections 3.2, 3.3 and 3.4, respectively.

### 3.1 Particle acceleration

High energy particle physics has been explored at CERN using a series of accelerators since the 1950s. Experimental discoveries have confirmed and helped to develop our theoretical understanding of the way particles interact. These successes have demanded the development of accelerators capable of providing higher energy and higher frequency collisions to the particle detectors. The accelerators that were originally constructed to provide interactions at lower energy experiments have been upgraded and connected by transfer tunnels to form the LHC injector chain. This supplies the LHC with well focused proton beams with enough energy to be further



Figure 3.1: An aerial photograph of the CERN site when looking towards the Geneva region. The LHC is located approximately 100 m underground, below the path shown by the orange line. Photograph from the CERN photography service [21].

accelerated by the LHC.

### 3.1.1 Injector chain

Protons are obtained from hydrogen gas and accelerated in the first stage of the injector chain to 50 MeV by a linear accelerator called Linac2. The protons are then passed via an 80 m long high-current beam line to the Proton Synchrotron Complex (PSC), comprising three proton synchrotrons of increasing radius. The proton energy is sequentially increased from 50 MeV to 1.4 GeV, 25 GeV and 450 GeV by the Proton Synchrotron Booster (PSB), Proton Synchrotron (PS) and Super Proton Synchrotron (SPS), respectively. To provide proton bunches that are suitably focused for further acceleration in the LHC, the accelerators in the injector chain were upgraded substantially between 1995 and 2000. The injector chain and LHC are shown in Figure 3.2.

### 3.1.2 The Large Hadron Collider

The LHC is a 27 km circumference, two-ring particle accelerator designed to collide protons with a centre-of-mass energy of 14 TeV. Bunches of protons from the injector chain are accelerated in opposite directions around the ring and collided at fixed interaction points. The LHC tunnel was originally excavated for the Large Electron-Positron Collider (LEP) and comprises 8 arced and 8 straight sections.

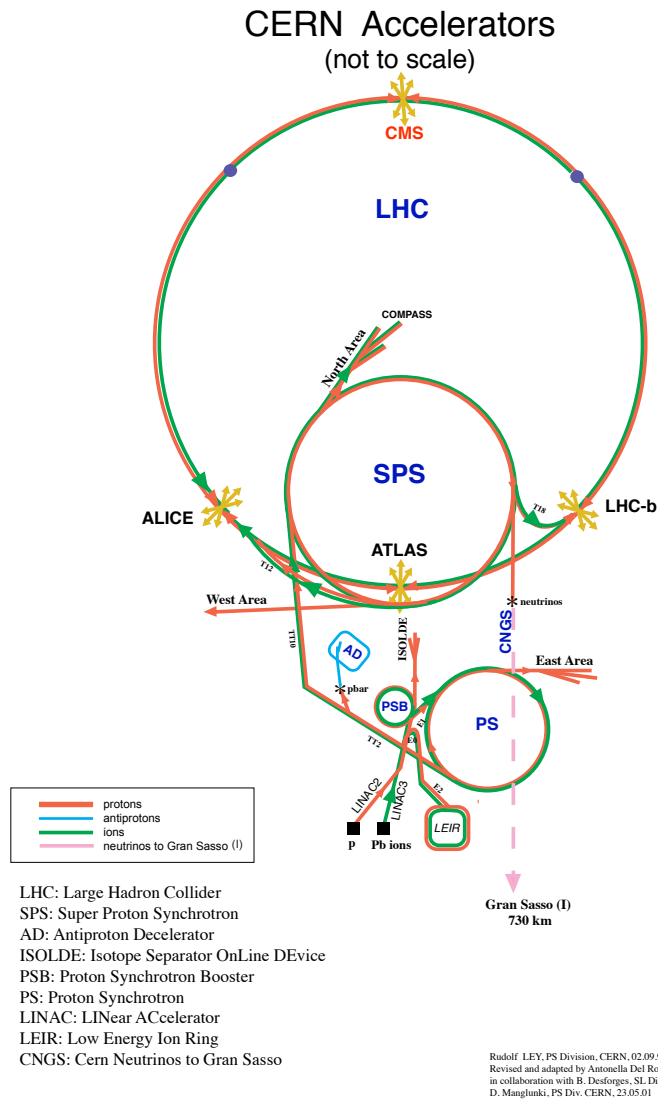


Figure 3.2: The LHC injector chain and LHC. The locations of the largest experiments and research facilities are labelled. Figure from Ref. [22].

Synchrotron radiation losses in the arced sections are compensated by accelerating Radio Frequency (RF) cavities in one of the straight sections. Protons experience less synchrotron radiation than electrons and so would be better suited to a more circular trajectory with shorter straight sections. However, the LHC benefited from significantly reduced construction cost by using the LEP tunnel in its original state.

The LHC uses twin bore magnets to facilitate the acceleration of protons in opposite directions. The two beampipes share a common support and cryostat system, as shown in Figure 3.3. Once accelerated to high energies, strong bending magnets are required to keep the protons within the LHC beampipe. The LHC uses liquid helium cooled superconducting dipole magnets that are capable of producing an 8.33 Tesla magnetic field for the circulation of 7 TeV proton beams.

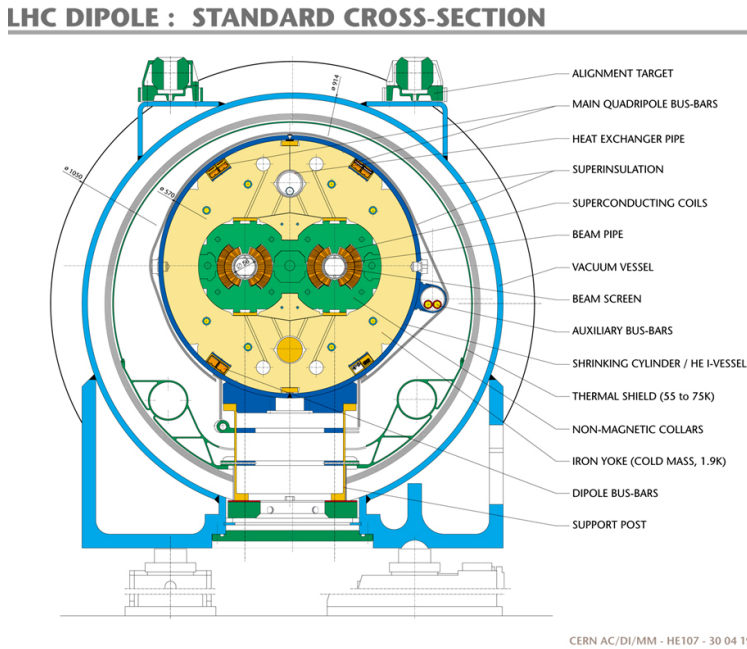


Figure 3.3: A cross section of the LHC twin-bore beampipe system.

### 3.1.3 LHC performance

One of the most important beam related parameters for the LHC experiments is the beam energy. The interactions provided by the LHC in 2011 are from proton-proton collisions with a centre of mass energy of 7 TeV, half of the nominal LHC design energy. This does not have a significantly negative impact on most LHCb analyses, as they involve particles such as bottom and charm mesons that are still abundantly produced at this lower energy.

A second parameter of particular interest to the experiments is the instantaneous *luminosity*, which is a measure of the particle collision rate. The number of events,  $N_{event}$ , produced at a collider such as the LHC is given by,

$$N_{event} = L\sigma_{event}, \quad (3.1)$$

where the integrated luminosity,  $L$ , is the integral over time of the instantaneous luminosity,  $\mathcal{L}$ , for an event type with cross section  $\sigma_{event}$ . The instantaneous luminosity for a gaussian beam distribution is given by,

$$\mathcal{L} = \frac{N_b^2 n_b f \gamma_r}{4\pi \varepsilon_n \beta^*} F, \quad (3.2)$$

where  $N_b$  is the number of particles in each bunch,  $n_b$  is the number of bunches in each beam,  $f$  is the frequency of beam revolution,  $\gamma_r$  is the relativistic gamma factor,  $F$  is the geometric luminosity reduction factor,  $\varepsilon_n$  is the normalised transverse

beam emittance and  $\beta^*$  is the amplitude function evaluated at the beam interaction region. The transverse emittance is a beam quality parameter related to how close the protons within a bunch are to one another in the direction perpendicular to the beam direction. It is approximately equal to the smallest aperture that the bunch could pass through. The amplitude function is a measure of how well focused the beam is at the interaction region. It is commonly referred to as the distance from the interaction region along the beam axis that the beam is twice its width at the interaction region.

The machine operators continually improved the LHC performance throughout 2010 and 2011, gradually moving the machine towards its design performance, corresponding to instantaneous luminosities of the order  $10^{34} \text{ cm}^{-2} \text{ s}^{-1}$ . The maximum number of bunches that can be stored within each LHC beam is 2808, however for early LHC running the beams had only a few bunches per beam. By the end of 2011 the LHC was running with 1380 bunches per beam. The number of protons per bunch was increased early in operation to the nominal value of approximately  $1.15 \times 10^{11}$  as this was the simplest way to achieve high instantaneous luminosities during early data taking.

The LHCb detector aims to trigger on events containing bottom and charm mesons. These can be distinguished from background events by identifying secondary vertices that are geometrically separated from the main interaction region. It becomes difficult to distinguish these types of event when more than one proton-proton interaction occurs within a single bunch crossing. The beams are intentionally misaligned at the LHCb interaction region to increase the fraction of events with only one primary interaction. This comes at the expense of a reduced instantaneous luminosity of approximately  $10^{32} \text{ cm}^{-2} \text{ s}^{-1}$ , which was consistently achieved in the data collection runs towards the end of 2011.

## 3.2 The LHCb detector

LHCb is a second generation  $B$ -physics experiment situated at the LHC. It aims to build on the impressive progress made over the past decade by other  $B$ -physics experiments such as BABAR and Belle, with interesting measurements having also recently come from the DØ and CDF experiments at the Tevatron. The current experimental results agree very closely with the Standard Model (SM). However, the amount of  $CP$  violation in the SM does not explain the matter-antimatter asymmetry that we observe through the absence of antimatter in the universe. The LHCb experiment aims to discover new physics beyond the SM by precise measurements of the CKM matrix parameters and the observation of rare or forbidden  $B$ -decay modes. New sources of  $CP$  violation could surface through changes in the expected

$CP$  phases due to the virtual effects of new particles in loop diagrams.

The LHCb detector [23] is located approximately 100 m underground in a cavern that previously housed the DELPHI experiment. In a proton collider,  $b\bar{b}$  pairs are most often produced by parton-parton interactions where one parton has significantly larger energy than the other. In this scenario the  $b\bar{b}$  pair are boosted in the direction of the higher energy parton in the laboratory rest frame, resulting in highly correlated  $b$  and  $\bar{b}$  flight directions, as shown by Figure 3.4.

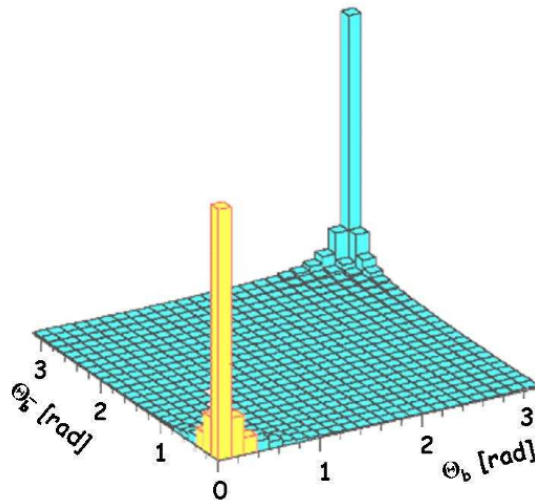


Figure 3.4: The  $b\bar{b}$  production cross section as a function of polar angle with respect to the beam axis, as simulated by PYTHIA [24]. The particles predominantly occupy the cone shaped regions around the beampipe axis at  $\theta = 0$  and  $\pi$ . Figure from Ref. [25].

The detector has been designed to take advantage of this spatial correlation by covering the high pseudorapidity (defined in next section) region to one side of the interaction region. The detector has a pseudorapidity acceptance of  $1.9 < \eta < 4.9$ , with 10–300 mrad and 10–250 mrad angular acceptance in the horizontal (charged particle bending) plane and vertical plane, respectively [26]. The layout of the LHCb sub-detectors is shown in Figure 3.5.

### 3.2.1 The LHCb coordinate system

LHCb uses a right-handed Cartesian coordinate system. The  $z$ -axis runs through the beampipe, pointing from the interaction region towards the muon detectors at the other end of the detector. The  $y$ -direction points vertically upwards and the  $x$ -direction points away from the centre of the LHC ring. The detector region near to the proton interaction region is referred to as *upstream*, and particles moving towards the other LHCb sub-detectors are said to travel *downstream*.

The pseudorapidity,  $\eta$ , is a commonly used parameter in particle physics that

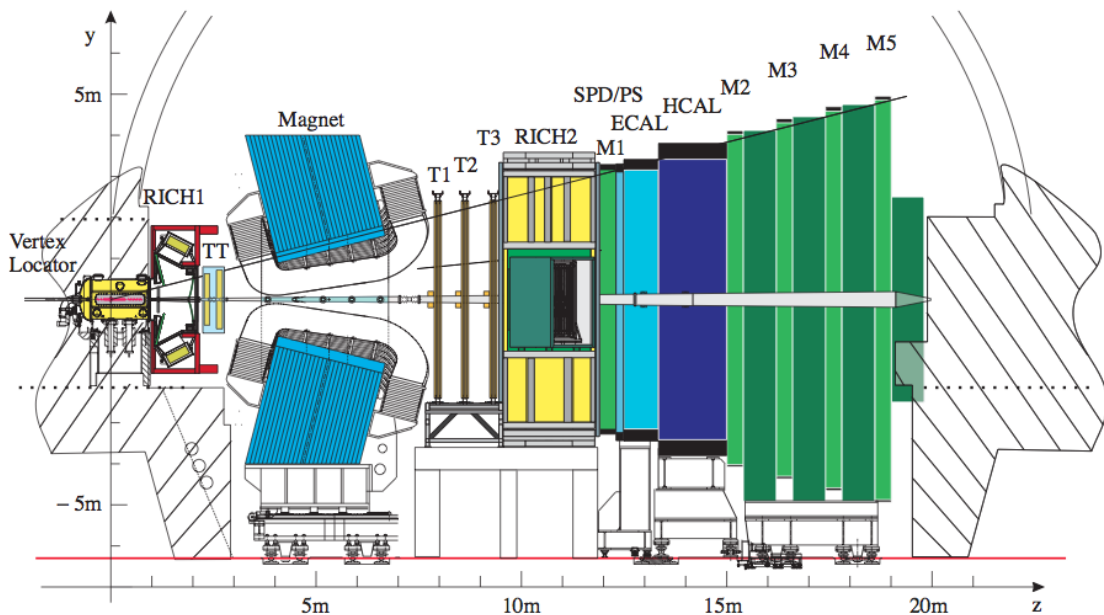


Figure 3.5: A schematic of the LHCb spectrometer. The sub-detectors are listed from the downstream interaction region ( $z = 0$ ) towards the upstream region: Vertex Locator (VELO), RICH1, Tracker Turicensis (TT), dipole magnet, Tracking stations (T1-3), RICH2, Scintillating Pad Detector (SPD), Calorimeter System (E/HCAL) and Muon System (M1-5). Figure from Ref. [27].

describes the position of a track with respect to the beampipe axis. It is defined as,

$$\eta = -\ln \left[ \tan \left( \frac{\theta}{2} \right) \right], \quad (3.3)$$

where  $\theta$  is the angle of a particle track with respect to the beam axis. The pseudorapidity is equal to zero for tracks travelling perpendicularly to the beam axis and goes to infinity as  $\theta$  approaches zero. Another commonly used coordinate is the azimuthal angle,  $\phi$ , which is defined in the  $x$ - $y$  plane, and is equal to zero when pointing along the  $x$ -axis.

### 3.2.2 Dipole magnet

A charged particle traversing a magnetic field experiences a force in the direction perpendicular to its motion and the field in which it is travelling. The direction of the force,  $F$ , depends on the charge,  $q$ , of the particle by the relation  $F = q(\mathbf{v} \times \mathbf{B})$ . The radius,  $r$ , of the curvature is related to the strength of the magnetic field,  $B$ , and the particle momentum in the bending plane,  $p_b$ , via the relation  $r = p_b/Bq$ . Thus it is possible to infer the charge and momentum of a particle by measuring the direction and radius of the track curvature.

The LHCb experiment uses a dipole magnet [28] with an integrated magnetic field of  $\int Bdl = 4 \text{ Tm}$  over 10 m in the  $z$ -direction. The magnet produces a field in

the  $y$ -direction of the detector, leading to curved trajectories in the  $x-z$  plane. The strength of the magnetic field in the  $y-z$  plane is shown in Figure 3.6. Differences in detector acceptance or performance in each half of the detector could induce a charge asymmetry in the recorded data, as particles with opposite charge are bent towards the different halves. An essential feature of the LHCb magnet for analyses involving small asymmetries<sup>1</sup> is the ability to reverse the polarity of the magnetic field. Detector bias can be partially cancelled by averaging results obtained from data that are collected with the different magnet polarities.

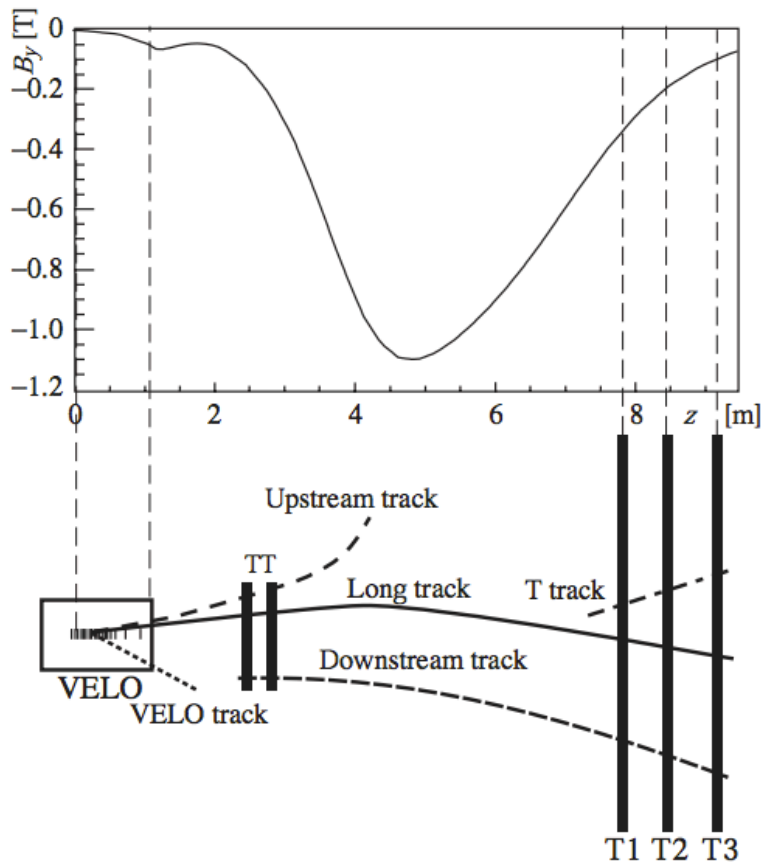


Figure 3.6: **Top:** The  $B_y$  component of the magnetic field along the  $z$ -direction for a particular magnet polarity. The strength of the field at a particular position is known with a relative precision of  $\delta B/B \sim 4 \times 10^{-4}$ . **Bottom:** The relative position of the tracking sub-detectors with respect to the magnetic field. Schematic examples of the various LHCb track types are shown. Figure from Ref. [27].

### 3.2.3 Tracking system

The LHCb tracking system is the set of sub-detectors that are used to reconstruct the trajectories of charged particles. It consists of a silicon-strip VERTex LOcator (VELO) and a set of four tracking stations: the Tracker Turicensis (TT) and the

<sup>1</sup> Such as the flavour-specific asymmetry measurement presented in Chapter 7.

three downstream tracking stations (T1–T3). The VELO [29] is used to reconstruct the primary vertices, and the detached vertices associated with the decay of short lived particles. Short tracks reconstructed in the VELO are used as seeds for *long track* reconstruction using hits in the further downstream tracking stations.

The tracking detectors are required to have excellent spatial resolution in order to efficiently reconstruct particle trajectories and keep the fake particle track reconstruction rate low. The tracking system comprises over  $12\text{ m}^2$  of silicon-strip detectors, with a read-out pitch in the range  $40\text{--}200\ \mu\text{m}$  and a position resolution of approximately  $60\ \mu\text{m}$ . The LHCb detector obtains excellent momentum resolution, of the order  $\sim 0.5\%$  of the particle’s momentum. Simulations [30] have shown that for particle momenta up to around  $80\text{ GeV}/c$ , the momentum resolution of the LHCb detector is dominated by multiple scattering.

The TT is located upstream of the LHCb magnet, whilst the three tracking stations, T1–3, are located downstream of the magnet. Each downstream tracking station is split into two sections: a silicon-strip Inner Tracker (IT) and a gas filled straw-tube Outer Tracker (OT). The IT surrounds the beampipe to give better resolution in the region with the highest particle flux. The OT covers the remaining outer acceptance region.

A particle passing through a silicon strip sensor will produce an electronic pulse in one or several adjacent silicon strips. This is referred to as a “cluster”. A typical cluster is 1–2 strips wide, although a small fraction of cluster are wider than 2 strips. The position of clusters with hits in more than one silicon strip is calculated as the charge-weighted average of the individual strip coordinates [31]. Clusters from the different layers of the tracking system are combined and reconstructed as tracks that represent the trajectory of the particle associated to the clusters.

### Vertex locator

Bottom and charm mesons have mean lifetimes of approximately 1 ps. This corresponds to typical flight distances from the primary vertex of approximately 1 cm. To measure the position of these vertices with sufficient precision to efficiently identify if a particle originated from a primary or detached vertex, the VELO is positioned around the interaction region, with the closest active region of the sensors only 8 mm from the beam. It comprises 88 silicon microstrip detectors that are spaced in the  $z$ -direction along the beampipe. Half of the sensors have silicon strips orientated in the radial direction ( $\phi$ -type) and the other half approximately perpendicular to this (R-type). The VELO is sensitive to the full LHCb acceptance and has additional sensitivity to tracks that travel in the backwards direction. A detailed description of the VELO hardware is given in Chapter 5, in which studies of the VELO performance and the impact of radiation damage are presented.

The VELO performed exceptionally well during the first two years of data taking. The sensors operate with an excellent ratio of signal-to-noise (S/N), as shown in Figure 3.7. The measured S/N ratios are within 18–22 for both sensor types and for all radial regions. This exceeds the pre-operation performance target [32] of initial S/N greater than 14. This results in efficient particle track reconstruction and low rates of fake clusters and tracks. For early data taking, the mean cluster reconstruction efficiency for particles incident on a sensor was measured to be greater than 99%, as is shown in Sec. 5.6.

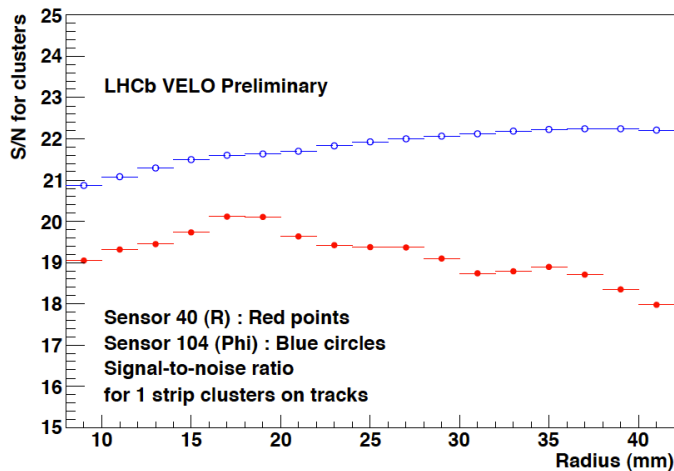


Figure 3.7: The ratio of signal-to-noise for single strip clusters, shown as function of sensor radius for an R-type and a  $\phi$ -type sensor. Figure from Ref. [33].

The impact parameter (IP) is defined as the distance of closest approach between a track and a vertex. The IP resolution is an important parameter for identifying whether a track was produced at a primary or detached vertex. The  $x$ -component of the IP resolution,  $IP_x$ , has been measured as a function of  $1/p_T$  and is shown in Figure 3.8(a). Particles with transverse momentum greater than  $1 \text{ GeV}/c$  have IP resolutions of less than  $35 \mu\text{m}$ , giving excellent primary and detached vertex separation.

The accuracy of track reconstruction influences the vertex resolution, momentum resolution and efficiency for which a VELO track is correctly matched to clusters in downstream tracking stations. A hit residual is the distance between a cluster and the track that the cluster is associated with. The width of the hit residual distribution is called the hit resolution, which is shown as a function of pitch for two ranges of projected angle in Figure 3.8(b). The strip pitch is defined as the spacing between the centre of adjacent silicon strips, and the projected angle is related to the angle of track incidence at the sensor plane with respect to the strip orientation (see Appendix A). Tracks with large projected angle are more likely to produce multistrip clusters, resulting in better hit resolutions.

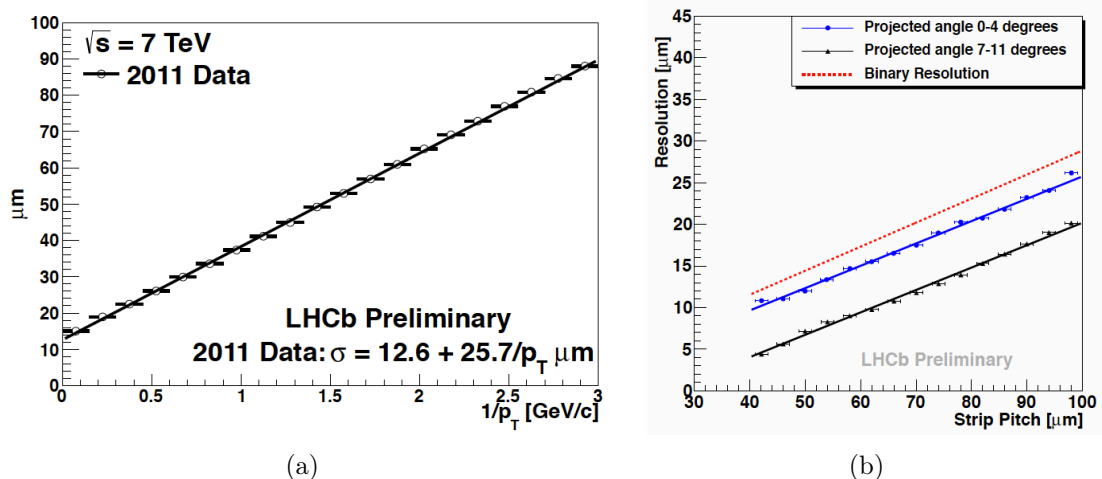


Figure 3.8: **a)** The value of  $IP_x$  as a function of  $1/p_T$  for 2011 data. The resolution of  $IP_x$  and  $IP_y$  have been found to be almost identical. **b)** The hit resolution as a function of sensor pitch for a particular sensor (for tracks with  $p > 10$  GeV). The binary resolution is the expected resolution for single strip clusters, which depends only on the strip pitch of the sensor. Figure from Ref. [33].

### Tracker Turicensis

The TT is used to reconstruct tracks produced by long-lived neutral particles that decay outside of the VELO. It can also be used to detect low momentum particles whose tracks are bent outside of the acceptance of the further downstream tracking stations and other sub-detectors. It consists of four layers arranged in two pairs that are separated by approximately 30 cm in the  $z$ -direction. The first and fourth planes have strips orientated in the vertical direction. The second and third planes have strips orientated at a stereo angle of  $+5^\circ$  and  $-5^\circ$  with respect to the vertical direction. The same four layer system with strips orientated at  $[0^\circ, 5^\circ, -5^\circ, 0^\circ]$  is also used in the three downstream tracking stations.

The TT sensors are 500 μm thick single sided  $p^+$ -on- $n$  type sensors with 183 μm strip pitch [34]. A schematic showing a sensor plane and the strip orientation is shown in Figure 3.9. The distance between a cluster and a track, when the cluster has not been used in the track reconstruction, is referred to as the *unbiased residual*. Figure 3.10(a) shows the unbiased residual distribution for clusters in the TT, corresponding to an unbiased resolution of 62 μm. For early data taking the TT had a S/N ratio in the range 12 to 15 and hit efficiency for high momentum tracks of 99.3%.

### Inner tracker

The IT covers approximately 1% of the LHCb acceptance region. It is located around the beampipe, on the opposite side of the peak magnetic field to the TT.

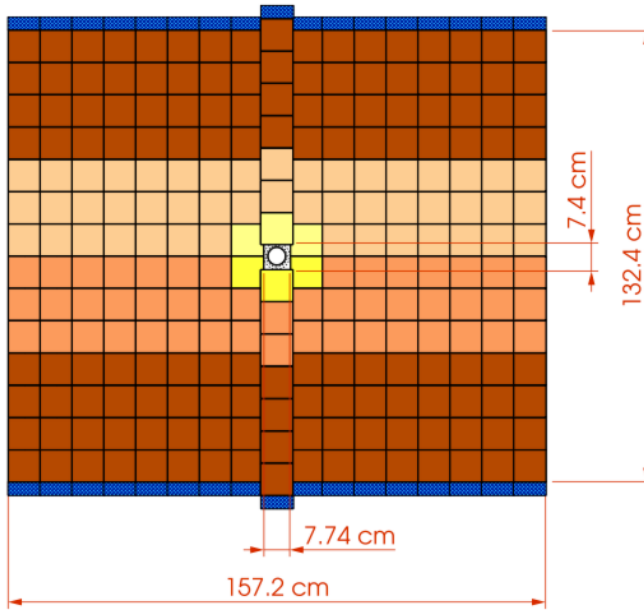


Figure 3.9: A schematic of the TT. Each small square with black outline is a sensor. Sets of 1, 2, 3 and 4 sensors are bonded together in the vertical direction leading to four different effective strip lengths (represented by the different sensor colours). The shortest strips (1 sensor long) are located near to the beampipe region where particle flux is highest. Figure from Ref. [35].

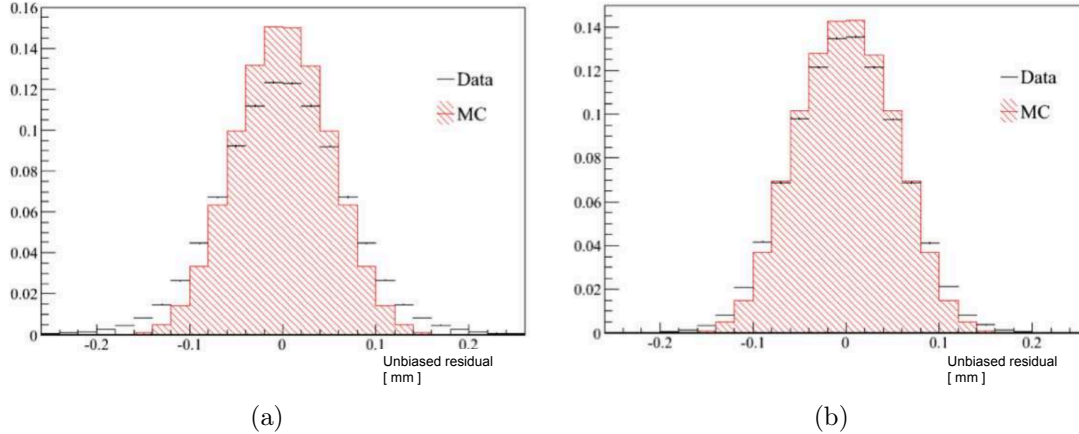


Figure 3.10: The unbiased residual distribution for **a)** the TT and **b)** the IT using 2010 data. Figures from Ref. [36].

The size and shape of an IT detection layer is shown in Figure 3.11. There are three IT stations positioned in front of one another along the  $z$ -direction. The stations have four detector boxes surrounding the beampipe, each with four layers that have strips orientated in the same way as was described for the TT. The IT sensors are made from single sided  $p^+$ -on- $n$  type silicon. Single sensors (top/bottom box) and sets of two sensors bonded together in the vertical direction (left/right box) have effective strip lengths of 11 cm and 22 cm, and use 320  $\mu\text{m}$  and 410  $\mu\text{m}$  thick silicon, respectively. The unbiased resolution of the sensors has been measured to

be  $58\ \mu\text{m}$ , as shown in Figure 3.10(b). For early data taking the IT had a S/N ratio of approximately 17 and hit efficiency for high momentum tracks of 99.65%.

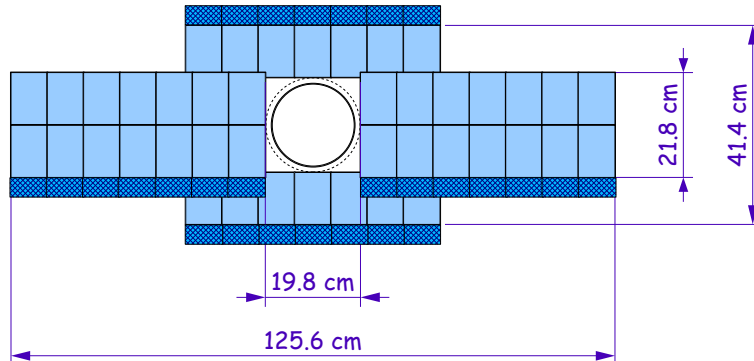


Figure 3.11: A schematic of the IT. Each small square with black outline is a sensor with 11 cm long strips. The outer tracking stations are positioned in close proximity to each of the IT stations in the  $z$ -direction, surrounding them in the  $x$ - $y$  plane (with a small overlap to prevent insensitive regions within the LHCb acceptance). Figure from Ref. [35].

### Outer tracker

The OT covers the full LHCb acceptance, except for the central region that is covered by the IT. It comprises approximately 55,000 gas-tight straw-tubes in 12 layers, each covering an area of approximately  $5 \times 6\ \text{m}^2$ . Drift-time detection technology is used, which has the benefit of being cheaper than silicon micro-strips and is suitable for coverage of large surface areas. Single hit resolutions have been measured [37] to be  $220\ \mu\text{m}$ , with average occupancies below 10%. The particle track momentum resolution,  $\Delta p/p$ , for tracks reconstructed using the VELO, TT and OT has been measured with data to be between 0.3% and 0.5%.

Each layer of the OT contains two rows of staggered straw-tubes of 4.9 mm diameter, as shown in Figure 3.12. The charge produced by an ionising particle traversing the detector is collected at anode wires running through the centre of the straw-tubes. The drift-time of the ionisation electrons results in a delay between a particle traversing a straw-tube and the charge being collected. The relative delay measured in different straw-tubes is used to precisely measure the track position at the detector plane. To ensure a fast signal drift-time (less than 50 ns) the straw-tubes are filled with a mixture of 70% Argon, 28.5%  $\text{CO}_2$  and 1.5%  $\text{O}_2$ . Ageing effects were observed in the OT in tests conducted prior to detector installation [38], with a reduction in the gain observed following exposure to particle fluence. This was found to be caused by the release of gases from the araldite AY103-1 support glue, which caused an insulating layer to form on the central anode wire. Small concentrations of oxygen in the gas mixture and continuous gas replacement (referred to as *flushing*)

were found to reduce the effect of gain loss due to ageing. Following the first  $1.3 \text{ fb}^{-1}$  of integrated luminosity delivered to the LHCb experiment, no significant gain loss has been observed [39].

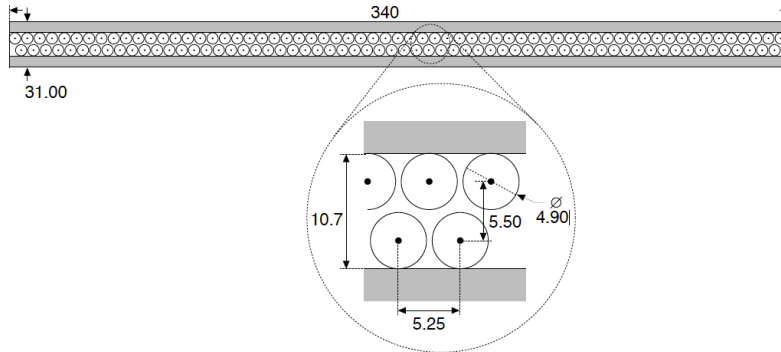


Figure 3.12: A cross section of an Outer Tracker module. All dimensions are in units of millimeters. Figure from Ref. [23].

### Track reconstruction

Particle trajectories are reconstructed using clusters from the various layers within each sub-detector. These tracks may only be a few tens of centimeters long. For example, tracks in the TT are only 30 cm long as this is the separation distance between the two modules. These short tracks are useful for studying the performance of a particular sub-detector, as is done with VELO tracks in the studies described in Chapter 5 and muon station tracks in Chapter 6. The shorter sub-detector tracks can be combined to make longer tracks that traverse larger detector regions. Some of the LHCb detector track types were shown in the bottom schematic of Figure 3.6. A brief description of the different track types is given below:

- **VELO Tracks:** Contain hits from the VELO sensors only. As the magnetic field strength is low in the VELO region, tracks are assumed to be linear.
- **TT Tracks:** Contain hits from only the four TT silicon planes.
- **T Tracks:** Contain hits from only the three tracking stations (IT or OT).
- **Muon Tracks:** Tracks reconstructed from hits in the muon stations (described in the following section).
- **Upstream Tracks:** Tracks with hits in the VELO and TT sub-detectors.
- **Downstream Tracks:** Tracks with hits in the TT and tracking stations.

- **Long Tracks:** Tracks with hits from the VELO and tracking stations. These tracks tend to have measurements in additional sub-detectors such as the TT, RICH and muon stations. As these tracks have the most information associated to them, they are the standard track type used for physics analyses at LHCb, such as the studies described in Chapters 6 and 7.

### 3.2.4 Particle identification

Analyses at the LHCb experiment require excellent particle identification (PID) to fully reconstruct exclusive decay channels. The typical final-state particles that reach the PID detectors without decaying are pions, kaons, protons, muons and electrons. These are efficiently identified using the RICH detectors, the calorimeters and the muon system.

#### Ring imaging Cherenkov detectors

Particles travelling in a material at a velocity faster than the speed of light in that material will emit photons in a process called Cherenkov radiation. The photons are emitted in a cone centred on the particle trajectory. The half angle of the cone,  $\theta_C$ , is related to the velocity of the particle,  $v$ , by the relation  $\cos \theta_C = 1/n\beta$ , where  $n$  is the refractive index of the material and  $\beta = v/c$ . Using these formulae and the measured momentum from the tracking system, the mass of the particle can be inferred.

For LHCb analyses it is particularly important to separate kaons and pions to reconstruct specific  $B$ -hadron decays. Particles with momentum in the range 2–65 GeV/ $c$  are identified using the RICH1 detector, which is located between the VELO and the TT. It uses aerogel and C<sub>4</sub>F<sub>10</sub> radiators and covers the full LHCb acceptance region. Particles with momentum up to approximately 100 GeV/ $c$  are identified further downstream by the RICH2 detector. It uses CF<sub>4</sub> radiators and covers a smaller acceptance region of 15–120 mrad horizontally and 100 mrad vertically [40]. The Cherenkov photons are projected as rings onto flat mirrors using spherical focusing mirrors. The rings are then reflected towards a series of photon detector arrays outside of the LHCb acceptance region. Similar optic systems are used for RICH1 and RICH2. The separation of the different charged particle types is apparent when plotting the Cherenkov angle against the particle momentum, as shown in Figure 3.13.

The LHCb analyses use the difference in the log likelihood,  $\Delta LL$  (or DLL), of two PID hypotheses to predict how likely it is that a particle is of one type as opposed to the other. For example, the difference in log likelihood between a proton and pion hypothesis,  $\Delta LL(p - \pi)$ , is positive if it is more likely that the particle is a

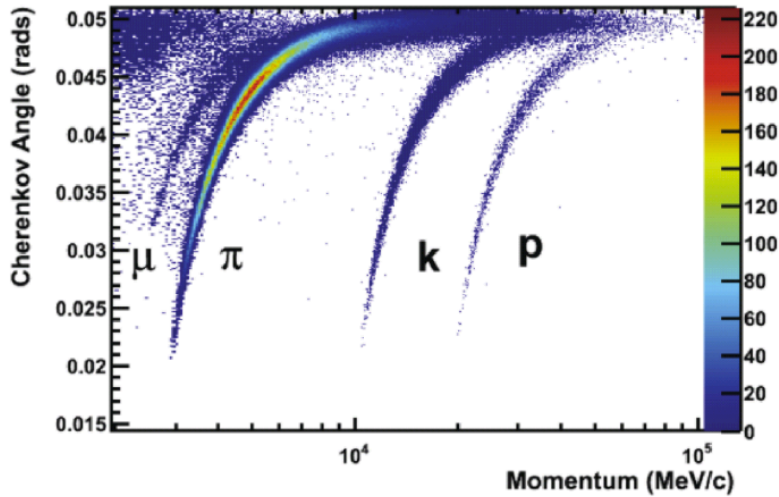


Figure 3.13: The Cherenkov angle as a function of particle momentum, measured using real data from the RICH2 detector. Figure from Ref. [41].

proton, and negative if it is more likely to be a pion. The PID efficiency of the RICH detectors has been evaluated using high purity data samples containing  $K_s^0$ ,  $\Lambda$  and  $\phi$  candidates, selected with kinematic constraints alone. The decay products of these particles are used to evaluate the PID efficiency of pions, protons and kaons. For example, the weak decay of  $\Lambda \rightarrow p\pi^-$  is typically displaced from the primary vertex. A sample with a distinct mass peak is obtained by selecting candidates for which two tracks have large IP with respect to the primary vertex and form a secondary vertex with one another. Using this sample, the PID efficiency for correctly identifying a proton, or for misidentifying a pion as a proton is shown for two different values of  $\Delta LL(p - \pi)$  in Figure 3.14.

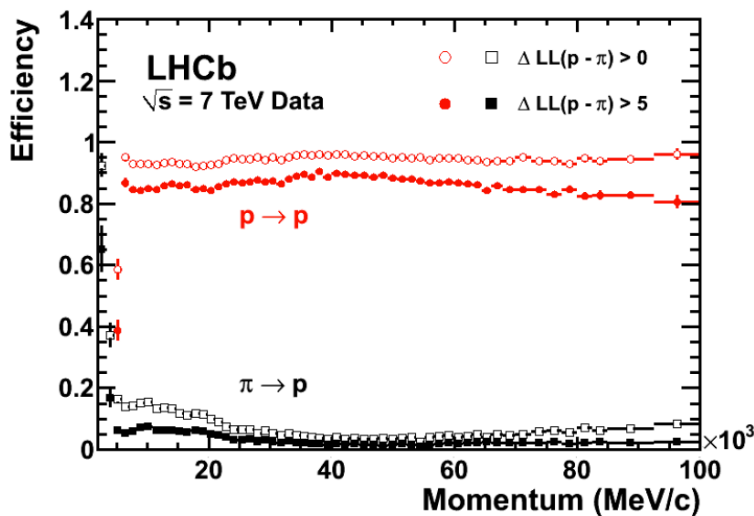


Figure 3.14: The PID efficiency for correctly identifying a proton (red) or mistakenly identifying a pion as a proton (black). For  $\Delta LL(p - \pi) > 5$  the proton is correctly identified more than 90% of the time with less than 10% pion misidentification. Figure from Ref. [41].

## Calorimetry

The LHCb calorimeter system primarily serves two functions. The first is to identify high transverse momentum hadrons, electrons and photons for the first level of the trigger system. The second is to provide additional information related to the PID, energy and position of particle tracks. Energetic particles traversing a material will interact with the atoms within the material. For dense materials this results in a cascade of secondary particles known as a shower. Electrons, positrons and photons predominantly produce particles in a material via pair production and Bremsstrahlung radiation, leading to electromagnetic showers. The characteristic path length of a charged particle that loses energy predominantly by electromagnetic interactions is the radiation length,  $X_0$ . This is the distance over which the energy of an electron is reduced to  $1/e$  of its original energy. Both charged and neutral hadrons also cause hadronic showers in materials through the strong force. The hadronic equivalent to the radiation length is the hadronic interaction length,  $\lambda_I$ . This is typically larger than the radiation length and so hadronic calorimeters are usually larger and positioned further downstream than electromagnetic calorimeters.

The LHCb calorimeter system comprises four detectors spaced along the  $z$ -direction surrounding the beampipe. All of the detectors operate on the principle of energy measurement by the collection of scintillation light from the shower, which is transferred to photo-multiplier tubes via wavelength-shifting fibres. The purpose of the wavelength-shifting fibres is to convert high energy photons into lower energy photons which are more suitable for collection.

The first two layers of the calorimeter system are the Scintillating Pad Detector (SPD) and Pre-Shower (PS) detectors. These are almost identical high granularity rectangular scintillation pads which are approximately 7.6 m wide and 6.2 m high. Modules are arranged for finer granularity near to the beam axis, with similar granularity patterns used for the SPD, PS and Electromagnetic Calorimeter (ECAL). Between the SPD and PS is a 15 mm thick layer of lead converter that contributes approximately  $2.5 X_0$ . As the SPD is the first scintillator that a particle produced at the interaction region will encounter, only charged particles will deposit a significant signal here. The lead layer is thick enough to produce an electromagnetic shower, thus backgrounds from neutral pions and photons can be suppressed by comparing signals from the SPD, PS and ECAL. Pion rejection of 99.6%, 99.6% and 99.7% is achieved whilst retaining 91%, 92% and 97% of electrons with 10, 20 and 50 GeV/ $c$  momentum, respectively. The distinction between signals produced by pions and electron in the PS is shown in Figure 3.15(a).

The LHCb calorimeters contain a mixture of absorber and scintillating materials. Such detectors are referred to as sampling calorimeters. The absorber is a

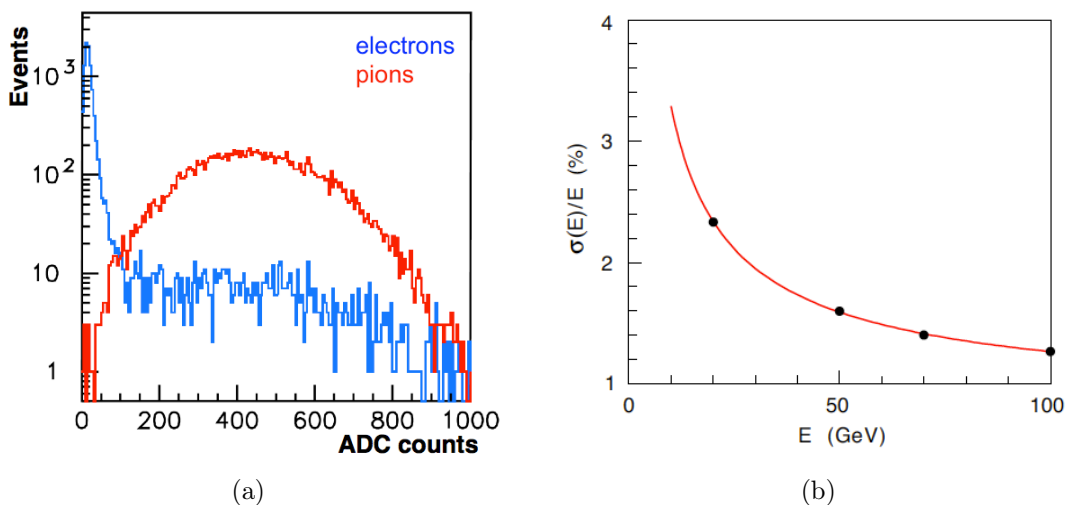


Figure 3.15: **a)** The magnitude of signals produced by pions and electrons in PS channels (in units of ADC counts, which are proportional to the deposited charge). **b)** The energy resolution of electrons against particle energy in an outer module of the ECAL. Figures from Ref. [23].

dense material that produces large particle showers in a relatively small space. The scintillating material absorbs the energy from the shower and re-emits it as light that can be collected and used to measure the energy of the incident particle. The ECAL comprises alternate layers of 2 mm thick lead and 4 mm thick scintillator tiles. The total calorimeter is 42 cm thick and contains 66 lead layers and 66 scintillating layers, corresponding to  $25 X_0$  and  $1.1 \lambda_I$ . The energy resolution of the ECAL is shown by Figure 3.15(b). It was determined using test beam data and measured to be  $\sigma_E/E \simeq (9\%/\sqrt{E}) \oplus 0.8\%$ , where  $E$  is the energy of the particle in GeV. The first uncertainty is due to fluctuations in the fraction of the shower that is detected and the second is due to detector related systematics.

Traditionally, calorimeters have had detector tiles orientated such that the particle trajectories are normal to the face of the tile, as is the case for the ECAL. The hadronic calorimeter (HCAL) however has an alternative design, with 10 mm thick iron absorber and 3 mm thick scintillating tiles orientated parallel to the beam axis (i.e. in the  $y-z$  plane). This unusual orientation gives good performance while benefiting from less complicated signal readout and simple detector assembly [42]. Tiles in consecutive layers of the HCAL are staggered to ensure particles pass through both iron absorber and scintillating material. The HCAL is segmented into square tiles of side length 131.3 mm and 262.6 mm in the inner and outer regions, respectively. The longitudinal depth of the HCAL corresponds to  $5.6 \lambda_I$ . Whilst this is not enough to fully contain all hadronic particle showers, it gives sufficient energy resolution to efficiently trigger on hadronic events. For particles with energies between 10 and 80 GeV the HCAL has an energy resolution of  $\sigma_E/E \simeq (69\%/\sqrt{E}) \oplus 9\%$ , where the

different components are the same as were described for the ECAL. The calorimeter system response to various impinging particle types is shown in Figure 3.16.

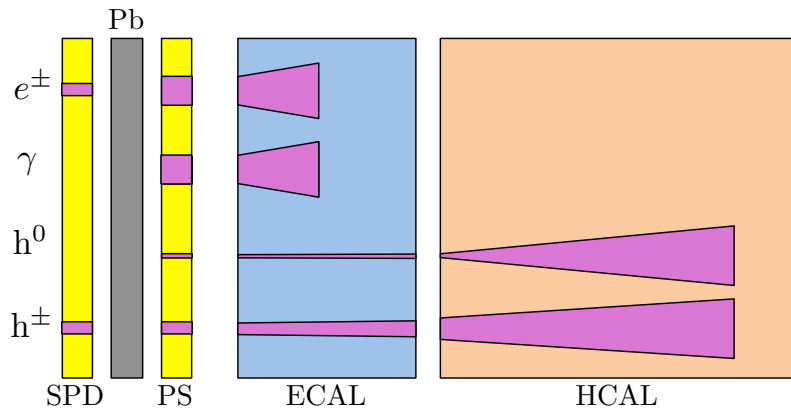


Figure 3.16: Schematic examples of how different particle types are identified using the various calorimeter sub-detectors. Electrons are distinguished from photons by the absence of a signal in the SPD in the case of a photon. Neutral hadrons will not leave a significant signal in the SPD but will produce a shower in the HCAL.

### Muon stations

Muons are present in many of the high priority LHCb analyses such as  $CP$  studies with the channel  $B_s^0 \rightarrow J/\psi(\mu^+\mu^-)\phi$ , searches for rare decays such as  $B_s^0 \rightarrow \mu^+\mu^-$  and the semileptonic charge asymmetry studied in this thesis via  $B_s^0 \rightarrow D_s^-\mu^+\nu_\mu$ . They are the most penetrating particles that can be directly detected at LHCb, hence the muon sub-detector system is positioned further downstream than any other sub-detector. The muon system consists of five downstream stations, as shown in Figure 3.17. The first station is located before the calorimetry system to improve the transverse momentum resolution of muon candidates. The four stations downstream of the calorimeters are separated by 80 cm thick iron absorbers to reduce the misidentification of less penetrating particles. Stand-alone muon trajectories are reconstructed using aligned hits from several muon stations. This gives fast muon identification with 20% transverse momentum resolution, which is an essential discriminant for use in the LHCb trigger. Additional description of the muon system hardware and the results of a muon identification efficiency study are given in Chapter 6.

## 3.3 Event triggers

Although the proton bunches collide at a rate of 40 MHz, only 10 MHz of these have interactions that are visible to the detector. Visibility is defined as when the interaction contains at least two charged particles with the necessary hits in the

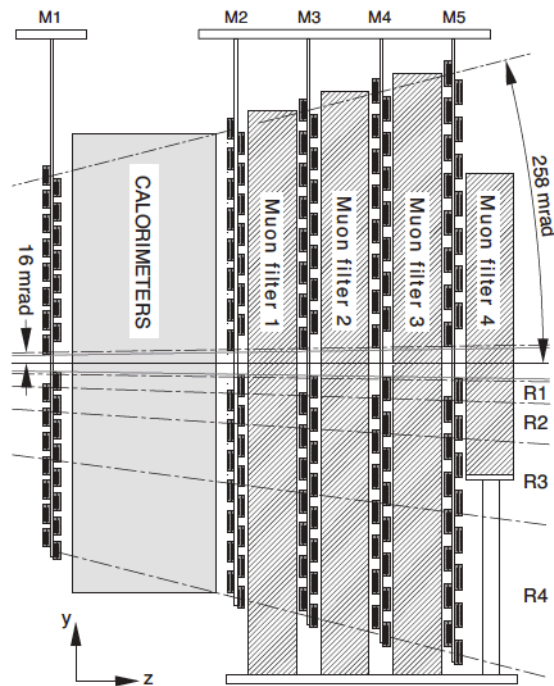


Figure 3.17: The LHCb muon system. Figure from Ref. [23]

VELO and tracking stations to be reconstructed as long tracks. Of the 10 MHz of visible crossings, around 100 kHz will produce a  $b\bar{b}$  pair and just 15% of these will have all of one of the  $b\bar{b}$  decay products within the LHCb acceptance region. Data storage limitations mean that only a small fraction of the total number of interactions can be recorded. The purpose of the LHCb trigger [43] is to decide which events should be recorded by very quickly evaluating some simple selection criteria that characterise events of interest to LHCb analyses. The LHCb experiment uses a two-level trigger system to reduce the event rate to the maximum event storage rate of approximately 3 kHz, as shown in Figure 3.18. A hardware based trigger (L0) first reduces the event rate to approximately 1 MHz. The second trigger level, the Higher Level Trigger (HLT), further reduces the rate to 3 kHz using software based selections. The triggers are briefly described below. The muon triggers that are of particular importance to the analysis presented in this thesis are described in greater detail in Chapter 6.

### 3.3.1 Level-0 trigger

As a result of the large  $B$ -meson mass, its decay products typically have larger transverse momentum than particles produced in background events. The L0 trigger exploits this property by using information from the calorimeters and muon chambers to select particles with large transverse energy and momentum. The L0 trigger uses custom made electronics that operate at the 40 MHz bunch crossing frequency.

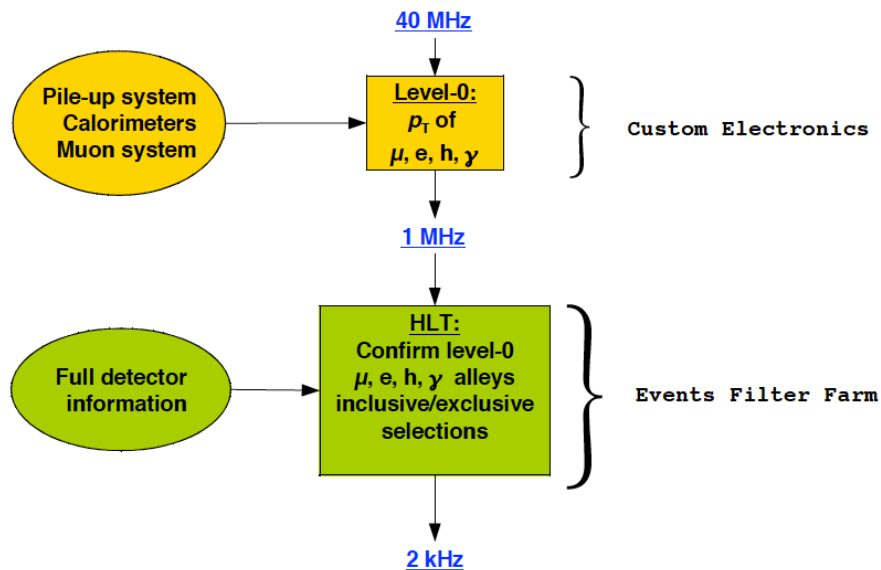


Figure 3.18: The LHCb trigger system. Figure from Ref. [23].

Information from the calorimeters and muon stations is used by the L0 Decision Unit (DU) to identify interesting events. The calorimeter based L0 trigger lines look for electrons, photons and hadrons with high transverse momentum. There are two muon based trigger lines that aim to select single muon and dimuon candidates. For the single muon line a single muon track is required to have greater than  $1.5 \text{ GeV}/c$  transverse momentum. The dimuon line requires that two muon candidates are measured with the sum of their absolute transverse momentum greater than  $1.3 \text{ GeV}/c$ .

Particularly complex events are vetoed using information from the Scintillating Pad Detector (SPD) and Pile-Up (PU) system, to avoid spending large amounts of time processing single events. These detectors provide the DU with the charged track multiplicity and number of primary interactions in the event, respectively. The PU system comprises four VELO R-type sensors positioned upstream of the interaction region that measure the number of primary proton-proton interactions. For the data collected in 2011, the events that pass the dimuon trigger must have less than 900 hits in the SPD, whereas for any other L0 trigger decision there must be less than 600 hits [44]. In addition, events with more than one primary vertex were rejected.

### 3.3.2 Higher level trigger

The full detector electronics are read out at a rate of  $\sim 1 \text{ MHz}$ , the input event rate to the HLT. This allows more complex event reconstruction using information from all of the LHCb sub-detectors. However, computing limitations mean that the majority of events must be discarded using only part of the information available.

The HLT is split into two levels named HLT1 and HLT2. The HLT1 reduces the rate from 1 MHz to approximately 40 kHz using selection variables obtained from the partially reconstructed events. The HLT decisions are evaluated by C++ applications on the Event Filter Farm (EFF), which consists of 2000 computing nodes. The HLT is a flexible, software based system that is easily modified to control the event triggering rate.

The HLT1 consists of a set of *alleys* that first confirm or reject the L0 decisions by matching tracks reconstructed in the tracking system with the hits in the calorimeters and muon stations (or in the case of neutral particles to check that there is not a compatible track in the tracking system). The rate is further reduced by applying event quality selection cuts such as requiring that tracks have a good fit  $\chi^2$  and by selecting tracks with large IP, a characteristic of particles produced in  $B$ -decays.

Events that pass any of the HLT1 alleys then have inclusive and exclusive algorithms run on them in the HLT2. At this stage the input rate is low enough for the remaining tracks in the event to be reconstructed. However, a simplified tracking algorithm is used to save time, and so looser track quality cuts are applied than would be used on offline data. Composite particles are reconstructed by combining several tracks which originate from a common vertex, allowing the selection of exclusive decay channels.

## 3.4 LHCb software

The LHCb software system is built on Gaudi [45], an architectural framework designed to be robust enough to withstand significant changes to experimental requirements and evolving technology. The Gaudi framework is designed to support all levels of the LHCb software [46] related to data processing. Such applications cover diverse operations such as event triggering, simulation, reconstruction and analysis. The LHCb applications are broadly associated to one of the three categories: simulation, reconstruction or analysis. The application flow diagram is shown in Figure 3.19.

### 3.4.1 Simulation

Monte Carlo (MC) simulated events are generated at LHCb using the Gauss [47] application. This is done in a two stage process, each of which make use of toolkits available in the physics community. The first stage uses external generators such Pythia [24] and EvtGen [48] to generate “events”, which are essentially a set of outgoing particles produced by an interaction between two colliding particles. In

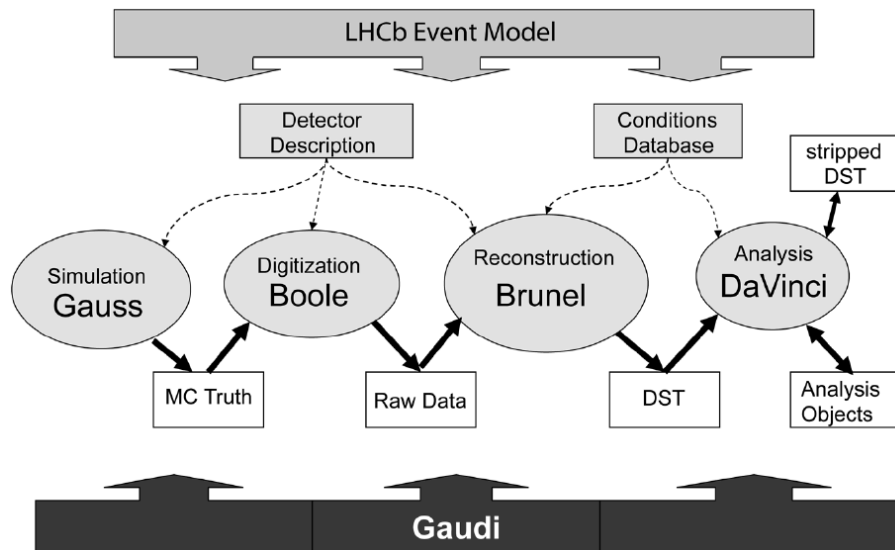


Figure 3.19: The flow of data and information with respect to the LHCb computing applications. Figure from Ref. [46].

the second stage the particle interactions such as multiple scattering and the subsequent decay of particles within the detector fiducial volume are simulated using GEANT4 [49, 50]. The output of `Gauss` are MC “hits” which represent the locations in the detector where the simulated particles would produce a signal.

The output of `Gauss` is used as an input to `Boole`, which takes the MC hits and simulates the electronic response of the detector. Data files are produced with simulated events stored in the same format as data from real particle interactions. The remaining applications in LHCb treat the files output by `Boole` in an identical way to the real data. This allows unbiased comparisons between MC predictions and real observations.

### 3.4.2 Reconstruction

The LHCb reconstruction application is named `Brunel`. This creates tracks, vertices and particle objects using either real data or the simulated output of `Boole`. The particle objects contain PID information from the various sub-detectors that can be used to assign a probability that the particle is of a particular type. This is a valuable discriminatory tool for many physics analysis.

Many of the sub-detectors have dedicated applications for emulating detector specific electronics and performance during detector commissioning and operation. The VELO uses the `Vetra` application to emulate the readout boards of the VELO sensors, and process VELO specific data. The radiation damage studies described in Chapter 5 use VELO tracks reconstructed from the raw sensor output, processed in the `Vetra` framework.

## Data analysis

Events used in specific analyses are selected offline using the `DaVinci` application. This allows users to select specific final states by combining the particles and vertices that are reconstructed by `Brunel`.

## LHCb DETECTOR UPGRADE STUDIES

The LHCb detector has been designed to operate at an instantaneous luminosity of  $\mathcal{L} = 2 \times 10^{32} \text{ cm}^{-2}\text{s}^{-1}$ , approximately two orders of magnitude less than the LHC design luminosity of  $10^{34} \text{ cm}^{-2}\text{s}^{-1}$ . This is achieved by misaligning the proton beams at the LHCb interaction region. Under these conditions the LHCb detector observes a greater fraction of events with single primary interactions, resulting in simpler triggering and event reconstruction.

The motivation for upgrading the LHCb detector is to collect data at a significantly greater rate than is currently possible. Following the detector upgrade [51], it is expected that an additional  $50 \text{ fb}^{-1}$  of data will be collected at a rate of approximately  $5 \text{ fb}^{-1}$  per year. The beams will be partially realigned to produce instantaneous luminosities of approximately  $1 - 2 \times 10^{33} \text{ cm}^{-2}\text{s}^{-1}$ , corresponding to an increase in the average number of collisions per bunch crossing to between two and four [52]. Both the trigger software and the detector hardware need to be improved to successfully process the associated increase in particle fluence. This chapter presents simulated performance studies of the TT detector at the upgraded luminosity, to test the viability of its use as part of the upgraded trigger.

Currently only the detector elements used by the L0 trigger are read-out at the 40 MHz bunch crossing rate. For the upgrade it is intended to read out all detector elements at 40 MHz, making it possible for the trigger to be entirely software based. With information available from all sub-detectors at the first level of the trigger, it is thought that the triggering efficiency for signal events could be improved by a factor of approximately 2, with no increase in the minimum bias retention rate [53].

### 4.1 Tracker Turicensis

A brief description of the Tracker Turicensis was given in Section 3.2.3. A more detailed description of the sensor layout is now given to aid the understanding of

the following studies. The TT is a silicon strip detector covering the full acceptance of LHCb. It is located downstream of the VELO, in the fringe field of the dipole magnet. It contains 896 silicon strip sensors distributed between four planar layers separated in the  $z$ -direction. The four layers are divided into two stations separated by approximately 30 cm. The first station, TTa, consists of the first and second layers with silicon strips at a  $0^\circ$  and  $+5^\circ$  orientation with respect to the vertical direction. The second station, TTb, consists of the third and fourth layers with strip orientations of  $-5^\circ$  and  $0^\circ$  [54].

Each layer is divided into detector modules, consisting of seven silicon sensors in the vertical direction (see Figure 3.9). There are two rows of modules in each plane, one above and one below the beampipe. Each module is divided into groups of sensors, called sectors, which are connected to the same electronic read-out. The sector layout of a single layer is shown in Figure 4.1. Strips from adjacent sensors within a sector are bonded together, resulting in effective strip lengths that are several sensors long. Sectors can be one, two, three or four sensors long. The smaller sectors are located around the beampipe where occupancy is higher and finer resolution is required. Each sensor is approximately 10 cm long and so the vertical coordinate of a single cluster is only known to lie within a 10 – 40 cm range. Due to the different detector plane orientations, information from clusters in the different layers is combined to reconstruct tracks with better resolution in the vertical direction [55].

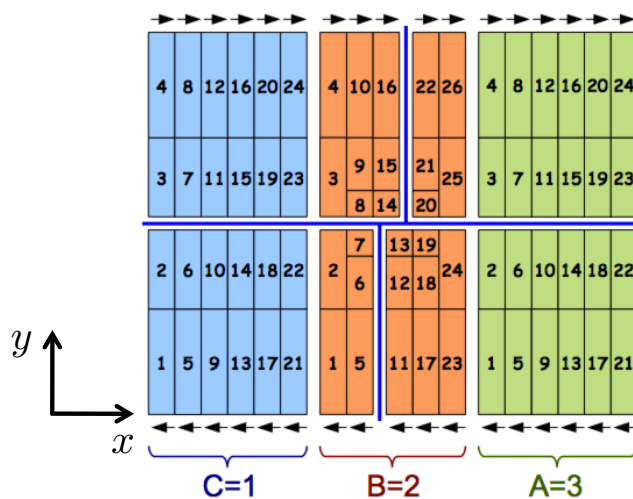


Figure 4.1: The sector numbering system used in the TT. Each layer is divided into three detector regions for electronic readout, represented by the sectors filled in blue, orange and green. Figure from Ref. [56].

## 4.2 The role of the TT in the upgrade

The trigger aims to select events containing particles with high transverse momentum ( $p_T$ ). These studies investigate the viability of making a quick  $p_T$  measurement using only clusters from the VELO and TT, for use in the upgraded trigger. This is an appealing prospect as the TT is close to the interaction region and so charged particles traversing here experience only the fringe of the magnetic field. Tracks reconstructed from hits in the VELO and TT are referred to as VeloTT tracks. Hits in the TT near to the straight line extrapolation of a VELO track are considered, due to the small magnetic field and the short distance between the detectors. This results in simple pattern recognition and quick track reconstruction. The difference between the slopes of the short tracks in the VELO and TT are used to measure the  $p_T$  of the VeloTT track.

The  $p_T$  resolution of VeloTT tracks has been measured using Monte Carlo (MC) simulated events, by comparing the measured  $p_T$  to the true  $p_T$  of the MC particle. This was simulated for both the current and upgrade luminosities, with results shown in Figure 4.2. The resolution, which is dominated by multiple scattering, is found to be approximately 15–25% of the MC particle’s true  $p_T$ , and is independent of the luminosity.

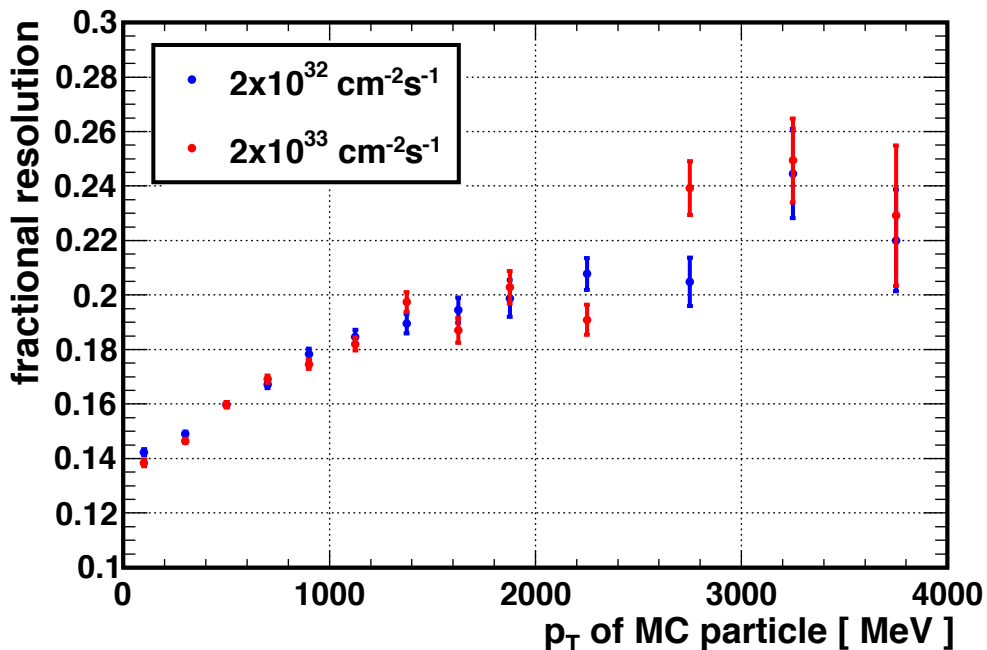


Figure 4.2: The fractional transverse momentum resolution,  $(\sigma_{p_T})/p_T$ , against the true transverse momentum of the MC particle.

### 4.3 Event simulation

Four datasets were generated for the purpose of these upgrade studies. The first and second consist of 4,672 and 3,901  $B_s^0 \rightarrow \phi\phi$  events at instantaneous luminosities of  $2 \times 10^{32} \text{ cm}^{-2}\text{s}^{-1}$  and  $2 \times 10^{33} \text{ cm}^{-2}\text{s}^{-1}$ , containing 273,796 and 545,067 MC matched VELO tracks, respectively. The VeloTT track resolutions shown in Figure 4.2 were measured using these samples. Only VELO tracks that have been matched to MC (i.e. are not fake tracks) have been included in these analyses. The third and fourth datasets contain 12,235 and 8,304 simulated minimum bias events at  $\mathcal{L} = 2 \times 10^{32} \text{ cm}^{-2}\text{s}^{-1}$  and  $\mathcal{L} = 2 \times 10^{33} \text{ cm}^{-2}\text{s}^{-1}$ , containing 345,641 and 821,702 MC matched VELO tracks, respectively.

The application versions used for these simulations are `Gauss v37r5`, `Boole v19r6` and `Brunel v35r6p1`. The simulations at upgraded luminosity have been run in the “minimal upgrade layout”. This contains modified algorithms that attempt to simulate events in the detector in an upgraded environment. This includes various proposed changes to the detector, such as removal of excess material to reduce the effects of multiple scattering. It is the minimal set of modifications to the current detector layout without implementing major changes.

### 4.4 Spillover subtraction

The LHC aims to collide bunches of protons at a rate of 40 MHz. This corresponds to a bunch crossing every 25 ns. A hit in a silicon strip is not measured as a single instantaneous value, but as an electronic pulse with a charge distribution that varies with time. When measuring events separated by such a short time it is important to know which bunch crossing an electronic signal corresponds to. The tails of the electronic pulse from a particle produced in a particular bunch crossing may contribute to the readouts of adjacent bunch crossings, thus producing false hits. This is called spillover and can result in fake tracks being mistakenly reconstructed from false hits.

When reading out electronics at 40 MHz, spillover can be suppressed by comparing the electronic pulses measured from consecutive bunch crossings in each channel. It has been found that an approximately constant fraction of the charge deposited in a channel from the previous bunch crossing ( $-25 \text{ ns}$ ) will be present in the readout of the current bunch crossing ( $0 \text{ ns}$ ). The corrected charge is estimated using the expression,

$$Q_{\text{corrected}} = Q_{\text{current}} - (C \cdot Q_{\text{previous}}), \quad (4.1)$$

where  $Q_{\text{current}}$  is the uncorrected charge in the current bunch crossing,  $Q_{\text{previous}}$  is the charge in the same channel for the previous bunch crossing, and  $C$  is a constant

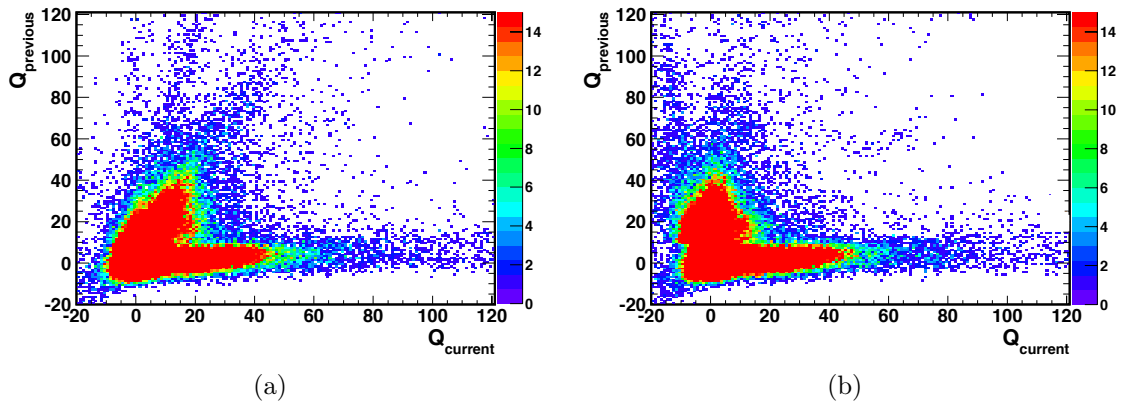


Figure 4.3: The magnitude of the charge collected in the current and previous readout of a particular channel is plotted **a)** before and **b)** after spillover subtraction. In **a)** two dominant bands are visible; the horizontal band predominantly contains hits from the current bunch crossing, whereas the band at approximately  $30^\circ$  to the vertical axis contains hits from the previous crossing that have partially spilled into the current readout. In **b)** the spillover subtraction method straightens the spillover band.

related to the fraction of spillover. The result of this spillover subtraction in the TT is shown by Figure 4.3. After correction with Equation 4.1, spillover can be reduced by discarding hits below some threshold (e.g. a suitable threshold for the distribution in Figure 4.3(b) is approximately 20 charge units.).

A subsequent study investigating the effectiveness of the spillover removal found that for simulated  $B_s^0 \rightarrow \phi\phi$  events at an instantaneous luminosity of  $2 \times 10^{33} \text{ cm}^{-2}\text{s}^{-1}$ , approximately 73% of false cluster hits were removed. This reduction was not as effective as was found for the other silicon strip sub-detectors, where spillover was reduced by 89.6% and 84.7% in the VELO and IT, respectively. For these studies a common spillover constant was used for TT sectors of various length. However, the various length sectors have different electronic properties which affect the amount of spillover. Shorter length sectors have smaller capacitance [57] and so are likely to produce electronic pulses of shorter duration.

The spillover constants for the different length sectors were measured using 100 simulated  $B_s^0 \rightarrow \phi\phi$  events at an instantaneous luminosity of  $2 \times 10^{33} \text{ cm}^{-2}\text{s}^{-1}$ . Spillover from the previous crossing into the current bunch crossing is less significant in the sectors with smaller sensor length, as shown by Figure 4.4. The spillover reduction method was modified to use different spillover subtraction constants in the different length sectors. This improved the percentage of fake hits removed in the TT by a further 6.3% to  $79.5\% \pm 0.5\%$ .

Spillover from the next bunch crossing (+25 ns) into the current readout is observed for single sensor sectors. This is shown in Figure 4.4(a) by the band of data around the dashed line with a slightly positive gradient. This effect is also observed in two-sensor long sectors, but not for those of length three or four sensors. In ad-

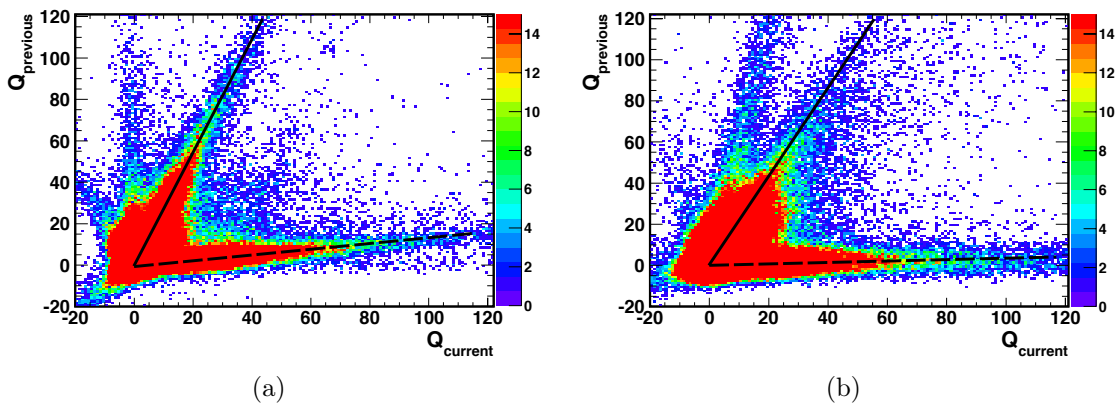


Figure 4.4: The spillover distribution for **a)** single sensor and **b)** four sensor sectors. The gradient of the spillover band in **a)** is steeper than that in **b)**, suggesting a smaller spillover effect in the shorter sectors. In **a)** the horizontal band is observed to increase for larger  $Q_{\text{current}}$ . This is due to the beginning of pulses in the next bunch crossing spilling into the current bunch crossing.

dition, spillover from two bunch crossing previous ( $-50$  ns) into the current bunch crossing is apparent in the three and four-sensor long sectors. This is shown by the band at a small angle to the  $y$ -axis in Figure 4.4(b).

After subtracting spillover from the next bunch crossing, the percentage of spillover hits removed increased by 5.5% to  $85.0\% \pm 0.5\%$ . This spillover reduction is comparable in effectiveness to the other silicon strip tracking sub-detectors. Table 4.1 summarises the spillover reduction for the various stages of implementation. The removal of spillover from two bunch crossings previous has not yet been implemented.

Table 4.1: A summary of the various spillover removal methods for simulated  $B_s^0 \rightarrow \phi\phi$  decays at an instantaneous luminosity of  $2 \times 10^{33} \text{ cm}^{-2}\text{s}^{-1}$ .

	# TT hits	# MC matched TT hits	# Spillover hits	Spillover hits removed [%]
No spillover removal	1634	1074	560	0
‘Previous’ removed (single spillover constant)	1224	1074	150	$73.2 \pm 0.6$
‘Previous’ removed (sector-specific constants)	1188	1073	115	$79.5 \pm 0.5$
‘Previous’ and ‘Next’ removed (sector-specific constants)	1162	1078	84	$85.0 \pm 0.5$

## 4.5 PatVeloTT

The algorithm that reconstructs VeloTT tracks is called `PatVeloTT`. This takes a VELO track and matches it to clusters in the TT. It is possible to measure tracks with momenta as low as 0.5 GeV using the TT, many of which would be bent outside of the downstream tracking stations acceptance region by the magnetic field. The VeloTT reconstruction algorithm, described in detail in Ref. [58], is outlined below.

Two windows are used for associating TT clusters with a particular VELO track, as shown in Figure 4.5. The *Search Window*,  $W_{\text{search}}$ , is opened about the coordinate of the straight line extrapolation of the VELO track to the TT midpoint,  $z_{\text{mid}}^{\text{TT}}$ . Combinations of clusters from the different layers that lie within  $W_{\text{search}}$  are considered for track reconstruction. For each of these clusters the difference between the  $x$  coordinate of the VELO track straight line extrapolation and the TT cluster hit,  $\Delta x$ , is calculated. For each cluster the  $\Delta x^{\text{norm}}$  is determined by scaling the  $\Delta x$  to the  $z_{\text{mid}}^{\text{TT}}$  plane. Clusters from different layers are associated to one another if their difference in  $\Delta x^{\text{norm}}$  is within the *Tolerance Window*,  $W_{\text{tol}}$ . If clusters from at least three different layers are within these window, they are reconstructed as a VeloTT candidate using the *simple fit* method.

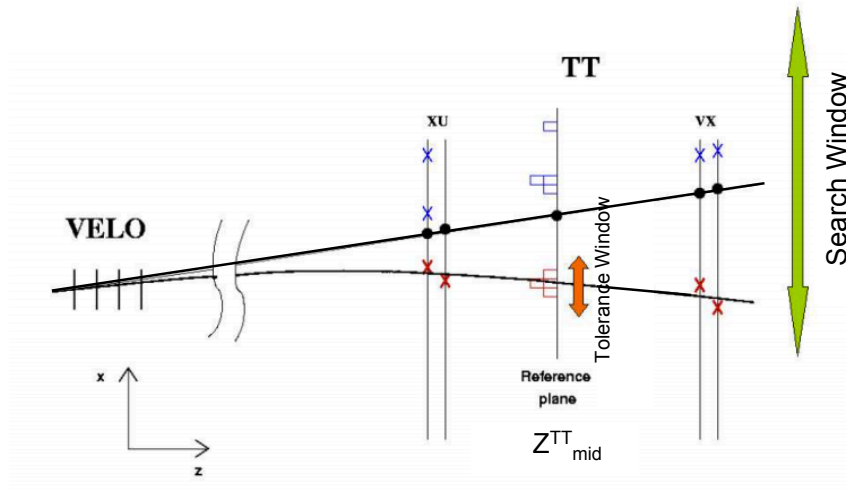


Figure 4.5: A schematic example of the PatVeloTT track reconstruction. The black circles represent the linear extrapolation of the VELO track to the TT planes and the crosses represent TT hits. Figure from Ref. [58].

The simple fit track reconstruction method has been designed for use as part of the LHCb trigger. It assumes that the short tracks reconstructed in the VELO and TT are linear and that they meet at a single point in the  $x$ - $z$  projection. The coordinate where they meet corresponds to the middle of the effective magnetic field, at half the  $Bdl$  integral. For high  $p_T$  tracks, such as those of concern when running as part of the trigger, this is a fair assumption. A least squares fit is performed

to measure the track momentum. This outputs a pseudo  $\chi^2$  corresponding to the quality of the fit, by combining the  $\chi^2$  of the VELO and the TT track segments. It is called a pseudo  $\chi^2$  because the errors do not consider the effect of multiple scattering and so are not statistically correct. It can however be used as a quality-of-fit parameter, to quickly discriminate between multiple VeloTT candidates associated to a single VELO track. When there are multiple VeloTT candidates, those with clusters in all four layers are favoured over candidates with clusters in only three layers. Candidates with clusters in the same number of layers are sorted by pseudo  $\chi^2$ , with the smallest selected as the “best” solution.

## 4.6 VeloTT multiplicity

A single track must be selected from the list of VeloTT candidates associated to a VELO track. The greater the number of candidates the smaller the chance of picking the “correct” one, if such a correct track exists. Using the simulated  $B_s \rightarrow \phi\phi$  data, the mean number of candidates was measured as a function of both the true  $p_T$  of the VELO track and the length of the TT sector that the “best” candidate is reconstructed in. The results are shown in Figures 4.6 and 4.7.

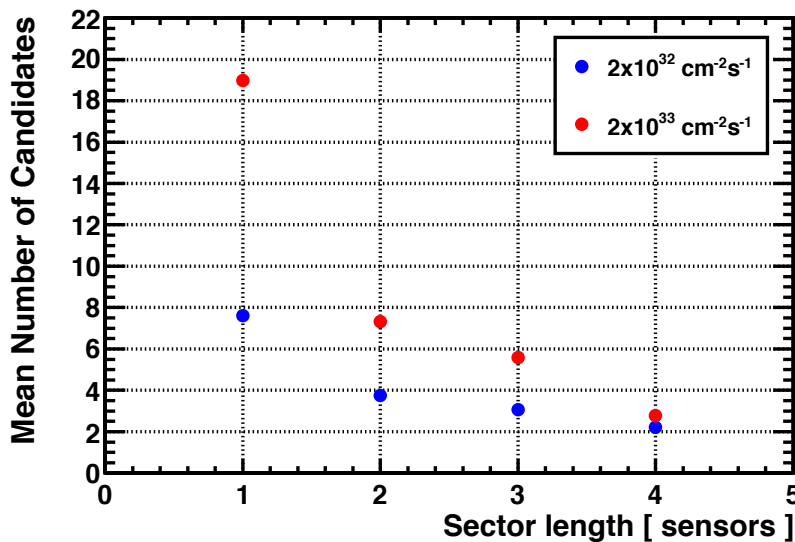


Figure 4.6: The mean number of VeloTT candidates associated to a single MC matched VELO track against the length of the sector in which the “best” track is reconstructed.

For  $\mathcal{L} = 2 \times 10^{32} \text{ cm}^{-2}\text{s}^{-1}$  and  $\mathcal{L} = 2 \times 10^{33} \text{ cm}^{-2}\text{s}^{-1}$  the mean number of VeloTT candidates associated to a VELO track is  $3.67 \pm 0.01$  and  $8.95 \pm 0.02$ . For these studies the improved spillover subtraction method described in Section 4.4 is used. Without this the mean number of candidates at the upgrade luminosity increases to approximately 13. The mean number of candidates is considerably higher in the single sensor sectors than the other sectors, showing little dependence on the

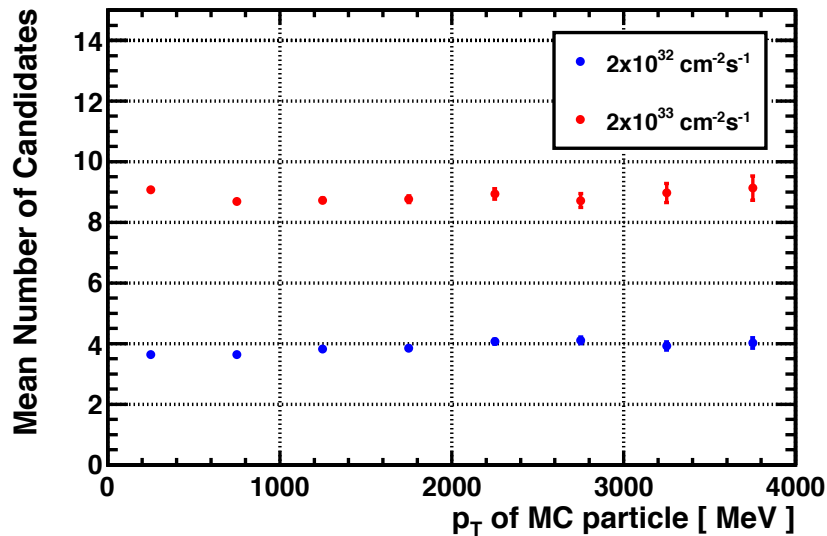


Figure 4.7: The mean number of candidates associated to a single MC matched VELO track against the true transverse momentum of the MC particle.

particles’  $p_T$ . These tracking multiplicities are an indicator of the occupancy problem that the current detector would experience at upgrade luminosities, particularly around the beampipe where the shorter sectors are positioned.

## 4.7 “Best” track selection

In the current form of the PatVeloTT algorithm, if there is at least one VeloTT candidate then a “best” track will always be selected from the list of candidates. However, if the particle has participated in some physics interaction that diverts it from the TT acceptance then there may not be a MC matched VeloTT track in the list of candidates. There is also the chance that the particle will pass through regions in the TT with gaps between sensors or dead silicon strips. If there is no “correct” track in the list of candidate then it is better to discard the VELO track, rather than select the best from a poor sample. Track quality parameters that could help to discriminate such poor track candidates are now discussed.

The simple fit method was designed to reconstruct the trajectory of particles very quickly as part of the trigger environment. A more complete fitting method would be to use the Kalman<sup>1</sup> fitting method used for offline track reconstruction. With the current computing power at LHCb it is not possible to do a Kalman fit for every VeloTT candidate. However, it is not known what computing resources will be available for the LHCb upgrade. If the computing power is available then the Kalman fitted  $\chi^2$  per degree of freedom ( $\chi^2/\text{DoF}$ ) could be used to select better

<sup>1</sup>This is where measurements are added one by one, with the fit updated after each addition. Multiple scattering is accounted for as a local kink in the track at a material boundary.

quality tracks and reduce the fake rate.

Figure 4.8 compares the pseudo and Kalman fitted  $\chi^2/\text{DoF}$  of the fake and successfully matched tracks. A cut on Kalman  $\chi^2/\text{DoF} < 4$  and pseudo  $\chi^2/\text{DoF} < 1000$  when selecting a “best” track is a good discriminator of fake tracks. When selecting tracks with reconstructed  $p_T$  greater than 0.5 GeV this reduces the fake rate by a factor of approximately 2.5, with a drop in efficiency of only 2–3% for both luminosities, as shown in the following section.

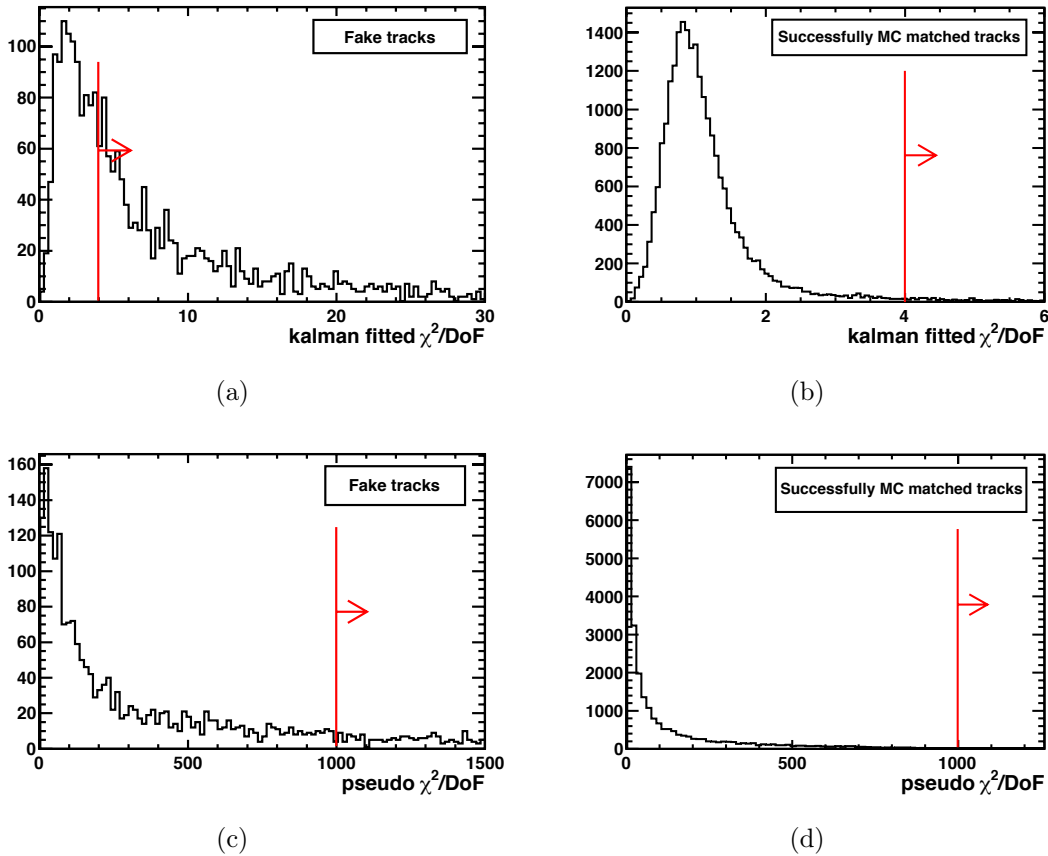


Figure 4.8: Figures **a)** and **b)** compare the Kalman fitted  $\chi^2/\text{DoF}$  for fake and successfully MC matched tracks, respectively. Figures **c)** and **d)** compare the pseudo  $\chi^2/\text{DoF}$  for fake tracks and successfully MC matched tracks, respectively. The red lines show the suggested cuts to remove a large fraction of fake tracks without significantly reducing the number of correctly matched tracks.

## 4.8 Efficiency and fake rate

Increases in the number of track candidates result in longer data processing times. They also increase the chance of reconstructing fake particles by incorrectly matching VELO and TT tracks. When a single track is chosen from the list of VeloTT candidates it is reconstructed either successfully or as a fake.

For success, the track must satisfy one of the following criteria:

- At least 70% of clusters associated to the VeloTT track are matched to MC information.
- If the VeloTT track has only 3 associated clusters, 2 of the 3 clusters are MC matched.

A track which does not pass these criteria is called a “fake” track. It is important for a trigger to select a high fraction of successfully matched tracks with a low fraction of fakes. When run as part of the trigger the key measurement from PatVeloTT is the  $p_T$  of charged particles. Events containing multiple high  $p_T$  tracks will pass the trigger. As such, the efficiency and fake rate of track reconstruction has been investigated for a range of reconstructed  $p_T$  cuts.

The efficiency is defined as the number of VeloTT tracks successfully reconstructed above the  $p_T$  cut, as a fraction of the total number of tracks with true  $p_T$  above the cut. Many low  $p_T$  particles detected in the TT are swept outside of the downstream T stations’ acceptance region. These tracks cannot be fully reconstructed by the downstream sub-detectors and so are generally not considered useful. Using MC information, only VELO tracks reconstructable in the T-stations contribute to the calculated efficiency.

The fake rate is the number of fake tracks reconstructed with a  $p_T$  above the cut, as a fraction of the total number of VeloTT tracks with reconstructed  $p_T$  above the cut (regardless of whether or not they are reconstructable in the T stations).

The efficiency and fake rate for the two studied luminosities are summarised in Table 4.2. The track retention is also shown, defined as the number of MC matched VELO tracks with true  $p_T$  above the respective  $p_T$  cut and at least one associated VeloTT candidate. The increase in instantaneous luminosity from  $2 \times 10^{32} \text{ cm}^{-2}\text{s}^{-1}$  to  $2 \times 10^{33} \text{ cm}^{-2}\text{s}^{-1}$  results in a drop in efficiency of between  $\sim 1.5\text{--}6.5\%$ , depending on the reconstructed  $p_T$  cut. More significant is the rise in the fake rate, which approximately doubles for all the reconstructed  $p_T$  cuts.

Table 4.3 shows the effect of the track quality  $\chi^2$  cuts discussed in Section 4.7 on the efficiencies and fake rates at an instantaneous luminosity of  $2 \times 10^{33} \text{ cm}^{-2}\text{s}^{-1}$ . The tighter track quality selection reduces the tracking efficiency by less than 3%, but more significantly reduce the fake rate by approximately a factor of 2 (for  $p_T$  cuts of greater than 0.5 GeV).

The efficiency as a function of the true  $p_T$  of the MC particle is shown in Figure 4.9. For a 1.5 GeV cut on the reconstructed  $p_T$ , the efficiency of tracks with true  $p_T$  greater than 2 GeV at  $\mathcal{L} = 2 \times 10^{32} \text{ cm}^{-2}\text{s}^{-1}$  is  $\sim 80\%$ . This is reduced by  $\sim 5\%$

Table 4.2: A summary of the efficiencies and fake rates for  $B_s^0 \rightarrow \phi\phi$  decays. The uncertainties of the efficiencies and fake rates are less than 0.5%.

	Luminosity [ $\text{cm}^{-2}\text{s}^{-1}$ ]	Using true $p_T$	Using reconstructed $p_T$		
		Track retention [% $\pm$ 0.1%]	Track retention [% $\pm$ 0.1%]	Efficiency [%]	Fake rate [%]
All $p_T$	$2 \times 10^{32}$	100	90.3	81.8	17.5
	$2 \times 10^{33}$	100	91.8	75.3	28.8
$p_T > 0.5 \text{ GeV}$	$2 \times 10^{32}$	46.6	37.6	76.2	7.1
	$2 \times 10^{33}$	43.1	33.4	71.5	13.1
$p_T > 1.0 \text{ GeV}$	$2 \times 10^{32}$	17.1	14.5	74.2	9.3
	$2 \times 10^{33}$	13.3	11.3	70.9	18.0
$p_T > 1.5 \text{ GeV}$	$2 \times 10^{32}$	8.2	7.4	73.6	11.6
	$2 \times 10^{33}$	5.6	5.3	72.0	23.6

 Table 4.3: Comparisons of the efficiency and fake rate at  $2 \times 10^{33} \text{ cm}^{-2}\text{s}^{-1}$  for  $B_s^0 \rightarrow \phi\phi$  decays, with and without the  $\chi^2$  cuts. The uncertainties of the efficiencies and fake rates are less than 0.5%.

	Selection method	Using true $p_T$	Using reconstructed $p_T$		
		Track retention [% $\pm$ 0.1%]	Track retention [% $\pm$ 0.1%]	Efficiency [%]	Fake rate [%]
All $p_T$	without cuts		91.8	75.3	28.8
	with cuts	100	84.9	73.7	21.2
$p_T > 0.5 \text{ GeV}$	without cuts		33.4	71.5	13.1
	with cuts	43.1	31.8	69.4	6.1
$p_T > 1.0 \text{ GeV}$	without cuts		11.3	70.9	18.0
	with cuts	13.3	10.6	68.5	7.5
$p_T > 1.5 \text{ GeV}$	without cuts		5.3	72.0	23.6
	with cuts	5.6	4.9	69.3	9.8

at the upgrade luminosity. The efficiency for both luminosities is  $\sim 50\%$  for the  $p_T$  bin just above the cut due to the  $\sim 20\%$  measurement resolution.

## 4.9 Efficiency losses

The track reconstruction efficiency for the two instantaneous luminosities investigated has been shown to be in the range  $\sim 70 - 80\%$ . The source of the  $\sim 20 - 30\%$  efficiency loss, and whether it could be recovered, is now investigated. For both instantaneous luminosities, when making a 1.5 GeV cut on reconstructed  $p_T$ :

- $\sim 3\%$  of the efficiency loss is due to selecting the wrong track.
- $\sim 20\%$  is from tracks outside the TT acceptance region.

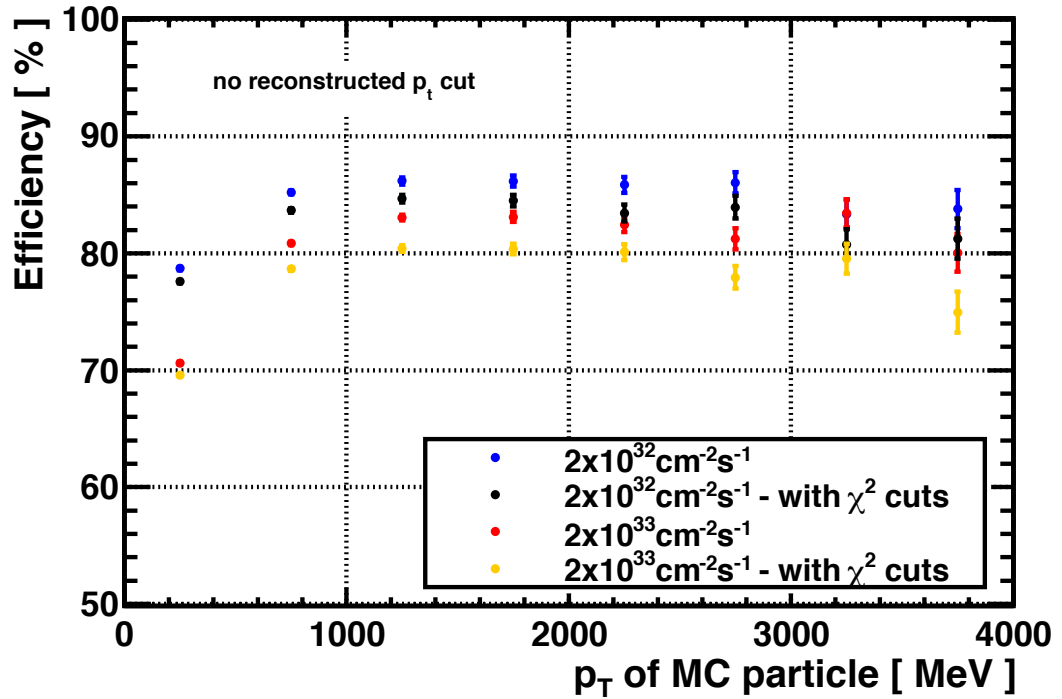
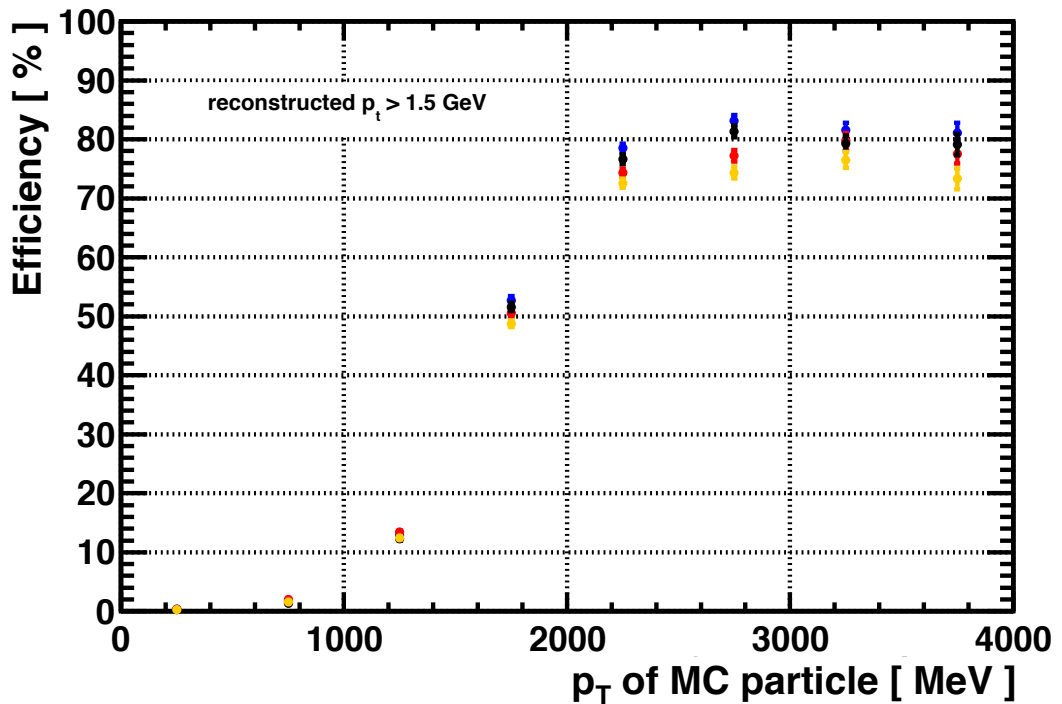
(a) No reconstructed  $p_T$  cut(b) 1.5 GeV reconstructed  $p_T$  cut

Figure 4.9: The efficiency of track reconstruction against the true transverse momentum of the MC particle. The efficiency is shown for the current “best” track selection, and also for the modified selection method involving cuts on the Kalman fitted  $\chi^2/\text{DoF}$ , as described in Section 4.7

- $\sim 77\%$  is from tracks within the TT acceptance region but where no successful candidate is constructed above the  $p_T$  cut.

The relative sources of efficiency loss are comparable for the two luminosities and are summarised in full in Table 4.4. The tracks that are not within the TT acceptance most likely travel through the beampipe region and so constitute an unavoidable acceptance loss with the current TT design.

The sources of inefficiency for tracks which are in the TT acceptance are given in Table 4.5. Of the tracks within the TT acceptance for which no correct candidate is constructed, around 60–70% are successfully reconstructed below the 1.5 GeV cut (i.e. successfully matched with true  $p_T > 1.5$  GeV and reconstructed  $p_T < 1.5$  GeV). These tracks are discarded due to the inherently large  $p_T$  resolution of tracks measured in the TT and could be recovered by making the reconstructed  $p_T$  cut lower. For example, if the  $p_T$  cut is lowered to 1 GeV then the efficiency for tracks with  $p_T > 1.5$  GeV at a luminosity of  $2 \times 10^{33} \text{ cm}^{-2}\text{s}^{-1}$  increases from approximately 72% to 84%.

Table 4.4: Relative contributions to efficiency loss. The uncertainties of values shown are less than 1%.

	Luminosity [ $\text{cm}^{-2}\text{s}^{-1}$ ]	Loss in efficiency [%]	Relative source of efficiency loss [%]		
			Choose wrong candidate	TT acceptance loss	No correct candidate
All $p_T$	$2 \times 10^{32}$	18.2	8.7	49.8	41.5
	$2 \times 10^{33}$	24.7	14.8	36.1	49.1
$p_T > 0.5$ GeV	$2 \times 10^{32}$	23.8	2.6	33.3	64.2
	$2 \times 10^{33}$	28.5	5.3	26.0	68.7
$p_T > 1.0$ GeV	$2 \times 10^{32}$	25.8	2.3	26.6	71.1
	$2 \times 10^{33}$	29.1	3.9	20.5	75.6
$p_T > 1.5$ GeV	$2 \times 10^{32}$	26.4	2.3	23.2	74.5
	$2 \times 10^{33}$	28.0	3.6	17.9	78.5

## 4.10 Minimum bias

The performance of the reconstruction algorithms on decays such as  $B_s^0 \rightarrow \phi\phi$  is of great interest, as they are characteristic of the channels that are investigated at LHCb. However, they are far from the typical events that the algorithm will see if used as part of the trigger. It is also important to investigate how the tracking algorithms perform on minimum bias events. Table 4.6 gives the efficiency and fake rate of simulated minimum bias track reconstruction at  $\mathcal{L} = 2 \times 10^{33} \text{ cm}^{-2}\text{s}^{-1}$ .

Table 4.5: Efficiency loss breakdown for tracks in TT acceptance for which no correct track exists in the list of VeloTT candidates. The uncertainties of values shown are below 1%.

	Luminosity [ $\text{cm}^{-2}\text{s}^{-1}$ ]	Loss in efficiency [%]	Relative source of efficiency loss [%]			
			No VeloTT candidate	Fake above $p_T$ cut	Fake below $p_T$ cut	Success below $p_T$ cut
All $p_T$	$2 \times 10^{32}$	7.6	26.3	73.7	—	—
	$2 \times 10^{33}$	12.2	10.0	90.0	—	—
$p_T > 0.5 \text{ GeV}$	$2 \times 10^{32}$	15.3	10.2	5.8	20.9	63.1
	$2 \times 10^{33}$	19.6	5.6	7.4	32.9	54.0
$p_T > 1.0 \text{ GeV}$	$2 \times 10^{32}$	18.3	6.2	4.4	19.3	70.1
	$2 \times 10^{33}$	22.0	3.9	3.7	28.7	63.8
$p_T > 1.5 \text{ GeV}$	$2 \times 10^{32}$	19.7	5.4	4.4	19.0	71.2
	$2 \times 10^{33}$	22.0	3.7	2.9	29.5	63.9

The absolute tracking efficiencies and fake rates are comparable to those found for  $B_s^0 \rightarrow \phi\phi$  type events in Table 4.3.

A typical trigger decision would be to first select events with at least two tracks with reconstructed  $p_T$  greater than a relatively loose cut of around 1 GeV. These tracks can then be extended to long tracks using clusters in the downstream T-stations. This would be faster than initially reconstructing the tracks in the T-stations as the VeloTT track position and  $p_T$  measurement aids pattern recognition algorithms by reducing the size of the cluster search windows. Long tracks have a momentum resolution of less than a percent, so a tighter cut of the order of 1.5 GeV could then be made to further reduce the rate.

For instantaneous luminosities of  $2 \times 10^{32} \text{ cm}^{-2}\text{s}^{-1}$  and  $2 \times 10^{33} \text{ cm}^{-2}\text{s}^{-1}$ , the percentage of minimum bias events containing two VeloTT tracks with measured  $p_T$  greater than 1 GeV is 36.3% and 81.5%, respectively. This study only considers events in which there is at least one MC matched VELO track. In reality some fraction of events have no VELO tracks at all. Simulations show that at instantaneous luminosities of  $2 \times 10^{32} \text{ cm}^{-2}\text{s}^{-1}$  and  $2 \times 10^{33} \text{ cm}^{-2}\text{s}^{-1}$  approximately 20% and 3% of minimum bias events contain no VELO tracks. Therefore the fraction of minimum bias events that would pass this hypothetical trigger selection is reduced to approximately 29% and 80% for the current and upgrade luminosities, respectively. This shows that for higher instantaneous luminosities, a simple track- $p_T$  based trigger would need to cut tighter than the pseudo trigger discussed in this study.

## 4.11 Conclusions and upgrade status

The studies presented in this chapter have shown that at an upgraded value of instantaneous luminosity, there is a substantial increase in the occupancy of the

Table 4.6: Comparisons of the efficiency and fake rate at  $2 \times 10^{33} \text{ cm}^{-2} \text{ s}^{-1}$  for minimum bias events, with and without the track quality  $\chi^2$  selection applied. All errors on efficiencies and fake rates are less than 0.5%.

	Selection method	Using true $p_T$	Using reconstructed $p_T$		
		Retention rate [% $\pm$ 0.1%]	Retention rate [% $\pm$ 0.1%]	Efficiency [%]	Fake rate [%]
All $p_T$	without cuts	100	91.4	75.4	28.3
	with cuts		84.9	74.0	20.7
$p_T > 0.5 \text{ GeV}$	without cuts	40.4	31.3	71.2	13.4
	with cuts		29.9	69.4	6.2
$p_T > 1.0 \text{ GeV}$	without cuts	10.7	9.3	70.9	20.2
	with cuts		8.7	68.7	8.7
$p_T > 1.5 \text{ GeV}$	without cuts	4.0	4.1	72.7	27.3
	with cuts		3.7	69.9	12.0

TT. The number of VeloTT candidate tracks is found to approximately double, with the single-sensor sectors in the high fluence beampipe region worst effected. It was found that approximately 80% of false hits due to spillover can be removed in the current detector layout. Without the spillover subtraction, the number of VeloTT candidates more than triples at the upgraded luminosity. For the TT to be used in the upgraded trigger, improvements to the current design are most likely required. Further studies are needed to determine the necessary increase in sector granularity.

The efficiency of correct and fake track reconstruction was investigated for various  $p_T$  selections. In going from  $\mathcal{L} = 2 \times 10^{32} \text{ cm}^{-2} \text{ s}^{-1}$  to  $\mathcal{L} = 2 \times 10^{33} \text{ cm}^{-2} \text{ s}^{-1}$  the fake rate approximately doubled and the efficiency of correct track reconstruction decreased by a few percent for tracks with  $p_T$  greater than 1 GeV. If the full Kalman fit is used, then by applying tighter track quality criteria the fake rate could be approximately halved for a small decrease in tracking efficiency. The  $p_T$  resolution of approximately 15 – 25% is responsible for a significant proportion of the efficiency loss, due to correctly matched tracks being reconstructed below the  $p_T$  threshold.

The current upgrade strategy is described in Ref. [51]. It is planned to make use of the TT in the upgraded detector trigger, and the TT is likely to revert to its original name of the Trigger Tracker. Increased granularity in the  $y$ -direction is planned, with sector lengths reduced to approximately 25% of their current size. This corresponds to effective strip lengths of approximately 2.5 cm near to the beampipe and 10 cm in outer regions. The amount of material between the interaction region and the TT will be reduced, leading to improved momentum resolution.

## RADIATION DAMAGE STUDIES OF THE LHCb VELO

The study of heavy flavour physics in the LHC environment requires precision track reconstruction and vertexing. This is achieved at the LHCb by positioning the VELO detector around the proton beam interaction region, with the closest active silicon sensor regions located only 8.2 mm from the beam axis. For the luminosity delivered by the LHC in 2010 and 2011, the VELO was exposed to higher particle fluences than any other silicon detector of the four major LHC experiments. This presents LHCb with the opportunity to lead the way in studies of radiation damage to silicon detectors in the high luminosity LHC environment. Careful monitoring of radiation damage to the sensors is essential to ensure the quality of data for LHCb physics analyses and to provide information relevant to the eventual detector replacement and upgrade.

This chapter presents several studies of radiation damage in the VELO detector. The theory of particle detection using silicon strips is first reviewed in Section 5.1, with particular emphasis on radiation induced changes to the detector properties. The detector hardware is described in Section 5.2. The special datasets used to study detector performance as a function of fluence and bias voltage are described in Section 5.3. Finally, studies of these data are presented in Sections 5.4, 5.5 and 5.6, and summarised in Section 5.7.

### 5.1 Particle detection using silicon

Silicon is the second most abundant element in the Earth's crust, with only oxygen present in greater amounts. Despite comprising approximately 28% of the Earth's crust [59], pure silicon crystals are rarely produced in nature. The majority of silicon is found in combination with oxygen in the form of complex silicates. However, by starting with a very pure form of sand ( $\text{SiO}_2$ ) it is possible to manufacture high purity silicon crystals with impurity concentrations of only a few

parts-per-billion. High energy particle physics experiments have benefit from extensive research conducted by the microelectronics industry, resulting in advanced industrial silicon crystal production techniques. A common aim when designing a particle detector is to minimise the amount of material that is present in the particle tracking region with which a particle may scatter or interact. A benefit of using silicon is that it can be produced in homogeneous, self-supporting pieces such that substantial supporting material is not necessary. Further details of both the silicon crystal growth process and the following discussion on the electrical properties of silicon can be found in Ref. [60].

Silicon atoms have an atomic number of fourteen, with four valence electrons in the outermost orbital. They solidify as crystals with a diamond lattice structure by each atom forming four covalent bonds with its neighboring atoms. An electron from an individual atom will occupy one of a series of well defined discrete energy levels. When many atoms are brought together into a formation such as a lattice, the outer electron orbitals interact to form closely spaced energy levels referred to as an energy band. At a temperature of absolute zero the electrons will occupy the lowest available energy states known as the *valence* band. The unoccupied higher energy levels are referred to as the *conduction* band. An electron in the valence band is bound to a silicon atom lattice site, whilst an electron in the conduction band is free to traverse the lattice.

The energy difference between the conduction band and valence band is known as the bandgap energy. Materials with a large bandgap energy, i.e. those with a value that is greater than  $\sim 9$  eV, are called insulators (e.g. glass). When the valence and conduction bands overlap, or the conduction band is partially filled, the material is called a conductor (e.g. a metal). Semiconductors are materials for which the magnitude of the bandgap energy is small. Electrons can transit between the conduction and valence bands with the energy provided by thermal excitations. Silicon is a semiconductor at atmospheric pressure and room temperature, with a bandgap energy of 1.12 eV. An electron in the conduction band is referred to as a negative free charge carrier. The absence of an electron at a lattice site from which an electron has been liberated is referred to as a “hole”. These are interpreted as positive free charge carriers which traverse the lattice in a similar way to an electron.

The conductivity of a pure silicon crystal is related to the number of thermally excited free charge carriers, which is relatively low at room temperature. It is possible to significantly alter the conductivity of silicon by introducing foreign dopant atoms to the material. Typically used dopants are phosphorus and boron, which have one more and one less valence electron than silicon, respectively. Phosphorus is a *donor* dopant, as when it occupies a lattice site four of its valence electrons form covalent bonds, whilst the fifth valence electron is weakly bound and easily elevated

to the conduction band. This increases the amount of negative free charge carriers and so donor doped silicon is referred to as “*n*-type”. Boron is an *acceptor* dopant. When it occupies a lattice site it readily accepts an additional electron from the valence band to make a fourth covalent bond. In doing so it creates a hole in the valence band that increases the amount of positive free charge carriers in the silicon. Acceptor doped materials are referred to as “*p*-type”. The dopant atoms introduce additional energy levels in the bandgap near to the conduction or valence band, as shown in Figure 5.1(a). At room temperature the majority of dopant atoms are ionised, significantly increasing the conductivity of the material.

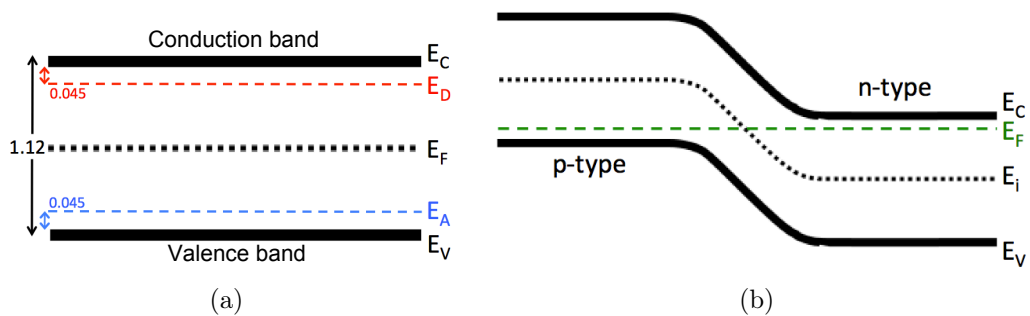


Figure 5.1: **a)** A bandgap diagram for silicon.  $E_F$  represents the Fermi level for undoped (i.e. *intrinsic*) silicon.  $E_D$  and  $E_A$  represent the dopant energy levels that are introduced by phosphorus and boron respectively [61]. **b)** The bandgap diagram for a *p*–*n* junction. When in thermal equilibrium the Fermi level must be constant across the material.  $E_i$  represents the position of the Fermi level in undoped silicon.

### 5.1.1 Silicon diodes

A silicon diode is created by bringing *n*-type and *p*-type silicon semiconductors into contact to make a *p*–*n* junction. The positive and negative free charge carriers diffuse across the boundary and combine to create a *depletion region* that is devoid of free charges. The ionised dopant atoms are distributed at fixed locations in the silicon lattice. Thus near to the junction boundary the *n*-type silicon obtains a net positive charge and the *p*-type a net negative charge. This static space-charge produces an electric field that opposes the further diffusion of free charges across the junction boundary. The corresponding built-in potential difference is referred to as  $V_{bi}$ . If one side of the *p*–*n* junction is doped significantly more than the other, the depletion region will extend further into the less doped region. Such junctions are referred to as “abrupt” and are commonly used in silicon detectors, where a high concentration dopant is implanted into a lower concentration doped bulk. The bandgap diagram for a *p*–*n* junction is shown in Figure 5.1(b).

A charged particle traversing a silicon lattice produces electron-hole pairs along its path by ionising the lattice atoms. In the absence of an external force the

free charge carriers that are produced will either recombine or diffuse through the material along a random path. When produced in the depletion region the electron-hole pair components are pulled in opposite directions by the electric field that is generated by the static space charge. The free charges can be collected at the edges of the silicon and used to measure the ionising particle's energy or position. Outside of the depletion region the electric field is small and so the efficiency for collecting charge that is produced in this region is reduced<sup>1</sup>. For efficient particle tracking it is desirable for the depletion region to extend across the entire silicon material. To increase the size of the depletion region a reverse bias can be applied to the  $p$ - $n$  junction, by applying a higher potential to the  $n$ -type side than the  $p$ -type side, as demonstrated by Figure 5.2. The size of the depletion region is increased by pulling the free charges away from the edges of the depletion region. The effective doping concentration,  $N_{eff}$ , is given by the difference in the concentrations of ionized donors and acceptors in the space charge region. The depletion voltage,  $V_{dep}$ , is the voltage required to fully deplete the silicon. It is related to the effective doping concentration by the relation [63],

$$V_{dep} + V_{bi} = \frac{q_0}{2\epsilon\epsilon_0} |N_{eff}| d^2 \quad (5.1)$$

where  $d$  is the depletion region depth,  $q_0$  is the electron charge and  $\epsilon\epsilon_0$  is the permittivity of silicon. For typical silicon detectors around 300  $\mu\text{m}$  thick the depletion voltage is significantly larger than the built-in voltage [61].

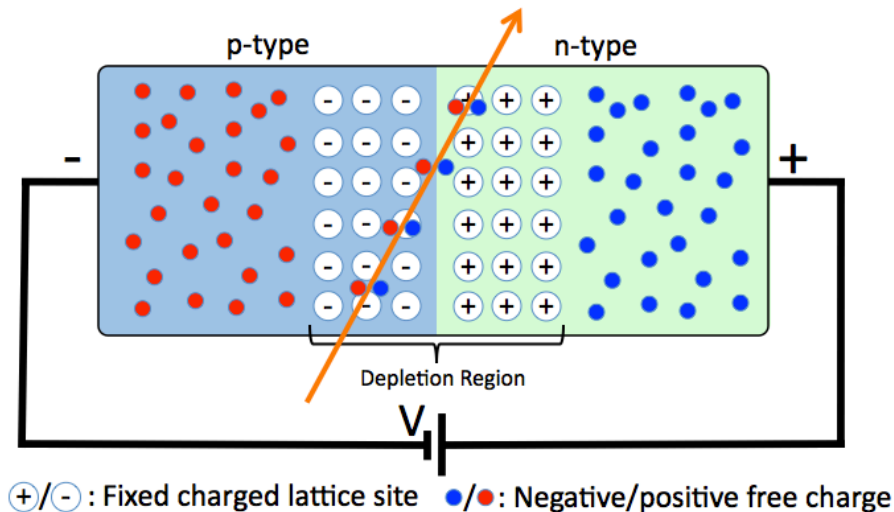


Figure 5.2: A schematic representation of a reverse biased  $p$ - $n$  junction. A particle track traversing the depletion region produces electron-hole pairs that are pulled in opposite directions by the electric field.

<sup>1</sup>It has been shown that near to 100% of the ionised charge is collected given a long enough charge collection time, even when large parts of the silicon are not depleted [62]. However, for particle physics detectors there are often strict timing constraints imposed by the beam crossing frequency.

When the  $p$ -type side of the junction is held at a higher voltage to the  $n$ -type the junction is said to be forward biased. A large forward bias reduces the size of the depletion region and results in a significant flow of current across the junction. If instead the junction is reverse biased, the electric field generated by the ionised lattice atoms prevents a current from flowing across the junction. Only a small *leakage* current is generated by thermally ionised atoms. For particle physics detectors this a useful property. The small leakage current in the absence of signal results in low levels of noise and efficient signal identification.

### 5.1.2 Particle energy loss

When a particle traversing a detector deposits all of its energy within the detection material, the amount of collected charge is proportional to the energy of the incident particle. Such detectors are called spectrometers. If the particle is not fully stopped by the detector then only the particle trajectory can be inferred. This is the most common use for silicon in modern high energy physics detectors such as the VELO, in which a particle passes through only 16% of a radiation length [64].

The rate of energy loss of a charged particle travelling through a material is described by the Bethe-Bloch equation. The relativistic charged particles produced at LHCb are mostly Minimum Ionising Particles (MIPs). These are particles for which the rate of energy loss when passing through a material is near to its minimum, as shown in Figure 5.3. The mean energy loss of an MIP in a silicon crystal is  $388 \text{ eV}/\mu\text{m}$  [65]. Despite the bandgap energy being only  $1.12 \text{ eV}$ , the average energy needed to produce an electron-hole pair in silicon is  $3.6 \text{ eV}$ . For silicon sensors of  $300 \mu\text{m}$  thickness (such as the VELO sensors) this corresponds to a mean value of approximately 32,300 electron-hole pairs produced per particle crossing. Due to the large tails in the deposited charge distribution of ionising particles in silicon, the most probable value of deposited charge is approximately 0.7 of the mean. Therefore the most probable number of electron-hole pairs produced by a MIP in silicon is approximately 22,400 electrons.

### 5.1.3 Radiation damage in silicon

The VELO sensors are subject to large fluences of high energy particles. Energetic particles traversing the silicon do not only ionise the silicon atoms to produce a signal, but also interact and impart energy on the silicon nuclei. Figure 5.4 shows some of the basic defects that are produced when a silicon nucleus is displaced from its lattice site. A nucleus displaced from its lattice site is called an interstitial. The combination of an interstitial and the vacancy in the lattice that the atom previously occupied is called a Frenkel pair. To create a Frenkel pair an energy

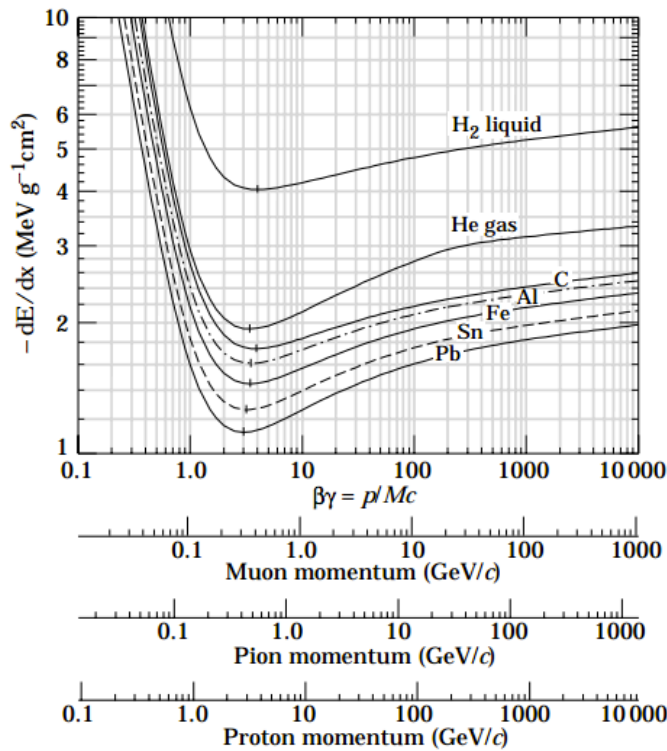


Figure 5.3: The rate of energy loss of a particle passing through a material shown as a function of  $\beta\gamma = p/Mc$ . MIPs have a  $\beta\gamma$  near to the minimum of the Bethe-Bloch equation, at a value of approximately 3. Figure from Ref. [65].

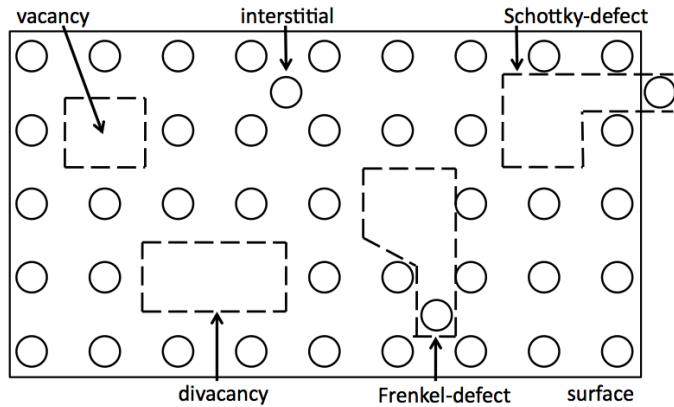


Figure 5.4: Some of the basic defects caused by radiation in silicon. Impurity atoms in the lattice can interact with these defects to form complex point defects. Figure from Ref. [67].

of approximately 25 eV must be transferred to the lattice atom [66]. The displaced silicon atom subsequently loses its energy through a combination of ionisation and further lattice displacement. At the end of a recoil the dominant interactions are with further silicon atoms and a dense *cluster* of defects is formed. The damage induced in silicon due to a recoiling atom is illustrated by Figure 5.5(a). The total amount of damage generated in the silicon lattice depends on the charge, mass and energy of the impinging radiation, as shown by Figure 5.5(b).

At non-zero temperatures the interstitials and vacancies are mobile within the

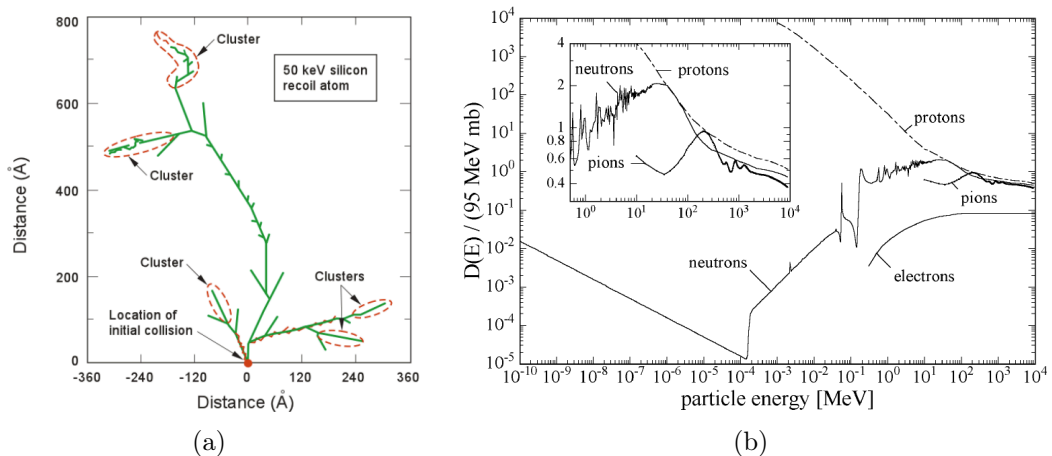


Figure 5.5: **a)** A recoiling silicon atom with an initial energy of 50 keV, as predicted by Monte Carlo simulation. Both the point defects along the recoiling atoms path and the clusters are responsible for the long term silicon damage. Figure taken and modified from [66]. **b)** The particle displacement damage functions in silicon as a function of particle energy. Plot from Ref. [63].

silicon. Interstitials and vacancies can interact in a process known as recombination, in which the displaced atom rejoins the lattice. Approximately 60% of all Frenkel pairs recombine, but in particularly disordered regions such as a cluster this can be as high as 95% [68]. The remaining interstitials, vacancies and impurities in the silicon can undergo many different types of interaction with one another. The point defects produced in such interactions change the electrical properties of the silicon by introducing additional energy levels to the silicon bandgap. These act as “stepping-stones” for electrons to more easily move between the valence and conduction bands. The introduction of microscopic defects leads to macroscopic changes in the electrical properties of the silicon [69]. Radiation induced changes to the operational parameters of a silicon detector are now discussed:

**Leakage Current** - Before irradiation, a fully depleted  $p-n$  junction draws a relatively small current, assuming contributions due to detector abnormalities such as surface scratches and cut edges are small<sup>1</sup>. The magnitude of current flow is related to the number of electron-hole pairs that are generated by thermal excitations in the silicon. Detectors are often operated at low temperatures to further reduce the leakage current and obtain a better ratio of signal to noise. Defects with energies near to the middle of the silicon bandgap act as efficient electron-hole generation sites. This can be interpreted as an electron from the valence band being elevated to the intermediate defect energy level, and then subsequently to the conduction band. Such defects are produced by impinging radiation, which leads to an increase in the sensor leakage current with fluence. A linear relationship between particle

<sup>1</sup>In reality these contributions can be large and are often dominant for unirradiated sensors.

fluence and leakage current is observed for a range of silicon substrates, as shown in Figure 5.6. Detailed studies of VELO sensor currents can be found in Refs. [70, 71].

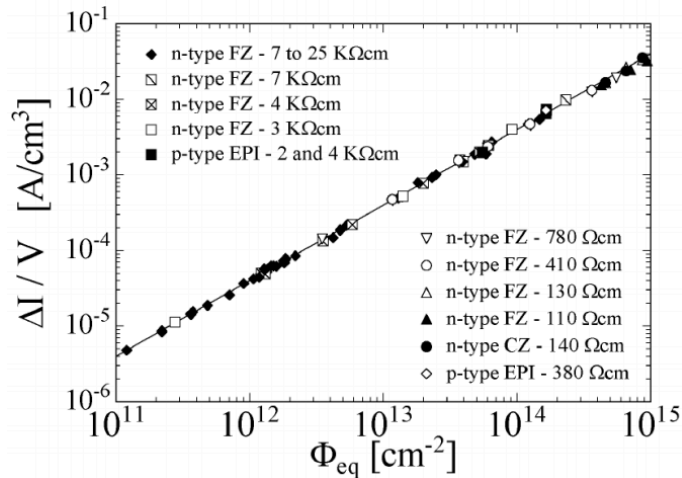


Figure 5.6: Measurements from Ref. [63] show a linear relationship between the induced bulk current and particle fluence (under well controlled annealing conditions - see Section 5.1.4).

**Depletion Voltage** - Radiation induced defects can behave similarly to donor or acceptor atoms. When the energy level of a donor defect is positioned near to the conduction band then it is easily ionised and positive space charge is introduced to the silicon. Similarly, an acceptor defect close to the valence band will lead to the introduction of negative space charge. The magnitude of the reverse bias required to fully deplete the silicon region is influenced by the introduction of additional free charge carriers. The evolution of the effective doping concentration of an initially *n*-type silicon bulk is shown in Figure 5.7. Following initial irradiation,  $|N_{eff}|$  is reduced due to the inactivation of donor dopants. This is caused by mobile defects forming complexes or entirely removing the donor atom from its lattice site. For a fixed width of silicon the depletion voltage is reduced to a value close to zero volts, as predicted by Eq. 5.1. With further irradiation the dominant process is the introduction of acceptor defects and an overall increase in the amount of positive free charge carriers. The *n*-type silicon effectively undergoes *type-inversion* and subsequently behaves like *p*-type silicon.

**Charge Collection Efficiency (CCE)** - A defect located near to either the conduction or valence band may trap free charge carriers traversing the silicon [72]. This may reduce the amount of charge collected by the detector, if the trapping time is longer than the signal collection window. Heavily irradiated silicon contains significant numbers of charge trapping defects, resulting in reduced particle detection efficiency and poorer separation of signal and noise. For heavily irradiated silicon the CCE of a sensor may be low even if fully depleted. Studies of the CCE in VELO sensors are presented in Section 5.5.

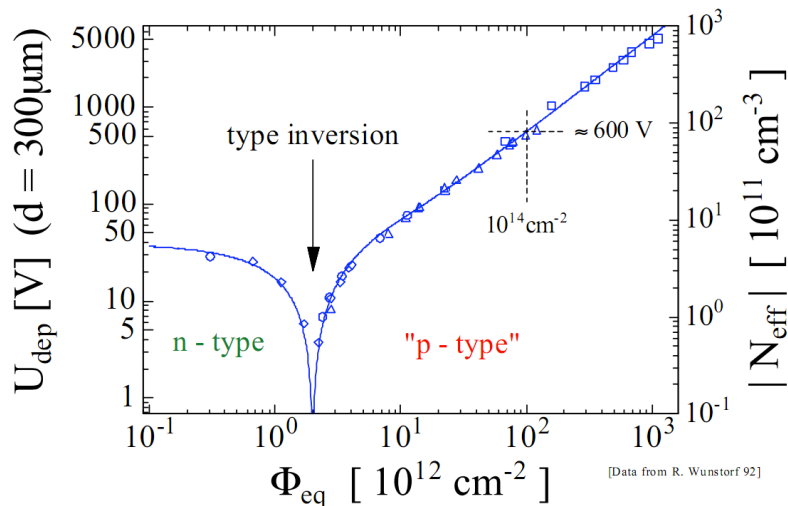


Figure 5.7: Depletion voltage measurements as a function of particle fluence for initially  $n$ -type silicon. Figure from Ref. [63].

### 5.1.4 Annealing

Over time, mobile defects can migrate through the silicon and undergo further interactions in a process known as “annealing”. Beneficial annealing occurs when the macroscopic properties revert to how they were at an earlier time. The leakage current will decrease, due to the removal of defects that have energy levels in the bandgap. The depletion voltage in  $n$ -type silicon will increase prior to type-inversion and decrease afterwards. The recombination of a silicon interstitial and a vacancy is an example of beneficial annealing. However, *reverse annealing* can also occur due to defects further interacting to form more complex defects. The effective doping concentration becomes more  $p$ -type and the depletion voltage decreases prior to type-inversion and increases afterwards. The leakage currents do not have this dual annealing response, and continue to decrease with large annealing time.

The rate of annealing is strongly related to the temperature of the silicon, as this influences both the rate at which a defect can migrate and the amount of vibrational energy available to aid complex formation or dissociation. A common practice is to freeze out annealing behaviour by cooling the silicon detectors. Typically, if the temperature of a detector is increased it will first undergo a period of beneficial annealing, followed by a more significant amount of reverse annealing.

## 5.2 VELO hardware

An introduction of the VELO detector and its performance during the first two years of data taking was given in Section 3.2.3. A more technical overview of the VELO is now given, to aid the understanding of the subsequently presented studies.

To prevent damage to the silicon sensors, the VELO comprises two halves retractable by 29 mm in the horizontal plane. Each half contains 42 half-disc shaped silicon-strip sensors. When the beams are in a stable orbit the two VELO halves are closed such that the colliding beams are surrounded by the silicon sensors. Half of the sensors have strips orientated in an approximately radial direction ( $\phi$ -type) and the other half perpendicular to this (R-type). A detector module consists of an R-type and a  $\phi$ -type sensor glued to a common support in a back-to-back configuration. An additional four R-type *pileup* sensors are positioned upstream of the interaction region. These provide the trigger with information regarding the number of proton interactions in an event. The spatial distribution of the 88 VELO sensors is shown in Figure 5.8. A summary of some of the silicon sensor properties is given in Table 5.1.

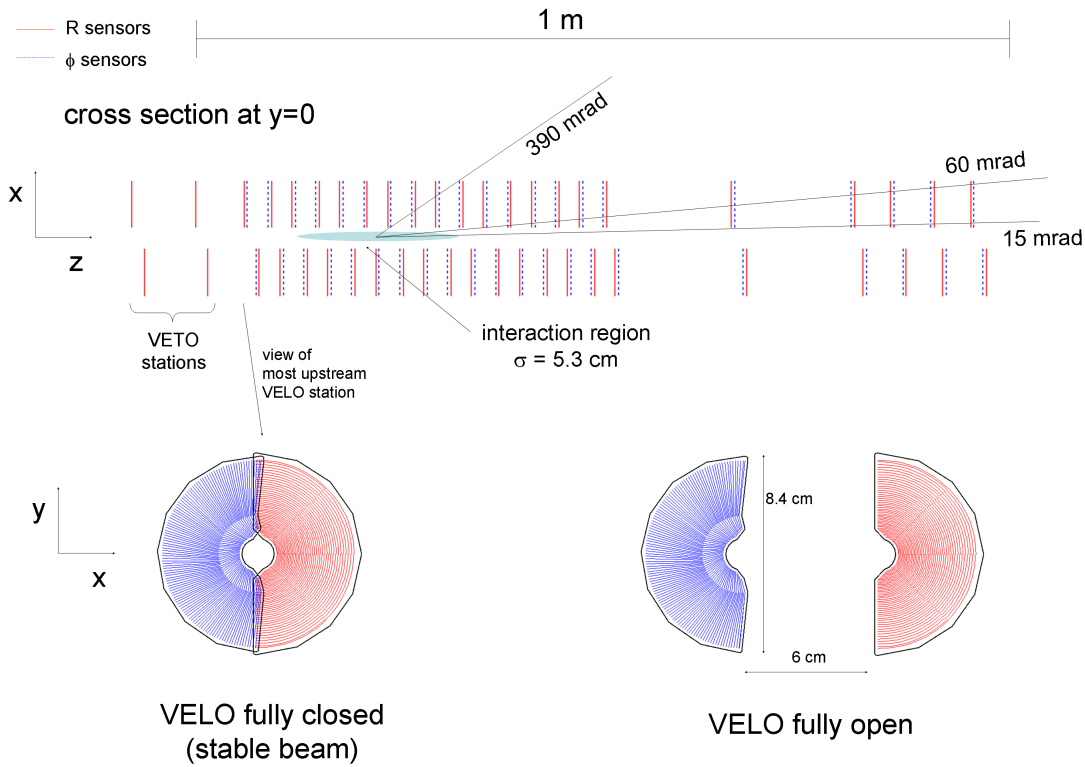


Figure 5.8: **Top:** The layout of the VELO sensors in the  $x$ - $z$  plane. The interaction region (represented by the grey ellipse) is at the upstream end of the detector. **Bottom:** The position of two sensors in the  $x$ - $y$  plane when the VELO is closed (**left**) or open (**right**). Figure from Ref. [73].

To protect the sensors from proton-beam induced Radio Frequency (RF) fields, each VELO half is stationed in a  $300\ \mu\text{m}$  thick aluminium-foil box that is held at a vacuum pressure of approximately  $10^{-7}$  mbar [23]. The RF-Foil box is isolated from the beampipe vacuum system, which maintains a lower pressure of the order  $10^{-9}$  mbar. The foil is meshed on each VELO half to allow the sensors to slightly

Table 5.1: Some VELO sensor design parameters. The sensor position along the beam axis is given relative to the beam interaction region. Parameters related to “routing lines” and “oxygen enhancement” are described in Sections 5.2.1 and 5.2.3, respectively.

Parameter	Value
Silicon thickness	300 $\mu\text{m}$
Strip pitch	40–100 $\mu\text{m}$
Strip width	11–38 $\mu\text{m}$
Routing line width	$\sim 11 \mu\text{m}$
Inner silicon edge to beam axis	7 mm
Radial distance of active strips from beam axis	8.2–42 mm
Sensor position along beam-axis	–300 to 750 mm
Oxygen enhancement [74]	$> 1 \times 10^{17} \text{ cm}^{-3}$

overlap in the  $x$ - $y$  plane when the detector is closed. This gives the VELO full coverage of the LHCb acceptance. The RF-Foil layout for a VELO half is shown in Figure 5.9. To freeze out silicon annealing, the VELO is nominally operated at a temperature of approximately  $-8^\circ\text{C}$ . This is achieved using an innovative two-phase liquid  $\text{CO}_2$  cooling system [75].

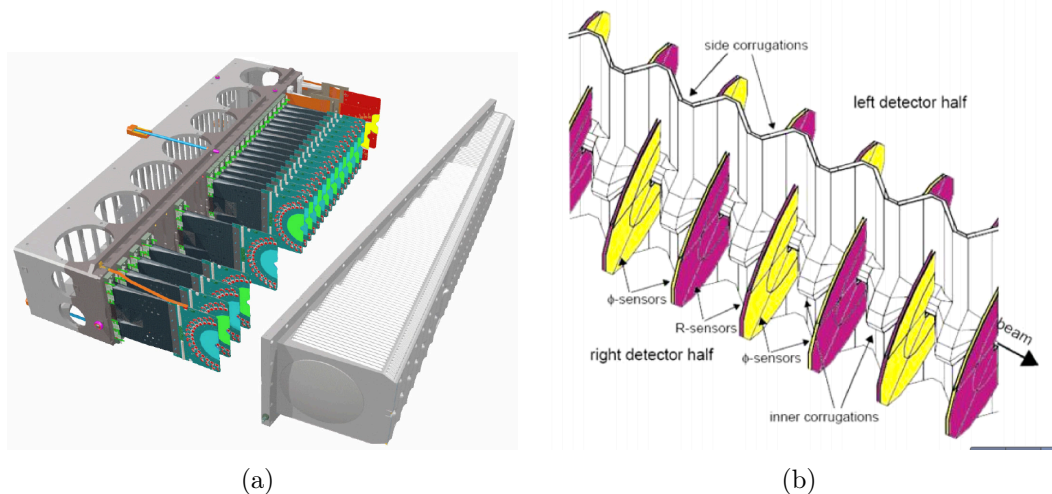


Figure 5.9: **a)** One half of the VELO with the modules and module supports (**left**) expanded from the RF-Foil box (**right**). **b)** A section of the closed VELO. The meshed RF-Foil surface allows the sensors from each half to overlap slightly. Figures from Ref. [23]. Both figures were produced using the detector geometry as simulated in GEANT4 [49, 50].

### 5.2.1 Strip layout

A strip in a VELO sensor comprises a narrow aluminium metal track running along the length of an  $n^+$  implant. This *first metal layer* is capacitively coupled to the implants for charge collection. Each sensor has 2048 strips that extend over the radial region of approximately 8–42 mm to one side of the beampipe. The *pitch*

describes the distance between the centre of adjacent strips. For VELO sensors the pitch ranges from approximately  $40\ \mu\text{m}$  at the innermost radius region to  $100\ \mu\text{m}$  at the outermost radius region. For R-type sensors the strips are located in four  $45^\circ$  regions containing 512 strips each, as shown by Figure 5.10(a). The pitch varies linearly as a function of the sensor radius. For  $\phi$ -type sensors the strips are divided into an inner and outer region, corresponding to radii less than and greater than approximately 17 mm. The inner region contains 683 strips, with the pitch ranging from approximately  $38\text{--}78\ \mu\text{m}$ . The outer region contains 1365 strips, with pitches varying from approximately  $39\text{--}97\ \mu\text{m}$ .

The R-type strips and inner  $\phi$ -type strips do not extend to the outer region of the sensor. Therefore each strip (first metal layer) is connected via a metal routing line to the edge of the sensor where the readout electronics are located, as shown in Fig.5.10(b). These routing lines are referred to as the *second metal layer* and are insulated from the bulk silicon and first metal layer by  $3.8 \pm 0.3\ \mu\text{m}$  of  $\text{SiO}_2$ . Due to the orientation of the strips, in R-type sensors the routing lines are positioned perpendicular to the sensor strips, whilst in the  $\phi$ -type they are parallel.

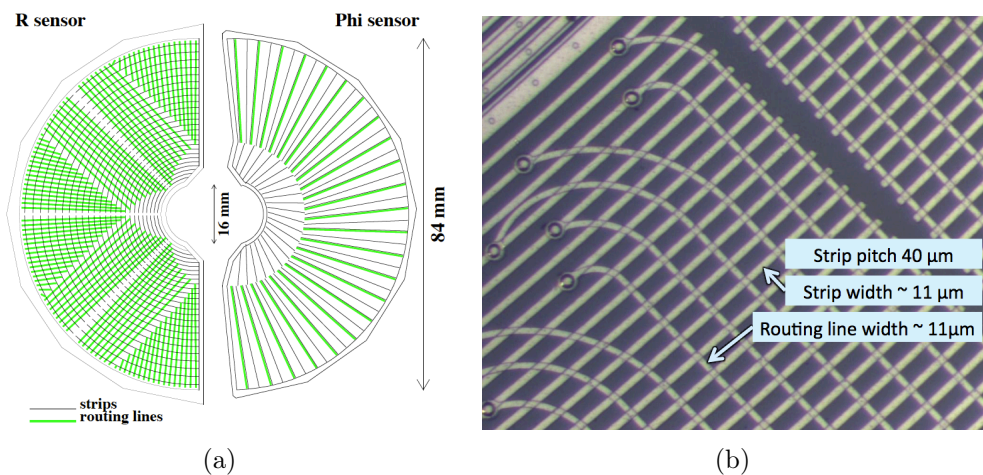


Figure 5.10: **a)** A schematic representation of an R-type and a  $\phi$ -type sensor, with the routing lines orientated perpendicular and parallel to the silicon strips, respectively. **b)** A photograph of the innermost region of an R-type sensor. Strips run from the bottom-left to the top-right. Each strip is connected to a routing line orientated perpendicularly to the strip.

All but two of the VELO sensors are  $n^+$ -on- $n$  type, comprising a highly doped  $n$ -type implant in an  $n$ -type bulk with a  $p$ -type backplane. A schematic of this configuration is shown in Figure 5.11. The other two sensors use  $n^+$ -on- $p$  silicon. They are installed in the upstream end of the VELO and are intended to be both performing detectors and an operational test of one of the leading LHC silicon upgrade technologies.

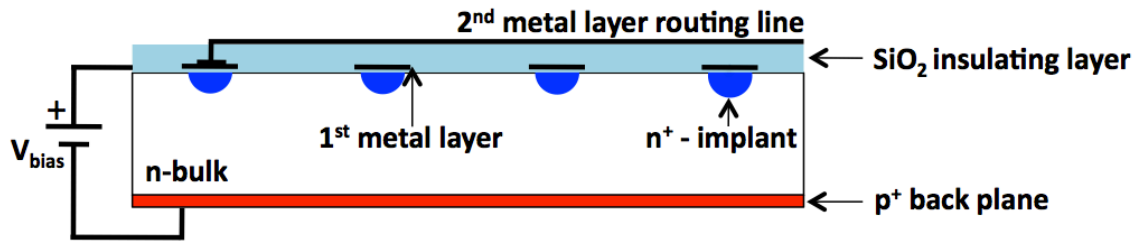


Figure 5.11: A schematic cross-section of a portion of an R-type sensor, showing the relative position of the two metal layers used to carry the readout signals in  $n^+$ -on- $n$  type sensors. The  $n^+$  implants and strips (into the page) run perpendicularly to the routing lines (left to right). For clarity the routing line of just one strip is shown. For the equivalent  $n^+$ -on- $p$  type sensor the  $n$ -type bulk is replaced by  $p$ -type.

## 5.2.2 Electronics

Strip signals are read out using 16 Beetle chips [76] per sensor. Each Beetle chip processes charge collected at 128 strips, with data output via four analogue links associated to 32 strips each. The chips accept input signals at the maximum LHC beam-crossing rate of 40 MHz. An analogue pipeline can store up to 160 events while waiting for a response from the first level of the trigger (L0). When the L0 trigger is fired the analogue data from each Beetle chip is sent to the TELL1 boards [77] via the repeater boards [78], for conversion into digital data. Analogue signals are converted into Analogue-to-Digital Converter (ADC) counts, where each ADC count corresponds to approximately 440 electrons [79]. In the absence of signal the ADC value of a strip would ideally be zero. However, individual channel offsets (referred to as a “pedestals”) and *common-mode* noise that effects all elements on an electrical pathway will bias the readout values. Pedestal and common-mode subtractions are applied to account for these sources of bias. In addition, average noise fluctuations of approximately 2–3 ADC counts occur in sensor channels, on top of which signal must be identified.

The majority of LHCb physics data is stored in a disk-space efficient format referred to as Zero-Suppressed (ZS) data. In this format, information is only stored for channels with relatively large amounts of charge, which are combined into *clusters*. A smaller fraction of data is stored as Non-Zero-Suppressed (NZS) data, where the ADC value of every strip on the sensor is stored. This is required for calibration studies and for evaluating the detector performance. Both types of data have been used in the studies described in this chapter.

## 5.2.3 Radiation hardness

The term “radiation hardness” is often used to describe how capable a detector is of operating in a radiation environment. Radiation damage is a continuous

process and so the decision of when a detector is no longer operational depends on the performance requirements of the experiment. The VELO has been designed to withstand five years of high luminosity running at the LHC. After type-inversion the depletion voltages of  $n^+$ -on- $n$  type sensors increase with further irradiation. At large bias voltages, electrical breakdown may occur in the silicon, leading to large leakage currents and permanent damage to the sensors. However, silicon sensors have been operated successfully at biases of over 1000 V, and so the limiting component in the VELO sensors is likely to be the power supply, which is only capable of producing a 500 V bias. When the depletion voltage exceeds this the sensor will not be fully depleted and sensor performance will degrade. Radiation induced effects such as reduced charge collection efficiency are also likely to degrade sensor performance, potentially well before the system hardware limits are reached (as discussed previously in Section 5.1.3).

The VELO sensors are oxygen enriched to increase their radiation hardness (see Table 5.1). The exact microscopic mechanisms that lead to the improved radiation hardness are not fully understood; however, as can be seen in Figure 5.12, studies have shown that the effect is significant for charged particle irradiation. An example of how enrichment may influence the detector evolution with fluence is now given. The most significant defects and impurities in detector grade silicon are interstitials ( $I$ ), vacancies ( $V$ ) and carbon interstitials ( $C_i$ ). Regarding donor removal, i.e. Phosphorus ( $P_s$ ), the most important reactions are  $V + P_s \rightarrow VP_s$  and  $C_i + P_s \rightarrow C_iP_s$ , the final products of which are not charged in the spacecharge region and so influence the effective doping concentration by removing the donor. Both  $V$  and  $C_i$  also interact with oxygen ( $O$ ) via interactions such as  $V + O \rightarrow VO$  and  $C_i + O_i \rightarrow C_iO_i$ . As  $VO$  does not contribute to any negative spacecharge it is beneficial to shield the donor removal by introducing concentrations of oxygen [80].

### 5.3 Charge Collection Efficiency scans

Particular detector parameters are expected to vary as a function of the bias voltage, as has been described in the previous sections. To study such parameters, five dedicated datasets have been collected between April 2010 and October 2011, known as charge collection efficiency (CCE) scans. The nominal bias voltage of VELO sensors during 2010 and 2011 data taking was 150 V. In a CCE scan, collision data is recorded with every fifth module (spaced in the  $z$  direction) operated at a voltage ranging between 0 and 150 V. The remaining modules are maintained at the nominal 150 V bias. Sensors with variable voltage are referred to as “test” sensors. The test sensors are removed from the reconstruction algorithms such that only hits from the 150 V operated sensors are used to reconstruct particle tracks. A track is

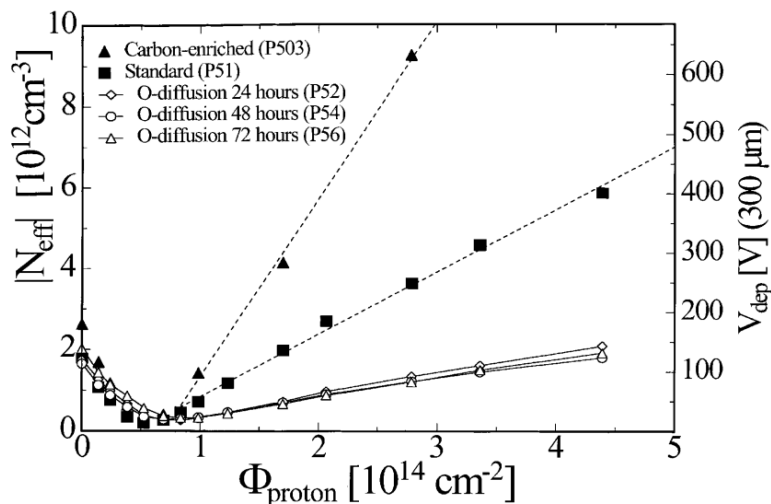


Figure 5.12: The effective doping concentration as a function of the charged particle fluence. Oxygen enrichment increases the radiation hardness compared to standard silicon by a factor of approximately three. In contrast, carbon enrichment decreases the radiation hardness of silicon. Figure from Ref. [81].

extrapolated to a coordinate on a test sensor and the set of five strips nearest to this coordinate are searched for deposited charge. This provides unbiased information on the amount of charge deposited by a particle as a function of bias voltage. ZS and NZS data formats are stored, to investigate both the clustering and charge collection efficiencies. The modified track reconstruction is performed within the VETRA framework, as described in Section 3.4.

The CCE scan data is collected at the expense of regular physics data, as colliding beams are required to produce the large number of tracks needed for these analyses. This imposes constraints on the regularity and length of the CCE scans. To reduce the data collection time the test sensors are arranged into patterns, as shown in Figure 5.13. In the first CCE scan, prior to significant sensor irradiation, a 1-in-3 pattern was used, with 6 test voltages: 10, 30, 50, 70, 100, 150 V. For the subsequent CCE scans, having improved the efficiency of the data collection procedure, an increased number of scan steps were used. For these scans a 1-in-5 pattern was used, with 13 test voltages: 0, 10, 20, 30, 40, 50, 60, 70, 80, 90, 100, 110, 150 V.

Several studies of the CCE scan data are presented in the following sections. The tracking resolution is investigated as a function of bias voltage and cluster inclusion thresholds in Section 5.4. The CCE is studied as a function of bias voltage in Section 5.5. Both of these studies use the magnitude of charge deposited on each silicon strip and therefore the NZS data is used. A study of the cluster reconstruction efficiency is presented in Section 5.6, for which ZS data is used.

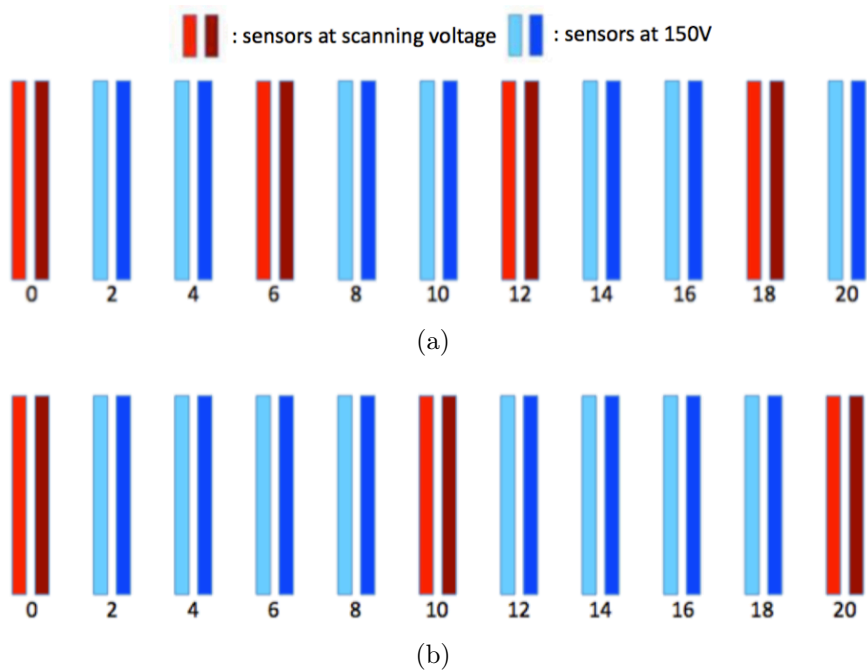


Figure 5.13: The sensor patterns used for the CCE scans. The numbers correspond to the module numbers, which increment in units of two between adjacent modules on a particular side of the detector. **a)** A 1-in-3 pattern. There are three different 1-in-3 patterns so that every sensor in the VELO can be studied. **b)** A 1-in-5 pattern. There are a total of five 1-in-5 patterns.

## 5.4 Tracking resolution

A cluster is defined as a set of between 1 and 4 adjacent strips with charge above the clustering thresholds. Particle track coordinates are measured using clusters from R-type and  $\phi$ -type sensors within a module. The cluster reconstruction algorithm uses two thresholds. The first is the *seeding* threshold, which for each strip is six times higher than the average noise in that strip. After a strip has passed the seeding threshold, additional neighboring strips are added to the cluster, provided they satisfy their *inclusion* thresholds. The inclusion threshold of each strip is set to 40% of the seeding threshold. If a cluster uses information from only one strip then the uncertainty on the cluster position is simply half the pitch:  $\Delta x_{rec} = p/2$ . The resolution in this binary situation is the root-mean-square deviation [82],

$$\sqrt{\langle \Delta x_{rec}^2 \rangle} = \sqrt{\frac{1}{p} \int_{-p/2}^{p/2} x^2 dx} = \frac{p}{\sqrt{12}}. \quad (5.2)$$

The spatial resolution of a cluster is improved when the charge is shared between multiple strips, provided the relative amount of charge deposited at each strip is taken into account. This is demonstrated schematically by Figure 5.14.

To calculate the central cluster position of multi-strip clusters in the VELO, a lin-

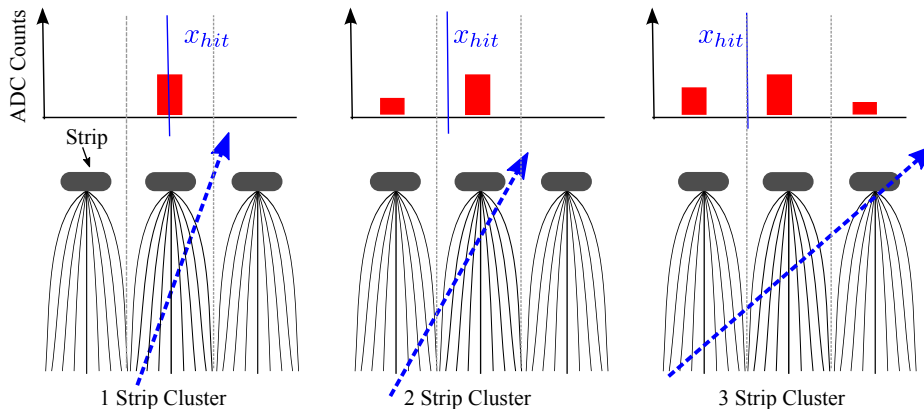


Figure 5.14: A schematic representation of the signal generated at several strips for particles traversing the sensor at various angles. The charge weighted average of adjacent strips determines the central position of the cluster,  $x_{hit}$ . Figure from Ref. [83]

ear charge distribution is assumed<sup>1</sup>. The central cluster position,  $x_{hit}$ , is determined using a pulse height weighted average over all included strips,  $i$ ,

$$x_{hit} = \sum_i w_i \cdot x_i, \quad (5.3)$$

where  $x_i$  is the position of the strip and  $w_i = q_i / \sum_i q_i$  is the fraction of total charge at a particular strip.

The unbiased residual is defined as the difference between the position of a cluster and the position of a particle track intercept, when the track has been reconstructed without using the cluster under investigation. The resolution is a strong function of the sensor strip pitch and the track projected angle<sup>2</sup>. The projected angle is related to both the angle at which a track is incident on the sensor and the angle of the strips in the sensor plane. For a particular range of strip pitch and projected angle, the unbiased residual distribution is fitted with a gaussian function. The width of the fitted function is taken as the unbiased resolution. This includes a component associated to the track extrapolation uncertainty; however, this is small compared to the resolution of the VELO sensors.

The CCE scan data described in Section 5.3 has been used to evaluate the unbiased cluster resolution as a function of sensor bias voltage. The dependence of the unbiased resolution on the inclusion thresholds has also been investigated. The following studies use only the data from the first CCE scan, in which there is negligible radiation damage to the sensors.

<sup>1</sup>Further improvements to cluster resolution could be obtained by accounting for a non-linear charge distribution between adjacent strips, as shown in Ref. [82].

<sup>2</sup>The projected angle is a difficult parameter to describe in text. For an intuitive schematic see Appendix A.

### 5.4.1 Cluster inclusion thresholds

A simple way to improve the resolution of the detector is to increase the proportion of multiple strip clusters. This can be achieved by lowering the cluster inclusion thresholds. Figure 5.15 shows the relative unbiased resolutions for several different cluster inclusion thresholds. In this study a fixed cluster inclusion threshold was used for all channels, as opposed to the nominal 40% of the seeding threshold. It is evident that for lower inclusion thresholds the unbiased resolution is reduced.

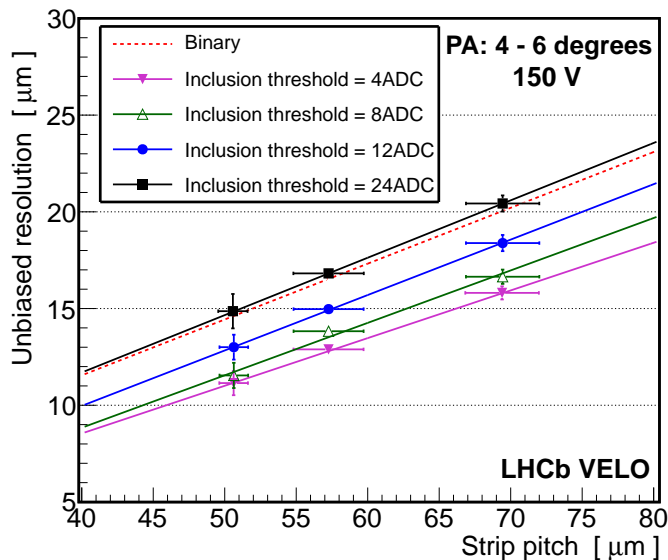


Figure 5.15: The unbiased resolution as a function of sensor pitch, shown for several inclusion thresholds (for an individual sensor). The range of track projected angle, PA, is displayed. The binary resolution obtained from Equation 5.2 is shown as the red dashed line. A cluster inclusion threshold of 24 ADC counts is comparable to the binary prediction.

Typical noise levels in VELO sensors are around 2–3 ADC counts. This corresponds to seeding thresholds of approximately 12–18 ADC counts and inclusion thresholds of approximately 5–7 ADC counts. By taking a weighted average of all bins of strip pitch and projected angle, the change in unbiased resolution when using an inclusion threshold of 3 ADC counts instead of 6 ADC counts is  $(-0.23 \pm 0.04) \mu\text{m}$ . The data sample used for this study did not have sufficient statistics to investigate sensors near to the interaction region, and so only the 23 furthest downstream modules are considered. Averaged across all the studied sensors, this corresponds to a modest improvement in the unbiased resolution of the order of a few percent. However, for specific regions of sensors with small pitch, and where the average track incidence is near perpendicular to the sensor, significantly larger improvements in resolution were found. By lowering the inclusion thresholds the number of fake clusters due to noise would remain unchanged, as this is dictated by the comparatively large seeding thresholds.

### 5.4.2 Overdepletion

Ionised electrons near to a strip are accelerated by the electric field towards the aluminium strip contact. Although an individual electron will experience many electromagnetic interactions with the silicon lattice, an overall electron drift velocity is generated. Electrons also diffuse in the direction perpendicular to the electric field lines, by randomly scattering with the lattice atoms. A sensor that is operated with a reverse bias voltage greater than its depletion voltage is described as *overdepleted*. For an overdepleted sensor [69] of thickness  $d$ , bias voltage  $V$  and depletion voltage  $V_{dep}$ , the electric field is increased throughout the sensor by an amount  $E_{add} = (V - V_{dep})/d$ . The drift velocity of the free charge carriers increases with the electric field, reducing the time in which they can diffuse perpendicularly. Therefore the number of multi-strip cluster is reduced when a sensor is overdepleted, due to less charge diffusing to neighboring strips.

The unbiased resolution has also been studied as a function of bias voltage, using a similar method to that which was described for the inclusion thresholds in the previous section. Before sensor irradiation, the majority of VELO sensor depletion voltages were less than 70 V<sup>1</sup>. The nominal bias voltage of the VELO sensors is 150 V, resulting in significant overdepletion during initial operation. The depletion voltages of  $n^+$ -on- $n$  type sensors decrease with irradiation until they type-invert, resulting in the sensors becoming further overdepleted with initial fluence.

Figure 5.16 shows the relative unbiased resolutions for a particular sensor as a function of strip pitch, for several bias voltages. The average change in unbiased resolution when reducing the bias voltage from 150 V to 100 V is  $(-0.37 \pm 0.04)$   $\mu\text{m}$ , whereas the change between 150 V and 70 V is  $(-1.17 \pm 0.04)$   $\mu\text{m}$ . The weighted mean is calculated using the 23 most downstream modules, over all projected angles and strip pitches. The largest improvements are observed in sensor regions with small pitch and low projected angle. In such regions a decrease in bias voltage to 100 V or 70 V resulted in as much as a 6% or 17% improvement in unbiased resolution.

It has been shown that the tracking resolution can be significantly improved by reducing the sensor bias voltages. However, it was decided that to maintain a consistent quality of data, and to avoid potential technical issues associated to changing the detector parameters, the nominal bias voltages were kept at 150 V for 2011 data running.

---

<sup>1</sup>Only the two  $n^+$ -on- $p$  type sensors had initial depletion voltages greater than 70 V.

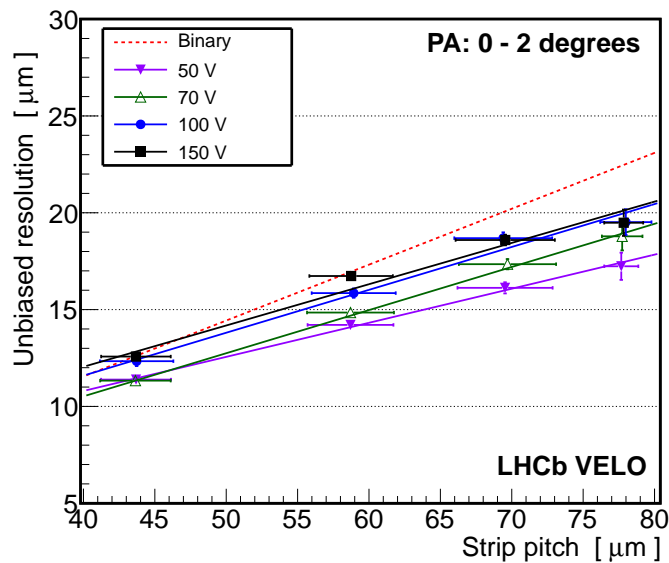


Figure 5.16: The unbiased resolution as a function of sensor pitch, for several bias voltages (in an individual sensor). The range of track projected angle, PA, is displayed. The binary resolution obtained from single strip clusters is shown for comparison.

## 5.5 Charge Collection Efficiency

Regular monitoring of the sensor depletion voltages is essential for maintaining good detector performance with particle fluence. For fluences delivered to the VELO within the first few years of operation, the change in depletion voltage for an  $n^+$ -on- $n$  type sensor is accurately described by the Hamburg model [84]. The effective doping of the  $n$ -type bulk changes over time due to radiation induced defects. Dominant mechanisms are expected to be the inactivation of phosphorous dopants in combination with the introduction of acceptors. For an oxygenated  $n^+$ -on- $p$  type sensor irradiated with charged hadrons there are expected to be competing mechanisms, with acceptor introduction partially compensated by initial oxygen induced acceptor removal [85, 86].

Following manufacture, the depletion voltage of each VELO sensor was measured by comparing the capacitance (C) to the bias voltage (V) across the sensor in C–V scans. When the depletion voltage is exceeded the capacitance reaches a minimum that is approximately constant with further increases in voltage. The corresponding C–V curves are shown in Figure 5.17. It is not possible to implement this technique after VELO installation and so alternative methods are used to extract information related to the depletion voltage.

### 5.5.1 Effective Depletion Voltages

The amount of charge collected by an under-depleted silicon strip increases as the bias voltage is increased. When the sensor is fully depleted any further increase

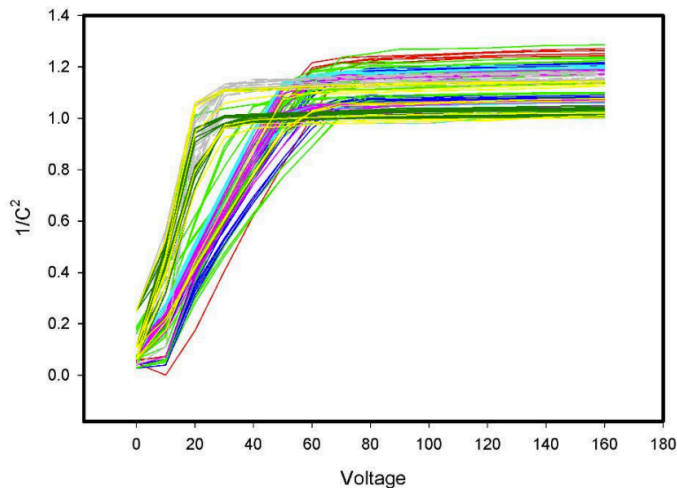


Figure 5.17: The C–V curves for VELO sensors before irradiation. Each line represents a single sensor. Figure from Ref. [74].

in bias voltage will not increase the amount of charge collected, given a sufficient signal collection time. The relationship between the charge collection efficiency (CCE) and the applied bias voltage has been exploited to measure a property of the sensor analogous to the depletion voltage, referred to as the effective depletion voltage (EDV).

The CCE scan data (described in Section 5.3) is used to determine the EDVs. A track is extrapolated to a coordinate on a test sensor, and the sum of the pedestal subtracted ADCs of the five nearest strips is measured. For each sensor and bias voltage, the ADC distribution is fitted using a gaussian convoluted with a Landau function, to determine the most probable value (MPV) of the ADC distribution. At large bias voltages the MPV of the ADC distribution reaches a plateau. The EDV is defined as the voltage at which the MPV of a sensor is equal to 80% of the plateau value, as shown in Figure 5.18. The threshold of 80% was chosen as it gives closest agreement with production measured depletion voltages (PDVs) determined with C–V measurements. The PDV and EDV of each sensor is shown in Figure 5.19, with the difference between the values obtained in each method less than 10 V for all sensors.

### 5.5.2 Effective Depletion Voltage with fluence

The particle fluence at each VELO sensor region is predicted using GEANT4 simulated events. The fluence is often presented in units of 1 MeV equivalent neutron fluence (or 1 MeV  $n_{\text{eq}}$ ). This is the fluence of 1 MeV neutrons that would produce the same radiation damage to a material as the particles responsible for the damage. Each particle is assigned a radiation damage factor using the NIEL scaling hypothesis [87], to obtain its equivalent damage in 1 MeV neutrons. The fluence is found

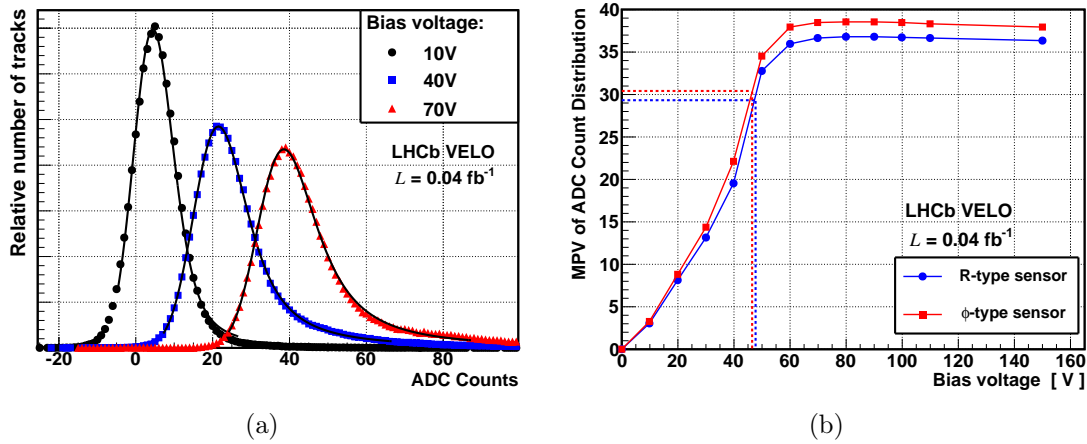


Figure 5.18: a) The fitted pedestal-subtracted ADC distribution (summed over the five strips nearest to extrapolated coordinate) for an R-type sensor at three bias voltages. b) The MPV of the fit to the ADC distribution as a function of bias voltage. The dashed lines represent the ADC that is 80% of the plateau value, and the corresponding EDV.

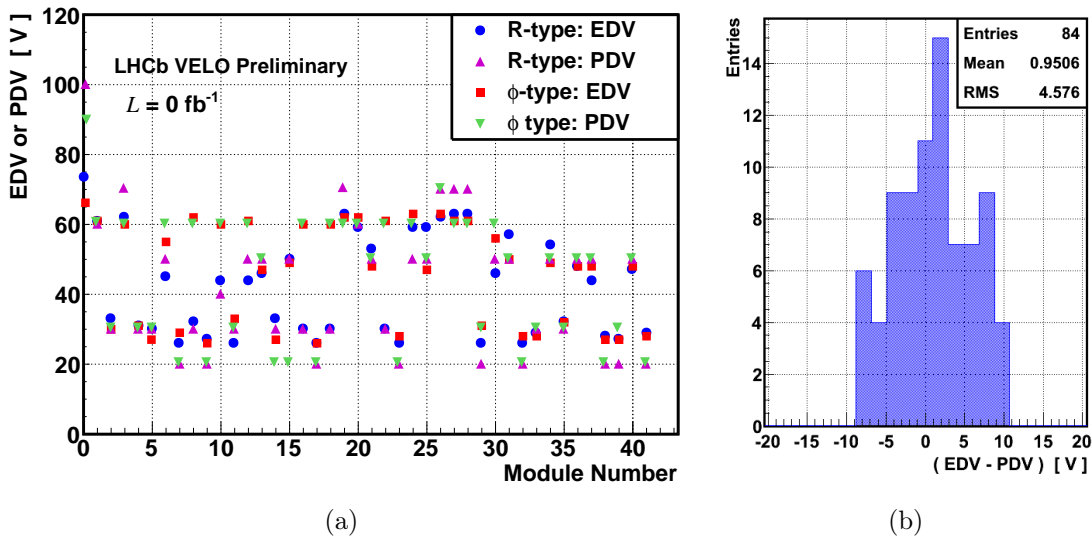


Figure 5.19: a) The EDVs measured before sensor irradiation are compared to the PDVs. b) The distribution of  $(EDV - PDV)$ , where  $|(EDV - PDV)| < 10$  V for all sensors and the RMS is less than 5.

to vary with the geometric location of the VELO sensors, as shown in Figure 5.20. It decreases with radial distance from the beam with an approximate  $1/r^{1.75}$  dependence. The position along the beam-pipe ( $z$ -direction) is also found to significantly affect the fluence incident on a sensor.

The leakage current in a silicon sensor increases linearly with particle fluence, as was discussed previously in Section 5.1.3. This relationship has been used to predict the change in the sensor currents as a function of luminosity, with the simulated fluences and sensor temperature history used as inputs. Good agreement is found between the predicted and measured sensor currents, as shown in Figure 5.21, thus

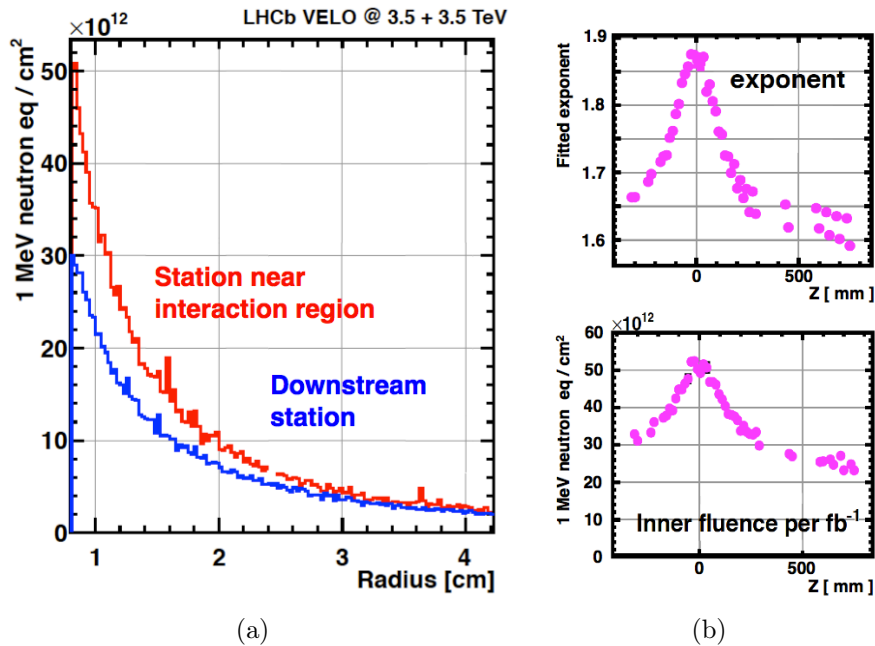


Figure 5.20: **a)** The fluence from  $1 \text{ fb}^{-1}$  of integrated luminosity as a function of radius for two VELO sensors, as seen in simulated proton-proton collisions at a 7 TeV centre-of-mass energy. **Top b)** The fitted exponent,  $k$ , for each sensor, where the fluence as a function of radius is fitted with the function  $Ar^k$ . The distribution of the fluence across the sensor becomes flatter with distance from the interaction region. **Bottom b)** The fluence at the innermost radius of each sensor against the  $z$ -coordinate of the sensor. Figures from Ref. [88].

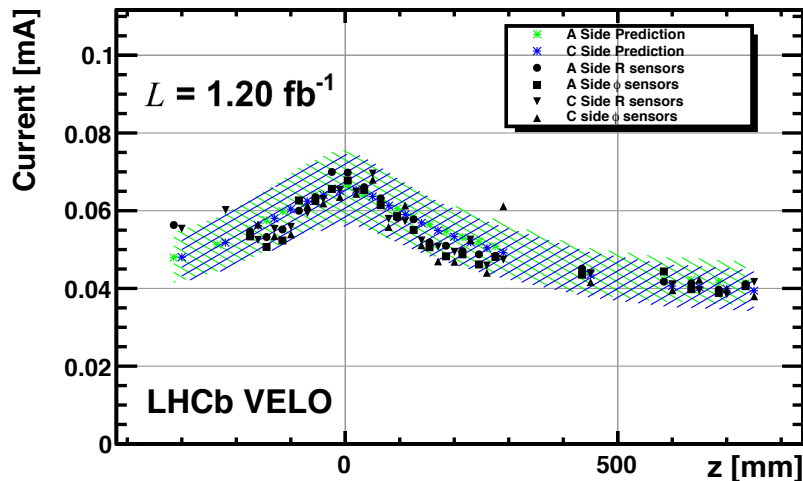


Figure 5.21: The leakage current against sensor  $z$ -coordinate after  $1.20 \text{ fb}^{-1}$  of integrated luminosity, normalised to  $0^\circ\text{C}$ . The data is in agreement with predictions, represented by the shaded region. The two VELO halves are referred to as the A and C sides of the VELO. Figure from Ref. [88].

validating the use of simulation to predict the fluences incident on VELO sensors.

To study the VELO sensors as a function of fluence, each sensor is divided into five radial regions, defined such that the fluence does not change by more than

a factor of two across a region. Before irradiation, the EDVs are expected to be approximately equal in each of the radial region within a sensor. This is consistent with the measurements shown in Figure 5.22. The distribution of the difference between the mean EDV of a sensor and the EDV measured in a particular radial region is centered on zero for all regions. The magnitude of variations about zero are less than 4 V, indicating the precision of the method.

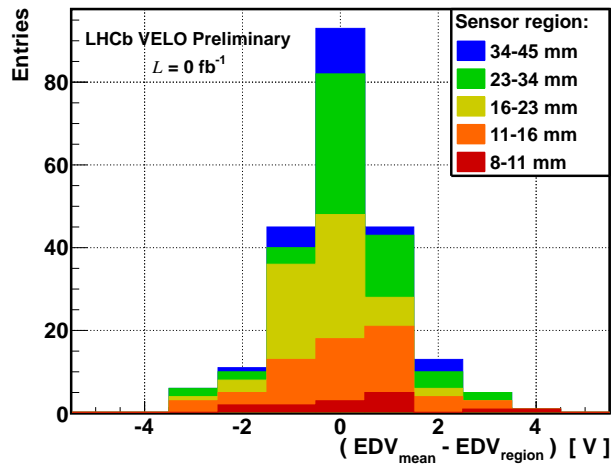


Figure 5.22: The EDV in a sensor region subtracted from the mean EDV of the sensor, shown for each sensor region.

Following  $0.43 \text{ fb}^{-1}$  of delivered luminosity, the EDV shifted significantly for many of the sensor regions, as shown by Figure 5.23. The EDV is found to decrease with fluence across all radial regions, as predicted by the Hamburg model. The decrease is largest in the inner radial regions of the sensors, consistent with expectations that these regions are exposed to higher fluences. The largest decreases in EDV are observed in sensors that had high initial depletion voltages.

The change in EDV with irradiation is shown for a particular  $n^+$ -on- $n$  type sensor in Figure 5.24(a). The EDV is seen to decrease with initial fluence across all radial regions. The innermost region undergoes an increase in EDV between  $0.80$  and  $1.22 \text{ fb}^{-1}$  of delivered luminosity, indicating that this part of the sensor has type inverted. The  $n^+$ -on- $p$  type sensors exhibit a decrease in EDV with initial fluence, as shown in Figure 5.24(b). This initial EDV decrease is understood to be caused by oxygen induced removal of boron interstitial acceptor sites, an effect that has been previously observed by others [85, 86].

The global EDV trend with particle fluence is shown in Figure 5.25. The minimum EDV observed for any sensor is  $\sim 18 \text{ V}$ . That the minimum is significantly greater than  $0 \text{ V}$  demonstrates the limit at which the direct comparison between the EDV and depletion voltage breaks down. The minimal EDV is dictated by the smallest potential difference required to collect charge from the silicon strips, which in turn depends on the charge collection window of the electronics. However, the

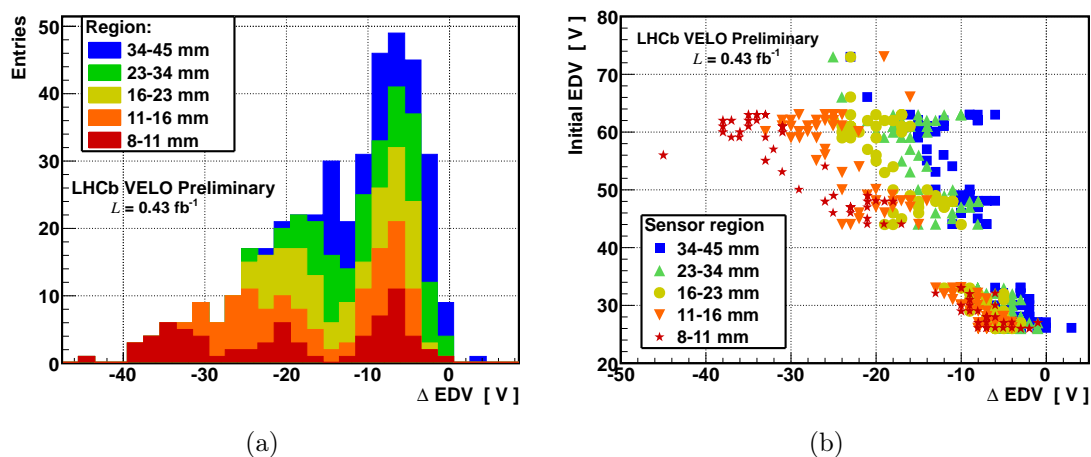


Figure 5.23: The EDV before irradiation, subtracted from the EDV after  $0.43 \text{ fb}^{-1}$  of integrated luminosity,  $\Delta\text{EDV} = (\text{EDV}_{0.43 \text{ fb}^{-1}} - \text{EDV}_{0 \text{ fb}^{-1}})$ , for **a)** each sensor radius region and **b)** as a function of the EDV before sensor irradiation. Negative values of  $\Delta\text{EDV}$  correspond to a decrease in EDV with fluence.

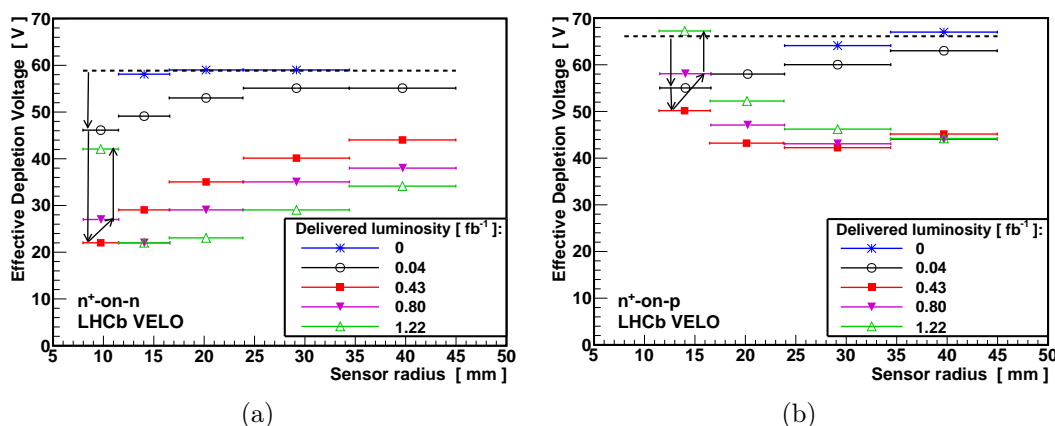


Figure 5.24: **a)** The EDV against sensor radius for an  $n^+$ -on- $n$  type sensor for each of the CCE scans. The dashed line shows the mean EDV across all radius regions prior to sensor irradiation, where some  $0 \text{ fb}^{-1}$  data points are not present due to low statistics. **b)** A similar plot for the  $n^+$ -on- $p$   $\phi$ -type sensor. The minimum EDV is  $\sim 40 \text{ V}$ , which is significantly higher than the minimum at  $\sim 20 \text{ V}$  observed for the  $n^+$ -on- $n$  type sensors.

true depletion voltage is expected to decrease to a value closer to 0 V. If no reverse bias is applied then there will only be a small electric field associated to the intrinsic voltage of the  $p$ - $n$  junction, hence the charge collection efficiency is low and an EDV of value less than around 20 V cannot be obtained.

It is expected that the sensors type invert at a fluence near to the EDV minimum. For all  $n^+$ -on- $n$  type sensors, this occurs at approximately the same fluence of  $(10 - 15) \times 10^{12} \text{ 1 MeV n}_{\text{eq}}$ . Annealing effects were negligible during this period, as the sensors were operated at low temperatures of approximately  $-8^\circ \text{C}$  (maintained throughout the majority of shutdown periods). The behaviour after type inversion is found to be independent of the initial EDV of the sensor, with an approximately

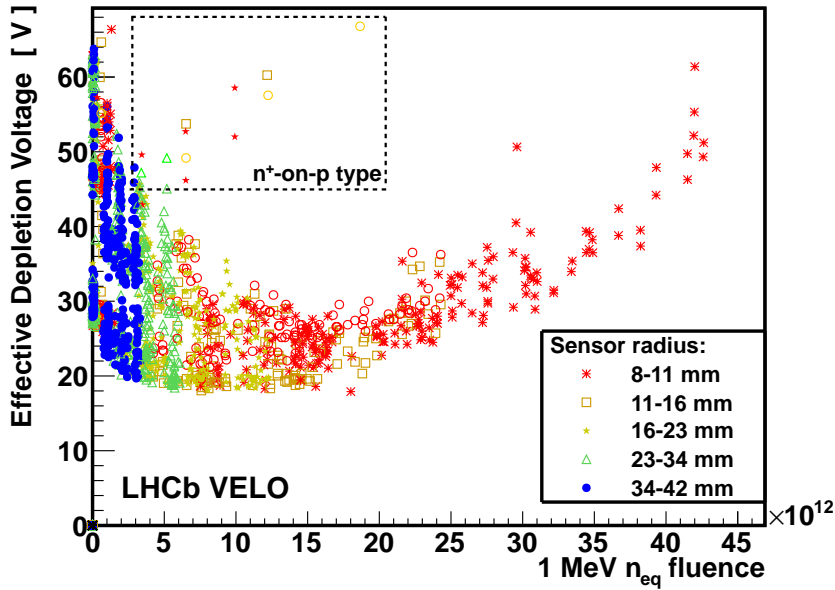


Figure 5.25: The EDV against fluence for different radial regions of VELO sensors. Data from all CCE scans is displayed. For many sensors the inner radius regions have type inverted.

linear increase in EDV with further fluence.

The entries within the dashed box in Figure 5.25 correspond to data from the  $n^+$ -on- $p$  type sensors. Initial decreases in EDV occurred up to a fluence of approximately  $3 \times 10^{12}$   $1 \text{ MeV } n_{\text{eq}}$ . After this, the EDV has increased with further fluence. The rate of increase is similar to that of the type inverted  $n^+$ -on- $n$  type sensors. A linear fit to the data gives a voltage increase with fluence of  $(1.43 \pm 0.16) \times 10^{-12} \text{ V}/1 \text{ MeV } n_{\text{eq}}$  for  $n^+$ -on- $p$  type sensors, which is compatible with the rate measured for  $n^+$ -on- $n$  type sensors of  $(1.35 \pm 0.25) \times 10^{-12} \text{ V}/1 \text{ MeV } n_{\text{eq}}$ . The gradient of the  $n^+$ -on- $p$  type sensors is fitted to all points with fluence greater than  $2 \times 10^{12}$   $1 \text{ MeV } n_{\text{eq}}$ , after the initial decrease in EDV. The precise fluence at which the  $n^+$ -on- $n$  type sensors invert is not obvious from Figure 5.25 and so the gradient is fitted over two ranges,  $(25 - 45) \times 10^{12}$   $1 \text{ MeV } n_{\text{eq}}$  and  $(30 - 45) \times 10^{12}$   $1 \text{ MeV } n_{\text{eq}}$ , with the mean of the two fitted values taken.

The EDVs of the  $n^+$ -on- $p$  type sensors begin to increase having received significantly less fluence than the  $n^+$ -on- $n$  type sensors. If the comparable rate of increase is maintained with further fluence then the  $n^+$ -on- $p$  type sensors will reach an EDV of 500 V, the hardware limit of the VELO system, having received approximately  $35 \times 10^{12}$   $1 \text{ MeV } n_{\text{eq}}$  less fluence than the  $n^+$ -on- $n$  type sensors. Using the measured rate of EDV increase, the  $n^+$ -on- $n$  type sensors will reach the 500 V hardware limit at a fluence of approximately  $380 \times 10^{12}$   $1 \text{ MeV } n_{\text{eq}}$ .

The relationship between the MPV and the applied bias voltage is shown for  $n^+$ -on- $n$  and  $n^+$ -on- $p$  type sensors in Figure 5.26. The rate of MPV increase with

bias voltage for the  $n^+$ -on- $p$  type sensor is approximately linear both before and after irradiation (see Figure 5.26(a)). In contrast, the  $n^+$ -on- $n$  type sensor collects a relatively small amount of charge when under-depleted, with a steep increase observed as the sensor approaches full depletion (see Figure 5.26(b)). After the  $n^+$ -on- $n$  type sensors have type inverted, the increase in MPV with increasing bias voltage becomes more linear (see Figure 5.26(c)).

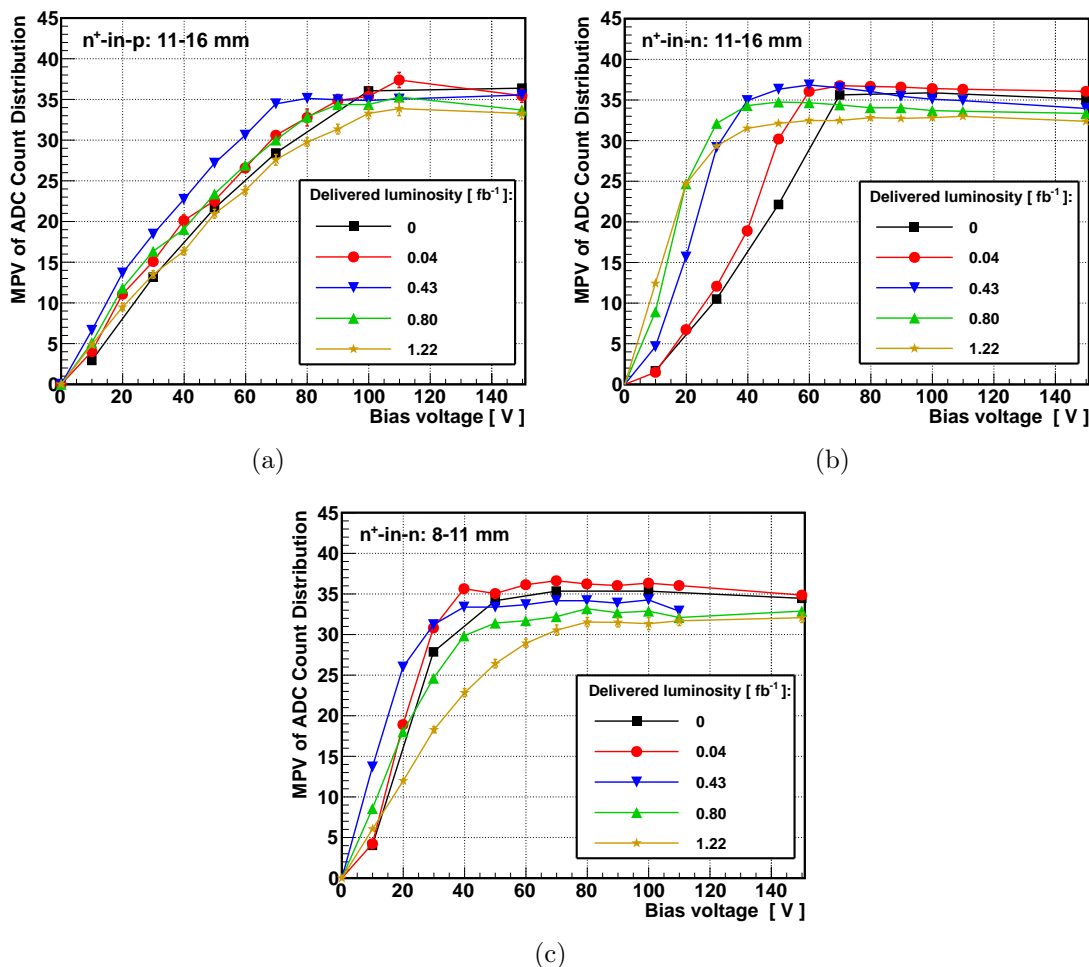


Figure 5.26: The MPV against bias voltage for **a)** an  $n^+$ -on- $p$  type sensor, **b)** an  $n^+$ -on- $n$  type sensor with a large initial depletion voltage and **c)** an  $n^+$ -on- $n$  type sensor with a small initial depletion voltage. After type-inversion the  $n^+$ -on- $n$  type sensor curve more closely resembles the shape of the  $n^+$ -on- $p$  type sensor curve.

The observed variations in the rate of MPV increase can be understood by considering the way in which each sensor type approaches full depletion. For unirradiated  $n^+$ -on- $n$  type sensors, the depletion region grows from the sensor back-plane (the  $p^+$  region) towards the strip contacts. Therefore when under-depleted, the region around the strips has poor conductivity and the collected charge is significantly reduced. The amount of collected charge increases rapidly as this region becomes depleted. For the  $n^+$ -on- $p$  and type inverted  $n^+$ -on- $n$  type sensors, the depletion region grows from the strip side of the sensor, hence the steadier increase in collected

charge as the depletion region expands.

The amount of charge collected, and therefore the MPV of the ADC distribution, is expected to change with fluence due to radiation induced changes to the silicon. When operated at the nominal bias voltage of 150 V, the mean MPV of all sensors was seen to increase by approximately 3% following  $0.04 \text{ fb}^{-1}$  of delivered luminosity. This may be due to operational changes made during early data collection. For example, adjustments to the timing settings could lead to a shift in the peak of the signal within the collection window, altering the total collected charge.

Following the initial increase in the mean MPV, a subsequent decrease was observed with further fluence, as is expected due to the introduction of charge trapping defects. This was evident in all of the sensors shown in Figure 5.26. The MPV of all VELO sensors when operated at 150 V is shown as a function of fluence in Figure 5.27. The initial increase in the mean MPV of approximately 3% is apparent. Following this, the mean MPV has decreased with further fluence. For  $\phi$ -type sensors the MPV at nominal sensor operation has decreased by approximately 4% in the

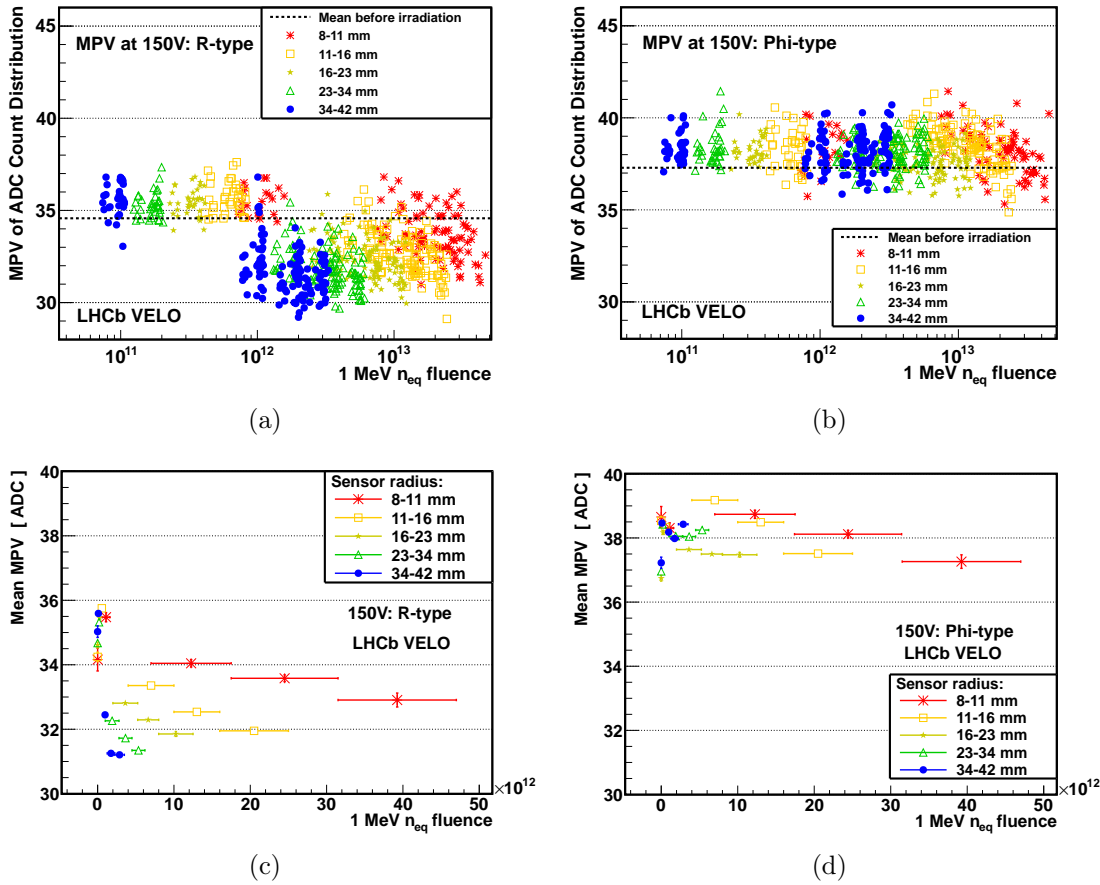


Figure 5.27: The MPV as a function of fluence, when operated at the nominal 150 V. The MPV for each radial region of each sensor is shown for **a)** R-type sensors, and **b)**  $\phi$ -type sensors. The mean MPV across all sensors before irradiation is shown by the dashed lines. The same data is collected into bins of fluence for **c)** R-type sensors and **d)**  $\phi$ -type sensors.

most irradiated regions, after receiving a fluence of  $40 \times 10^{12} \text{ 1 MeV n}_{\text{eq}}$ . The R-type sensors exhibit an even larger reduction in their MPVs. This is due to a charge loss mechanism related to the second metal layer of the R-type sensors, which is described in detail in Section 5.6.1. For R-type sensors the MPV is reduced by approximately 8% in the inner regions that have received a fluence of  $40 \times 10^{12} \text{ 1 MeV n}_{\text{eq}}$ . The outer regions of the sensor are most significantly affected by the second metal layer effect. In these regions the MPV decreased by approximately 12% following a fluence of just  $2 \times 10^{12} \text{ 1 MeV n}_{\text{eq}}$ .

### Hamburg model comparison

The irradiation induced change in the depletion voltage is modeled as a function of time, temperature and fluence by the Hamburg Model. It has three components: a short term annealing component, a stable damage component and a reverse annealing component. By combining this model with LHCb luminosity measurements and VELO sensor temperature readings, a prediction for the change in depletion voltage as a function of fluence has been made. Figure 5.28 displays the measured EDV of the VELO sensors and the Hamburg predictions for sensors of different initial depletion voltages. Good agreement is observed for low fluences and for higher fluences after type inversion, with significant deviations in between. After type inversion, the Hamburg model shows little dependence on the initial EDV of the sensor, in agreement with data.

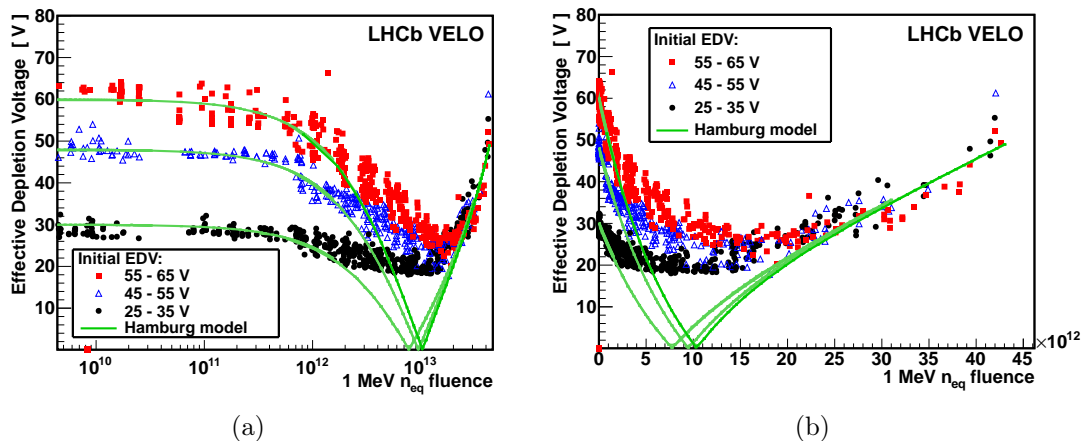


Figure 5.28: The EDV from data is compared to Hamburg model predicted depletion voltages, against fluence on **a)** a log scale and **b)** a linear scale. Figures from Ref. [88]

### 5.5.3 Noise scans

The CCE scan data described in Section 5.5.1 requires proton beams, and so are collected at the expense of physics data. A second method has been developed

to monitor radiation damage [88], utilising the relationship between the intrinsic electronic noise of the pre-amplifier and the capacitance of the sensor. Data scans for this study can be collected regularly as proton collisions are not required.

In undepleted silicon, several sources of input capacitance are identified, the most dominant of which is the inter-strip impedance. For  $n^+$ -on- $n$  sensors before type inversion, the depletion region grows with increasing voltage from the  $p^+$  backplane (the opposite side to the strips). When the sensor is fully depleted, the space-charge reaches the strips and the inter-strip resistance increases by several orders of magnitude, resulting in a decrease in sensor noise [89]. For  $n^+$ -on- $n$  type sensors following type inversion, and for  $n^+$ -on- $p$  type sensors, the depletion region grows from the strip side of the silicon. In this situation the strips are immediately isolated at the application of a bias voltage and the relationship between noise and voltage cannot be exploited to extract information related to the depletion voltage.

The intrinsic noise in VELO sensors is determined by subtracting the mean ADC value (or *pedestal*) and a common mode noise term. Figure 5.29 shows the inverse of the intrinsic noise as a function of voltage for an  $n^+$ -on- $n$  and  $n^+$ -on- $p$  type sensor. For the  $n^+$ -on- $p$  both before and after irradiation, and  $n^+$ -on- $n$  after irradiation (having type inverted) the distribution is flat, thus little information related to the sensor depletion voltages can be extracted. For the  $n^+$ -on- $n$  type sensor prior to type inversion, an increase in voltage results in a decrease in noise until a plateau is reached when the sensor is fully depleted.

The noise scan data can be used to identify whether an  $n^+$ -on- $n$  type sensor has type inverted. Only R-type sensors are investigated as the strip orientation allows for the identification of strips that have been subject to a specific fluence. Following

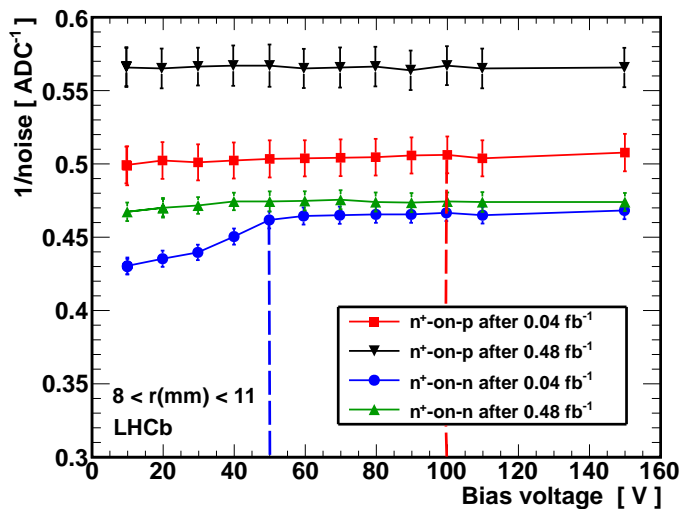


Figure 5.29: The inverse of the sensor noise against bias voltage for a particular  $n^+$ -on- $n$  and  $n^+$ -on- $p$  type sensor, for two values of integrated luminosities. The C-V scan measured initial depletion voltages are shown by the dashed lines.

a delivered luminosity of approximately  $0.80 \text{ fb}^{-1}$ , 40 of the sensors were identified as having type inverted in the first radial region (8–11 mm), while in the second region (11–16 mm) 21 sensors were identified. Similar information can be extracted from the CCE data. A sensor region is defined as type inverted when the measured EDV has reached a minimum and subsequently begun to increase. Following the same luminosity, the CCE method identified 21 and 5 type inverted sensors in the first and second radial regions, which is considerably fewer than is found with the noise method. This discrepancy is understood by examination of Figure 5.28(b), in which the minimum of the Hamburg model prediction and the point at which the EDVs begin to increase are separated by a fluence of approximately  $10 \times 10^{12} \text{ 1 MeV n}_{\text{eq}}$ . The noise scan method is not subject to the same fluence lag. Following a delivered luminosity of  $1.2 \text{ fb}^{-1}$ , the CCE method identifies 39 and 21 sensors as having type inverted in the two radial regions. This is in good agreement with the noise method, with the same 39 and 21 sensors identified by each method (and the noise method identifying one additional sensor in the 8–11 mm region).

## 5.6 Cluster Finding Efficiency

All physics analyses at LHCb rely on efficient track reconstruction using clusters from the VELO sensors. A cluster is defined as one or several adjacent strips with charge above a particular threshold. The cluster finding efficiency (CFE) of the VELO has been measured using large samples of regular physics data. The modified track reconstruction used by the CCE analysis is also used to study the CFE, where the track intercept with a test sensor is instead searched for the presence of a cluster. As regular physics data is used, all of the sensors are operated at the nominal 150 V bias.

Before sensor irradiation the CFE of each VELO sensor was measured. The results of these measurements are shown in Figure 5.30. Tracks are required to have a  $\chi^2$  per degree of freedom less than 1.25, to reduce the fraction of tracks for which a cluster is not found due to inaccurate track interpolation. Each track is required to have hits in the two modules upstream and two modules downstream of the test sensor. With these tracking requirements the two modules at each end of each VELO half cannot be studied and so these sensors are neglected. Evaluated using 100,000 tracks per sensor, the mean CFE of the remaining VELO sensors is 99.45%. If individual strips that have been identified as bad are neglected then the CFE increases to 99.97%.

To identify strips with particularly poor performance, the distribution of strip-numbers is studied for each sensor, for strips located at the track intercept when a cluster is not found. An example of such a distribution is shown by Figure 5.31. A

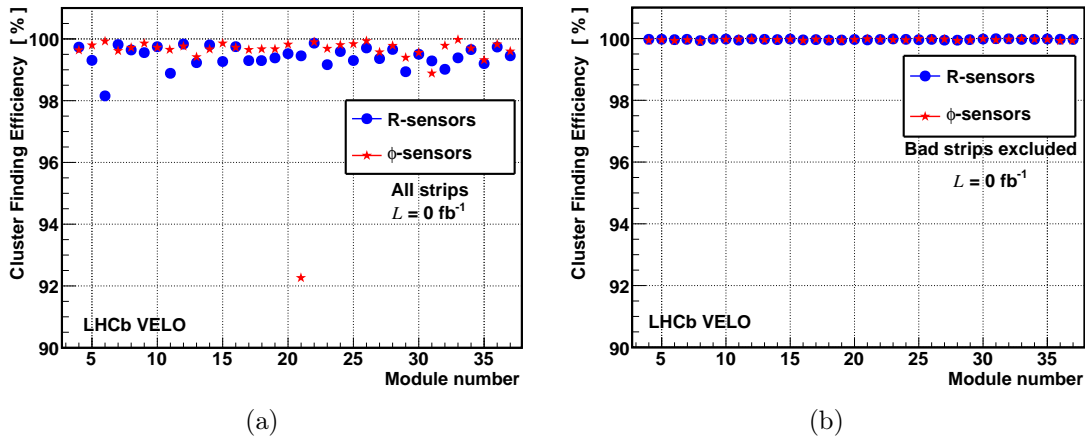


Figure 5.30: The cluster finding efficiency before sensor irradiation shown for **a)** sensors with all strips included and **b)** sensors with bad strips excluded. The  $\phi$ -type sensor in module 21 has a particularly low CFE when all strips are included. This sensor has a broken Beetle chip, hence the  $\sim 1/16$  reduction in CFE.

bad-strip finding algorithm is executed on these distributions to identify strips for which a large proportion of tracks have not produced a cluster. A strip is bad if the number of entries for a particular strip is four times the average of the nearest 30 strips. It is required that 500,000 tracks are used for each sensor. The distribution of track intercepts on the test sensor when a cluster is not found is shown in the  $x$ - $y$  plane in Figure 5.32. Bad strips are visible in both R-type and  $\phi$ -type sensors.

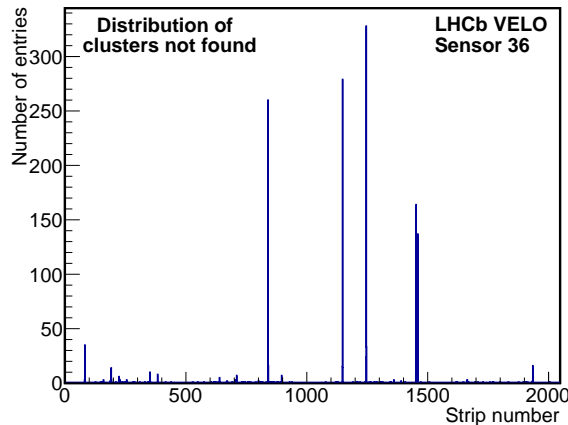


Figure 5.31: The distribution of strip numbers for which a cluster is not found (for a particular sensor). Bad strips manifest as distinct spikes on the spectrum.

The number of bad strips were also measured by alternative methods prior to VELO installation, with both visual and detector performance related techniques. Approximately 0.55% of strips were identified as bad. This is in agreement with measurements from the CFE method, in which 0.77% of strips were found to be bad after VELO installation, but prior to significant irradiation. The CFE method found 86% of the same bad strips as the pre-installation measurements. Following

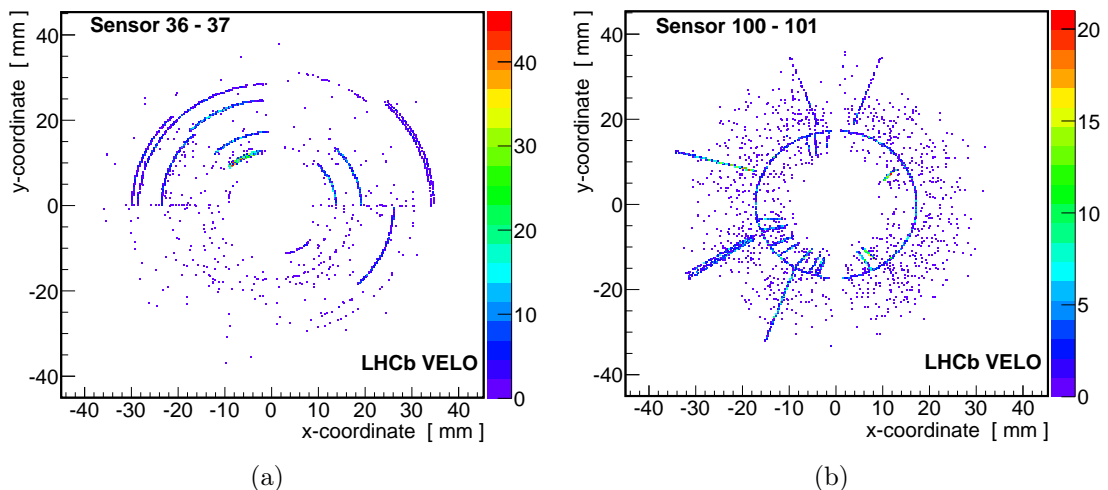


Figure 5.32: The location in the  $x$ - $y$  plane of the track intercept when a cluster is not found for **a)** an R-type sensor and **b)** a  $\phi$ -type sensor. The inefficient HV boundary region at a radius of approximately 17 mm is visible in the  $\phi$ -type sensor.

a further  $1.2 \text{ fb}^{-1}$  of delivered luminosity, 1.12% of strips were identified as bad.

### 5.6.1 Second metal layer

The CCE scan samples have also been used to measure the CFE as a function of sensor bias voltage and fluence. After irradiation the CFE in many sensors decreased significantly, as shown in Figure 5.33. The inefficiency was unexpected and found to be particularly prevalent at large sensor radii and high bias voltages. The rate of CFE decrease is not proportional to the delivered luminosity, but instead exhibits a rapid drop between the  $0.04$  and  $0.43 \text{ fb}^{-1}$  data scans.

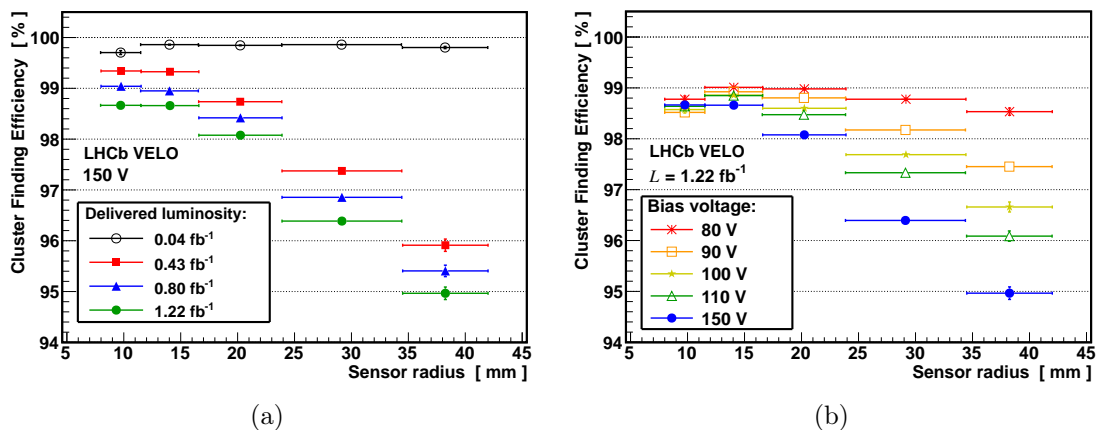


Figure 5.33: The CFE for an R-type  $n^+$ -on- $n$  sensor as a function of sensor radius for **a)** different amounts of delivered luminosity and **b)** several different bias voltages.

To determine the source of the CFE decrease, a large sample of regular LHCb physics data has been used to measure the CFE for small spatial regions on a sensor at the nominal 150 V bias. The result of this is shown in Figure 5.34, displayed below a diagram illustrating the layout of the second-metal-layer readout lines. There is a clear correspondence between the two figures, with high CFE measured in regions that are devoid of routing lines.

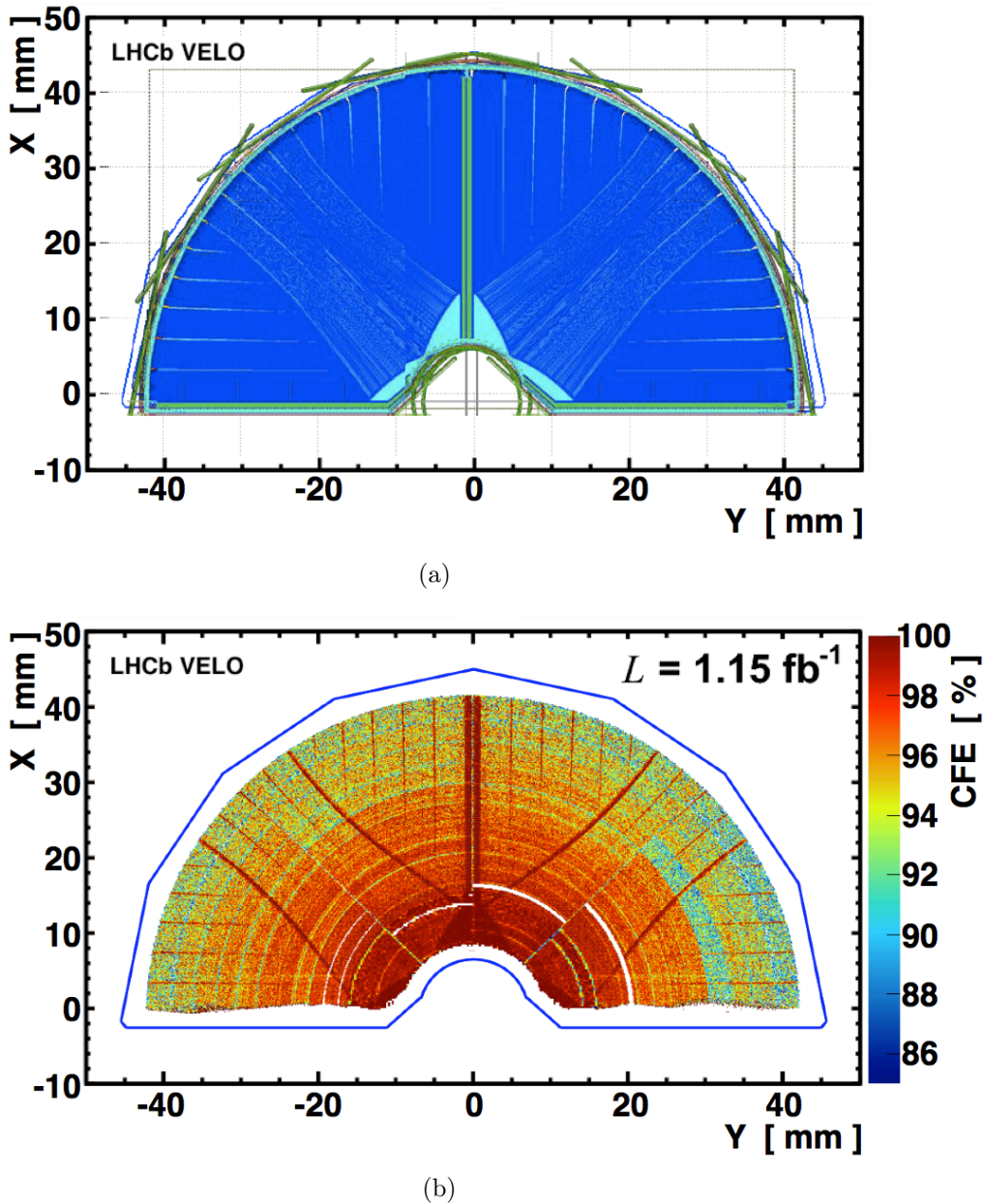


Figure 5.34: **a)** The layout of the second-metal-layer routing lines on an R-type sensor. The darker regions represent the presence of routing lines, and the lighter regions their absence. **b)** The CFE shown in small spatial regions of an R-type sensor. Areas with near to 100% CFE match the regions where there are no routing lines present.

Using precise track extrapolation, the CFE loss has been investigated as a function of the distance between a track intercept with a sensor, and the nearest strip

and routing line. This is shown in Figure 5.35. The CFE is improved for track intercepts that are near to the strip implants. Conversely, the CFE is reduced when a track intercept is far from a strip and near to a routing line. Similar effects have been observed in other experiments [90, 91].

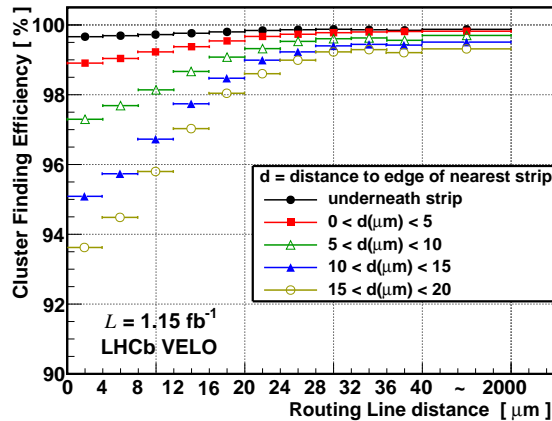


Figure 5.35: The CFE as a function of the distance between the particle intercept and the nearest routing line, for several bins of the distance between the particle intercept and closest strip edge. Large CFE decreases are observed for small routing line distances and large strip distances. This is consistent with the hypothesis that the strips shield the routing lines from charge.

The source of the CFE loss is hypothesised in terms of charge induction on the second metal layer. Prior to irradiation, ionised electrons will drift along the field lines, most of which terminate at the  $n^+$  implants. Hence the majority of the signal will be induced on the implants, which are strongly capacitively coupled to the readout strips. The drifting charge is expected to be collected well within the  $\sim 20$  ns readout period of the electronics, and no signal is expected on neighbouring electrodes (with the exception of capacitive coupling and cross-talk effects, which are measured to be low).

Irradiation may cause modifications to the field line structure, such that not all field lines terminate on the implants. In addition, there may be charge trapping effects which delay the drift of charge, resulting in charge sampling before the electrons have reached the implants. In both of these situations there will be a net induced charge on nearby electrodes, such as the routing lines. In Figure 5.33(b), the CFE was seen to worsen with increasing bias voltage. This appears to disfavour the contribution due to trapping, as an increase in bias voltage should result in faster collection times. However, the bias voltage may also effect the field line structure. In reality, it is likely that the charge loss to the second metal layer is due to several competing mechanisms.

The CFE loss also exhibits a significant radial dependence, as was shown by Figure 5.33. This can be understood by considering two competing mechanisms.

The implant strip width and the fractional area covered by the strips increases with radius, resulting in reduced charge loss, due to greater strip shielding. However, the fractional area covered by the second metal layer also increases with radius, due to the greater density of lines, increasing the amount of pickup. The latter effect is dominant, hence the overall charge loss is greater at large sensor radii.

In addition to lowering the clustering efficiency, charge induced on a routing line may introduce a noise cluster. The cluster ADC distribution from R-type sensors has a low ADC peak associated to noise clusters that has grown with fluence, as shown in Figure 5.36(a). The noise clusters are predominantly single strip clusters located at small radius regions of R-type sensors. The fraction of induced noise clusters increases when tracks traverse a sensor near to a routing line and far from a strip, as shown in Figure 5.36(b).

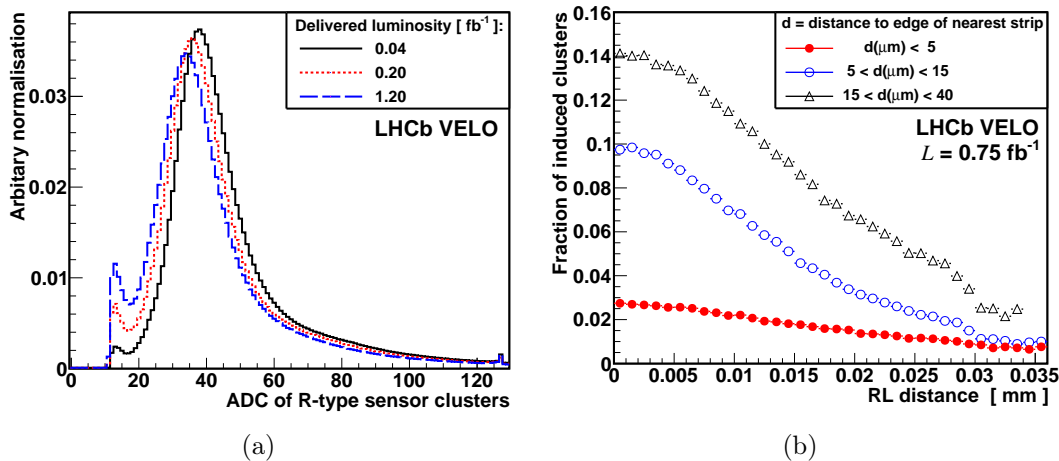


Figure 5.36: For R-type sensors: **a)** The ADC spectrum of all clusters seen for three different integrated luminosities. The limit at 10 ADC counts is imposed by the clustering thresholds. **b)** The fraction of reconstructed clusters that are induced on routing lines as a function of the distance to the nearest routing line and strip. This is determined from the number of track intercepts for which the inner strip associated to the nearest routing line has a 1 strip cluster with less than 35 ADC counts.

The CFE decrease is not observed in  $\phi$ -type sensors as the routing lines from inner strips were intentionally placed directly above the outer strips to minimise pick-up. This is made possible by the  $\phi$ -type sensors strip orientation. The CFE loss could be partially recovered by lowering the cluster reconstruction thresholds. However, this comes at the expense of a worse signal to background ratio, which leads to higher rates of fake tracks reconstructed from noise induced clusters.

The R-type  $n^+$ -on- $p$  and  $n^+$ -on- $n$  sensors have a similar CFE dependence on the strip and routing line distance, as shown in Figure 5.37(a). Figure 5.37(b) shows the MPV of the collected charge distribution as a function of bias voltage for an  $n^+$ -on- $n$  and an  $n^+$ -on- $p$  type sensor. At the nominal bias voltage of 150 V, the MPV of the  $n^+$ -on- $n$  and  $n^+$ -on- $p$  are approximately equal, both before and after

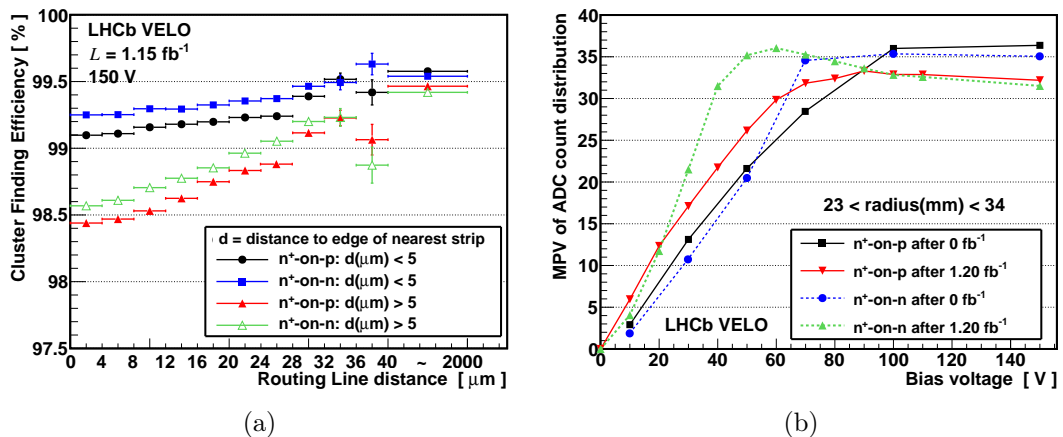


Figure 5.37: a) The CFE as a function of the distance between the particle intercept and the nearest routing line and strip edge, compared for an  $n^+$ -on- $n$  and  $n^+$ -on- $p$  sensor. b) The MPV as a function of bias voltage for an  $n^+$ -on- $n$  and  $n^+$ -on- $p$  sensor.

irradiation. For the irradiated  $n^+$ -on- $n$  type sensor, the MPV reaches a maximum at around 60 V after which it is observed to decrease with increasing bias voltage. This decrease in MPV leads to a reduced CFE, and is attributed to the second metal layer effect. Therefore less charge is lost to the second metal layer when operating the  $n^+$ -on- $n$  sensor at a lower than nominal voltage.

The  $n^+$ -on- $p$  type sensor does not exhibit a charge collection loss (and resulting CFE decrease) dependence on voltage. This may be due to the depletion region in the  $n^+$ -on- $p$  type sensor growing from the strip side of the silicon instead of from the sensor backplane. This is supported by the observation that after type inversion the voltage dependence in  $n^+$ -on- $n$  type sensors is reduced, as shown in Figure 5.38.

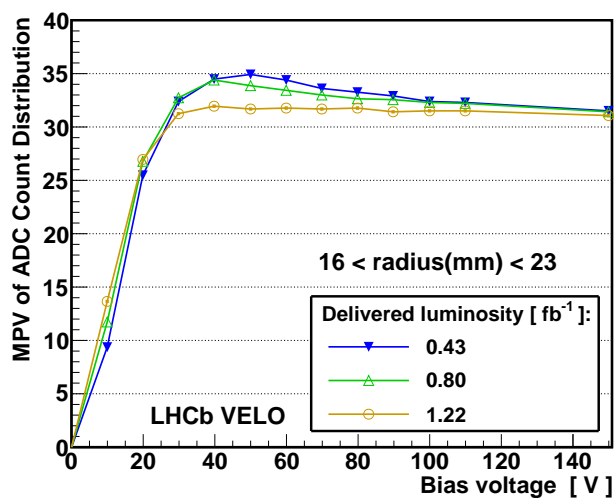


Figure 5.38: The MPV as a function of bias voltage for an R-type sensor at three values of delivered luminosity. The sensor is identified as having type inverted in the  $1.22 \text{ fb}^{-1}$  scan, for which the MPV dependence on voltage is no longer present.

To evaluate the voltage dependence of all VELO sensors, the difference in the measured CFE in sensors at 150 V and 80 V,  $\Delta\text{CFE}_v$ , has been investigated. An additional CCE scan collected following  $1.91 \text{ fb}^{-1}$  of delivered luminosity is used. Following this luminosity, all of the sensor regions with radius 8–11 mm and 11–16 mm are type inverted. The results are given in Table 5.2. In the low radius type-inverted regions there is no longer a negative CFE voltage dependence. Instead the voltage dependence is reversed, with larger CFEs measured at higher voltages, as would be expected if the charge loss is dominated by charge trapping effects.

Table 5.2: The change in CFE,  $\Delta\text{CFE}_v = \text{CFE}_{150\text{V}} - \text{CFE}_{80\text{V}}$ , averaged over all R-type sensors. Following only  $0.04 \text{ fb}^{-1}$  of integrated luminosity there is no significant CFE dependence on voltage. After  $0.43 \text{ fb}^{-1}$  there is a large negative voltage dependence, particularly in the outer radius regions. After  $1.91 \text{ fb}^{-1}$  the mean values of  $\Delta\text{CFE}_v$  in the 8–11 mm and 11–16 mm regions (where all sensors have type inverted) have become positive.

Delivered luminosity	$\Delta\text{CFE}_v = \text{CFE}_{150\text{V}} - \text{CFE}_{80\text{V}} [\%]$				
	8–11 mm	11–16 mm	16–23 mm	23–34 mm	34–42 mm
$0.04 \text{ fb}^{-1}$	$-0.05 \pm 0.06$	$0.04 \pm 0.02$	$-0.01 \pm 0.01$	$-0.06 \pm 0.04$	$0.03 \pm 0.03$
$0.43 \text{ fb}^{-1}$	$-0.09 \pm 0.09$	$-0.19 \pm 0.02$	$-0.30 \pm 0.01$	$-0.76 \pm 0.03$	$-1.84 \pm 0.19$
$1.22 \text{ fb}^{-1}$	$-0.03 \pm 0.28$	$-0.06 \pm 0.02$	$-0.21 \pm 0.02$	$-0.57 \pm 0.04$	$-1.15 \pm 0.40$
$1.91 \text{ fb}^{-1}$	$0.12 \pm 0.11$	$0.15 \pm 0.06$	$-0.15 \pm 0.05$	$-0.85 \pm 0.11$	$-1.49 \pm 0.34$

## 5.7 Summary

The charge collection efficiency scan samples have been used to study a variety of sensor properties related to sensor performance and radiation damage. It has been shown that modest improvements to the tracking resolution could be achieved by reducing the clustering thresholds. In addition, the tracking resolution could be improved by over 15% in particular sensor regions by decreasing the sensor bias voltages to values closer to the sensor depletion voltages.

The effects of radiation damage have been observed in all of the LHCb VELO sensors. The first observation of  $n^+$ -on- $n$  sensor type inversion at the LHC is reported. Analysis of the charge collection efficiencies has proven an effective method for tracking the evolution of the sensor depletion voltages. Measurements of the effective depletion voltages have been shown to agree well with the Hamburg model predictions, with divergences observed near to sensor type inversion. Findings with the noise scan method were found to agree well with the charge collection efficiency studies.

A significant decrease in the cluster finding efficiency in R-type sensors due to the second metal layer has been observed. In the worst affected regions of sensors, the

cluster finding efficiency is reduced by over 5%. Despite this relatively large localised inefficiency, studies of the VELO tracking efficiencies show no degradation associated to this effect, within the errors of  $\pm 0.3\%$ . For the  $n^+$ -on- $n$  type sensors before type inversion the magnitude of the charge loss is greatest at large bias voltages. For type inverted  $n^+$ -on- $n$  type sensors, and  $n^+$ -on- $p$  type sensors, a voltage dependence is not observed.

The two  $n^+$ -on- $p$  sensors have been studied in detail, with results providing valuable information for the detector upgrade. The maximum bias voltage that the VELO hardware can deliver is 500 V. If the effective depletion voltages continue increasing at the currently observed rates with further irradiation, the  $n^+$ -on- $p$  type sensors will reach the 500 V hardware limit having received approximately  $35 \times 10^{12} \text{ 1 MeV n}_{\text{eq}}$  less fluence than an equivalent  $n^+$ -on- $n$  type sensor. This corresponds to approximately  $1 \text{ fb}^{-1}$  of integrated luminosity in the highest particle fluence region of the VELO. It is expected that the VELO could be exposed to approximately  $5 \text{ fb}^{-1}$  of additional integrated luminosity before the depletion voltages in the highest irradiated sensor regions exceed 500 V.



---

FLAVOUR-SPECIFIC ASYMMETRIES USING  
SEMILEPTONIC  $B$  DECAYS: METHOD AND  
EFFICIENCY CORRECTIONS

---

The flavour-specific asymmetry,  $a_{\text{fs}}$ , is a measure of the  $CP$ -violating phase due to mixing in the neutral  $B$  meson system. It has two components, corresponding to  $B^0$  and  $B_s^0$  mixing, referred to as  $a_{\text{fs}}^d$  and  $a_{\text{fs}}^s$  respectively. In terms of the observable particle decay widths,  $a_{\text{fs}}$  is defined as the asymmetry of  $B$ -mesons that oscillate prior to decay,

$$a_{\text{fs}}^q = \frac{\Gamma(\overline{B}_q^0 \rightarrow B_q^0 \rightarrow f) - \Gamma(B_q^0 \rightarrow \overline{B}_q^0 \rightarrow \overline{f})}{\Gamma(\overline{B}_q^0 \rightarrow B_q^0 \rightarrow f) + \Gamma(B_q^0 \rightarrow \overline{B}_q^0 \rightarrow \overline{f})}, \quad (6.1)$$

with  $q = d, s$ . In the Standard Model (SM) these parameters are highly suppressed by the GIM mechanism factor of  $\mathcal{O}(m_c^2/m_b^2)$  and due to the ratio  $|\Gamma_{12}^{s,d}/M_{12}^{s,d}| \sim \mathcal{O}(m_b^2/m_W^2)$  [92]. Their SM predicted values are  $a_{\text{fs}}^d = (-4.1 \pm 0.6) \times 10^{-4}$  and  $a_{\text{fs}}^s = (1.9 \pm 0.3) \times 10^{-5}$  [14], where  $a_{\text{fs}}^s$  is an order of magnitude smaller than  $a_{\text{fs}}^d$  due to an additional two powers of the suppressive Wolfenstein parameter. Any measured enhancement over these small predicted values would be an indication of new physics.

This chapter describes a time-integrated measurement of  $a_{\text{fs}}^s$  using the exclusive semileptonic  $B_s^0 \rightarrow D_s^- \mu^+ \nu_\mu$  decay. Unless stated otherwise charge conjugation is assumed throughout. In addition, factors of  $c$  and  $c^2$  are often omitted for convenience. The theory of a time-integrated approach is first reviewed in Section 6.1. The experimental status of  $a_{\text{fs}}$  is then discussed in Section 6.2. The various components of the measurement are described in Section 6.3. Finally, the determination of muon selection efficiencies (a crucial part of this analysis) is presented in Sections 6.4 and 6.5.

## 6.1 An untagged time-integrated approach

The goal of this section is to show how the quantities that are measurable with the LHCb detector can be related to  $a_{\text{fs}}^s$ . The formalism is based on that of Ref. [13]. Although the following description refers to mixing in the  $B_s^0$  system, the equivalent relations for  $B^0$  mixing are obtained by the replacement  $s \rightarrow d$ .

The physical  $B$ -system eigenstates can be expressed as a linear combination of the two flavour eigenstates. The light and heavy states are defined as,

$$|B_L^s(t)\rangle = p|B_s^0(t)\rangle + q|\bar{B}_s^0(t)\rangle \quad \text{and} \quad |B_H^s(t)\rangle = p|B_s^0(t)\rangle - q|\bar{B}_s^0(t)\rangle, \quad (6.2)$$

with the normalisation condition  $|p|^2 + |q|^2 = 1$ . The flavour-specific asymmetry is related to the mixing constants  $q$  and  $p$  by the relation  $a_{\text{fs}}^s = 1 - |q/p|^2$ . The term ‘‘flavour-specific’’ refers to channels in which the decay of a  $B_s^0$  meson to the final state  $f$  is allowed at tree level, whereas the direct decay of the conjugate initial state to the same final state  $\bar{B}_s^0 \rightarrow f$  is forbidden. The semileptonic decay  $B_s^0 \rightarrow D_s^- \mu^+ \nu_\mu$  is one such channel. The relatively large branching fraction and the presence of a muon (which is a powerful triggering discriminant) make this a suitable channel for the measurement of  $a_{\text{fs}}^s$ . The decay width of the generic  $B_s^0 \rightarrow f$  decay is given by,

$$\Gamma(B_s^0(t) \rightarrow f) = \mathcal{N} |\langle f | \mathcal{S} | B_s^0(t) \rangle|^2, \quad (6.3)$$

where  $\mathcal{N}$  is a time-independent normalisation factor and  $\mathcal{S}$  is the scattering matrix. Common shorthand for the decay amplitudes in such processes are,

$$A_f = A(B_q^0 \rightarrow f) = \langle f | \mathcal{S} | B_q^0 \rangle \quad \text{and} \quad \bar{A}_f = A(\bar{B}_q^0 \rightarrow f) = \langle f | \mathcal{S} | \bar{B}_q^0 \rangle. \quad (6.4)$$

The corresponding amplitudes  $A_{\bar{f}}$  and  $\bar{A}_{\bar{f}}$  are obtained by the exchange  $f \rightarrow \bar{f}$ . A useful parameter in the study of  $CP$ -violation due to mixing is,

$$\lambda_f = \frac{q \bar{A}_f}{p A_f}. \quad (6.5)$$

This parameter describes the interference of the  $B_q^0 \rightarrow f$  and  $\bar{B}_q^0 \rightarrow f$  decays, by relating the relative phase of  $q/p$  (due to mixing) and  $\bar{A}_f/A_f$  (due to the specific nature of the decay). Equations 6.3–6.5 can be used<sup>1</sup> to express the decay widths to the final state  $f$  in terms of  $\lambda_f$ , the decay amplitude  $A_f$ , and the mixing parameters

---

<sup>1</sup>The intermediate steps are described in Ref. [13].

$\Delta m$  and  $\Delta\Gamma$ ,

$$\Gamma(B_s^0 \rightarrow f) = \mathcal{N}|A_f|^2 e^{-\Gamma t} \left[ \frac{1 + |\lambda_f|^2}{2} \cosh\left(\frac{\Delta\Gamma t}{2}\right) + \frac{1 - |\lambda_f|^2}{2} \cos(\Delta m t) - \operatorname{Re}\lambda_f \sinh\left(\frac{\Delta\Gamma t}{2}\right) - \operatorname{Im}\lambda_f \sin(\Delta m t) \right], \quad (6.6)$$

$$\Gamma(\bar{B}_s^0 \rightarrow f) = \mathcal{N}|A_f|^2 \frac{1}{1 - a_{\text{fs}}^s} e^{-\Gamma t} \left[ \frac{1 + |\lambda_f|^2}{2} \cosh\left(\frac{\Delta\Gamma t}{2}\right) - \frac{1 - |\lambda_f|^2}{2} \cos(\Delta m t) - \operatorname{Re}\lambda_f \sinh\left(\frac{\Delta\Gamma t}{2}\right) + \operatorname{Im}\lambda_f \sin(\Delta m t) \right]. \quad (6.7)$$

The corresponding decay widths to the conjugate state  $\bar{f}$  are,

$$\Gamma(B_s^0 \rightarrow \bar{f}) = \mathcal{N}|\bar{A}_{\bar{f}}|^2 (1 - a_{\text{fs}}^s) e^{-\Gamma t} \left[ \frac{1 + |\lambda_{\bar{f}}|^{-2}}{2} \cosh\left(\frac{\Delta\Gamma t}{2}\right) - \frac{1 - |\lambda_{\bar{f}}|^{-2}}{2} \cos(\Delta m t) - \operatorname{Re}\lambda_{\bar{f}} \sinh\left(\frac{\Delta\Gamma t}{2}\right) + \operatorname{Im}\lambda_{\bar{f}} \sin(\Delta m t) \right], \quad (6.8)$$

$$\Gamma(\bar{B}_s^0 \rightarrow \bar{f}) = \mathcal{N}|\bar{A}_{\bar{f}}|^2 e^{-\Gamma t} \left[ \frac{1 + |\lambda_{\bar{f}}|^{-2}}{2} \cosh\left(\frac{\Delta\Gamma t}{2}\right) + \frac{1 - |\lambda_{\bar{f}}|^{-2}}{2} \cos(\Delta m t) - \operatorname{Re}\lambda_{\bar{f}} \sinh\left(\frac{\Delta\Gamma t}{2}\right) - \operatorname{Im}\lambda_{\bar{f}} \sin(\Delta m t) \right]. \quad (6.9)$$

As may be expected,  $a_{\text{fs}}^s$  appears in the formulae for decays in which the initial  $B$  meson has oscillated prior to decay. Such processes are referred to as wrong-sign (WS) decays, where  $\Gamma(B_s^0 \rightarrow \bar{f}) = \Gamma^{WS}$  and  $\Gamma(\bar{B}_s^0 \rightarrow f) = \bar{\Gamma}^{WS}$ . The right-sign (RS) tree-level allowed decays are  $\Gamma(B_s^0 \rightarrow f) = \Gamma^{RS}$  and  $\Gamma(\bar{B}_s^0 \rightarrow \bar{f}) = \bar{\Gamma}^{RS}$ .

For flavour-specific channels, the WS decay amplitudes do not contribute, giving  $\bar{A}_f = A_{\bar{f}} = \lambda_f = 1/\lambda_{\bar{f}} = 0$ . In addition, channels with no (or insignificant) direct  $CP$ -violation can be chosen such that  $|A_f| = |\bar{A}_{\bar{f}}|$ . Semileptonic neutral  $B$ -meson decays satisfy both these criteria, leading to the simplified decay widths,

$$\Gamma^{RS} = \mathcal{N}|A_f|^2 e^{-\Gamma t} (\mathcal{F}^+ / 2), \quad (6.10)$$

$$\bar{\Gamma}^{WS} = \mathcal{N}|A_f|^2 (1 - a_{\text{fs}}^s)^{-1} e^{-\Gamma t} (\mathcal{F}^- / 2), \quad (6.11)$$

$$\Gamma^{WS} = \mathcal{N}|\bar{A}_{\bar{f}}|^2 (1 - a_{\text{fs}}^s) e^{-\Gamma t} (\mathcal{F}^- / 2), \quad (6.12)$$

$$\bar{\Gamma}^{RS} = \mathcal{N}|\bar{A}_{\bar{f}}|^2 e^{-\Gamma t} (\mathcal{F}^+ / 2), \quad (6.13)$$

where  $\mathcal{F}^\pm = (\cosh(\Delta\Gamma t/2) \pm \cos(\Delta m t))$ . To first order, the tagged asymmetry,

$A_{\text{tag}}$ , is defined by the wrong-sign decay widths,

$$A_{\text{tag}} = \frac{\bar{\Gamma}^{WS} - \Gamma^{WS}}{\bar{\Gamma}^{WS} + \Gamma^{WS}} = \frac{1 - (1 - a_{\text{fs}}^s)^2}{1 + (1 - a_{\text{fs}}^s)^2} = a_{\text{fs}}^s + \mathcal{O}(a_{\text{fs}}^s{}^2), \quad (6.14)$$

which is valid for small asymmetries. This requires the flavour of the initially produced  $B$  meson to be identified in a process known as “tagging”. The sensitivity of a tagged analysis is related to the effective tagging efficiency, which represents the effective statistical reduction in the data sample due to tagging inefficiencies. This has been measured at LHCb to be  $\sim 2\%$  [93]. To maximise the statistical power of a data sample, an untagged approach can be pursued instead. The untagged decay width to a particular final state,  $f$ , is obtained by the linear combination  $\Gamma[f, t] = \Gamma^{RS} + \bar{\Gamma}^{WS}$ . The untagged width of the conjugate final state is  $\Gamma[\bar{f}, t] = \bar{\Gamma}^{RS} + \Gamma^{WS}$ . The relationship between  $a_{\text{fs}}^s$  and the untagged asymmetry,  $A_{\text{untag}}$ , is obtained by inserting Equations 6.10–6.13 into the untagged decay widths to give,

$$A_{\text{untag}} = \frac{\Gamma[f, t] - \Gamma[\bar{f}, t]}{\Gamma[f, t] + \Gamma[\bar{f}, t]} = \frac{a_{\text{fs}}^s}{2} - \frac{a_{\text{fs}}^s}{2} \frac{\cos(\Delta m t)}{\cosh(\Delta\Gamma t/2)} + \mathcal{O}(a_{\text{fs}}^s{}^2), \quad (6.15)$$

which is again only valid for small  $a_{\text{fs}}^s$ . Therefore with the input of  $B$  mixing parameters such as  $\Delta m$  and  $\Delta\Gamma$ , the value of  $a_{\text{fs}}^s$  can be determined without any knowledge of the initial  $B$  meson state. This formula does not consider potential bias due to production, background or detector induced asymmetries. The following section addresses the first of these biases. Detector and background related bias are discussed in the latter parts of this chapter.

### 6.1.1 Production asymmetry

The initial imbalance in the number of valence quarks and antiquarks in proton-proton collisions (such as those at the LHC) can result in particle-antiparticle production asymmetries. To account for this, the normalising factors in Equations 6.11 and 6.13 are redefined, such that  $\mathcal{N} \rightarrow \bar{\mathcal{N}}$ . The production asymmetry,  $a_p$ , is defined as,

$$a_p = \frac{\mathcal{N} - \bar{\mathcal{N}}}{\mathcal{N} + \bar{\mathcal{N}}}. \quad (6.16)$$

Incorporating a potential production asymmetry, the first-order untagged asymmetry can be rederived, giving,

$$A_{\text{untag}} = \frac{a_{\text{fs}}^s}{2} + \left[ a_p - \frac{a_{\text{fs}}^s}{2} \right] \frac{\cos(\Delta m t)}{\cosh(\Delta\Gamma t/2)}. \quad (6.17)$$

The time dependence of this equation can be removed by integrating over all  $B$  lifetimes. When doing this, another effect must be considered. To obtain high purity  $B$ -meson samples, experiments will typically trigger on candidates that are well separated from the primary interaction vertices, thus rejecting the majority of short-lived candidates. The acceptance function,  $\epsilon(t)$ , describes this effect. It has been determined for the selection of  $B_s^0$  candidates at LHCb using Monte Carlo simulated events [94], as shown in Figure 6.1. It is described by the relation,

$$\epsilon(t) = \frac{[1 + \beta(t - t_0)][a(t - t_0)]^n}{1 + [a(t - t_0)]^n}, \quad (6.18)$$

where  $a = 1.382$ ,  $n = 1.771$ ,  $t_0 = 0.07742$  and  $\beta = -0.0494$ . Incorporating the acceptance function and integrating over all  $B_s^0$  lifetimes, the time-integrated untagged asymmetry,  $A_{\text{untag}}^{TI}$ , is defined (to first order in  $a_{\text{fs}}$ ) as,

$$A_{\text{untag}}^{TI} = \frac{\Gamma[f] - \Gamma[\bar{f}]}{\Gamma[f] + \Gamma[\bar{f}]} = \frac{a_{\text{fs}}}{2} + \left[ a_p - \frac{a_{\text{fs}}}{2} \right] \frac{\int_{t=0}^{\infty} e^{-\Gamma t} \cos(\Delta m t) \epsilon(t) dt}{\int_{t=0}^{\infty} e^{-\Gamma t} \cosh\left(\frac{\Delta \Gamma t}{2}\right) \epsilon(t) dt}. \quad (6.19)$$

The ratio of integrals has been evaluated for  $B_s^0 \rightarrow D_s^- \mu^+ \nu_\mu$  decays, with a value of 0.2% obtained<sup>1</sup>. The production asymmetry is expected to be less than a few percent [95, 96], which reduces the size of the  $a_p$  term to approximately  $\mathcal{O}(10^{-4})$ . This is negligible compared to the target precision of this analysis, which is of order  $\mathcal{O}(10^{-3})$ . Neglecting these small terms, the untagged time-integrated asymmetry is

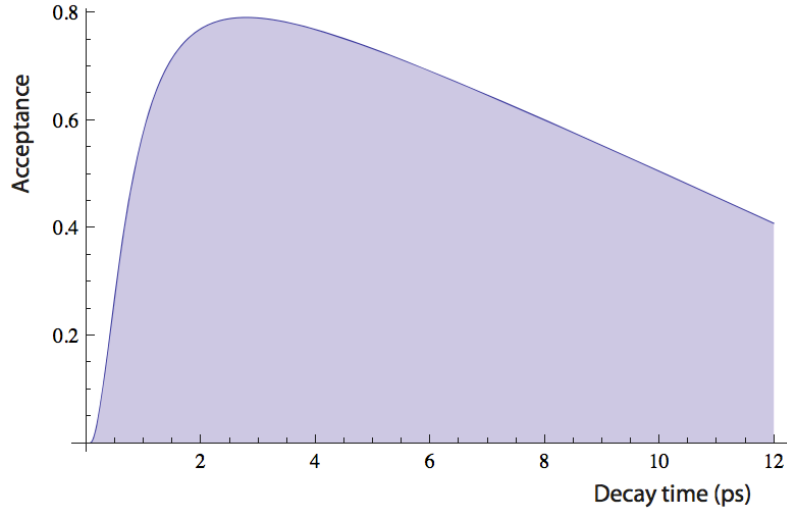


Figure 6.1: The  $B_s^0$  acceptance function, as determined using simulated Monte Carlo events, with the LHCb detector geometry and analysis selection criteria taken into account. Figure from Ref. [94].

<sup>1</sup>A similar calculation for  $B^0 - \bar{B}^0$  mixing returns a significantly larger value of approximately 33%. As such, an untagged and time-integrated approach cannot be pursued for the  $B^0$  system at LHCb.

simply,

$$A_{\text{untag}}^{TI} = \frac{\Gamma[f] - \Gamma[\bar{f}]}{\Gamma[f] + \Gamma[\bar{f}]} = \frac{a_{\text{fs}}}{2} = \frac{N[D_s^- \mu^+] - N[D_s^+ \mu^-]}{N[D_s^- \mu^+] + N[D_s^+ \mu^-]}, \quad (6.20)$$

where  $N[D_s^- \mu^+]$  and  $N[D_s^+ \mu^-]$  are the time-integrated  $B_s^0$  and  $\bar{B}_s^0$  yields. In reality, the measurement of  $a_{\text{fs}}$  is complicated by sources of bias such as detector-induced charge asymmetries, which are discussed shortly.

## 6.2 Experimental status

Over the past few decades, increasingly precise measurements of  $a_{\text{fs}}$  have been made by a variety of experiments. The majority of measurements to date have been untagged and time-integrated. A  $B$ -meson produced at a particle collider predominantly comes from the hadronisation of a  $b$  or  $\bar{b}$  quark from a  $b\bar{b}$  pair. If two muons of the same charge are detected, each of which is produced by semileptonic  $B$ -decays, one of the two  $B$ -mesons from the  $b\bar{b}$ -pair must have oscillated prior to decay. Asymmetries in such like-sign dilepton events can be used to determine  $a_{\text{fs}}$ , using vast statistics in inclusive analyses. This is the approach that has been used by the majority of previous measurements. Due to the use of semileptonic channels,  $a_{\text{fs}}$  is often referred to as  $a_{\text{sl}}$ .

Table 6.1: Measurements of  $CP$  violation in  $B^0$  and  $B_s^0$  mixing. When two errors are quoted, the first is statistical and the second is systematic.

Experiment	[Ref]	Method	$a_{\text{sl}}^d$ [%]	$a_{\text{sl}}^s$ [%]
Belle	[97]	dileptons	$(-0.11 \pm 0.79 \pm 0.0085)$	—
BaBar	[98]	$B^0 \rightarrow D^{*-} l^+ \nu_l$	$(0.06 \pm 0.17^{+0.36}_{-0.32})$	—
DØ	[99]	$B^0 \rightarrow D^{(*)-} \mu^+ X$	$(0.68 \pm 0.45 \pm 0.14)$	—
DØ	[100]	$B_s^0 \rightarrow D_s^- \mu^+ X$	—	$(-1.12 \pm 0.74 \pm 0.17)$
DØ	[17]	dimuons	$(-0.12 \pm 0.52)$	$(-1.81 \pm 1.06)$
World average	[101]	HFAG combination	$(-0.03 \pm 0.21)$	$(-1.09 \pm 0.40)$

To produce large samples of  $B^0 \bar{B}^0$  and  $B^+ B^-$  pairs, experiments such as BaBar, Belle and CLEO collided particles at the centre-of-mass energy of the  $\Upsilon(4S)$  resonance. This is below the threshold required to produce  $B_s^0 \bar{B}_s^0$  pairs and so it is only possible to measure the  $a_{\text{fs}}^d$  component of  $a_{\text{fs}}$  at these experiments. The Heavy Flavor Averaging Group (HFAG) [101] have combined the results from the  $\Upsilon(4S)$  experiments and found  $a_{\text{fs}}^d = (0.02 \pm 0.31)\%$ , which is dominated by the recent measurement by the BaBar collaboration [98]. All measurements of  $a_{\text{sl}}^d$  to date have been consistent with the small SM predicted value. A selection of  $a_{\text{fs}}$  measurements are summarised in Table 6.1. The dimuon measurement shown from the DØ experiment uses data containing both  $B^0$  and  $B_s^0$  mesons, hence information related to both  $a_{\text{fs}}^d$

and  $a_{\text{fs}}^s$  can be extracted. The total asymmetry,  $A_{\text{sl}}^b = (-0.787 \pm 0.172 \pm 0.093)\%$ , is discrepant with SM predictions, and is discussed in greater detail in the following section.

### 6.2.1 Evidence for an anomalous like-sign dimuon asymmetry from the DØ experiment

The DØ experiment has found the only evidence for a non-zero value of  $a_{\text{fs}}$  [16,17]. The dilepton asymmetry,

$$A_{\text{sl}}^b = (-0.787 \pm 0.172 \pm 0.093) \times 10^{-2}, \quad (6.21)$$

was determined using  $p\bar{p}$  collision data corresponding to  $9\text{fb}^{-1}$  of integrated luminosity. This is approximately four standard deviations from the SM prediction. Due to inclusive event selection, the measured asymmetry has contributions from both  $a_{\text{fs}}^d$  and  $a_{\text{fs}}^s$ . The result is projected as a band in the  $a_{\text{sl}}^d - a_{\text{sl}}^s$  plane in Figure 6.2. The relative contribution to the asymmetry from  $B^0$  and  $B_s^0$  oscillations has been investigated by dividing the dataset into samples of different muon track impact parameter (IP)<sup>1</sup>. The mean lifetime of  $B^0$  mesons is significantly shorter than their oscillation period. Particles with large IP are typically long-lived, and are therefore

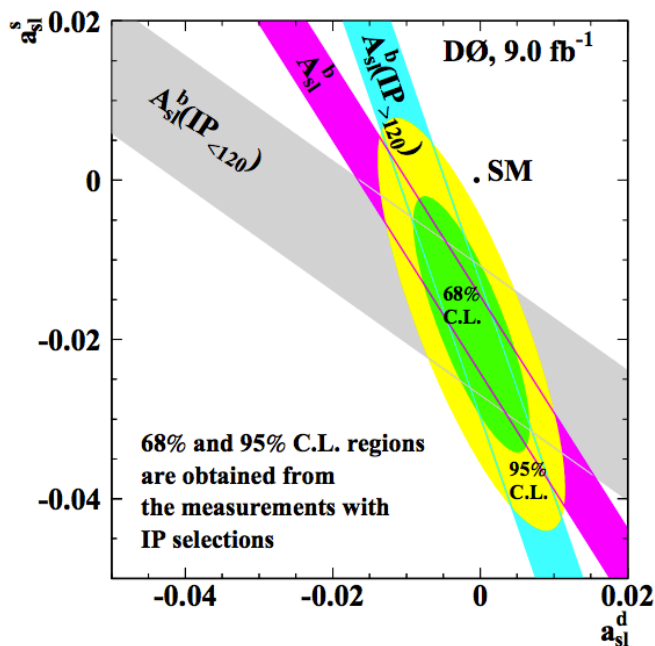


Figure 6.2: The DØ collaboration result projected into the  $a_{\text{sl}}^d - a_{\text{sl}}^s$  plane. Measurements from two subsets of data with muon IP greater than and less than  $120\ \mu\text{m}$  are also shown. Figure from Ref. [17].

<sup>1</sup>The impact parameter is the distance of closest approach between a track and the primary interaction region.

more likely to have oscillated prior to decay. The relative fraction of candidates that have oscillated which are  $B^0$  mesons is enhanced by selecting subsets of data that contain muons with large IP. Using this approach, the components of  $a_{\text{fs}}$  were measured to be  $a_{\text{fs}}^d = (-0.12 \pm 0.52)\%$  and  $a_{\text{fs}}^s = (-1.81 \pm 1.06)\%$ , with a correlation coefficient between the two quantities of  $-0.799$ . This suggests that a significant proportion of the measured asymmetry is due to  $B_s^0$  oscillations.

### 6.3 Analysis method

The anomalous like-sign dimuon asymmetry measured at the  $D\bar{O}$  Experiment is an exciting hint of a region in which new physics could be discovered. It is now the responsibility of experiments such as LHCb to determine  $a_{\text{fs}}$  with greater precision. The LHCb detector operates in a challenging environment for measuring small  $CP$  asymmetries. Asymmetric initial conditions may result in significant production asymmetries, though for the time-integrated measurement of  $a_{\text{fs}}^s$  at LHCb, the influence of the production asymmetry is small, as was discussed Section 6.1.1. In addition, the content of the high-multiplicity, hadronic events must be well understood to account for possible background-induced asymmetries.

The LHCb detector was described in Chapter 3. To reduce detector-induced bias, the polarity of the 4 Tesla LHCb dipole magnet has been regularly reversed during 2010 and 2011 running. The precision vertexing and excellent particle identification of the LHCb detector allows for efficient reconstruction of exclusive  $B$ -meson decay channels. Excellent mass resolution of approximately 7 MeV is used to identify the flavour of  $B^0$  and  $B_s^0$  candidates, leaving little ambiguity over which  $a_{\text{fs}}$  component is measured.

The like-sign dimuon result from the  $D\bar{O}$  Experiment suggests a large negative value of  $a_{\text{fs}}^s$ . It is therefore this component of  $a_{\text{fs}}$  that has been first investigated at LHCb. Additionally, the simple treatment of the  $B_s^0$  production asymmetry makes this an easier measurement than  $a_{\text{fs}}^d$ . The exclusive  $B_s^0 \rightarrow D_s^- \mu^+ \nu_\mu$  decay is investigated, with the subsequent decay  $D_s^- \rightarrow \phi(\rightarrow K^+ K^-) \pi^-$ . The leading quark flow diagram for this decay channel and an example signal candidate from real data are shown in Figure 6.3. Requiring that the kaons are produced by a  $\phi$  meson significantly reduces the combinatoric background under the  $D_s^-$  peak, and ensures that the kaons have similar momentum spectra, as shown by Figure 6.4. Kaons that have the same sign electric charge as the  $D_s^\pm$  candidates are found to have slightly harder momentum spectra, irrespective of the magnetic field polarity. The kaon candidate with the same sign and different sign of electric charge to the  $D_s^\pm$  meson are referred to as same sign (SS) and different sign (DS) kaons.

The kinematic differences between the SS and DS kaons are enhanced for data

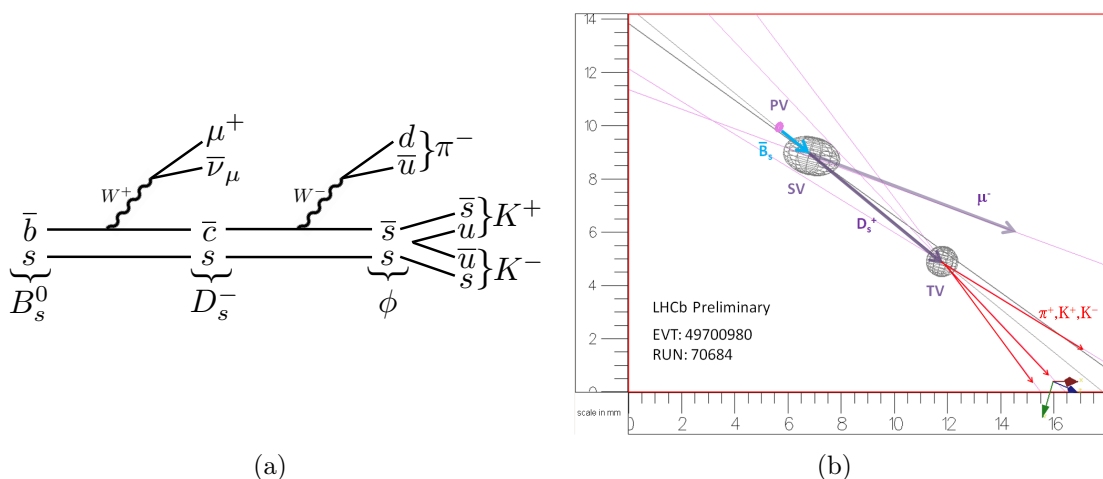


Figure 6.3: **a)** A quark flow diagram for the channel used in this analysis. **b)** The reconstruction of a semileptonic  $B_s^0$  decay from real data at LHCb. Figure from Ref. [102].

that are triggered on the  $\phi \rightarrow K^+K^-$  candidate by the inclusive- $\phi$  HLT2 trigger line, as shown in Figure 6.5. However, the kinematics of the SS kaons from  $B_s^0$  and  $\bar{B}_s^0$  are very similar, even when biased by this additional trigger selection, as shown by Figure 6.6. Due to their similar kinematics, kaon detection-induced asymmetries largely cancel when both a SS and DS kaon are required. Residual bias due to the small differences in  $K^+K^-$  kinematic spectra has been further investigated at LHCb, and found to be of order  $10^{-4}$  or below. Kaon selection-induced bias is therefore considered negligible for this analysis.

### 6.3.1 Data selection

Having been selected by the LHCb trigger, data are further selected offline in a process referred to as *stripping*, in which more manageable data samples are constructed by analysis-specific stripping algorithms known as stripping lines. The lines used in this analysis are listed in Table 6.2. All data used were collected during the 2011 run, corresponding to approximately  $1 \text{ fb}^{-1}$  of integrated luminosity. The selection and reconstruction software versions **Stripping17**, **Reco10** and **DaVinci v29r3** were used. Signal data are triggered on the muon candidate, as large samples of muon calibration data are available, with which selection-induced bias can be measured. Data collected with each magnet polarity are analysed independently.

The offline (post-trigger) selection criteria are summarised in Table 6.3. Many of the symbols used are described in the following text. The listed criteria were chosen to obtain high-purity semileptonic  $B$ -meson samples, and are based on those used for previous semileptonic studies at LHCb [103]. The detectable particles are the daughter muons ( $\mu^+$ ) and hadrons ( $K^+$ ,  $K^-$ ,  $\pi^-$ ), produced in  $B_s^0$  and  $D_s^-$  decays, respectively. To reduce fake-track induced backgrounds, the daughter muons and

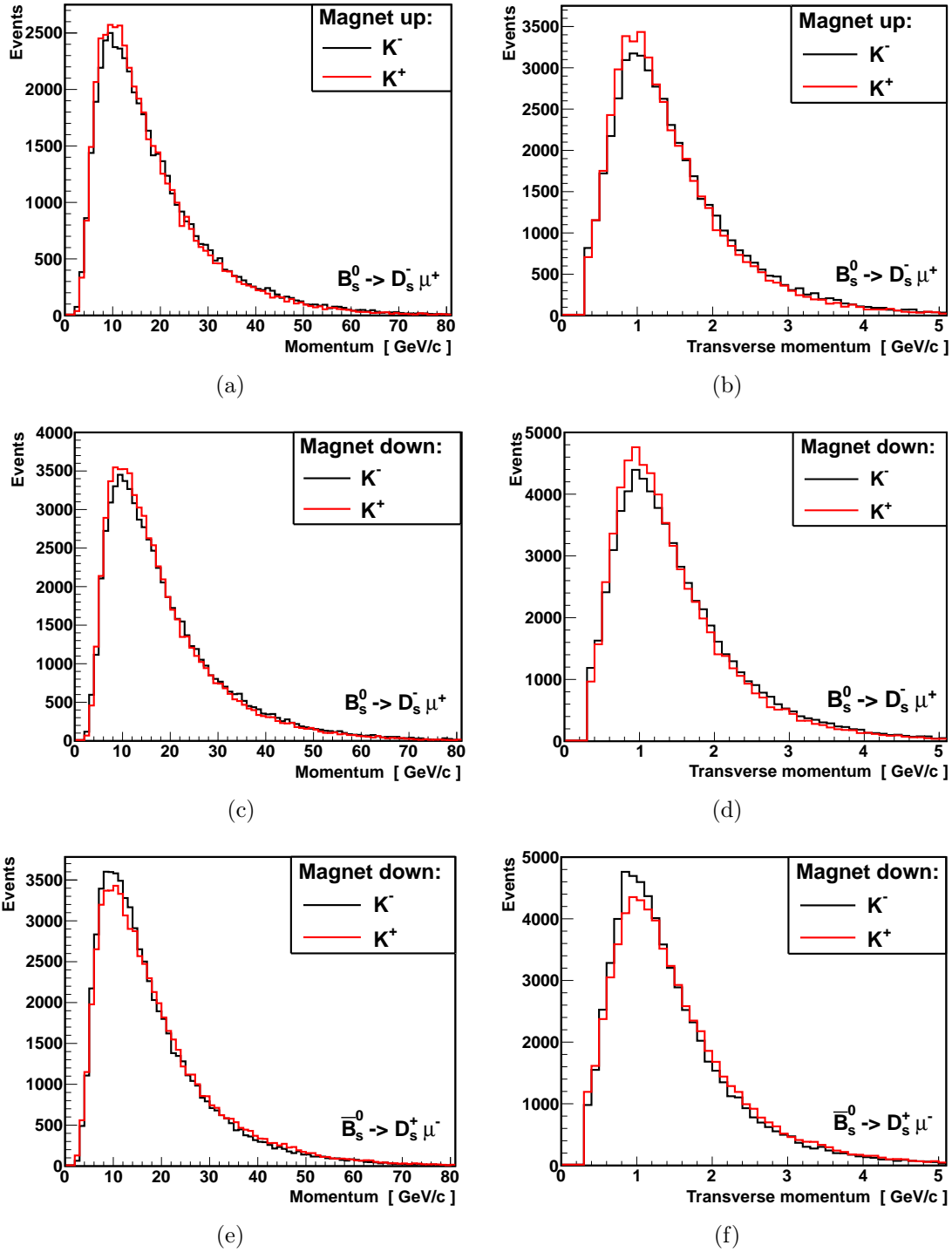


Figure 6.4: The kaon momenta distribution for **a)** magnet up  $D_s^- \mu^+$  type events, **c)** magnet down  $D_s^- \mu^+$  type events and **e)** magnet down  $D_s^+ \mu^-$  type events. The corresponding plots for the kaon transverse momenta distributions are shown by **b)**, **d)** and **f)**.

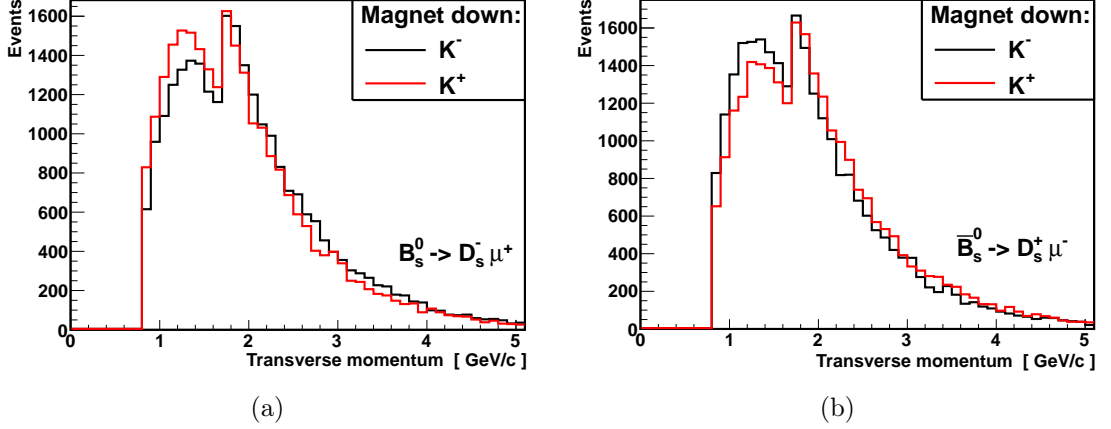


Figure 6.5: The kaon transverse momentum distributions for a)  $D_s^- \mu^+$  and b)  $D_s^+ \mu^-$  type events that are selected by the HLT2 inclusive- $\phi$  trigger with magnetic field polarity down. The discontinuity at approximately 1.8 GeV is due to the requirement for one of the  $\phi$  daughters to also have been selected by the HLT1 single track trigger (which in turn requires that the track has  $p_T > 1.8$  GeV).

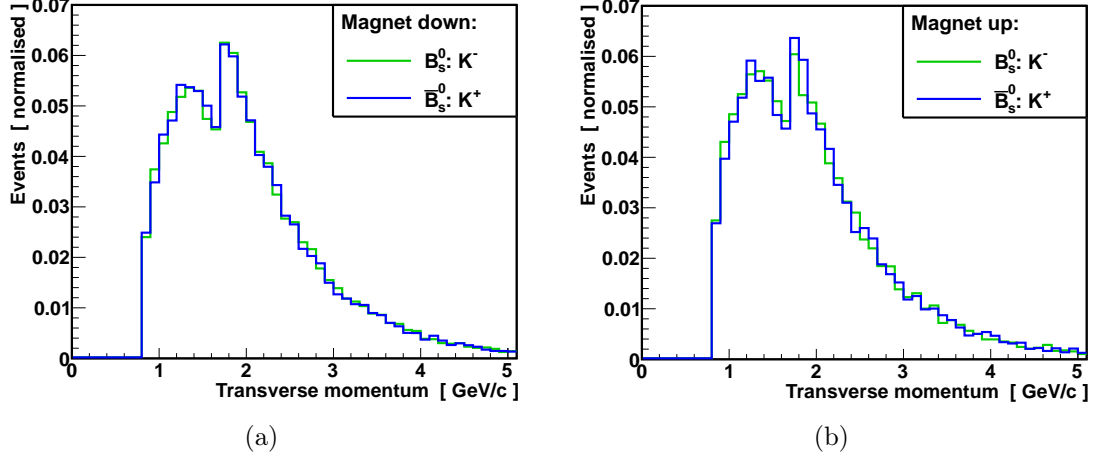


Figure 6.6: The SS kaon transverse momenta distributions for a) magnet down and b) magnet up polarity data selected by the HLT2 inclusive- $\phi$  trigger. The equivalent DS kaons spectra exhibit similar agreement.

Table 6.2: The data samples used in this analysis. The first sample contains the signal  $B_s^0$  events. The other three samples are calibration data.

Stream	Stripping		Recorded luminosity [ $\text{fb}^{-1}$ ]	
	Line		Magnet up	Magnet down
Semileptonic	Strippingb2DsMuXPhiPi		0.45	0.60
PID	MuIDCalib_JpsiFromBNoPIDNoMip		0.45	0.60
Bhadron	All lines		0.45	0.60
CharmCompleteEvent	StrippingD0ForBXX		0.45	0.60

CHAPTER 6. FLAVOUR-SPECIFIC ASYMMETRIES USING  
SEMILEPTONIC  $B$  DECAYS: METHOD AND EFFICIENCY CORRECTIONS

Table 6.3: The offline selection criteria for the semileptonic candidates used in this analysis. The symbols used are described in the surrounding text.

Particle candidate	Selection			
Muon	$6 < p(\text{GeV}) < 100$		$1.2 < p_{\text{T}}(\text{GeV}) < 10$	
	$\chi^2(\text{IP})$	$> 4$	IsMuon	$= 1$
	nShared	$= 0$	PID( $\mu$ )	$> 0$
	$\chi^2/\text{DoF}(\text{track})$	$< 3$	$2 < \eta < 5$	
Hadrons ( $K^+, K^-, \pi^-$ )	$p$	$> 2 \text{ GeV}$	$p_{\text{T}}$	$> 0.3 \text{ GeV}$
	sum of $p_{\text{T}}$	$> 2.1 \text{ GeV}$	$\chi^2(\text{IP})$	$> 9$
	$\chi^2/\text{DoF}(\text{track})$	$< 4$	Kaon PID( $K$ )	$> 4$
$\phi$ -meson	$\chi^2/\text{DoF}(\text{Vertex fit})$	$< 25$		
	$ m(K^+K^-) - m(\phi)_{\text{PDG}} $	$\leq 20 \text{ MeV}$		
$D_s^-$ -meson	$p(\phi\pi)$	$> 0.8 \text{ GeV}$	$\phi\pi$ sum of $\chi^2(\text{IP})$	$> 4$
	DIRA	$> 0.99$	IP	$< 7.4 \text{ mm}$
	$\chi^2/\text{DoF}(\text{Vertex fit})$	$< 6$	$\chi^2(\text{FD})$	$> 100$
	$ m(D_s^-) - m(D_s^-)_{\text{PDG}} $	$\leq 200 \text{ MeV}$		
$B_s^0(D_s^- \mu^+)$	$3.1 \text{ GeV} < m(D_s^- \mu^+) < 5.1 \text{ GeV}$		DIRA	$> 0.999$
	$\chi^2/\text{DoF}(\text{Vertex fit})$	$< 6$	$2 < \eta < 5$	
	$z(D_s^-) - z(B_s^0)$	$> 0$		
Global Event Cuts	number of long tracks $< 250$			

hadrons are required to have track fit  $\chi^2$  per degree of freedom ( $\chi^2/\text{DoF}$ ) less than 3 and 4 respectively. Due to the large mass of the parent  $B$  meson, tracks are required to have minimum values of momentum ( $p$ ) and transverse momentum ( $p_{\text{T}}$ ).

The impact parameter (IP) is the distance of closest approach between a particle track and a vertex. Typical flight distances of the  $B_s^0$  and  $D_s^-$  prior to decay are  $\sim 1 \text{ cm}$ . Therefore hadrons and muons will usually originate from vertices that are displaced (or “detached”) from the primary vertex. Tracks are required to have large IP  $\chi^2$ , so as to select tracks that are inconsistent with having been produced at the primary vertex. The two kaon tracks must have good likelihoods for being kaons, as determined using the particle identification (PID) of the RICH system (i.e.  $\text{PID}(K) > 4$ , where  $\text{PID}(K)$  represents the difference in log-likelihood between a kaon and pion hypothesis). The kaons must also be consistent with having come from a common vertex with an invariant mass within  $\pm 20 \text{ MeV}$  of the known  $\phi$  mass.

Particle identification and track quality criteria are applied to the muon candidate to suppress background events. Charge bias induced by this selection is measured with calibration data, as described in Section 6.4. To reduce fake muon selection, candidate tracks that share muon station hits with other muon candidates are rejected (i.e. nShared = 0).

Particle tracks are used to reconstruct the decay vertices of the short-lived  $B_s^0$ ,  $D_s^-$  and  $\phi$  mesons. Vertex fits with large vertex  $\chi^2/\text{DoF}$  are excluded to reduce combinatoric background. The  $D_s^-$  is required to have an IP less than 7.4 mm and a

flight distance  $\chi^2$  greater than 100, where the flight distance (FD) is defined as the distance between the PV and the  $D$  decay vertex (the  $\chi^2$  hypothesis is based on a FD of zero). This discriminates against  $D_s^-$  mesons produced at the primary vertex. The cosine of the angle between the  $D_s^-$  momentum direction and the vector from the primary vertex to the  $D_s^-$  decay vertex (DIRA) must be greater than 0.99. In addition the  $D_s^-$  and  $\mu^+$  must be consistent with having come from a common vertex that is displaced from the primary vertex, with DIRA  $> 0.999$  and have invariant mass near to the known  $B_s^0$  mass. Finally, the  $D_s^-$  decay vertex is required to have been produced further downstream than the decay vertex of the  $B_s^0$ .

Although data-driven techniques have been employed wherever possible, several Monte Carlo (MC) samples have been generated specifically for these studies. They are listed in Table 6.4. The primary purpose of the simulations is to determine the selection efficiencies of potentially asymmetric backgrounds, as described in Section 7.3.6.

Table 6.4: The MC samples generated for this analysis. Generator-level selection criteria are defined by the LHCb-specific ‘‘Event type’’ code.

Event type	Channel	Generated events [ $\times 10^6$ ]
13774002	$B_s^0 \rightarrow D_s^- \mu^+ \bar{\nu}_\mu X$	20
11876001	$B^0 \rightarrow D_s^- DX$	5
12875601	$B^+ \rightarrow D_s^- DX$	5
13873201	$B_s^0 \rightarrow D_s^- D_s^+$	5
15894301	$\Lambda_b \rightarrow D_s^- \Lambda_c^+ X$	10

### 6.3.2 The master formula

Incorporating the effects of detector and background induced bias, the untagged time-integrated asymmetry (given previously by Equation 6.20) becomes,

$$A_{\text{untag}}^{TI} = \frac{a_{\text{fs}}^s}{2} = \frac{N[D_s^- \mu^+] - N[D_s^+ \mu^-] \times \frac{\epsilon(\mu^+)}{\epsilon(\mu^-)}}{N[D_s^- \mu^+] + N[D_s^+ \mu^-] \times \frac{\epsilon(\mu^+)}{\epsilon(\mu^-)}} - A_b - A_{\mu\pi}^{\text{track}}, \quad (6.22)$$

where  $N[D_s^\mp \mu^\pm]$  are the measured yields of  $D_s^\mp \mu^\pm$  pairs,  $\epsilon(\mu^\pm)$  are the muon selection efficiencies,  $A_b$  is the background-induced asymmetry, and  $A_{\mu\pi}^{\text{track}}$  is the tracking-induced asymmetries for muons and pions. To determine  $a_{\text{fs}}^s$ , each of these components are considered independently. The event yield determination is presented in Section 7.1. The method used to determine the muon triggering and PID efficiencies is discussed in the following section. Finally, the background and tracking corrections,  $A_{\mu\pi}^{\text{track}}$  and  $A_b$ , are presented in the Sections 7.3.6 and 7.3.7.

## 6.4 Muon efficiencies

Each level of the LHCb software uses an independent detector alignment; hence to investigate potential bias, the individual trigger and PID selection efficiencies are investigated independently. The total muon selection comprises several single-muon based selections. This section presents the determination of  $\epsilon_{PID}(\mu^\pm)$ ,  $\epsilon_{L0}(\mu^\pm)$  and  $\epsilon_{HLT1}(\mu^\pm)$ , using large unbiased calibration data samples. Trigger efficiencies are evaluated using the TISTOS method. This involves associating detector hits used by the trigger decision unit with offline selected track hits. Candidates are sorted into two categories:

- **TIS:** The event is triggered independently of the signal, i.e. the event would be selected by the trigger even if the signal candidate were to be discarded.
- **TOS:** The event is triggered on the signal, i.e. the event would be selected by the trigger, even if all other event measurements were to be discarded.

A particular particle candidate is referred to as TIS or TOS in a trigger if it satisfies the above criteria. In the following discussion the semileptonic  $D_s^- \mu^+$  data are referred to as the signal sample. A large fraction of the signal muons are TOS in the L0 and HLT1 single-track trigger algorithms. The TOS efficiencies of these triggers are determined independently for each muon charge. Calibration muons are required to be TIS at all trigger levels, to ensure that they are unbiased by the trigger and are therefore suitable for measuring the efficiency of a TOS selection.

### 6.4.1 The muon system

The LHCb muon system serves two primary purposes: to select events containing muons with large transverse momentum in the trigger, and to assign muon PID information to long tracks identified by the tracking system. It comprises five tracking stations (M1–5) spaced along the beam axis at distances of 12.1, 15.2, 16.4, 17.6 and 18.8 meters downstream of the primary interaction region. The first station is placed before the calorimetry system and provides critical information to the L0 trigger regarding the transverse momentum of muon candidates. The other four stations are located downstream of the calorimeters. Each muon station has four quadrants, covering the regions to the top left/right and bottom left/right of the beampipe region. Each quadrant is divided into four regions with dimensions and logical pad size which scale by a factor of two between regions, as shown by Figure 6.7.

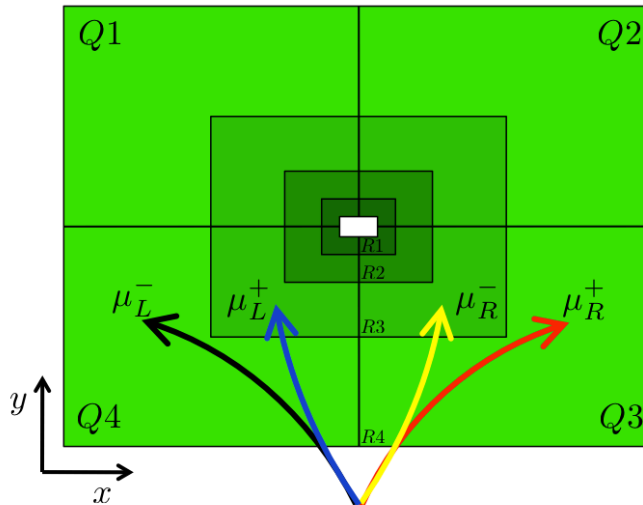


Figure 6.7: A schematic view of a muon station in the  $x$ - $y$  plane. The station quadrants are labelled  $Q1$ – $4$ . Within each quadrant there are four granularity regions,  $R1$ – $4$ , represented by the different shades of green. The highest granularity region is located near the beampipe region (white box) where particle multiplicities are largest. The curved lines show the bending direction for particles travelling downstream in magnet down polarity, for particles pointing towards the left ( $\mu_L^\pm$ ) and right ( $\mu_R^\pm$ ) sides of the muon stations.

## 6.4.2 Calibration samples

Two muon calibration samples have been collected for determining the muon selection efficiencies. The first sample is the standard LHCb muon calibration line, which was designed to collect large amounts of muons from  $J/\psi \rightarrow \mu^+\mu^-$  decays. The  $J/\psi$  candidates are required to have come from a detached vertex to increase the proportion that were produced via  $B$  decay channels. Due to the large statistics, the data are stored in a memory-efficient format known as  $\mu$ DSTs, in which only information associated to signal particles is stored and detector information from other particles is discarded.

The observation of a large L0 muon-trigger induced charge bias is described in Section 6.4.7. A second calibration sample has been collected to further investigate this bias and cross-check the results obtained with the first calibration sample. Although this second sample has fewer statistics, the data is stored in full DST data format, in which detector information from the full event is stored. In this format, it is possible to access the L0 muon “trigger object” responsible for the above mentioned charge asymmetry. Each of these calibration data are described below.

This first calibration sample is selected by the `MuIDCalib_JpsiFromBNoPIDNoMip` stripping line. Candidates are chosen such that one muon, the *tag*, has enough hits in the muon chambers to satisfy the boolean “IsMuon” criteria listed in Table 6.5. A second muon candidate, the *probe*, is identified as any long track that forms a good vertex with the tag muon. The invariant mass of the tag and probe is required to

Table 6.5: To satisfy the IsMuon criteria, a muon candidate is required to have hits in particular muon stations. Which stations are required depends on the momentum of the candidate [104].

Candidate momentum [ GeV ]	Muon stations
$3 \leq p < 6$	M2 + M3
$6 \leq p < 10$	M2 + M3 + (M4 OR M5)
$p \geq 10$	M2 + M3 + M4 + M5

be within a  $\pm 200$  MeV mass window of the  $J/\psi$  mass. No PID information related to the probe is used in the stripping decision. The full set of tag and probe cuts are listed in Table 6.6. From this relatively loose set of selection criteria the  $J/\psi$  mass resonance is visible on top of a moderate combinatoric background. The ratio of the number of events before and after any additional selection is used to measure the efficiency of the selection. This is made possible by the narrow width of the  $J/\psi$ , which is prominent even when only one muon has been identified. Due to the presence of the tag muon, this sample is referred to as the muon selection (MS).

Table 6.6: The MS sample stripping and offline selection criteria.

Particle candidate	Selection
Tag and probe	$p > 3$ GeV ; $p_T > 0.8$ GeV long track $\chi^2/\text{DoF} < 3$ ; $\chi^2(\text{IP}) > 10$
Tag specific	$p > 6$ GeV ; $p_T > 1.5$ GeV $\chi^2(\text{IP}) > 25$ ; IsMuon = 1 L0Global_TIS Hlt1Global_TIS Hlt2Global_TIS
$J/\Psi$ selection	$ m(J/\Psi) - m(J/\Psi)_{\text{PDG}}  \leq 200$ MeV $\chi^2/\text{DoF}(\text{Vertex fit}) < 8$ Separation from primary vertex $\chi^2 > 225$

The second sample is collected by searching all of the Bhadron stripping lines for events containing  $J/\Psi \rightarrow \mu^+ \mu^-$  candidates. The  $J/\Psi$  are selected using purely kinematic criteria, hence the data are referred to as the kinematically selected (KS) sample. The selection criteria are listed in Table 6.7. Because no PID information is applied to either muon candidate, the  $J/\Psi$  resonance sits on a large combinatoric background, which can be significantly reduced by requiring that one of the tracks satisfies the IsMuon criteria. An identical approach is used to measured the muon selection efficiencies with this sample as is used for the MS sample.

The fitted MS and KS  $J/\Psi$  yields are shown in Table 6.8. Both samples contain significantly more muon candidates than are present in the signal sample, with

Table 6.7: The KS sample stripping and offline selection criteria.

Particle candidate	Selection
Candidates	$p > 3 \text{ GeV}$ ; $p_T > 1.2 \text{ GeV}$ $\chi^2/\text{DoF} < 3$ ; $\chi^2(\text{IP}) > 4$ $\eta[2, 5]$ ; CloneKiller
Investigated track	L0Global_TIS Hlt1Global_TIS Hlt2Global_TIS
$J/\Psi$ selection	$ m(J/\Psi) - m(J/\Psi)_{\text{PDG}}  \leq 150 \text{ MeV}$ $\chi^2/\text{DoF}(\text{Vertex fit}) < 11$
General	Number of long tracks $< 250$

Table 6.8: The fitted  $J/\Psi \rightarrow \mu^- \mu^+$  yields for each calibration sample.

		Magnet down	Magnet up
MS	$\mu^-$	1, 116, 008	818, 366
	$\mu^+$	1, 138, 180	801, 458
KS	$\mu^-$	378, 407	270, 539
	$\mu^+$	384, 545	266, 872

approximately 50 k, 300 k and 1 000 k candidates per magnet polarity and muon-charge in the signal, KS and MS samples, respectively.

### 6.4.3 Muon distributions

For a particular magnet polarity, oppositely charged muon tracks are bent towards opposite sides of the detector. A useful tool for studying the muon candidate distributions is the `TrackStateProvider`, which extrapolates long tracks to a specific  $z$ -coordinate in the LHCb detector. The extrapolated coordinate of the MS sample probes at M1 is compared to that of the signal muons in Figure 6.8.

#### Fiducial selections

The muon and tracking stations each have an inactive rectangular beampipe region centred on  $x = 0 = y$ . Coupled with the magnetic field, this results in regions of phase-space with approximately 100% charge asymmetries. For example, a muon traversing the detector near to the beampipe region of one tracking station may be bent by the magnetic field into the inactive beampipe region of a downstream station. However, an oppositely charged muon with identical momentum will remain within the detector acceptance, as it is bent in the opposite direction. This effect

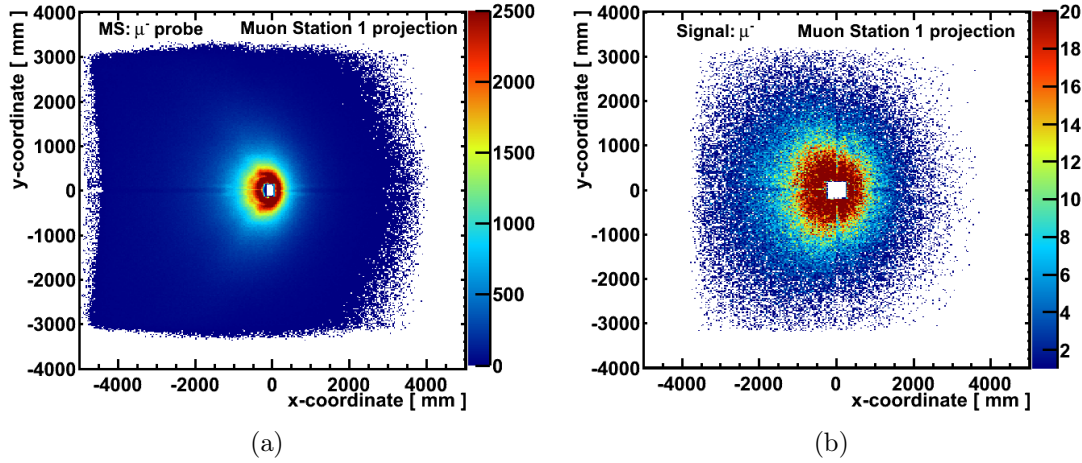


Figure 6.8: The projection of muon candidates at M1 for **a)** the MS sample probes and **b)** the semileptonic signal data. The calibration muons are distributed over a larger surface area, with many located outside of the muon station acceptance (i.e.  $|x| > \sim 3500$  mm and  $|y| > \sim 3000$  mm).

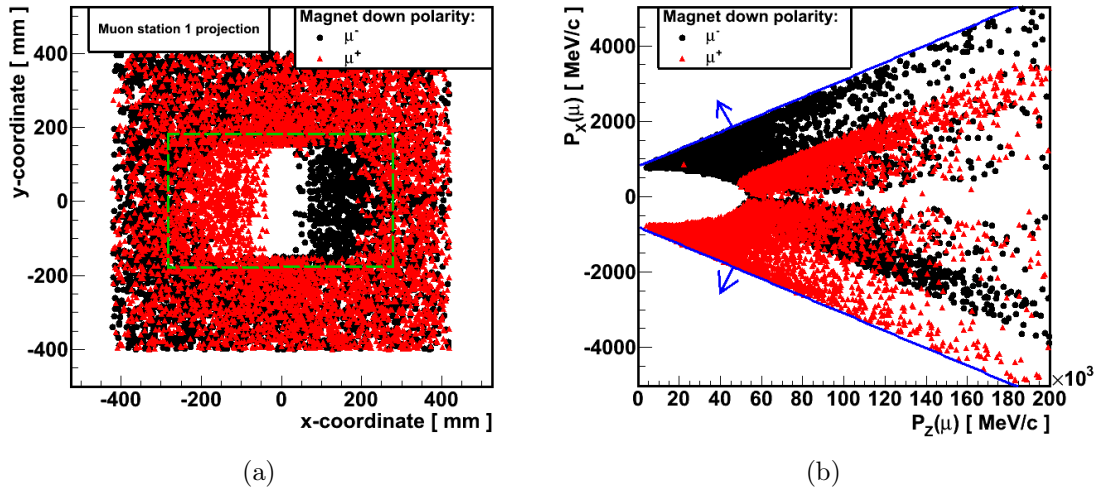


Figure 6.9: **a)** The projected coordinate of MS probe muons traversing near to the M1 beampipe region (i.e.  $|x| < 400$  mm and  $|y| < 400$  mm). The dashed green line represents the inner detector boundary. **b)** The probe muon distribution in the  $p_x-p_z$  plane, for candidates within the green dashed box in Figure **a)**. The solid blue lines represent the exclusion required to remove events within the  $\sim 100\%$  charge asymmetry region.

is demonstrated by Figure 6.9. The fiducial selection required to remove these large asymmetry regions is shown in Figure 6.9(b). A similar acceptance effect is observed for candidates traversing the outer acceptance regions of the muon chambers, as shown in Figure 6.10. The analytical forms of the inner and outer fiducial selections are given in Table 6.9. The inner fiducial selection does not need to be applied to candidates with  $|p_y/p_z| > 0.016$ , as these candidates cannot pass through the beampipe region of the muon stations.

The fiducial exclusion regions are overlaid with the signal data in Figure 6.11.

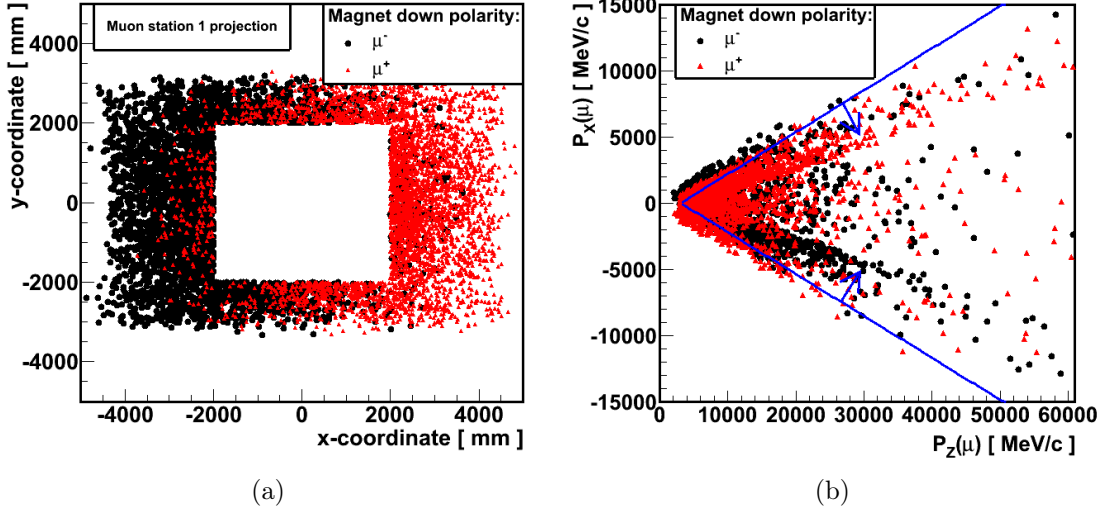


Figure 6.10: **a)** The projected coordinate of MS probe muons traversing near to the M1 outer acceptance region (i.e.  $|x| > 2000$  mm and  $|y| > 2000$  mm). **b)** The probe muon distribution in the  $p_x-p_z$  plane, for the candidates shown in Figure **a)**. The solid blue lines represent the exclusion required to remove the large charge asymmetry regions.

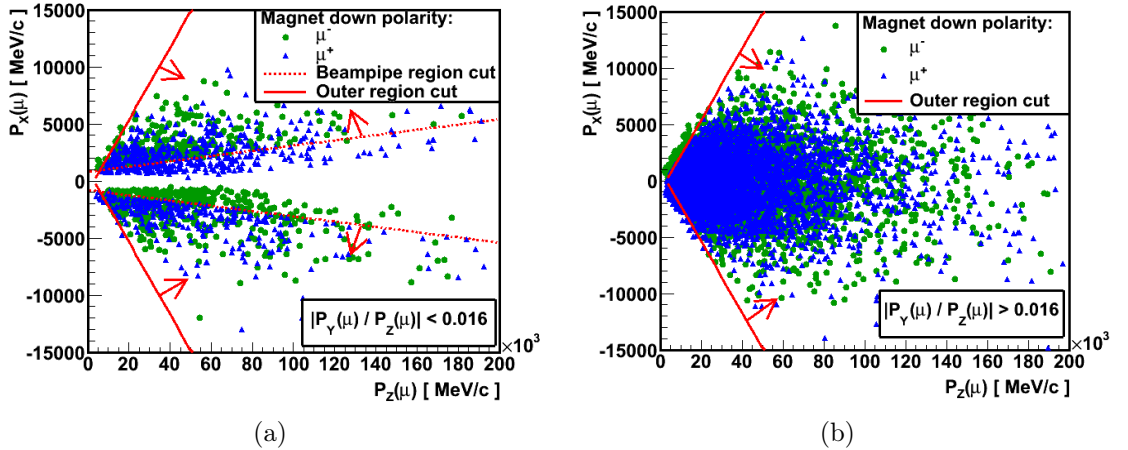


Figure 6.11: **a)** The projection of the signal muon candidates in the  $p_x-p_z$  plane for data with **a)**  $|p_y/p_z| < 0.016$  and **b)**  $|p_y/p_z| > 0.016$ .

Table 6.9: The muon candidate fiducial selections, where momentum components are in units of MeV.

Detector region	Selection
Beampipe (if $ p_y/p_z  \leq 0.016$ )	$ p_x  \geq (0.023 \times p_z) + 800$
Outer region	$ p_x  \leq 0.317 \times (p_z - 3100)$

Regions with  $\sim 100\%$  charge asymmetry similar to those seen in the calibration samples are observed. It has been suggested [105] that these localised regions with large asymmetries could bias the measurement of a small charge asymmetry, particularly as the signal data are highly concentrated on the central beampipe region (as was

seen in Figure 6.8(b)). However, when applied to the signal, the fiducial selection removes only  $\sim 1.5\%$  of candidates, suggesting that the effect on the measured value of  $a_{\text{fs}}^s$  will be small. The influence of fiducial data selections on  $a_{\text{fs}}^s$  is investigated further in Chapter 7.

### Kinematic distributions

The muon selection efficiencies are functions of variables such as the muon  $p$  and  $p_T$ , as is shown later in Sections 6.4.5 to 6.4.7. Figure 6.12 compares the kinematic spectra of the signal and calibration data. The L0, HLT1 and offline selections are applied to all data shown. The spectra from the various samples are generally in good agreement. The most significant differences are seen in the  $p_T$  distributions, with greater proportions of MS data at low  $p_T$ . The measurement of  $a_{\text{fs}}^s$  is conducted in kinematic bins of the muon candidate parameters to suppress bias due to kinematic differences. The binning strategy is described in Section 7.1.4.

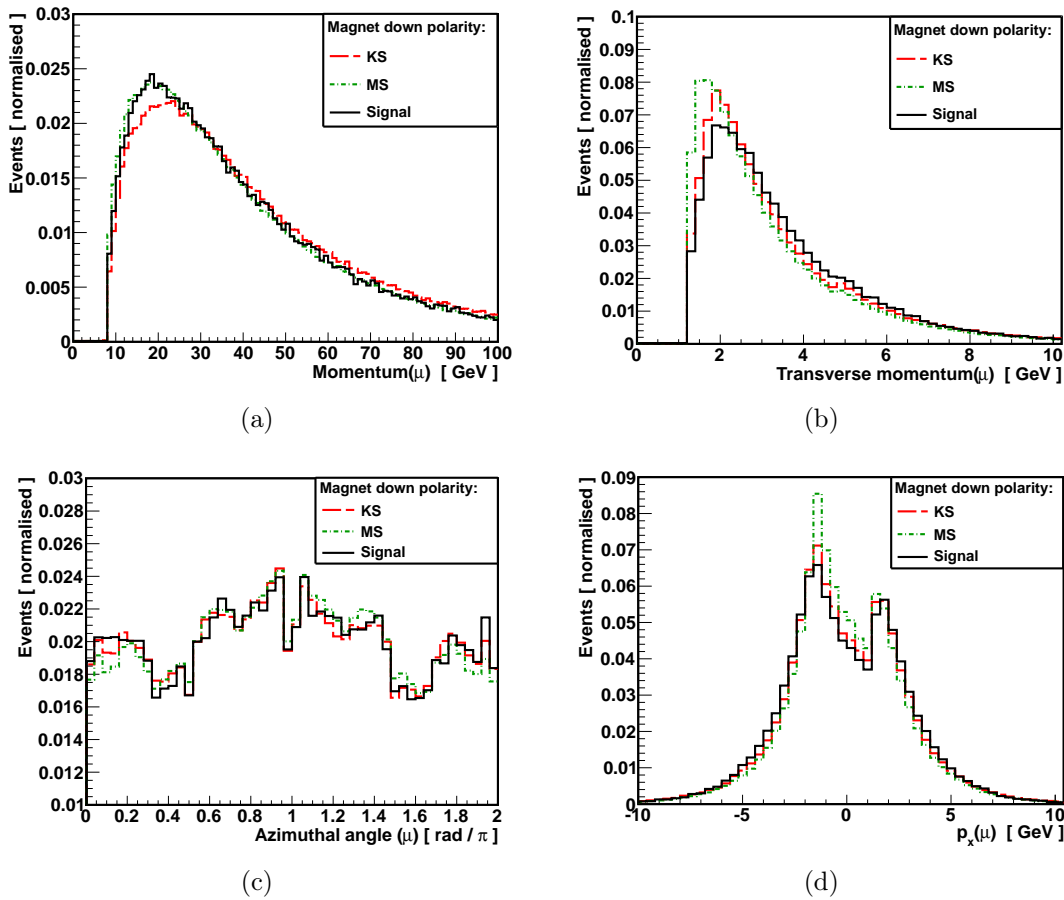


Figure 6.12: A comparison of signal and calibration  $\mu^-$  distributions for **a)** momentum, **b)** transverse momentum, **c)** azimuthal angle ( $\phi$ ) and **d)**  $x$ -component of momentum ( $p_x$ ).

### 6.4.4 Efficiency finding method

Muon selection efficiencies are determined by measuring the  $J/\psi$  mass resonance yields both before and after the application of a selection. For each real  $J/\psi \rightarrow \mu^+ \mu^-$  decay, either one or both muons may be used as probes. Therefore the statistical uncertainty between the positive and negative muon efficiencies are positively correlated (although the efficiencies themselves are uncorrelated). When taking the ratio of efficiencies this leads to an overestimation in their uncertainties. However, the statistical uncertainties associated to the muon calibration sample are small compared to those of the signal, and so the effects of correlated uncertainties are expected to be small. Two different methods have been used to measure the  $J/\psi$  yields. They are described below.

#### Mass spectrum fitter

All calibration data can be divided into two categories, those that pass some selection criteria, and those that fail it. These are referred to as *pass* and *fail* events in the subsequent discussion. An unbinned maximum likelihood fit is executed using the `Roofit` fitting software within the `ROOT` framework (v3r54) [106]. The  $J/\psi$  resonance is modelled by a double *Crystal Ball* function, where the Crystal Ball shape [107] is given by,

$$f(x; \alpha, n, \bar{x}, \sigma) = N \cdot \begin{cases} \exp\left(-\frac{(x-\bar{x})^2}{2\sigma^2}\right) & , \text{ for } \frac{x-\bar{x}}{\sigma} > -\alpha \\ A \cdot \left(B - \frac{x-\bar{x}}{\sigma}\right)^{-n} & , \text{ for } \frac{x-\bar{x}}{\sigma} \leq -\alpha \end{cases} , \quad (6.23)$$

with,

$$A = \left(\frac{n}{|\alpha|}\right)^n \cdot \exp\left(-\frac{|\alpha|^2}{2}\right) \quad \text{and} \quad B = \frac{n}{|\alpha|} - |\alpha|.$$

The function has a gaussian core with mean  $\bar{x}$  and width  $\sigma$ . It has a radiative tail to one side of the core associated with photon emission, with its shape defined by  $n$  and  $\alpha$ . The two Crystal Ball components are allowed to have different widths, but are constrained to have the same  $\bar{x}$ ,  $\alpha$  and  $n$ . The background is described by a linear function. This model has been chosen based on that used in previous  $J/\psi$  analyses [108] and is found to describe the data well. Variations to this model and the resulting influence this has on the measurement of  $a_{\text{fs}}^s$  are investigated in Section 7.3.1. The pass subset, fail subset and total dataset are fitted simultaneously, with the efficiency of a specific selection defined as a fitting parameter. Figure 6.13 shows an example fit result obtained with this method.

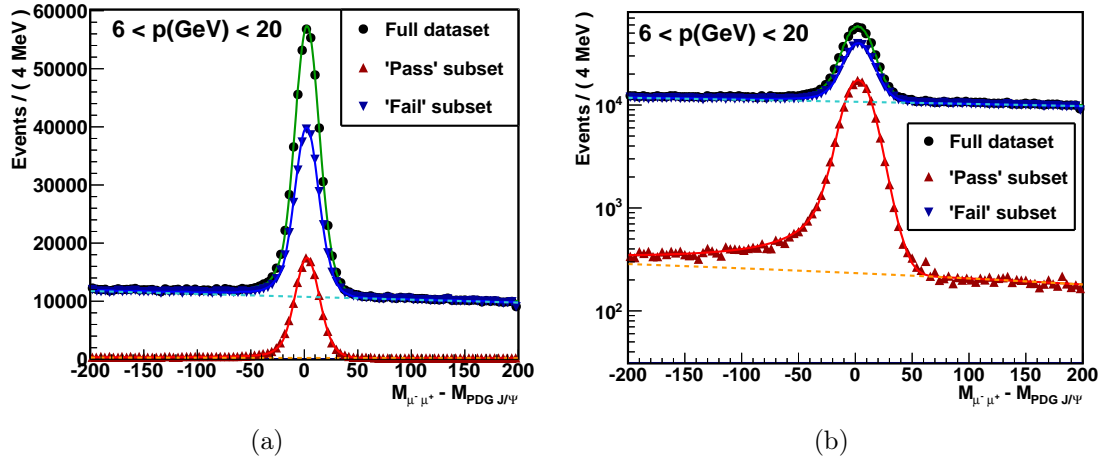


Figure 6.13: A fit to the invariant mass of the tag and probe muon candidates is shown on a) a linear and b) a logarithmic scale, for a particular range of probe momentum and magnet polarity down.

### Background counting method

As a cross-check of the fitting method, a second method has been developed to determine the  $J/\psi$  yields. The total number of background candidates are found by fitting the sideband regions (in which there is little signal) to estimate the background yield in the signal region. An example of this method is shown by Figure 6.14.

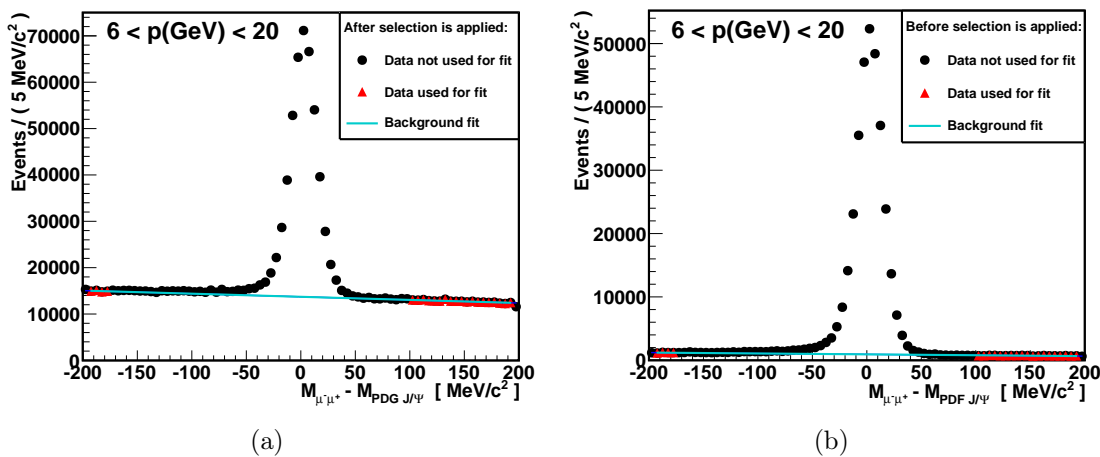


Figure 6.14: The invariant mass of the tag and probe muon candidates a) before and b) after the muon selection is applied. A linear fit is made to the sidebands in which there is little signal (red triangles). The number of  $J/\psi$  candidates is calculated by subtracting the expected number of background candidates from the total number of candidates within the signal region ( $\pm 30 \text{ MeV}$ ).

### 6.4.5 Offline muon identification efficiency

All signal muon candidates are required to satisfy the offline PID criteria, regardless of the way in which the event was triggered. One of the requirements is for the muon to have  $\text{PID}(\mu) > 0$ . The value of this parameter is determined by first linearly extrapolating a long track to the muon system. A momentum dependent search window is defined around the extrapolated track intercept with each muon station. Hits within these windows are used to construct muon tracks. For candidates with momenta in the range  $3 < p(\text{GeV}) < 6$ , hits must be found in at least two of M2–M4. For candidates with  $p > 6$  GeV there must be hits in at least three of M2–M5. For each candidate that passes these criteria the probability that the candidate is a muon is calculated, taking into account the distance between the extrapolated track position and the station hits. The probability that a particle is or isn't a muon is used to determine the Difference Log Likelihood,  $DLL = \log[p_\mu/p_{\text{not-}\mu}]$ , known as  $\text{PID}(\mu)$ . In addition to the  $\text{PID}(\mu) > 0$  requirement, the muon candidate must also satisfy the IsMuon conditions (see Table 6.5) and have nShared equal to zero (i.e the track shares no hits with other muon candidates). The combination of these three muon PID criteria is referred to as MuID, with efficiency,  $\varepsilon_{\text{MuID}}$ , defined as,

$$\varepsilon_{\text{MuID}} = \frac{(\text{IsMuon}(\mu) = 1) \ \& \ (\text{PID}(\mu) > 0) \ \& \ (\text{nShared}(\mu) = 0)}{\text{Calibration selection}}. \quad (6.24)$$

The ‘‘Calibration selection’’ corresponds to the yield of  $J/\psi$  candidates that pass the calibration sample selection criteria, and the ‘&’ sign represents the logical AND of the various criteria.

#### MS sample

The MuID efficiency is shown as a function of  $p$  and  $p_T$  in Figures 6.15(a) and 6.15(b). Measurements are shown for the MS sample with magnet down polarity. The efficiency ratio,  $\varepsilon_{\text{MuID}}(\mu^+)/\varepsilon_{\text{MuID}}(\mu^-)$ , is shown for both magnet polarities as a function of  $p$  and  $p_T$  in Figures 6.15(c) and 6.15(d). No significant charge asymmetry is evident for muon momenta below 50 GeV. However a magnetic field dependent charge asymmetry of the order  $\pm 1\%$  is observed for muons with  $p > 50$  GeV, which is attributed to a beampipe induced acceptance effect.

The influence of the beampipe region on the MuID efficiency is shown in Figure 6.16(a), with large charge asymmetries observed at small muon station  $x$ -coordinates. As would be expected for an acceptance induced effect, the sign of the asymmetry switches with the magnetic field polarity. The asymmetry approximately cancels when the efficiency for one muon charge is compared to the efficiency for an oppositely charged muon traversing the other side of the muon

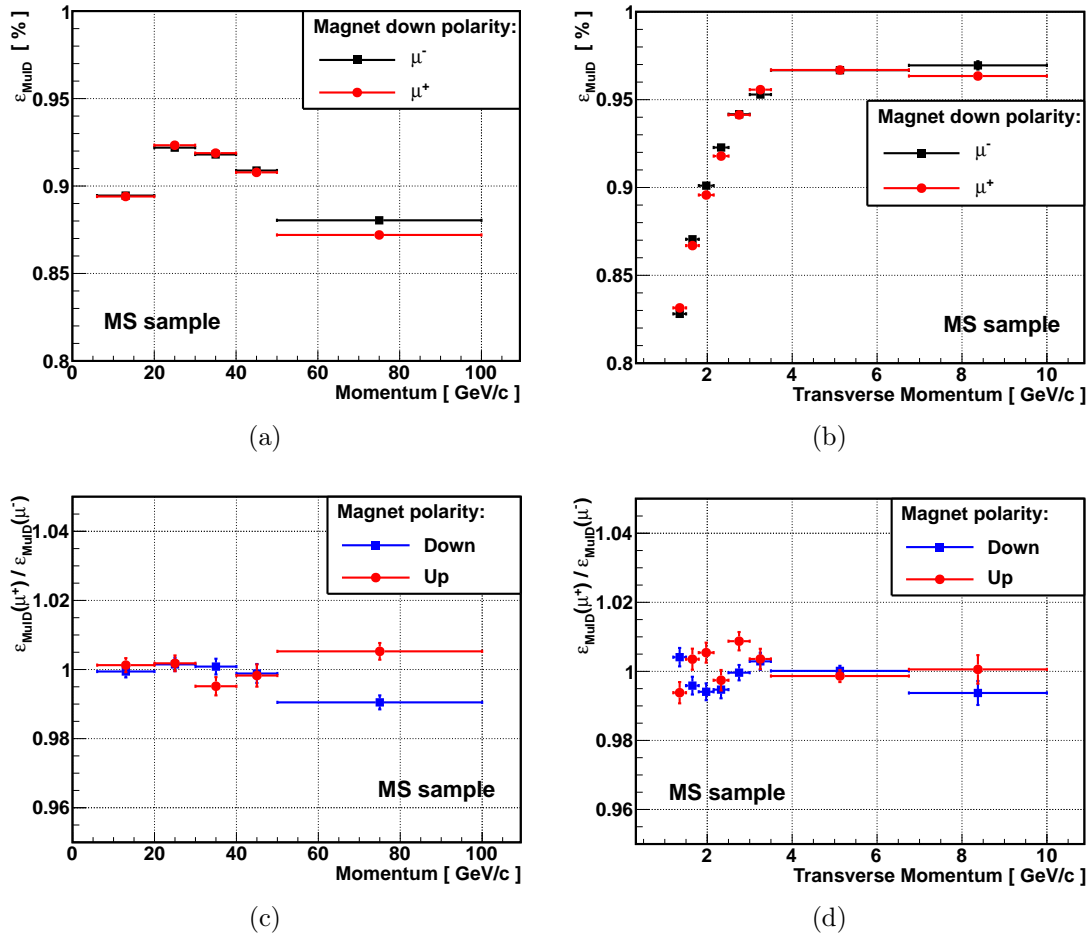


Figure 6.15: The MuID efficiency measured using magnet down polarity MS calibration data in bins of muon **a)** momentum and **b)** transverse momentum. The ratio of positive to negative MuID efficiency is shown as a function of muon **c)** momentum and **d)** transverse momentum.

system, as shown in Figure 6.16(b).

### KS sample

Because the KS sample is collected using no PID requirements, the  $J/\psi$  resonance must be identified on top of a large combinatoric background, as shown in Figure 6.17(a). The background is significantly reduced by requiring that the “tag” muon candidate (i.e. the one that is not being investigated) satisfies the IsMuon criteria, as shown in Figure 6.17(b). The  $J/\psi$  yields are reduced by only a few per cent, in exchange for a far greater decrease in the combinatoric background, thus reducing the fitting uncertainty of  $\varepsilon_{\text{MuID}}$ .

The MuID efficiencies and efficiency ratios measured with the KS sample are shown in Figure 6.18. Measured as a function of muon momenta, the MuID efficiencies are approximately 1–3% higher than those measured with the MS sample. This increased efficiency is possibly due to the method with which the KS sample

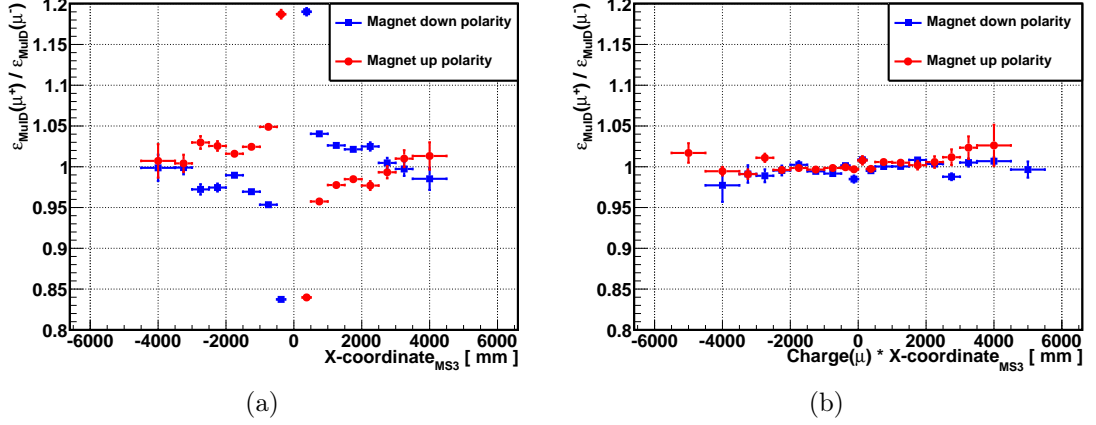


Figure 6.16: **a)** The MuID efficiency ratio in bins of the muon candidate  $x$ -coordinate at M1. **b)** The efficiency ratio in a “reflected” binning scheme, where MuID efficiencies of one muon charge are compared to those of the oppositely charged muon traversing the opposite side of the detector (i.e. the reflected position about the  $y$ -axis at  $x = 0$ ).

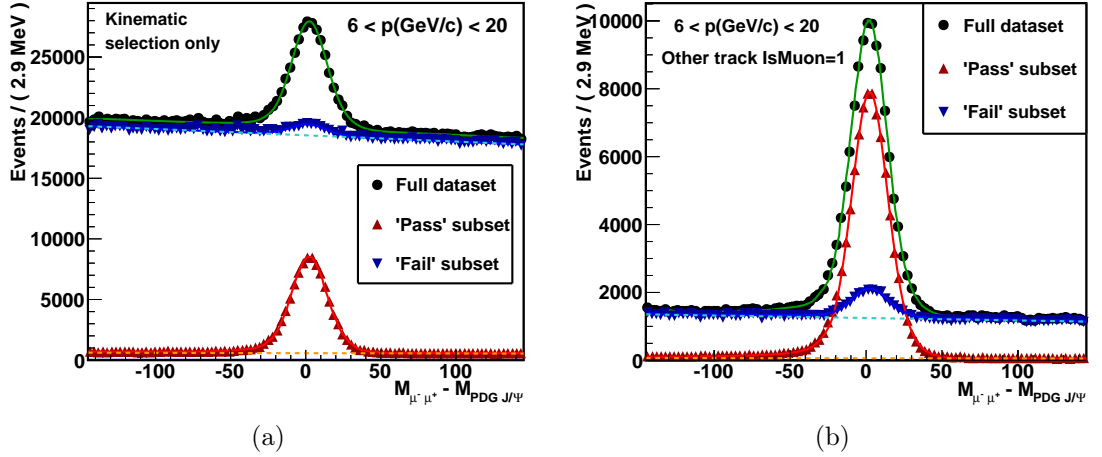


Figure 6.17: The invariant mass of the  $J/\psi$  candidate **a)** before and **b)** after the “tag” leg is required to satisfy the IsMuon criteria.

is selected, by searching the Bhadrion stripping stream for events containing  $J/\Psi$  candidates. The muon is required to be TIS at each level of the trigger. However, no such equivalent TIS requirement is applied to the stripping lines. Some fraction of KS events may have been selected by stripping lines that reconstruct  $J/\Psi$  candidates and therefore require muons that have passed particular PID criteria. This would bias the sample towards higher MuID efficiencies, as is observed when comparing Figures 6.15(a) and 6.18(a). To err on the side of caution, the KS sample is not used to determine MuID efficiencies. However, the KS sample is still used to measure the trigger efficiencies, as described in the following sections.

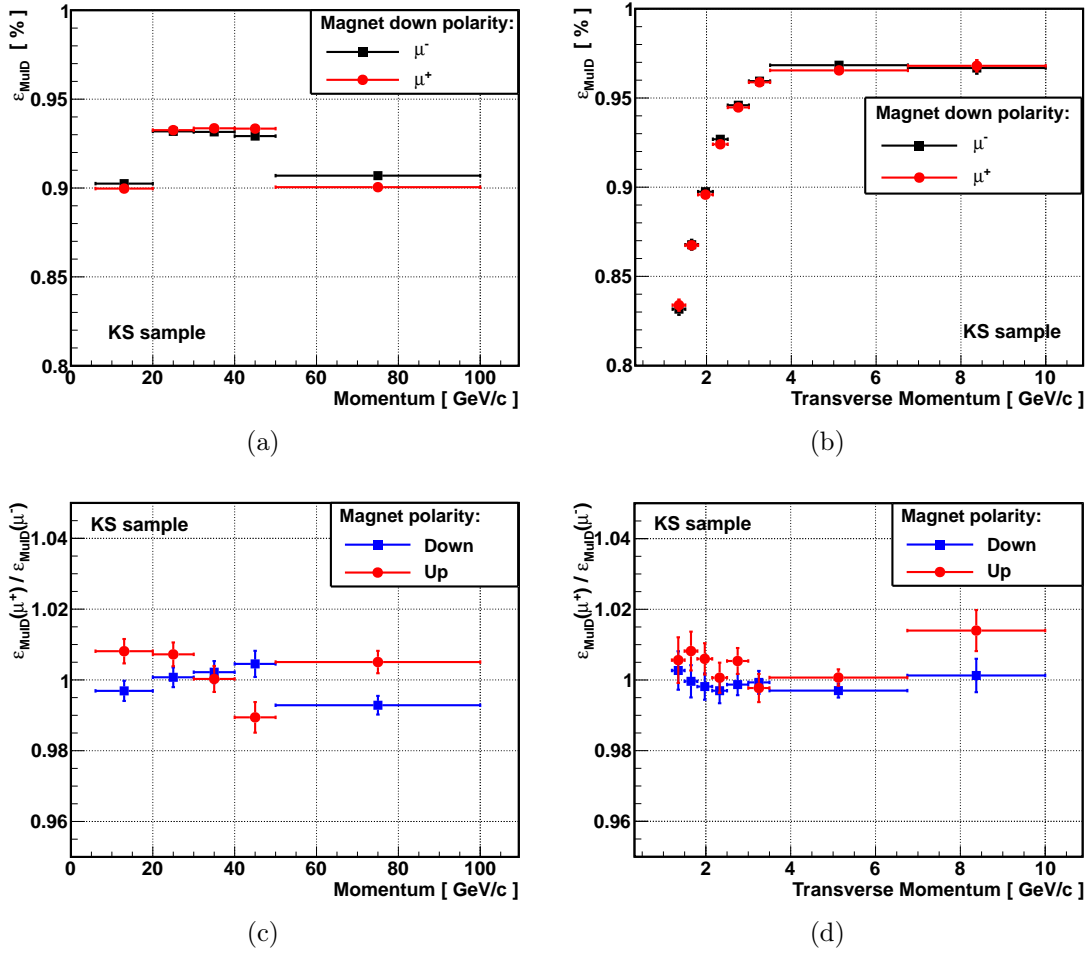


Figure 6.18: The MuID efficiency measured using magnet down polarity KS calibration data in bins of muon **a)** momentum and **b)** transverse momentum. The ratio of positive to negative MuID efficiency is shown as a function of muon **c)** momentum and **d)** transverse momentum.

### 6.4.6 The HLT1 trigger

A large fraction of the signal is triggered by the muon candidate in the HLT1 single-track triggers. The HLT1 efficiency,  $\epsilon_{\text{HLT1}}$ , is defined by the logical OR of the muon being TOS on one of three trigger lines,

$$\epsilon_{\text{HLT1}} = \frac{\mu_{\text{TOS}}(\text{Hlt1TrackAllL0} \parallel \text{Hlt1TrackMuon} \parallel \text{Hlt1SingleMuonHighPT})}{(\text{Calibration selection}) \ \& \ (\text{MuID})}, \quad (6.25)$$

where “MuID” is the offline muon selection that was described in the previous section. The Hlt1TrackAllL0 [109] trigger inclusively select events containing  $B$  and  $D$  mesons. It works on the principle that the  $B$  decay products will typically contain at least one detached track with high momentum. The Hlt1TrackMuon line has an identical structure to the Hlt1TrackAllL0, except that the selection requirements are relaxed slightly for tracks that have IsMuon true. The Hlt1SingleMuonHighPT

trigger has no IP criteria, in exchange for larger  $p_T$  requirements.

Figure 6.19 shows the HLT1 muon efficiencies and efficiency ratios determined with the MS sample. Particularly high efficiencies are observed at very large  $p_T$  due to the inclusion of events triggered by the Hlt1SingleMuonHighPT line. HLT1 induced charge asymmetries are of order  $\sim 1\%$  and flip sign with magnetic field polarity. Good agreement is found between measurements made with the MS and KS samples, as shown by Figure 6.20.

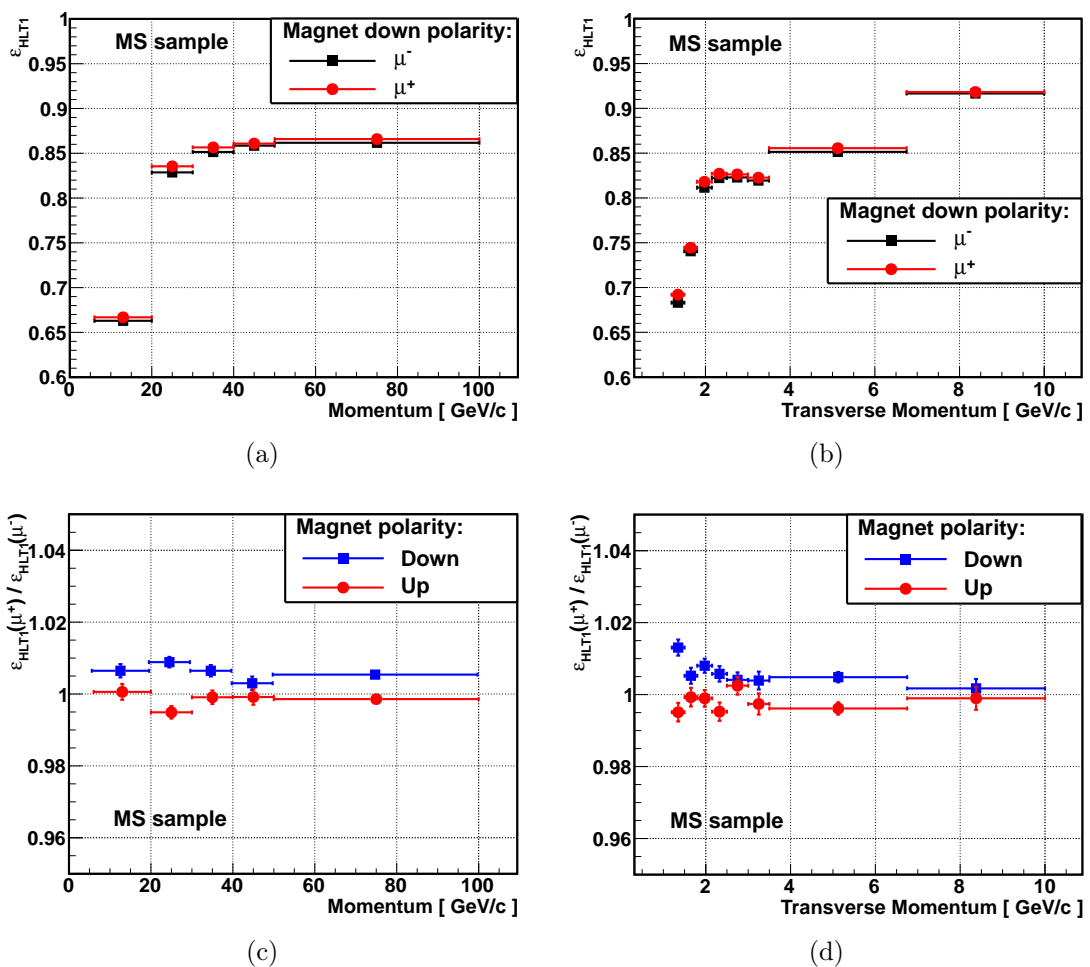


Figure 6.19: The HLT1 efficiency measured using magnet down polarity MS calibration data in bins of **a)** muon momentum and **b)** transverse momentum. The ratio of positive to negative efficiencies is shown as a function of muon **c)** momentum and **d)** transverse momentum.

### 6.4.7 The L0 muon trigger

For the L0 Muon trigger [110], muon tracks are reconstructed as straight lines through the muon system, as they experience only the fringe of the magnetic field in this region. Tracks are required to have hits in the first two muon stations, from which the  $p_T$  of the track is determined with a resolution of approximately

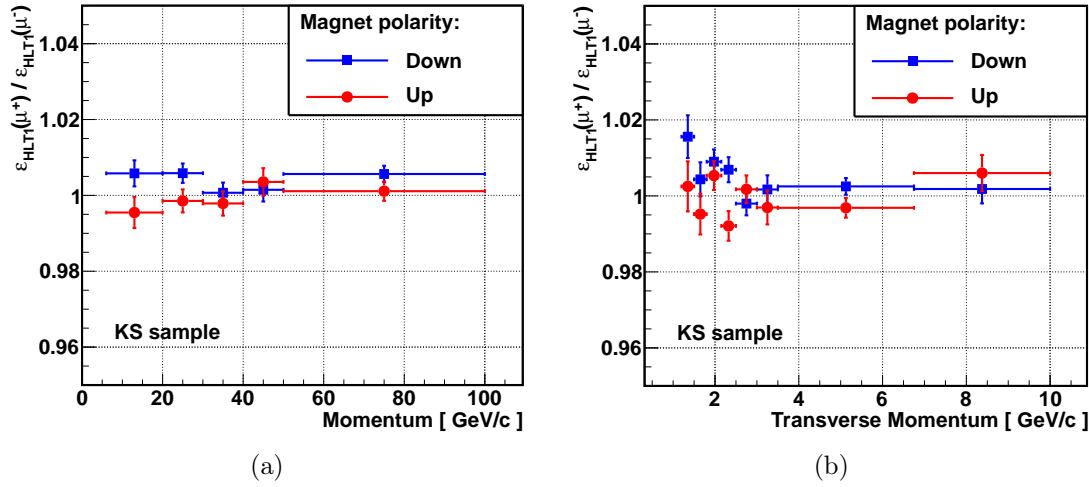


Figure 6.20: The ratio of positive to negative HLT1 efficiencies measured with the KS calibration sample, shown as a function of muon **a)** momentum and **b)** transverse momentum.

20%. Tracks are reconstructed using only hits from a single quadrant of adjacent muon stations (e.g. a tracks hits may be located in the top-left quadrant of each muon station, but cannot be located in the top-left of one station and top-right of another), leading to a reduction in efficiency near to the quadrant boundaries. This inefficiency was apparent in the signal distribution shown in Figure 6.8(b).

L0 muon tracks are assumed to have come from the primary interaction region, with the influence of the magnetic field estimated as a single “kick” to the candidate’s momentum vector [111]. This method is demonstrated by Figure 6.21. To speed up the decision making time, the geometric location of the detector elements in M1 and M2 are matched to precalculated  $p_T$  values, using a look-up table (LUT) of hit combinations.

The L0 trigger efficiency is defined as the fraction of muon candidates that are TOS on the L0Muon trigger with respect to the candidates that have passed the MuID and HLT1 selections,

$$\varepsilon_{L0} = \frac{\mu_{\text{TOS}}(\text{L0Muon})}{(\text{Calibration selection}) \ \& \ (\text{MuID}) \ \& \ (\text{HLT1})}. \quad (6.26)$$

The L0 muon efficiencies and efficiency ratios determined with the MS sample are shown in Figure 6.22. The L0Muon trigger requires that the L0 measured  $p_T$  of candidates is greater than 1480 MeV, resulting in the rapid change in  $\varepsilon_{L0}$  around this value. Across all momentum regions and at low transverse momentum the efficiency of negative muons is seen to be significantly different to those of positively charged muons. Efficiency ratios diverge from unity by approximately  $\pm 5\%$ , showing little dependence on muon momentum. The asymmetry is a strong function of  $p_T$ , with efficiency ratios diverging from unity by more than 20% in the lowest  $p_T$  regions.

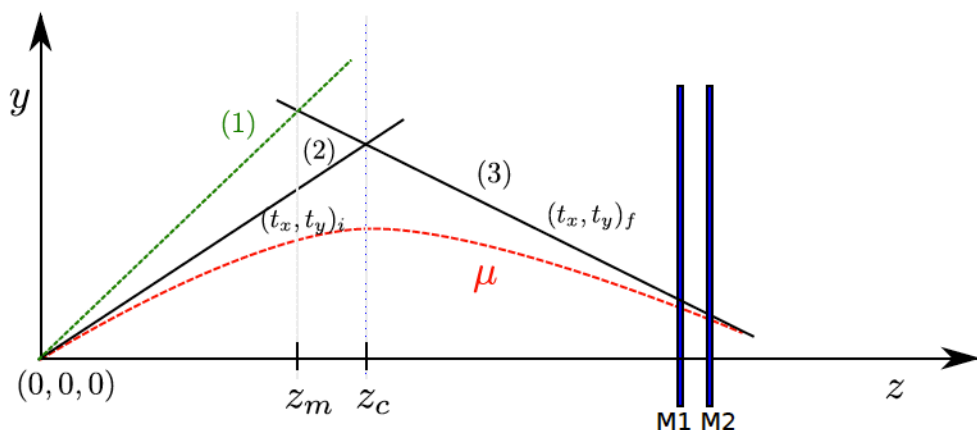


Figure 6.21: A schematic showing how the candidate  $p_T$  is estimated in the L0 muon trigger. The straight muon track (3) is first extrapolated to the centre of the nominal magnetic field,  $z_m$ . The magnetic field along the path defined by tracks (1) and (3) is integrated to determine the magnetic field experienced by a particle following this particular trajectory. The result of this integration is used to more accurately estimate the centre of the magnetic field,  $z_c$ , experienced by the candidate. Track (2) is defined by the intercept of  $z_c$  with track (3). The slopes of tracks (2) and (3),  $(t_x, t_y)_{i,f}$ , are then compared to estimate the  $p_T$  of the true particle (red dashed line). Figure from Ref. [83].

The efficiency ratios determined using the KS sample are shown in Figure 6.23. As a function of momentum, the measured asymmetry is approximately 1% smaller than that observed with the MS sample. However, as a function of  $p_T$ , the asymmetry is compatible in all but the lowest data bin. This suggests that the difference is due to differences in the  $p_T$  distributions of the calibration samples. This is consistent with the asymmetry being largest in the MS sample, as this sample contains a larger proportion of low  $p_T$  tracks (see Figure 6.12(b)).

### The L0 trigger asymmetry

The L0 and offline measured transverse momentum distributions are compared in Figure 6.24(a). A bias in the determination of the L0  $p_T$  results in one charge being more likely to satisfy the L0Muon criteria than the other. Further investigation revealed that the L0 reconstruction uses a simplified geometry that does not adequately represent the real detector. A data driven method has been implemented to correct this bias. A modified LUT is constructed by comparing L0 hit coordinates in muon stations 1 and 2 to offline reconstructed particles with well measured  $p_T$ . The modified LUT is used to determine the “corrected” LUT  $p_T$ . Figure 6.24(b) shows that this modified parameter is charge symmetric with respect to the offline  $p_T$ .

To determine the LUT  $p_T$  the L0 muon “trigger-object” must be accessed. This is not possible in the  $\mu$ DST data format of the MS sample, whereas for the full DST KS sample it is. The threshold value of the LUT  $p_T$  must be larger than the original

L0Muon selection of 1480 MeV, to remove the surplus of charge favoured events. A value of  $LUT(p_T) > 1640$  MeV is found to significantly reduce the asymmetry, as shown by the efficiency ratios in Figure 6.25. A residual  $p_T$  dependent asymmetry of around 1% remains. The modified LUT L0 efficiency,  $\varepsilon'_{L0}$ , is defined as

$$\varepsilon'_{L0} = \frac{\mu_{TOS}(L0\text{Muon}) \ \& \ (LUT(p_T) > 1640 \text{ MeV})}{(\text{Calibration selection}) \ \& \ (\text{MuID}) \ \& \ (\text{HLT1})}. \quad (6.27)$$

Two approaches have been pursued to account for the L0 muon charge bias. The first is to simply measure the L0 charge asymmetry,  $\varepsilon_{L0}$ , using the high statistics calibration samples. Measurements are made in several-dimensional data binning schemes to reduce bias due to kinematic differences between the signal and calibration samples. Particular care is taken to use small kinematic bins at low  $p_T$ , where the L0 bias is largest.

A second method is used as a cross-check of the first, in which the LUT  $p_T$

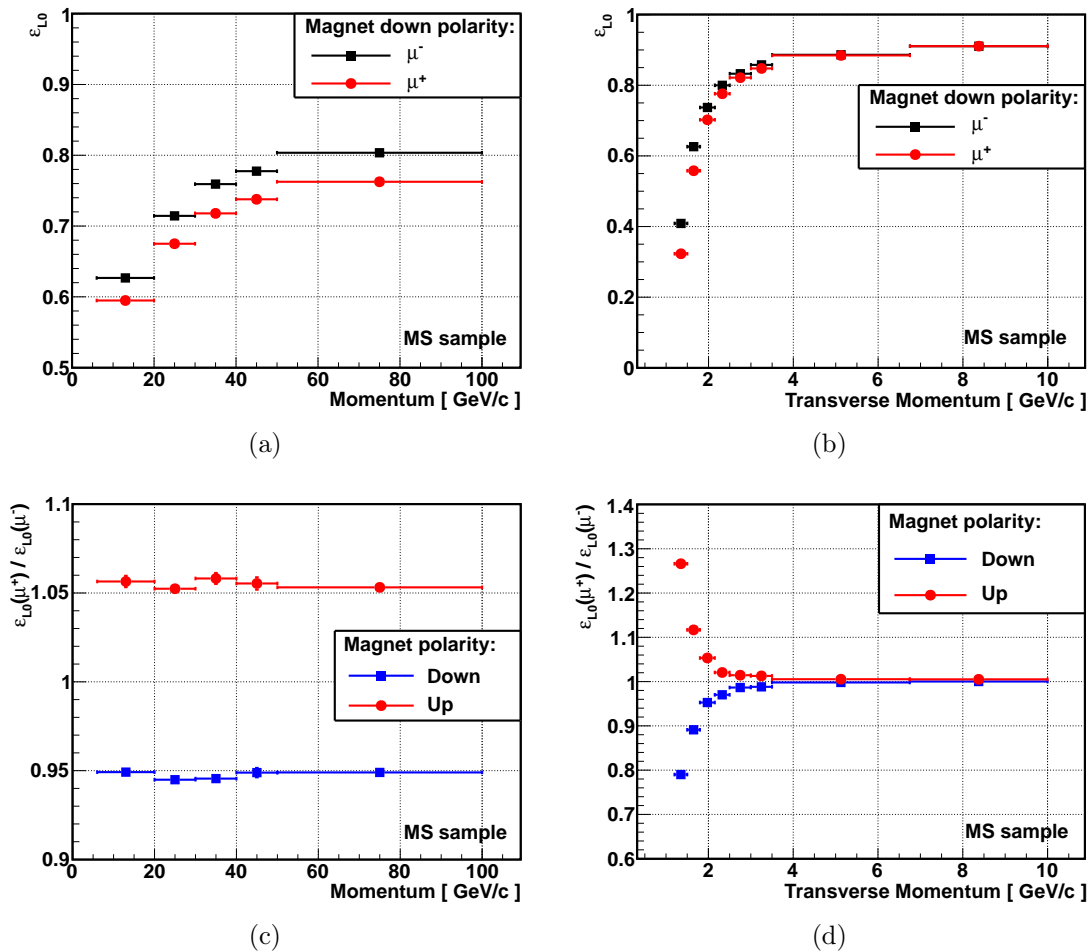


Figure 6.22: The L0 efficiency measured using magnet down polarity MS calibration data in bins of muon a) momentum and b) transverse momentum. The ratio of positive to negative efficiencies is shown as a function of muon c) momentum and d) transverse momentum.

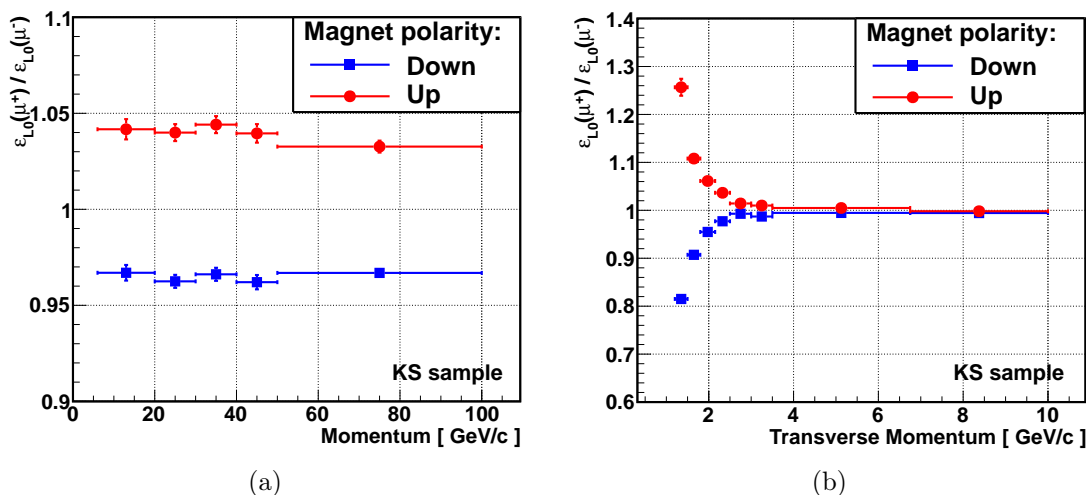


Figure 6.23: The ratio of positive to negative L0 efficiencies measured with the KS calibration sample, shown as a function of muon **a)** momentum and **b)** transverse momentum.

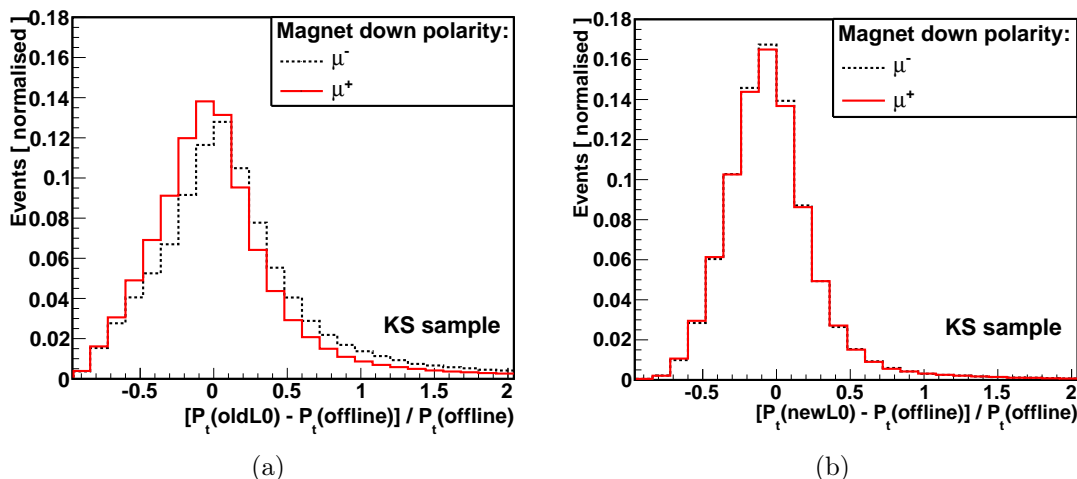


Figure 6.24: **a)** The difference between the L0 and offline measured  $p_T$ , divided by the offline measured value. A shift in the mean of this distribution between positive and negative muon candidates shows that (for magnet down polarity) the negatively charge muons are on average assigned a higher value of  $p_T$  by the L0 reconstruction. **b)** The same as for Figure **a)**, except the original L0  $p_T$  value is replaced by the corrected LUT value. The large charge asymmetry is removed.

selection is added to the event selection criteria of the analysis, and  $\varepsilon'_{L0}$  is used instead of  $\varepsilon_{L0}$ . This comes at the expense of a small fraction of data, as the L0 threshold of this selection is larger than is used in the real trigger. This method can only be pursued with the full DST KS sample, and has a larger uncertainty due to the lower KS statistics. Results obtained with these two methods are compared in Chapter 7.

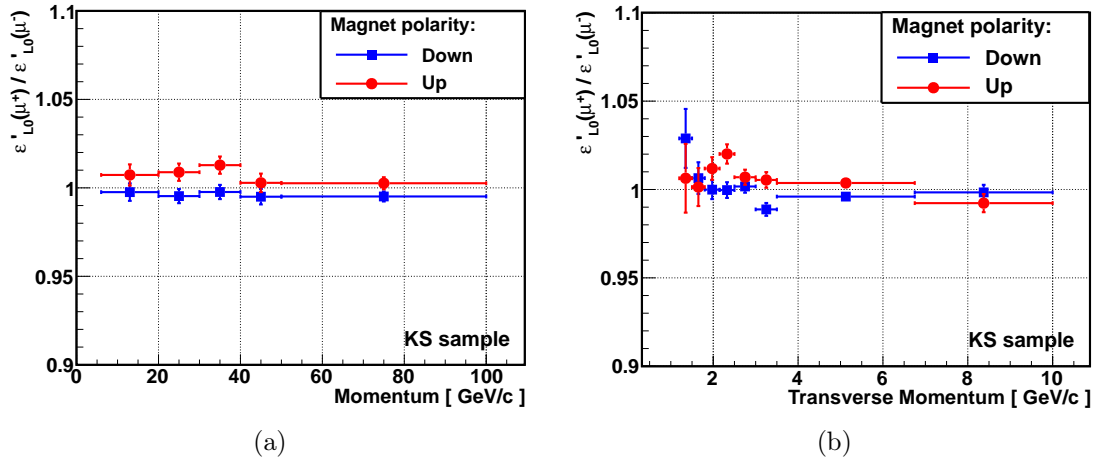


Figure 6.25: The efficiency ratio of the modified L0 trigger selection using the KS calibration sample, shown as a function of muon **a)** momentum and **b)** transverse momentum.

### 6.4.8 The total muon efficiency

The total muon efficiency ratios used to correct the signal yields in Equation 6.22,  $\epsilon(\mu^+)/\epsilon(\mu^-)$ , are found by multiplying together the individual efficiencies discussed in the previous sections,

$$\frac{\epsilon(\mu^+)}{\epsilon(\mu^-)} = \frac{\epsilon_{\text{MuID}}(\mu^+) \cdot \epsilon_{\text{HLT1}}(\mu^+) \cdot \epsilon_{L0}(\mu^+)}{\epsilon_{\text{MuID}}(\mu^-) \cdot \epsilon_{\text{HLT1}}(\mu^-) \cdot \epsilon_{L0}(\mu^-)}. \quad (6.28)$$

When the LUT  $p_T$  correction is applied, the L0 components  $\epsilon_{L0}(\mu^\pm)$  are replaced with  $\epsilon'_{L0}(\mu^\pm)$ . The total efficiency ratio is shown as a function of  $p$  and  $p_T$  in Figure 6.26. As may be expected, the ratios are dominated by the large L0 trigger induced asymmetry.

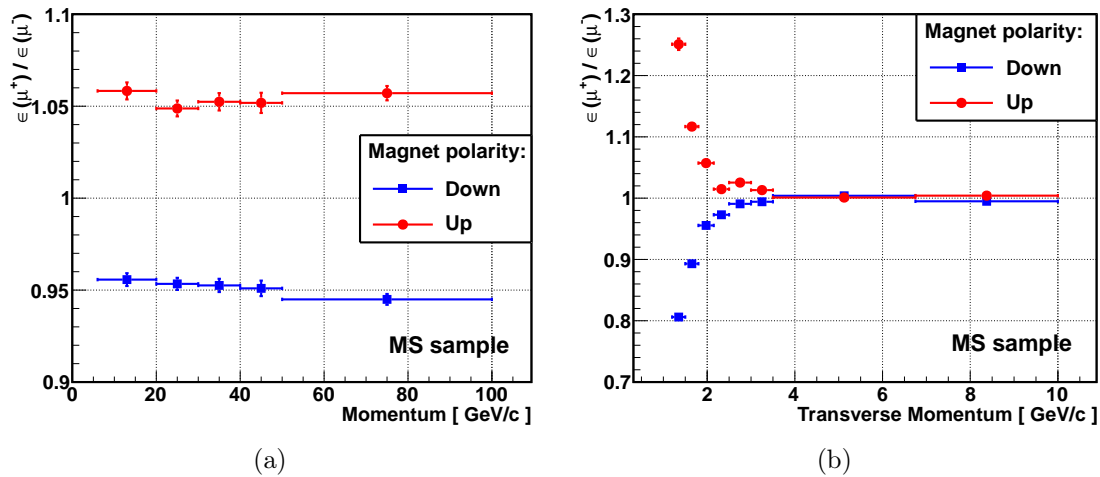


Figure 6.26: The total muon efficiency ratio from MS calibration data in bins of **a)** momentum and **b)** transverse momentum.

## 6.5 The HLT2 trigger

In the HLT2 the majority of data are selected by the multi-body topological trigger lines [112] and the inclusive- $\phi$  trigger. Signal data are analysed in two independent samples of approximately equal statistics. In the first sample the  $\phi$  particle is required to be TOS in the inclusive- $\phi$  line. Due to the symmetric nature of the  $\phi \rightarrow K^+K^-$  decay, it is assumed that no charge bias could be induced by this selection. This assumption is further investigated in Section 7.3.3. In the second sample the  $B_s^-$  candidate is required to be TOS in one of the three topological lines: H1t2TopoMu2BodyBBDT, H1t2TopoMu3BodyBBDT or H1t2TopoMu4BodyBBDT. These triggers use a multivariate approach to inclusively select 2, 3 and 4 body candidates containing at least one muon.

To investigate the potential bias induced by the multivariate topological trigger lines, an independent study [113] has been carried out using  $B \rightarrow D\mu\nu$  decays, with  $D \rightarrow K\pi\pi$ . This channel has a similar topology to the signal, with approximately 16 times the production rate. The same selection criteria are applied as are used for signal selection, except for the criteria that are specific to the  $\phi \rightarrow K^+K^-$  decay. In this study the kaon candidate is referred to as “H1”, and the lower and higher  $p_T$  pions are referred to as “H2” and “H3”.

To maximise the statistical power of the calibration sample, each of the muon and hadrons are studied individually. First the efficiency of the muon selection is considered. The efficiency comprises a numerator and denominator defined by the number of candidates that pass the following criteria. The denominator contains candidates for which H1, H2 and H3 are all TOS in the three body H1t2TopoMu3BodyBBDT line. The numerator is then the subset of candidates for which the muon is TOS in the H1t2TopoMu4BodyBBDT line. The efficiencies and efficiency ratios determined with this method are shown as a function of muon momenta in Figure 6.27. No significant charge bias is observed.

Using this method the efficiency for each final state particle can be investigated in turn. For example, to study the H2 efficiency, the denominator contains events for which the muon, H1 and H3 are TOS in the H1t2TopoMu3BodyBBDT line. The numerator is then the subset of data for which the H2 is TOS in the H1t2TopoMu4BodyBBDT line. Figure 6.28 shows the efficiency ratios for the combination of results obtained from the three  $D$  daughters. No significant charge asymmetry is observed due to the HLT2 topological trigger. The overall topological trigger bias is determined to be less than  $10^{-3}$  at the 68% confidence level. As this sample accounts for approximately 50% of the total signal sample, a systematic uncertainty of  $5 \times 10^{-4}$  is assigned.

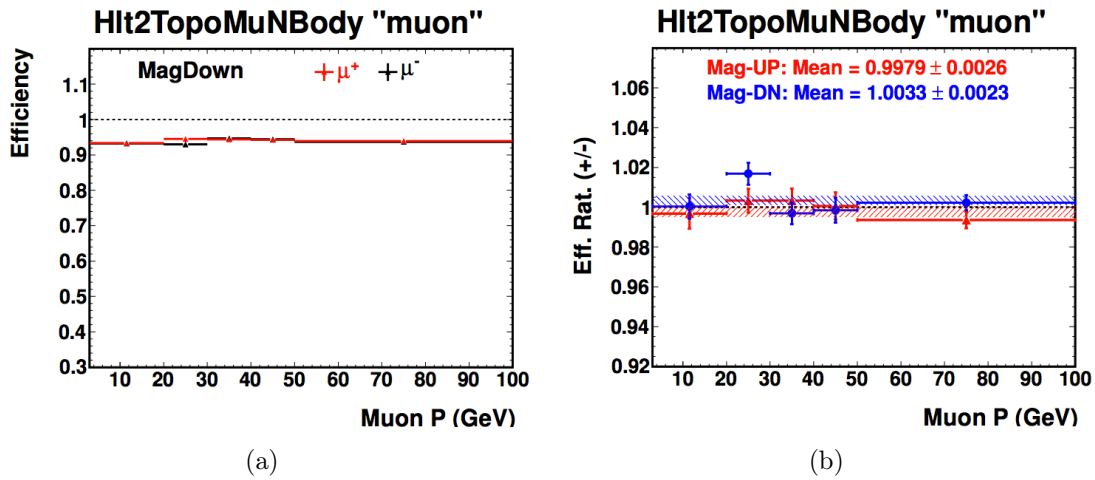


Figure 6.27: The **a)** efficiencies and **b)** efficiency ratios of muon selection in the HLT2 four body topological trigger. Figures from Ref. [113].

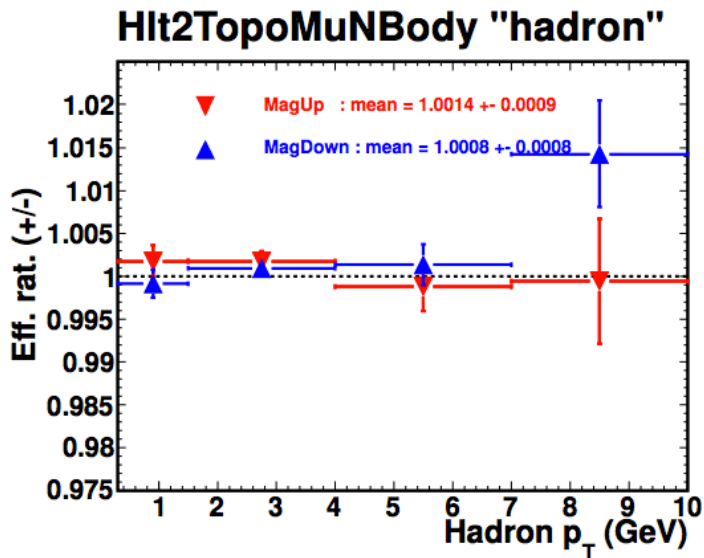


Figure 6.28: The hadronic efficiency ratios in the HLT2 topological trigger, with results combined from the three daughter hadrons. Figure from Ref. [113].

## FLAVOUR-SPECIFIC ASYMMETRIES USING SEMILEPTONIC $B$ DECAYS: RESULTS

In this chapter a time-integrated, untagged measurement of  $a_{\text{fs}}^s$  is presented. The determination of signal yields and the corresponding raw charge asymmetries are first presented in Section 7.1. The measured asymmetry is then presented in Section 7.2, which is determined by combining the raw signal yields with the muon efficiency measurements from Section 6.4. Various systematic studies and additional corrections related to background and tracking induced bias are presented in Section 7.3. Finally, the main result is given in Section 7.4.

### 7.1 Signal yield determination

The purpose of data fitting is to determine the relative yields of  $D_s^\mp \mu^\pm$  candidates, by distinguishing signal from background. The signal yields are then used in Equation 6.22 to determine  $a_{\text{fs}}^s$ . A two-dimensional unbinned maximum likelihood fit is implemented in the `Roofit` [106] framework. The first dimension is the invariant mass of the  $D_s^-$  candidate, in which signal  $D_s^-$  is separated from combinatoric and  $D^-$  backgrounds. The combinatoric background is generically referred to as “Detached” background. The mass range of interest is that within  $\pm 80$  MeV of the  $D_s^-$  mass. Charm mesons produced directly via  $pp \rightarrow c\bar{c}X$  interactions are referred to as “Prompt” background, where  $X$  indicates the sum over all possible additional final states. The charm mesons produced via semileptonic  $B_s^0$  decay are referred to as “DfB” (i.e  $D$  from  $B$ ). The Prompt and DfB candidates are indistinguishable in the  $D_s^\pm \rightarrow K^+K^-\pi^\pm$  mass spectrum, as both peak at the  $D_s^-$  mass. DfB candidates typically have larger values of impact parameter (IP) than Prompt, as they originate from vertices that are separated from the primary interaction region. The second fitting dimension is therefore the logarithm of the IP of the  $D_s^-$ , referred to as  $\log(\text{IP})$ .

The Prompt  $\log(\text{IP})$  shape has been determined using a topologically similar calibration sample of  $B_s^0 \rightarrow D_s^- X$ . The  $D_s^-$  from these data are required to pass the same selection criteria as the signal  $D_s^-$ . The  $D_s^-$  is then combined with a charged hadron that satisfies the same kinematic criteria as the signal muon but fails the IsMuon criteria and has  $\text{PID}(\mu) < 0$ . This hadron is referred to as a “fake muon”. When the  $\text{PID}(K)$  of the fake muon is greater than or less than zero it is referred to as a kaon or pion. These modified selection criteria ensure that the calibration sample contains an enhanced fraction of Prompt events compared to that of the signal sample. A single bifurcated gaussian<sup>1</sup> is found to adequately model the shape of the Prompt component, as shown in Figure 7.1. The Prompt shape is determined in several bins of fake muon momenta, and fixed when fitting sub-samples of the signal that contain muon candidates in the same momentum range. The relative

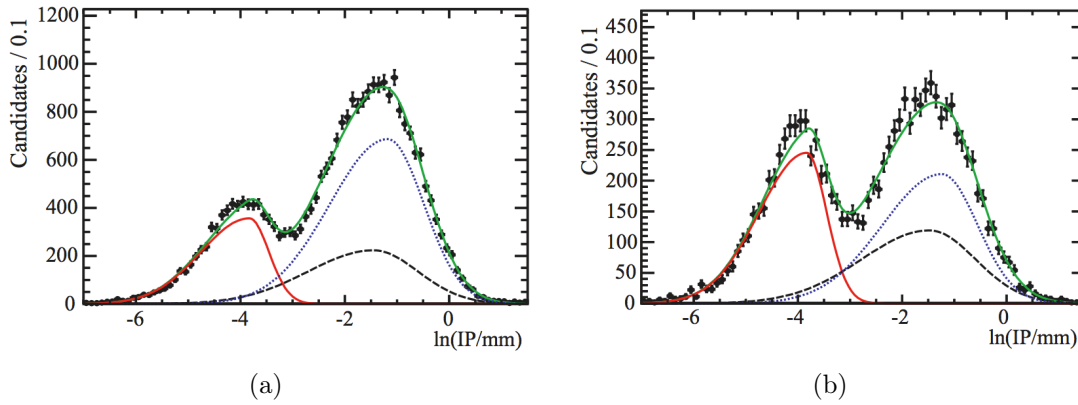


Figure 7.1: Example fits to the  $B_s^0 \rightarrow D_s^- X$  data samples when the fake muon is identified as **a)** a pion and **b)** a kaon. The short-dashed blue, long-dashed black and solid red curves represent the DfB, Detached and Prompt components. Figures from Ref. [94].

normalisation of the Prompt component is allowed to vary in the fitting process. A single bifurcated gaussian is also used to model the shape of the DfB and Detached components, with all associated parameters determined by the fitter. The total PDF used to describe the signal  $\log(\text{IP})$  distribution is,

$$\begin{aligned} \text{PDF}(l) = & n_{\text{DfB}} \cdot \text{BiFurGauss}(\mu_{\text{DfB}}, \sigma_{\text{DfB}}^L, \sigma_{\text{DfB}}^H, l) + n_{\text{Pro}} \cdot \text{BiFurGauss}(l) \\ & + n_{\text{Det}} \cdot \text{BiFurGauss}(\mu_{\text{Det}}, \sigma_{\text{Det}}^L, \sigma_{\text{Det}}^H, l), \end{aligned} \quad (7.1)$$

where  $l$  indicates the observable,  $n$  is the component yield and BiFurGauss is the bifurcated gaussian function with mean  $\mu$ , low width  $\sigma^L$  and high width  $\sigma^H$ . The subscripts DfB, Pro and Det refer to the DfB, Prompt and Detached components. Only the parameters that are allowed to vary in the fit are shown; hence the Prompt

<sup>1</sup>A bifurcated gaussian has a similar parameterisation to a gaussian, except it can have different widths on the low and high side of the mean.

component is shown as a function of  $l$  only<sup>1</sup>.

For the invariant  $D_s^-$  mass distributions, the DfB and Prompt components are each modelled by double gaussian functions, comprising two gaussians with different widths and a common mean. The Detached component is modelled using a first order Chebychev polynomial, which is constrained by the sideband regions in which the signal contamination is negligible. The total PDF used to describe the  $D_s^-$  mass distribution is,

$$\begin{aligned} \text{PDF}(m) = & (n_{\text{DfB}} + n_{\text{Pro}})(f_n) \cdot \text{Gauss}(\mu, \sigma_n, m) \\ & + (n_{\text{DfB}} + n_{\text{Pro}})(1 - f_n) \cdot \text{Gauss}(\mu, \sigma_w, m) \\ & + n_{\text{Det}} \cdot \text{Chebychev}(a_0), \end{aligned} \quad (7.2)$$

where  $m$  indicates the observable,  $n$  is the component yield,  $f_n$  is the fraction of the double gaussian that is described by the narrow component, Chebychev is the first order polynomial function with fitting parameter  $a_0$ , and Gauss is the gaussian function with mean  $\mu$  and width  $\sigma$ . The subscript  $n$  and  $w$  correspond to the narrow and wide gaussian components. To aid fit stability, the wide gaussian width is defined to be a multiple of the narrow width,  $\sigma_w = \sigma_n R$ , where  $R$  is a fitted parameter of value greater than one.

The two dimensional data distribution is simultaneously fitted by the product of  $\text{PDF}(l)$  and  $\text{PDF}(m)$ . Figures 7.2 and 7.3 show examples of the fitted signal data, on linear and logarithmic scales.

### 7.1.1 Raw yields and charge asymmetries

The fitted DfB yields and the corresponding raw charge asymmetry,

$$A_{\text{raw}} = \frac{N[D_s^- \mu^+] - N[D_s^+ \mu^-]}{N[D_s^- \mu^+] + N[D_s^+ \mu^-]}, \quad (7.3)$$

have been determined as a function of the muon  $p$  and  $p_T$  using the two-dimensional fitting procedure described previously. The results are summarised in Tables 7.1 and 7.2, for both before and after the application of the L0 muon trigger LUT correction, and as a function of the muon candidate  $p$  and  $p_T$  in Figures 7.4 and 7.5. When the LUT correction is not applied, an average charge asymmetry of approximately  $\pm 2\%$  is observed. This raw asymmetry is consistent with having been induced by the L0 Muon trigger bias discussed in Section 6.4.7. It changes sign with magnetic field polarity and is largest for muon candidates with low  $p_T$ . The total signal yields and raw asymmetries obtained when fitting in bins of  $p$  or  $p_T$  are con-

<sup>1</sup>The PDFs used to describe the calibration samples in Figure 7.1 are identical to Equation 7.1, except the Prompt BiFurGauss component is also a function of  $\mu_{\text{Pro}}$ ,  $\sigma_{\text{Pro}}^L$  and  $\sigma_{\text{Pro}}^H$ .

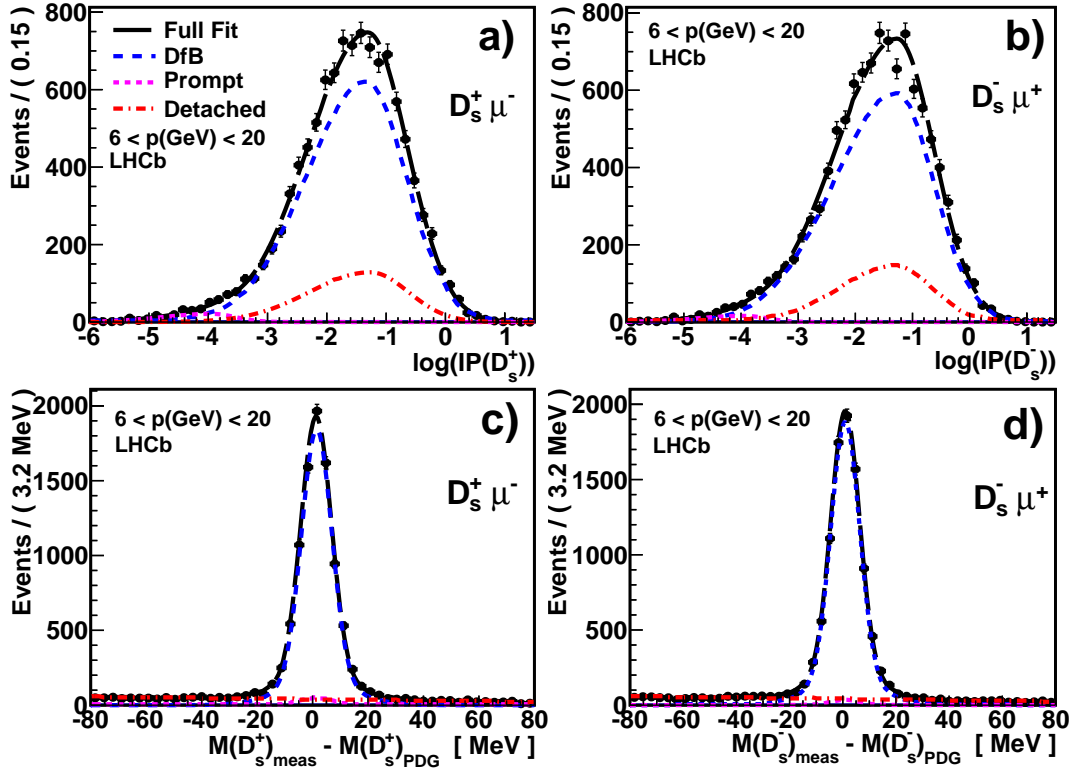


Figure 7.2: Projections of the signal fit in  $\log(\text{IP})$  (upper row) and mass (lower row), with muon momenta in the range  $6 \leq p(\text{GeV}) < 20$  and collected with upward polarity magnetic field. The  $\chi^2/\text{DoF}$  and  $p$ -values of the fitted distributions in Figures [a, b, c, d] are  $\chi^2/\text{DoF} = [0.97, 1.25, 0.89, 0.70]$  and  $p\text{-value} = [0.49, 0.19, 0.60, 0.84]$ .

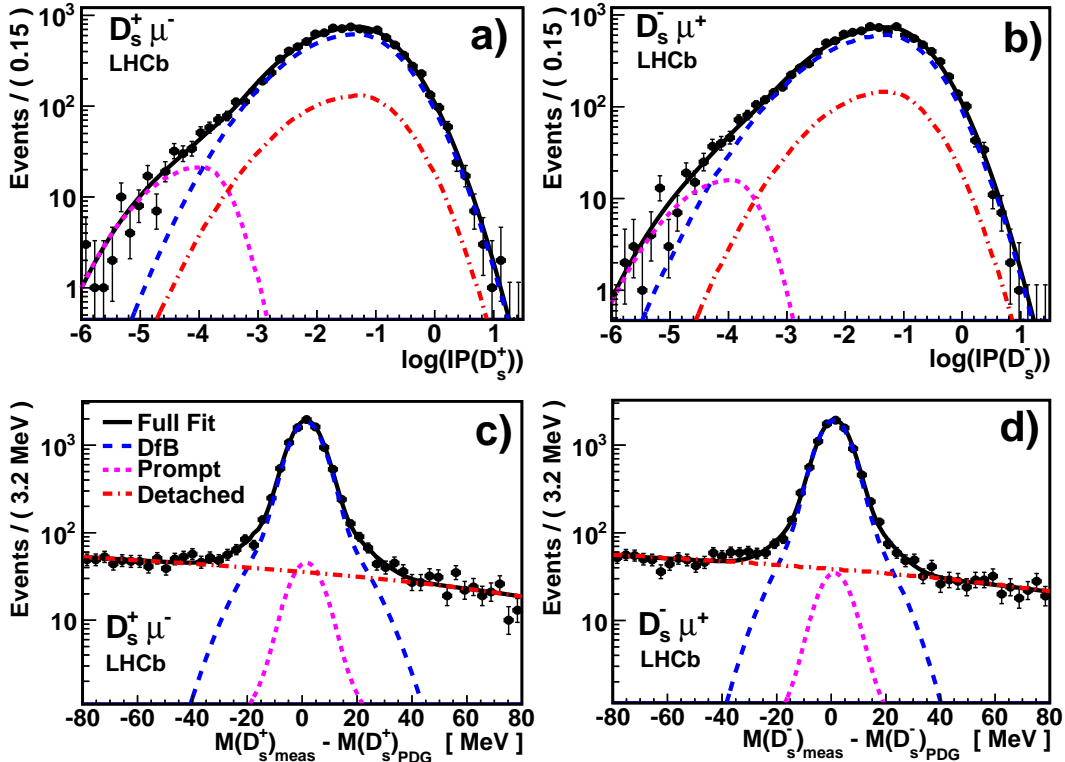


Figure 7.3: The fitted distribution from Figure 7.2 shown on a logarithmic  $y$ -axis scale.

## 7.1. SIGNAL YIELD DETERMINATION

Table 7.1: The signal yields and raw asymmetries determined with the two-dimensional fitter, without the L0 LUT correction.

$p$ [GeV]	Magnet up			Magnet down		
	$D_s^- \mu^+$	$D_s^+ \mu^-$	$A_{\text{raw}}[\%]$	$D_s^- \mu^+$	$D_s^+ \mu^-$	$A_{\text{raw}}[\%]$
6 – 20	$9779 \pm 118$	$9544 \pm 110$	$1.22 \pm 0.84$	$13185 \pm 127$	$14049 \pm 131$	$-3.17 \pm 0.66$
20 – 30	$9314 \pm 107$	$9017 \pm 111$	$1.62 \pm 0.85$	$12800 \pm 125$	$13203 \pm 126$	$-1.55 \pm 0.68$
30 – 40	$7412 \pm 96$	$7114 \pm 97$	$2.05 \pm 0.95$	$9943 \pm 110$	$10352 \pm 111$	$-2.01 \pm 0.76$
40 – 50	$5376 \pm 81$	$5050 \pm 79$	$3.12 \pm 1.10$	$7152 \pm 96$	$7455 \pm 98$	$-2.08 \pm 0.93$
50 – 100	$10799 \pm 112$	$10321 \pm 110$	$2.27 \pm 0.75$	$14645 \pm 139$	$14753 \pm 134$	$-0.37 \pm 0.66$
<b>Total</b>	$42681 \pm 232$	$41046 \pm 229$	$1.95 \pm 0.39$	$57726 \pm 269$	$59813 \pm 270$	$-1.78 \pm 0.32$
$p_T$ [GeV]						
1.2 – 1.5	$2192 \pm 55$	$1776 \pm 47$	$10.46 \pm 1.90$	$2449 \pm 57$	$3101 \pm 65$	$-11.75 \pm 1.45$
1.5 – 1.8	$3717 \pm 69$	$3422 \pm 68$	$4.13 \pm 1.38$	$4816 \pm 77$	$5260 \pm 84$	$-4.40 \pm 1.10$
1.8 – 2.1	$5261 \pm 84$	$4931 \pm 80$	$3.24 \pm 1.15$	$6872 \pm 92$	$7447 \pm 94$	$-4.01 \pm 0.90$
2.1 – 2.5	$5064 \pm 78$	$4967 \pm 84$	$0.97 \pm 1.14$	$6890 \pm 95$	$7088 \pm 93$	$-1.41 \pm 0.94$
2.5 – 3.0	$6308 \pm 90$	$6112 \pm 87$	$1.58 \pm 1.01$	$8626 \pm 106$	$8815 \pm 103$	$-1.09 \pm 0.84$
3.0 – 3.5	$4881 \pm 78$	$4803 \pm 85$	$0.80 \pm 1.19$	$6715 \pm 96$	$6775 \pm 90$	$-0.44 \pm 0.97$
3.5 – 6.8	$13228 \pm 126$	$12994 \pm 126$	$0.89 \pm 0.68$	$18376 \pm 149$	$18467 \pm 150$	$-0.25 \pm 0.57$
6.8 – 10.0	$2030 \pm 48$	$1996 \pm 47$	$0.85 \pm 1.67$	$2987 \pm 60$	$2854 \pm 57$	$2.27 \pm 1.43$
<b>Total</b>	$42681 \pm 231$	$41000 \pm 230$	$2.01 \pm 0.39$	$57731 \pm 270$	$59806 \pm 270$	$-1.77 \pm 0.32$

Table 7.2: The signal yields and raw asymmetries determined with the two-dimensional fitter, with the L0 LUT correction applied.

$p$ [GeV]	Magnet up			Magnet down		
	$D_s^- \mu^+$	$D_s^+ \mu^-$	$A_{\text{raw}}[\%]$	$D_s^- \mu^+$	$D_s^+ \mu^-$	$A_{\text{raw}}[\%]$
6 – 20	$8714 \pm 109$	$8699 \pm 106$	$0.09 \pm 0.87$	$12062 \pm 121$	$12518 \pm 123$	$-1.85 \pm 0.70$
20 – 30	$8629 \pm 104$	$8609 \pm 108$	$0.11 \pm 0.87$	$12243 \pm 122$	$12278 \pm 122$	$-0.14 \pm 0.70$
30 – 40	$6969 \pm 94$	$6858 \pm 97$	$0.81 \pm 0.98$	$9614 \pm 108$	$9768 \pm 107$	$-0.79 \pm 0.78$
40 – 50	$5091 \pm 79$	$4945 \pm 81$	$1.46 \pm 1.13$	$6975 \pm 95$	$7052 \pm 95$	$-0.54 \pm 0.95$
50 – 100	$10327 \pm 110$	$10127 \pm 109$	$0.98 \pm 0.76$	$14376 \pm 137$	$14116 \pm 131$	$0.91 \pm 0.67$
<b>Total</b>	$39730 \pm 223$	$39238 \pm 225$	$0.62 \pm 0.40$	$55270 \pm 263$	$55731 \pm 260$	$-0.42 \pm 0.33$
$p_T$ [GeV]						
1.2 – 1.5	$1296 \pm 42$	$1278 \pm 39$	$0.70 \pm 2.24$	$1757 \pm 47$	$1847 \pm 48$	$-2.48 \pm 1.85$
1.5 – 1.8	$2749 \pm 60$	$2786 \pm 61$	$-0.68 \pm 1.54$	$3940 \pm 70$	$3907 \pm 71$	$0.41 \pm 1.27$
1.8 – 2.1	$4687 \pm 78$	$4571 \pm 77$	$1.25 \pm 1.19$	$6402 \pm 88$	$6660 \pm 89$	$-1.97 \pm 0.95$
2.1 – 2.5	$4833 \pm 76$	$4810 \pm 80$	$0.24 \pm 1.14$	$6714 \pm 93$	$6726 \pm 90$	$-0.08 \pm 0.97$
2.5 – 3.0	$6175 \pm 89$	$6031 \pm 86$	$1.18 \pm 1.02$	$8532 \pm 106$	$8638 \pm 103$	$-0.61 \pm 0.86$
3.0 – 3.5	$4826 \pm 77$	$4787 \pm 84$	$0.41 \pm 1.19$	$6668 \pm 95$	$6718 \pm 90$	$-0.37 \pm 0.98$
3.5 – 6.8	$13176 \pm 126$	$12960 \pm 126$	$0.83 \pm 0.68$	$18310 \pm 149$	$18389 \pm 150$	$-0.21 \pm 0.57$
6.8 – 10.0	$2016 \pm 47$	$1990 \pm 47$	$0.64 \pm 1.68$	$2969 \pm 59$	$2833 \pm 57$	$2.34 \pm 1.44$
<b>Total</b>	$39757 \pm 222$	$39213 \pm 224$	$0.69 \pm 0.40$	$55293 \pm 264$	$55716 \pm 260$	$-0.38 \pm 0.33$

sistent with one another, indicating that the fitting procedure is relatively stable. Following the application of the LUT correction the charge asymmetry is reduced significantly. A residual raw asymmetry of approximately  $\pm 0.5\%$  is observed, with the same sign-dependence on the magnetic field polarity as is seen without the application of the LUT correction. In addition, the  $p_T$  dependence of the asymmetry is no longer observed.

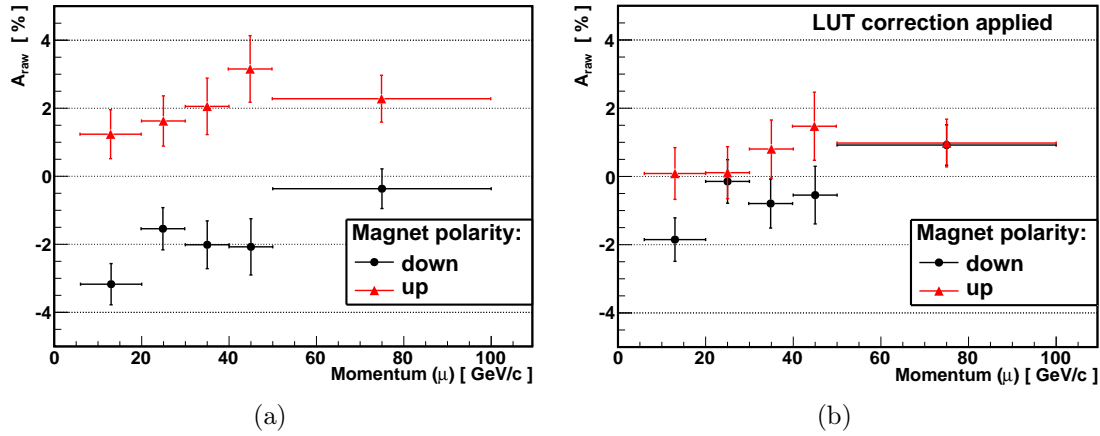


Figure 7.4: The raw charge asymmetry in signal data as a function of muon  $p$ , a) without and b) with the LUT correction.

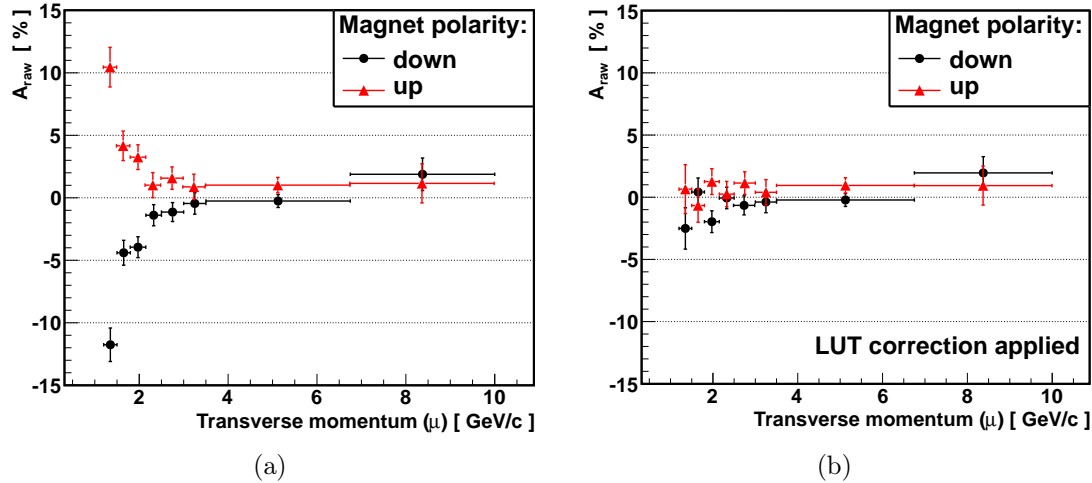


Figure 7.5: The raw charge asymmetry in signal data as a function of muon  $p_T$ , a) without and b) with the LUT correction.

### 7.1.2 Prompt component

The relative fractions of DfB and Prompt candidates have been determined using the two-dimensional fitting model described previously. The results are shown as a function of the muon candidate momentum in Table 7.3. The Prompt component constitutes approximately 1.5% of the  $D_s^-$  peak, showing little dependence on the magnetic field polarity or charge of the final state. The largest concentrations are found in samples with low muon momentum. The  $D_s^\pm$  production asymmetry has been measured at LHCb to be  $(-0.33 \pm 0.22 \pm 0.10)\%$  [114]. Thus the potential bias due to asymmetric Prompt production is expected to be of order  $\sim 10^{-4}$ . This is small compared to the statistical precision of this analysis. The fitting procedure can therefore be simplified by discarding the  $\log(\text{IP})$  component of the signal model, the sole purpose of which is to determine the Prompt signal contribution

(this background is still considered in Section 7.3.6, where corrections and systematic uncertainties associated to backgrounds are evaluated). Results presented in the remainder of this chapter use this simplified model, in which the data are fitted as a function of the  $D_s^-$  mass only.

Table 7.3: The fraction of the  $D_s^-$  peak attributed to the Prompt component.

$p$ [GeV]	Prompt component [%]			
	Magnet up		Magnet down	
	$D_s^- \mu^+$	$D_s^+ \mu^-$	$D_s^- \mu^+$	$D_s^+ \mu^-$
6–20	$1.8 \pm 0.3$	$2.4 \pm 0.3$	$1.6 \pm 0.2$	$1.7 \pm 0.2$
20–30	$1.6 \pm 0.2$	$1.3 \pm 0.2$	$1.1 \pm 0.2$	$1.5 \pm 0.2$
30–40	$1.5 \pm 0.2$	$0.9 \pm 0.2$	$1.2 \pm 0.2$	$1.0 \pm 0.2$
40–50	$1.1 \pm 0.2$	$0.8 \pm 0.2$	$1.2 \pm 0.2$	$1.4 \pm 0.2$
50–100	$1.0 \pm 0.2$	$1.0 \pm 0.2$	$1.1 \pm 0.1$	$1.1 \pm 0.1$
<b>Total</b>	$1.4 \pm 0.1$	$1.3 \pm 0.1$	$1.2 \pm 0.1$	$1.3 \pm 0.1$

### 7.1.3 Fitting consistency

The stability of data fitting is of particular importance for this analysis, as quirks in the fitting procedure may influence the relative data yields and induce a bias. The  $D_s^-$ -mass signal model described previously is based on previous studies of semileptonic  $B$ -decays at LHCb [115], for which both real and simulated data were investigated. The raw asymmetry has been investigated using several variations of this model. For the Detached background shape, first and second order Chebychev polynomials have been used. In addition, the shape of the Detached distribution has been studied over an extended mass range (ER) that encompasses the  $D^-$  peak. The ER is defined by the region between 160 MeV below and 80 MeV above the  $D_s^-$  mass. The  $D_s^-$  shape is fitted with both single and double gaussian functions.

The raw asymmetries obtained with these fitting variations are given as functions of the muon candidate  $p$  and  $p_T$  in Table 7.4. The choice of binning parameter should not change the measured raw asymmetry, as the data are selected such that the total number of candidates is identical in each of the  $p$  and  $p_T$  binning schemes. When using a single gaussian to model the  $D_s^-$  peak, the raw asymmetries obtained in each binning scheme are consistent with one another, irrespective of the background model or fitting range. An example of a fitted distribution using a single gaussian is shown in Figure 7.6. The data at the peak and in the tails (at approximately  $\pm 20$  MeV) of the  $D_s^-$  distribution are not well described by this model. Typical  $\chi^2$  per degree of freedom are in the range 2–4 and have  $p$ -values less than 0.01. Although these quality-of-fit parameters suggest this is a poor description of the data, for

Table 7.4: The raw asymmetry in % for several variations to the fitting model. The order of the polynomial used to describe the Detached background is shown on each row.

Model	Magnet up		Magnet down		Mean	
	$p$	$p_T$	$p$	$p_T$	$p$	$p_T$
Single-gaussian						
Poly(1 <sup>st</sup> )	$0.88 \pm 0.36$	$0.87 \pm 0.36$	$-0.68 \pm 0.30$	$-0.68 \pm 0.30$	0.10	0.10
Poly(2 <sup>nd</sup> )	$0.92 \pm 0.36$	$0.91 \pm 0.36$	$-0.68 \pm 0.31$	$-0.68 \pm 0.31$	0.12	0.12
ER : Poly(2 <sup>nd</sup> )	$0.89 \pm 0.36$	$0.88 \pm 0.36$	$-0.67 \pm 0.30$	$-0.68 \pm 0.30$	0.11	0.10
Double-gaussian						
Poly(1 <sup>st</sup> )	$0.70 \pm 0.35$	$0.80 \pm 0.35$	$-0.48 \pm 0.30$	$-0.45 \pm 0.30$	0.11	0.17
Poly(2 <sup>nd</sup> )	$0.65 \pm 0.36$	$0.96 \pm 0.36$	$-0.33 \pm 0.30$	$-0.51 \pm 0.30$	0.16	0.23
ER : Poly(2 <sup>nd</sup> )	$0.73 \pm 0.36$	$0.84 \pm 0.36$	$-0.44 \pm 0.30$	$-0.49 \pm 0.30$	0.15	0.17

this analysis it is the relative yield of  $D_s^+ \mu^-$  with respect to  $D_s^- \mu^+$  candidates that is of interest. The consistency of the fitted asymmetries therefore suggests that the single-gaussian model can be used effectively to determine the signal charge-asymmetry. However, this is only true if the shapes of the  $D_s^+$  and  $D_s^-$  tails do not differ significantly.

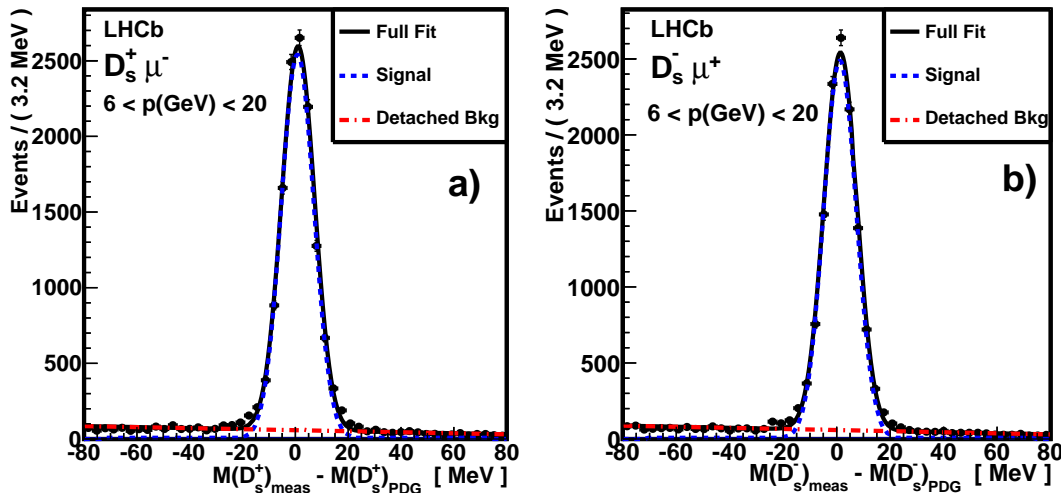


Figure 7.6: Fitted signal distributions for a)  $D_s^+ \mu^-$  and b)  $D_s^- \mu^+$  type candidates. A single gaussian and first order polynomial were used to model the  $D_s^-$  peak and Detached background data, respectively.

The raw asymmetries determined using double-gaussian models showed significant variations between the two binning schemes. Changes were also observed when using different background models. Examples of data distributions fitted with a double-gaussian shape are shown in Figures 7.7 and 7.8, over the regular and ER fitting ranges. Typical  $\chi^2$  per degree of freedom for each of these models are 0.8–1.2 and 0.7–0.9 respectively, with  $p$ -values distributed approximately evenly between 0 and 1. This suggests that these models describe the shape of the total dataset well. However, as is apparent when comparing Figures 7.7(a) and 7.7(b), the width of the wider gaussian component can vary significantly between  $D_s^+ \mu^-$  and  $D_s^- \mu^+$  data.

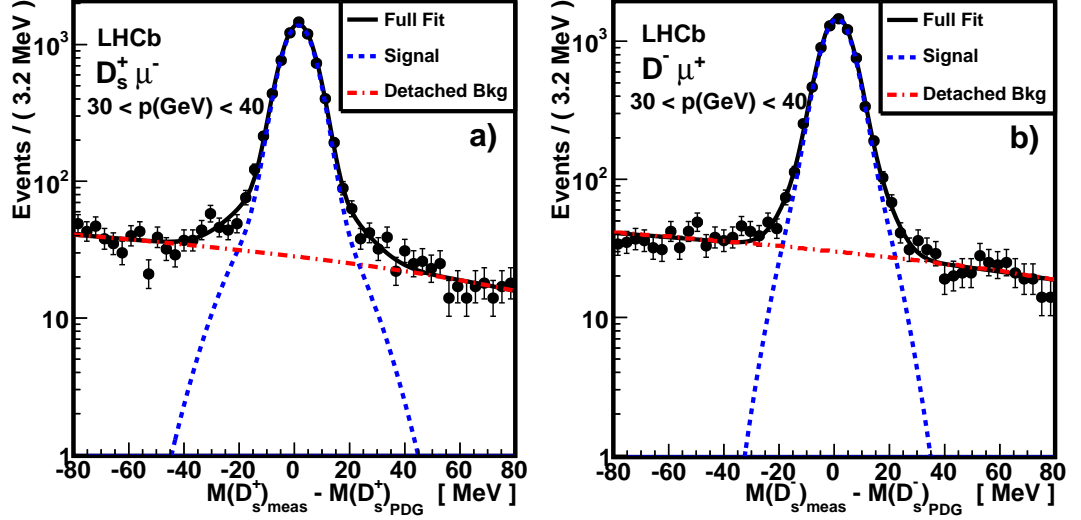


Figure 7.7: Fitted signal distributions for a)  $D_s^+ \mu^-$  and b)  $D_s^- \mu^+$  type candidates. A double gaussian and first-order polynomial were used to model the  $D_s^-$  peak and Detached background data. This particular fitted data-sample is chosen as it demonstrates a case in which the width of the wider gaussian component varies significantly between  $D_s^+ \mu^-$  and  $D_s^- \mu^+$  data.

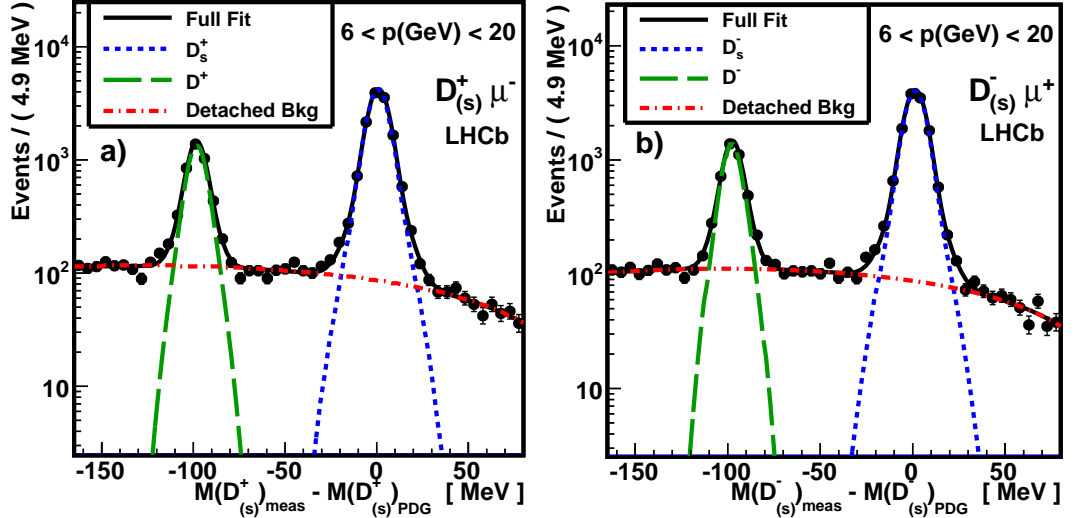


Figure 7.8: Fitted signal distributions for a)  $D_s^+ \mu^-$  and b)  $D_s^- \mu^+$  type candidates in the ER. A double gaussian and second-order polynomial were used to model the  $D_s^-$  peak and the Detached background.

Such large differences in the true signal shapes are not expected, and are potentially induced by statistical fluctuations in regions near to the tails of the  $D_s^-$  peak.

The width of the wider gaussian,  $\sigma_w$ , is constrained in the fitter to equal the width of the narrow gaussian,  $\sigma_n$ , multiplied by the width ratio,  $R$ , such that  $\sigma_w = \sigma_n R$ . The value of  $R$  has been fitted to the data and shows little dependence on magnetic field polarity, muon charge, muon momentum or transverse momentum, as shown in Figure 7.9. To prevent bias due to the  $D_s^+ \mu^-$  and  $D_s^- \mu^+$  having significantly different wide-gaussian widths, a simultaneous fit is performed to  $D_s^+ \mu^-$  and  $D_s^- \mu^+$

data, in which  $R$  is shared by the fits. All other fitting parameters are allowed to vary independently of one another. This is referred to as the shared width-ratio (SWR) constraint. The fitted raw asymmetries obtained with the SWR constraint are shown in Table 7.5.

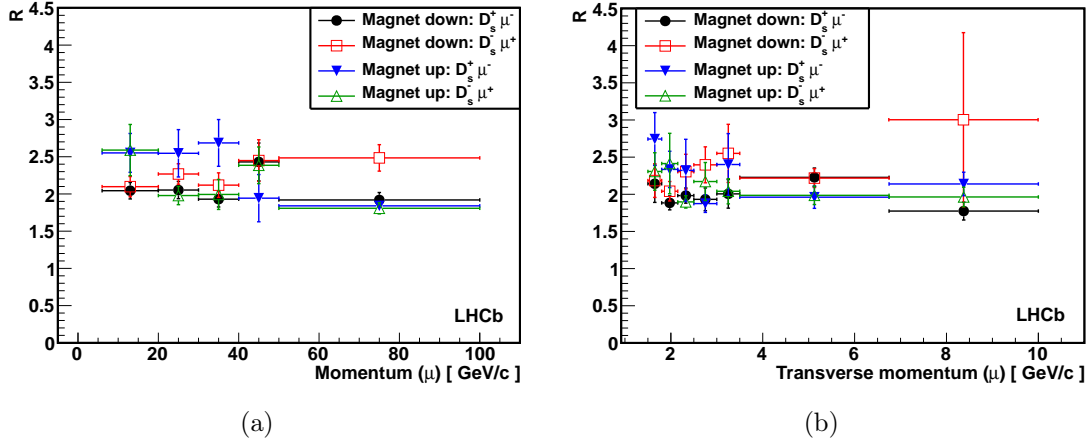


Figure 7.9: The wide to narrow gaussian-width ratio,  $R$ , versus the muon candidate **a)**  $p$  and **b)**  $p_T$ . For a particular magnetic field polarity, the value of  $R$  shows no significant dependence on the charge of the  $D_s^\pm \mu^\mp$ .

Table 7.5: The raw asymmetry in % when the SWR constraint is applied. The single-gaussian method is shown for reference. The order of the polynomial used to describe the Detached background is shown on each row.

Model	Magnet up		Magnet down		Mean	
	$p$	$p_T$	$p$	$p_T$	$p$	$p_T$
Single-gaussian						
Bkg – Poly(1 <sup>st</sup> )	$0.88 \pm 0.36$	$0.87 \pm 0.36$	$-0.68 \pm 0.30$	$-0.68 \pm 0.30$	0.10	0.10
Double-gaussian						
Poly(1 <sup>st</sup> ) – SWR	$0.88 \pm 0.35$	$0.86 \pm 0.35$	$-0.67 \pm 0.30$	$-0.67 \pm 0.30$	0.11	0.09
Poly(2 <sup>nd</sup> ) – SWR	$0.97 \pm 0.36$	$0.91 \pm 0.36$	$-0.75 \pm 0.30$	$-0.75 \pm 0.30$	0.11	0.08
ER : Poly(2 <sup>nd</sup> ) – SWR	$0.92 \pm 0.36$	$0.88 \pm 0.36$	$-0.70 \pm 0.30$	$-0.71 \pm 0.30$	0.11	0.08

Results from the various binning schemes and models are consistent with one another when using the SWR constraint, with differences in the mean asymmetry of up to 0.03% observed.

### 7.1.4 Kinematic binning

In Section 6.4 the kinematics of the calibration and signal samples were shown to not quite match. To suppress bias due to kinematic differences, data are analysed in three-dimensional bins defined by the properties of the muon candidate. Two such binning schemes have been used, each of which is sensitive to effects induced by the detector acceptance. The muon identification and triggering efficiencies were shown

to vary as a function  $p$ . Thus both binning schemes use five muon candidate  $p$  bins, defined by the thresholds: 6 – 20 – 30 – 40 – 50 – 100 GeV. The other two binning-dimensions divide the data into subsamples with sensitivity to the muon candidate  $p_T$  and track intercept location with the muon stations, to account for the large L0 trigger induced bias and acceptance effects. The two binning schemes are shown schematically in Figure 7.10. The first uses the  $x$  and  $y$  translational components of the muon momentum,  $p_x$  and  $p_y$ , to define 10 additional bins per momentum bin. The second uses the muon candidate  $p_T$  and azimuthal angle,  $\phi$ , which are defined at the  $B$ -meson decay vertex, to define 12 additional bins per momentum bin.

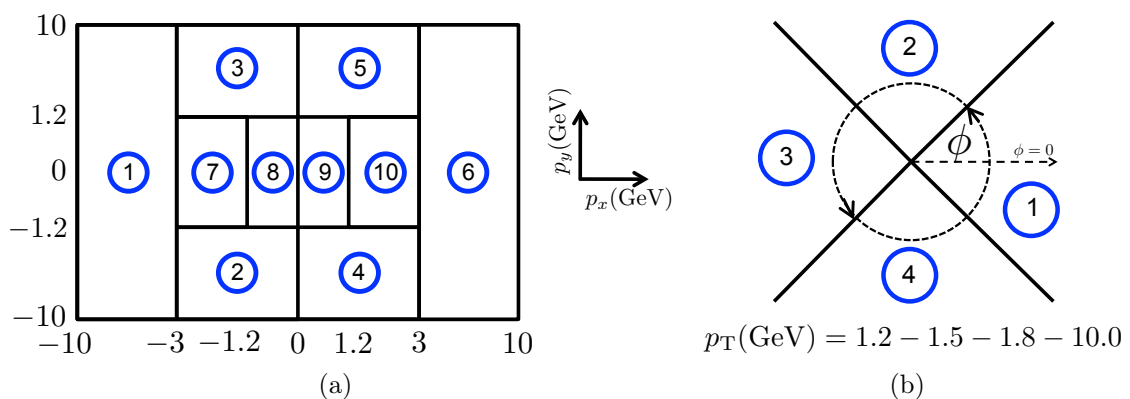


Figure 7.10: A schematic representation of **a)** the  $p$ - $p_x$ - $p_y$  and **b)** the  $p$ - $p_T$ - $\phi$  binning schemes.

The signal yields are determined in each of the three-dimensional data bins. This corresponds to 50 and 60 bins in the  $p$ - $p_x$ - $p_y$  and  $p$ - $p_T$ - $\phi$  binning schemes, per magnetic field polarity and type of final-state (i.e.  $D_s^- \mu^+$  or  $D_s^+ \mu^-$ ). The raw asymmetry in each binning scheme is then calculated by taking the mean of the measured asymmetries in each sub-bin, weighted by the uncertainty of each measurement.

In each three-dimensional sub-bin there are between about 50 and several thousand candidates. The fitting procedure must therefore be stable for data samples of widely varying size. It was shown in the previous section that when the SWR constraint is used the raw asymmetry changed by approximately 0.1% between  $p$  and  $p_T$  binning schemes. However, the averaged magnetic field polarity value changed by only 0.03%. The raw asymmetries obtained in each of the three-dimensional binning schemes are given for various fitting models in Table 7.6. The values obtained in each binning scheme vary substantially, with differences of over 0.5% observed. In addition, there are large differences between the results obtained using different Detached background models and fitting ranges.

The inconsistencies seen in Table 7.6 indicate that the signal models described in the previous section cannot be used to accurately determine the relative  $D_s^+ \mu^-$

Table 7.6: The raw asymmetry in % when using the three-dimensional binning schemes. The order of the polynomial used to describe the Detached background is shown on each row.

Model	Magnet up		Magnet down		Mean	
	$p_x - p_y$	$p_T - \phi$	$p_x - p_y$	$p_T - \phi$	$p_x - p_y$	$p_T - \phi$
Single-gaussian						
Bkg – Poly(1 <sup>st</sup> )	$0.88 \pm 0.37$	$1.32 \pm 0.36$	$-0.69 \pm 0.31$	$-1.09 \pm 0.31$	0.10	0.12
Double-gaussian						
Poly(1 <sup>st</sup> ) – SWR	$0.93 \pm 0.38$	$1.46 \pm 0.38$	$-0.65 \pm 0.31$	$-1.09 \pm 0.31$	0.14	0.30
Poly(2 <sup>nd</sup> ) – SWR	$0.92 \pm 0.41$	$1.48 \pm 0.41$	$-0.65 \pm 0.36$	$0.25 \pm 0.34$	0.14	0.86
ER : Poly(2 <sup>nd</sup> ) – SWR	$0.91 \pm 0.36$	$1.22 \pm 0.36$	$-0.73 \pm 0.31$	$-0.31 \pm 0.30$	0.09	0.46

and  $D_s^- \mu^+$  yields in the fine binning schemes. Figure 7.11 shows the fitted data in a particular  $p-p_x-p_y$  bin with low signal statistics. The shape of the fitted  $D_s^+ \mu^-$  peak is unlike that observed in the larger data samples. This is likely to have been caused by fluctuations in the Detached background near to the  $D_s^-$  peak, in combination with the low Detached yields in regions further away from the  $D_s^-$  resonance. In addition, a large charge asymmetry is observed between  $D_s^+ \mu^-$  and  $D_s^- \mu^+$ . These data contain candidates with low muon  $p_T$ , for which a larger fraction of candidates will traverse the central detector region. Thus, a large raw asymmetry is induced by acceptance effects related to the inactive beampipe region.

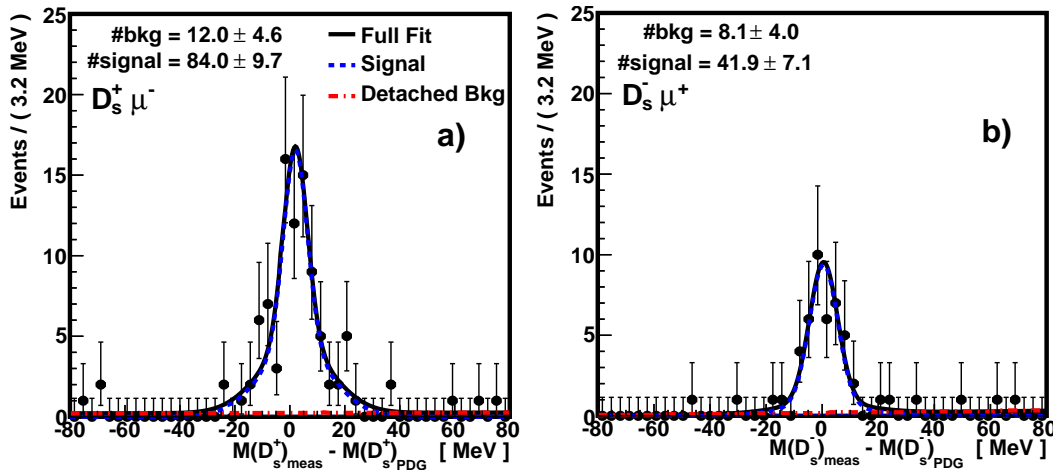


Figure 7.11: The fitted data from a particular  $p-p_x-p_y$  bin for a)  $D_s^+ \mu^-$  and b)  $D_s^- \mu^+$  type candidates. The binning dimensions are defined by  $[p, p_x, p_y] = [30 \rightarrow 40, -1.3 \rightarrow 0, -1.2 \rightarrow 1.2]$ . A double-gaussian  $D_s^-$  peak and first order Detached background model is used.

The fitted wide to narrow gaussian-width ratio,  $R$ , is shown in each of the  $p_x-p_y$  sub-bins in Figure 7.12, for several coarse bins in  $p$ . The sub-bin values of  $R$  show no strong dependence on sub-bin, although it is worth mentioning that  $R$  is correlated to other fitting parameters (such as  $f_n$ ) and so deviations are not unexpected. A constrained signal model is suggested to improve the stability of the fitting in data

bins with low signal yields. The data is first fitted in coarse bins of muon candidate  $p$ , which was shown to produce stable results in Section 7.1.3. The shape of the fitted  $D_s^-$  peak is then constrained in each  $p_x-p_y$  and  $p_T-\phi$  sub-bin, to that fitted in the coarser  $p$  bin. This approach is referred to as the constrained sub-bin (CSB) method. The parameters that are fixed to those found in the coarser bins are the ratio of wide to narrow gaussian-widths ( $R$ ) and the fraction of the  $D_s^-$  peak that is described by the narrower gaussian component ( $f_n$ ). All other parameters are allowed to vary in the fitting process.

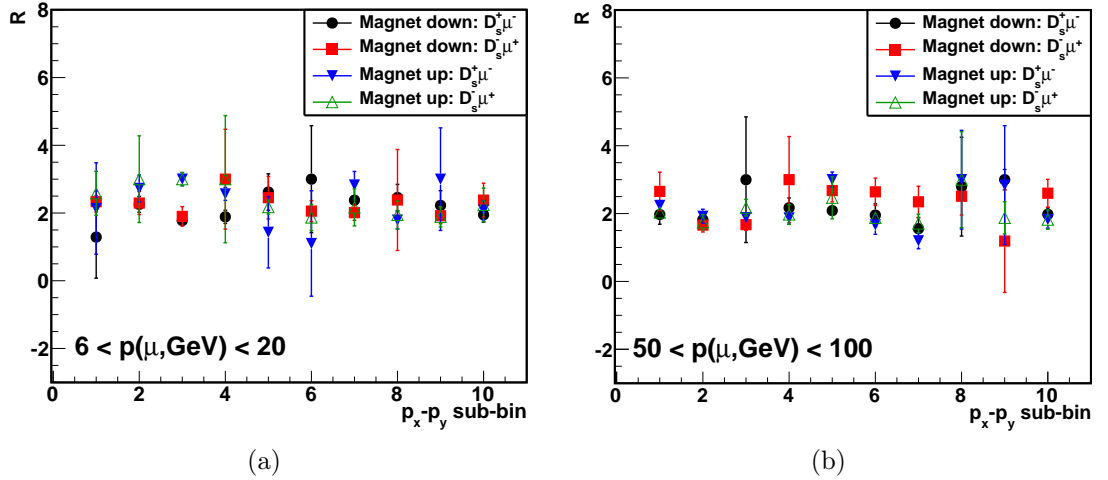


Figure 7.12: The wide to narrow gaussian-width ratio ( $R$ ) for the  $p_x-p_y$  sub-bins in the momentum range **a)** 6–20 GeV and **b)** 50–100 GeV.

The raw asymmetries obtained with the CSB method are given in Table 7.7. The results from the double-gaussian models with both first and second order Detached background shapes are consistent with one another and those found using unconstrained fitting models in the coarser binning schemes (see Table 7.5). The values vary by up to 0.08% for a particular magnetic field polarity, whereas the mean varies by only 0.04%. The results obtained using the extended fitting range still vary significantly between binning schemes. It appears that the larger number of free fitting parameters in this model leads to inconsistent results when fitting to data bins with low statistics.

### Reflected binning

The combination of the LHCb detector geometry and the magnetic field leads to large charge asymmetries in some of the kinematic sub-bins, as was seen in Figure 7.11. This is also shown in Figure 7.13(a), where asymmetries of up to  $\sim 50\%$  are seen in some of the 50  $p-p_x-p_y$  sub-bins. These large, acceptance induced asymmetries will mostly cancel when all of the kinematic bins are considered. For example, in a particular magnetic field polarity, the raw asymmetries in bins

Table 7.7: The raw asymmetry in % when using the three-dimensional binning schemes and CSB method. The unconstrained single-gaussian method is shown for reference. The order of the polynomial used to describe the Detached background is shown on each row.

Model	Magnet up		Magnet down		Mean	
Single-gaussian	$p_x-p_y$	$p_T-\phi$	$p_x-p_y$	$p_T-\phi$	$p_x-p_y$	$p_T-\phi$
Bkg – Poly(1 <sup>st</sup> )	$0.88 \pm 0.37$	$1.32 \pm 0.36$	$-0.69 \pm 0.31$	$-1.09 \pm 0.31$	0.10	0.12
Double-gaussian (CSB)						
Poly(1 <sup>st</sup> ) – SWR	$0.90 \pm 0.37$	$0.85 \pm 0.37$	$-0.66 \pm 0.31$	$-0.68 \pm 0.31$	0.12	0.09
Poly(2 <sup>nd</sup> ) – SWR	$0.89 \pm 0.38$	$0.90 \pm 0.38$	$-0.74 \pm 0.33$	$-0.66 \pm 0.31$	0.08	0.12
ER : Poly(2 <sup>nd</sup> ) – SWR	$1.27 \pm 0.36$	$1.32 \pm 0.36$	$-0.78 \pm 0.30$	$-0.52 \pm 0.30$	0.24	0.40

5 and 6 of Figure 7.13(a) have opposite sign and approximately equal magnitudes. In addition, if the values within a particular bin are averaged over both magnetic field polarities, the detector induced asymmetry will mostly cancel. However, if the fitted uncertainty of a measurement is calculated incorrectly, then the weighted mean will be biased towards the values with smaller uncertainties. Thus binning schemes with large initial raw asymmetries are sensitive to bias due to poor fitting.

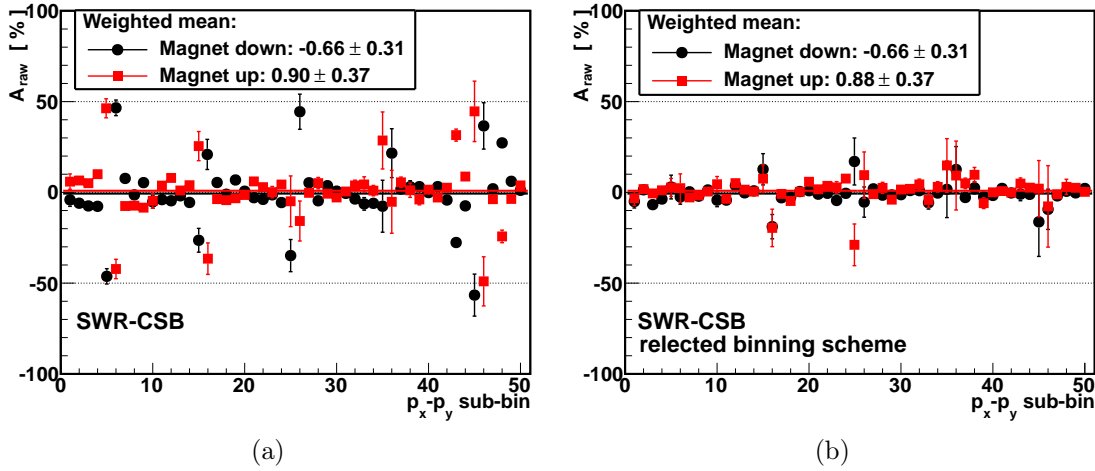


Figure 7.13: The  $p-p_x-p_y$  raw asymmetries when using a double-gaussian  $D_s^-$  peak model with first order Detached background and the SWF and CSB constraints, for **a)** the regular and **b)** the reflected binning schemes. The weighted averages of all  $p_x-p_y$  bins are shown by the solid horizontal lines.

An alternative way of binning the data is to use a *reflected* binning scheme, where the signal yields of one charge are compared to those of the other charge in the bin that is reflected about the  $p_y$ -axis. With reference to the  $p-p_x-p_y$  binning schematic in Figure 7.10, this corresponds to the comparison of the positively charge muon candidates in bin numbers 1, 2, 3, 7 and 8 with the negatively charged candidates in bin numbers 6, 4, 5, 10 and 9, respectively. For the  $p-p_T-\phi$  binning scheme the muon candidates of one charge in bin number 1 are compared to those of the opposite charge in bin number 3.

The raw asymmetries obtained when adopting the reflected scheme are shown in Figure 7.13(b), where deviations from the mean are significantly reduced compared to the regular binning scheme. The raw asymmetries obtained when using the reflected scheme are given in Table 7.8. Excellent agreement is found between the different binning schemes and fitting models. Observed variations in the weighted mean are less than 0.06%, even when using the previously inconsistent ER model.

Table 7.8: The raw asymmetry in % when using the three-dimensional reflected binning schemes. The order of the polynomial used to describe the Detached background is shown on each row.

Model	Magnet up		Magnet down		Mean	
	$p_x - p_y$	$p_T - \phi$	$p_x - p_y$	$p_T - \phi$	$p_x - p_y$	$p_T - \phi$
Single-gaussian						
Bkg – Poly(1 <sup>st</sup> )	$0.87 \pm 0.38$	$0.88 \pm 0.37$	$-0.68 \pm 0.32$	$-0.69 \pm 0.32$	0.10	0.10
Double-gaussian (CBS)						
Poly(1 <sup>st</sup> ) – SWR	$0.88 \pm 0.37$	$0.89 \pm 0.37$	$-0.66 \pm 0.31$	$-0.67 \pm 0.31$	0.11	0.11
Poly(2 <sup>nd</sup> ) – SWR	$0.95 \pm 0.39$	$0.99 \pm 0.39$	$-0.75 \pm 0.33$	$-0.79 \pm 0.33$	0.10	0.10
ER : Poly(2 <sup>nd</sup> ) – SWR	$0.95 \pm 0.36$	$0.90 \pm 0.36$	$-0.65 \pm 0.27$	$-0.59 \pm 0.30$	0.15	0.15

The model used to determine the signal yields with which  $a_{\text{fs}}^s$  is measured in the following section is the double-gaussian  $D_s^-$  peak with a first order Detached background. This is the simplest model that describes the data well and has also been shown to provide consistent results. Both the SWR and CSB constraints are used to aid fit stability. The reflected binning scheme is used to protect from bias associated to poor fit quality.

## 7.2 The measured asymmetry

In the previous sections it was shown that the signal yields and muon selection efficiencies can be accurately determined. With these ingredients, the measured asymmetry is calculated in each of the kinematic sub-bins, using Equation 6.22. The tracking and background corrections ( $A_{\mu\pi}^{\text{track}}$  and  $A_b$ ) are temporarily neglected. These are small compared to the muon corrections and are discussed independently in Section 7.3. The sub-bin boundaries are modified slightly from those described in Section 7.1.4, with muons of  $p_T$  below 1.5 GeV excluded from the analysis. This reduces the dataset by only a few percent and removes the data that are most significantly biased by the L0 muon trigger. The revised binning schemes are shown schematically in Figure 7.14.

Two methods have been used to correct for muon-selection induced bias. In the first, the LUT correction is not applied and the muon selection efficiencies alone are used to correct bias. With this approach the data must be divided into fine kinematic bins at low muon candidate  $p_T$ , as it is in this region that the L0 trigger bias is largest.

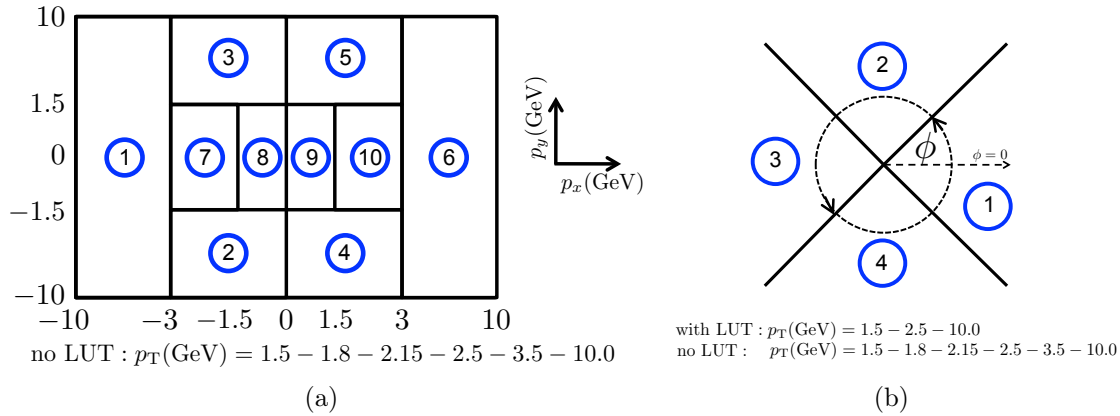


Figure 7.14: The revised data binning thresholds. **a)** The  $p$ - $p_x$ - $p_y$  scheme. When the LUT correction is not applied, muon efficiencies are determined in additional bins of  $p_T$ . **b)** The  $p$ - $p_T$ - $\phi$  scheme. There are two sets of  $p_T$  bin thresholds, the finer of which is used when the LUT correction is not applied. Both schemes also have five bin of  $p$  defined by the thresholds: 6 – 20 – 30 – 40 – 50 – 100 GeV.

With the  $p$ - $p_T$ - $\phi$  binning scheme this is simply achieved by measuring the signal yields and muon selection efficiencies in fine bins of  $p_T$ , resulting in 100 sub-bins per magnetic field polarity. For the  $p$ - $p_x$ - $p_y$  scheme, a fourth dimension is required. In addition to the bins of  $p$ ,  $p_x$  and  $p_y$ , the muon selection efficiencies are measured in bins of  $p_T$ , for which the binning thresholds are shown in Figure 7.14(a). Only the muon selection efficiencies are measured in this additional dimension, which is possible due to the large calibration sample statistics. The signal data yields are measured in only the 50  $p$ - $p_x$ - $p_y$  sub-bins. The  $p_T$  distribution of the  $D_s^-$  peak candidates (defined as those that are within  $\pm 20$  MeV of the  $D_s^-$  mass) is then used to determine the fraction of signal in each of the additional  $p_T$  sub-bins.

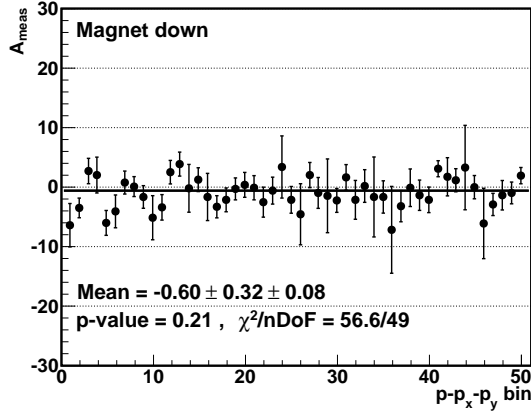
In the second method the LUT correction is applied to both the signal and KS calibration samples. The sensitivity to detector bias at low  $p_T$  is reduced and coarser data binning can be used. In the  $p$ - $p_x$ - $p_y$  binning scheme the additional  $p_T$  dimension is not needed and the signal yields and muon efficiencies are determined in the regular 50 sub-bins. For the  $p$ - $p_T$ - $\phi$  binning scheme a coarser  $p_T$  binning is used, resulting in a total of 40 sub-bins. The raw asymmetry obtained in each analysis strategy is given both before and after the application of the LUT correction in Table 7.9. Results obtained in each binning scheme are consistent with one another.

The measured asymmetry,  $A_{\text{meas}}$ , is determined in each of the three-dimensional sub-bins. The total measured asymmetry is calculated by taking the mean of all sub-bin results, weighted to the uncertainty of each measurement. The results obtained when using the MS calibration sample (without the LUT correction) are shown in Figure 7.15. For each binning scheme and magnet polarity, the various sub-bin measurements are found to be statistically compatible with the weighted mean.

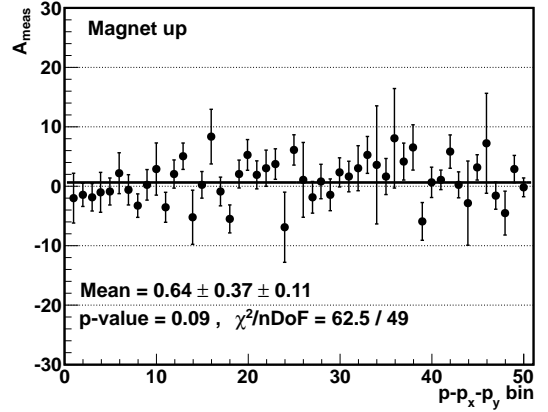
The measured asymmetries are consistent with having no dependence on the

Table 7.9: The raw asymmetries with the revised binning schemes, both with and without the LUT correction. The raw asymmetries obtained in coarse bins of  $p$  and  $p_T$  are also shown for comparison.

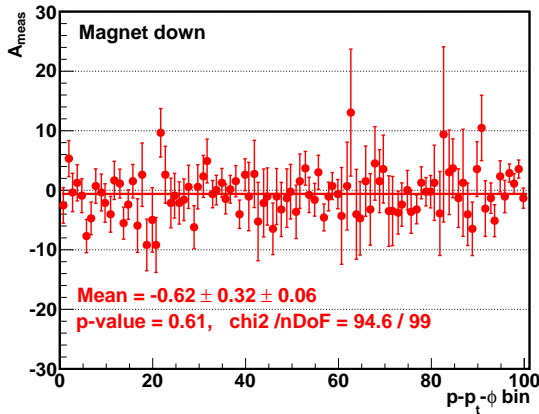
Binning scheme	Raw asymmetry [%]		
	Magnet down	Magnet up	Arithmetic mean
<hr/>			
L0 uncorrected			
$p$	$-1.57 \pm 0.30$	$1.79 \pm 0.35$	$0.11 \pm 0.23$
$p_T$	$-1.58 \pm 0.30$	$1.77 \pm 0.35$	$0.09 \pm 0.23$
$p-p_x-p_y$	$-1.56 \pm 0.31$	$1.78 \pm 0.37$	$0.11 \pm 0.24$
$p-p_T-\phi$	$-1.57 \pm 0.31$	$1.79 \pm 0.37$	$0.11 \pm 0.24$
<hr/>			
L0 corrected			
$p$	$-0.59 \pm 0.30$	$0.93 \pm 0.36$	$0.17 \pm 0.24$
$p_T$	$-0.60 \pm 0.30$	$0.90 \pm 0.36$	$0.15 \pm 0.24$
$p-p_x-p_y$	$-0.58 \pm 0.32$	$0.94 \pm 0.38$	$0.17 \pm 0.25$
$p-p_T-\phi$	$-0.58 \pm 0.32$	$0.93 \pm 0.38$	$0.17 \pm 0.25$



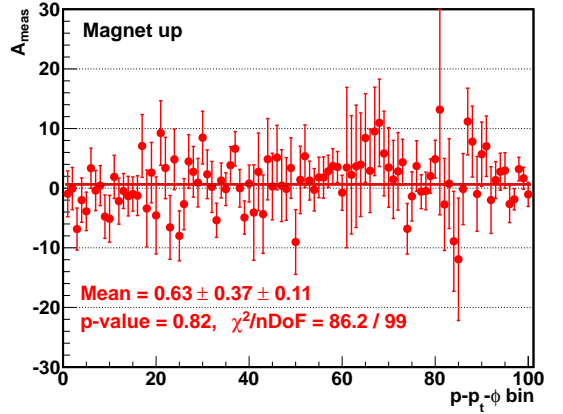
(a)



(b)



(c)



(d)

Figure 7.15: The measured asymmetry in each sub-bin of the  $p-p_x-p_y$  binning scheme is shown for **a)** magnet down and **b)** magnet up polarity data. The  $p-p_T-\phi$  binning scheme results are shown for **c)** magnet down and **d)** magnet up polarity data. A horizontal fit (the weighted average) to the sub-bins is shown by a solid line. The quality-of-fit parameters and fitted results are displayed on each figure.

momentum of the muon candidate, as shown in Figure 7.16. The results obtained in each momentum bin are also consistent when using different binning strategies and muon calibration samples. The total measured asymmetries from each magnetic field polarity are summarised in Table 7.10. The results from the different magnetic field polarities are inconsistent with one another at the confidence level of approximately 2.5 standard deviations. This could simply be a statistical fluctuation; however, it may be an indication of residual detector bias.

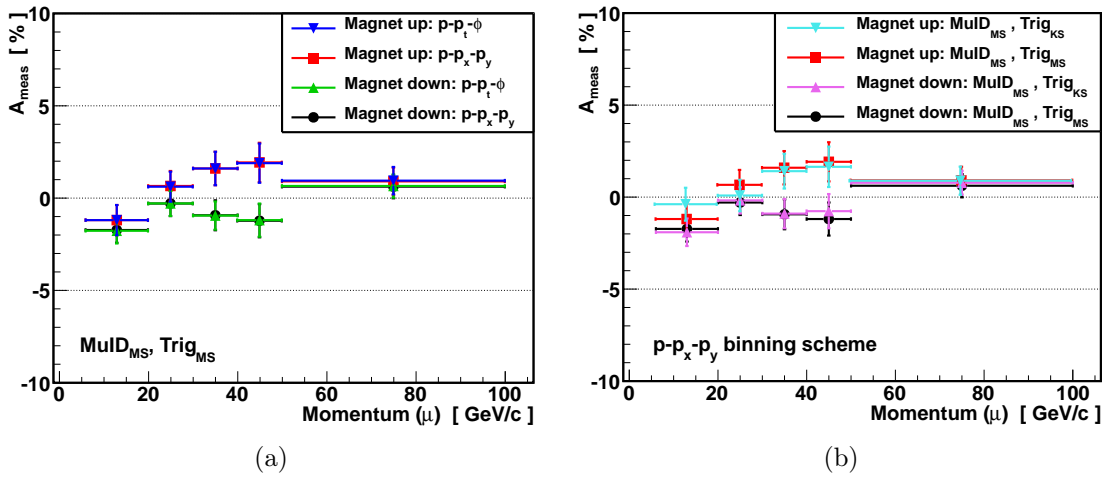


Figure 7.16: The measured asymmetry as a function of the muon candidate momentum for a) the two binning schemes and b) the two muon calibration samples used to correct trigger induced bias. In b), the labels “Trig<sub>KS</sub>” and “Trig<sub>MS</sub>” identify which calibration sample is used, and correspond to measurements for which the L0 LUT correction is and is not applied, respectively.

Table 7.10: The measured asymmetry for each magnetic field polarity and their arithmetic mean. The MuID corrections used in all measurements are obtained with the MS sample. The calibration sample that has been used to correct trigger bias is labelled on each row. The first uncertainty is due to the signal statistics and the second is due to the statistics of the muon calibration samples.

Binning scheme	Measured asymmetry [%]		
	Magnet down	Magnet up	Arithmetic mean
<hr/>			
L0 uncorrected			
MS: $p-p_x-p_y$	$-0.60 \pm 0.32 \pm 0.08$	$0.64 \pm 0.37 \pm 0.11$	$0.02 \pm 0.24 \pm 0.07$
MS: $p-p_T-\phi$	$-0.62 \pm 0.32 \pm 0.06$	$0.63 \pm 0.37 \pm 0.11$	$0.01 \pm 0.24 \pm 0.06$
KS: $p-p_x-p_y$	$-0.59 \pm 0.32 \pm 0.09$	$0.59 \pm 0.37 \pm 0.13$	$0.00 \pm 0.24 \pm 0.08$
KS: $p-p_T-\phi$	$-0.61 \pm 0.32 \pm 0.09$	$0.61 \pm 0.37 \pm 0.13$	$0.00 \pm 0.24 \pm 0.08$
<hr/>			
L0 corrected			
KS: $p-p_x-p_y$	$-0.48 \pm 0.32 \pm 0.11$	$0.62 \pm 0.38 \pm 0.13$	$0.07 \pm 0.25 \pm 0.09$
KS: $p-p_T-\phi$	$-0.52 \pm 0.32 \pm 0.11$	$0.57 \pm 0.38 \pm 0.13$	$0.02 \pm 0.25 \pm 0.09$

The statistical power of the data sample is maximised by taking the weighted average of the results obtained with each magnet polarity. However, a larger fraction

of data was collected with magnet down polarity, giving greater weight to the result obtained with this polarity. The weighted average is therefore sensitive to residual asymmetries. To err on the side of caution, the final result is obtained by taking the arithmetic mean of results from each magnetic field polarity, in order to cancel potential residual bias. The mean varies by only 0.07% when using different binning schemes and muon calibration samples. A systematic uncertainty of 0.04% is assigned (approximately half the observed variation) due to the imperfect kinematic matching of the calibration and signal muons.

The largest source of detector asymmetry that has been identified is from the L0 muon trigger, which was seen to vary strongly with the  $p_T$  of the muon candidate. The measured asymmetry, however, shows no significant dependence on muon candidate  $p_T$ , as shown in Figure 7.17. This suggests that if there is a residual detector bias, it is unlikely to have been induced by the L0 muon trigger. This statement is further supported by the good agreement between results obtained with and without the application of the LUT correction. Additional systematic studies and further corrections to the measured asymmetry are discussed in the following sections.

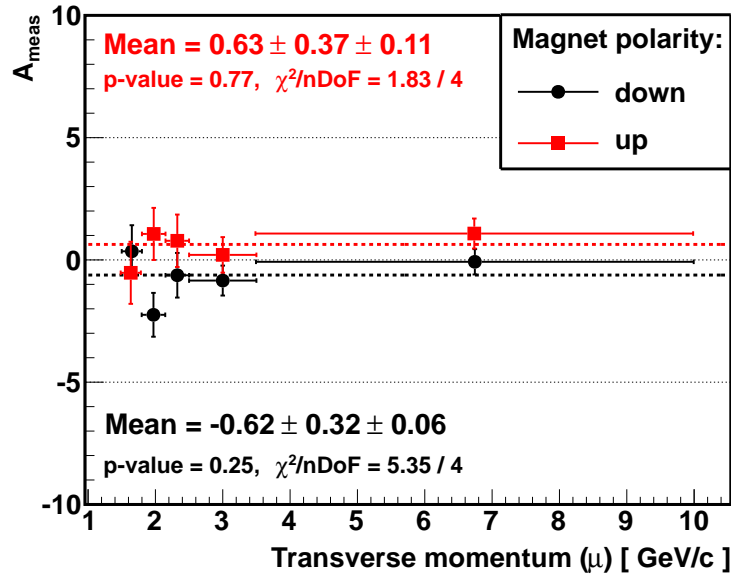


Figure 7.17: The measured asymmetry as a function of the muon candidate  $p_T$ , when the MS sample is used in the  $p$ - $p_T$ - $\phi$  binning scheme without the LUT correction applied. A horizontal fit (equal to the weighted average) to both the magnetic field up and down polarity results is shown by the dashed lines. The corresponding fit parameters are displayed on the figure.

## 7.3 Systematic studies and further corrections

Various systematic studies have been performed as cross-checks of the measured asymmetries presented in the previous section. In addition to these tests, the cor-

rections associated to pion and muon tracking bias, and background induced asymmetries are given.

### 7.3.1 Data fitting models

Data fitting is a crucial aspect of this analysis, for determining both the signal yields and the muon selection efficiencies. The model used to describe the signal was discussed in detail in Section 7.1. A systematic uncertainty of 0.05% is assigned to the signal fitting procedure. This is based on the raw asymmetry variations seen between different binning schemes and signal models in Tables 7.5 and 7.8, and those seen for the final fits used to determine  $a_{\text{fs}}^s$  in Table 7.9.

The fitting model used to determine the muon selection efficiencies via the tag and probe method was chosen based on that used in previous  $J/\psi$  analyses at LHCb [108], and by choosing a parameterisation that gives good fitting stability and quality-of-fit. The nominal fitting model comprises a double Crystal Ball (CB) function<sup>1</sup> with a first order background shape. The two CB's have independent means and widths, with a shared value of the  $\alpha$  parameter, and the  $n$  parameter fixed to equal 1. Variations to this model have very little influence on the measured asymmetry, as shown by Table 7.11. Models in which: a single CB is used, the two CB's have a common mean, and where the CB has  $n = 5$  (which forces the distribution to have a larger radiative tail component) have been investigated. Each of these variations leave the mean measured asymmetry unchanged, despite worsening the quality-of-fit parameters significantly. The background ‘‘counting method’’ described in Section 6.4.4 has also been used, for which the background shape in the signal region is estimated using the data sidebands. This makes no assumption about the signal peak shape. Even with this simple model, the central value changes by only 0.01%. The measured asymmetry has shown no significant dependence on the fitting model, therefore no systematic uncertainty is assigned.

Table 7.11: The measured asymmetry for various fitting methods using the MS sample in the  $p-p_{\text{T}}-\phi$  binning scheme, without the application of the LUT correction.

Fitting model	Measured asymmetry [%]		
	Magnet down	Magnet up	Arithmetic mean
Nominal	$-0.62 \pm 0.32 \pm 0.06$	$0.63 \pm 0.37 \pm 0.11$	$0.01 \pm 0.24 \pm 0.06$
Single CB	$-0.62 \pm 0.32 \pm 0.06$	$0.64 \pm 0.37 \pm 0.11$	$0.01 \pm 0.24 \pm 0.06$
Shared CB mean	$-0.62 \pm 0.32 \pm 0.06$	$0.63 \pm 0.37 \pm 0.11$	$0.01 \pm 0.24 \pm 0.06$
$n(\text{CB}) = 5$	$-0.62 \pm 0.32 \pm 0.06$	$0.63 \pm 0.37 \pm 0.11$	$0.01 \pm 0.24 \pm 0.06$
‘‘Counting method’’	$-0.57 \pm 0.32 \pm 0.07$	$0.60 \pm 0.37 \pm 0.12$	$0.02 \pm 0.24 \pm 0.07$

<sup>1</sup>The CB parameterisation is described in Section 6.4.4.

### 7.3.2 Fiducial selection

It was shown in Section 6.4.3 that there are regions of muon phase-space with large, acceptance-induced charge asymmetries, which mostly cancel when the entire muon phase-space is considered. Fiducial selections can be applied to exclude these regions. Similar selections can be applied to the pion candidate, the criteria of which are listed in Table 7.12, and were determined in studies described in Ref. [113]. To investigate potential residual bias due to this effect, the measured asymmetry is determined following various combinations of the fiducial selections. The findings are given in Table 7.13. The change in the mean measured asymmetry is of similar magnitude to the systematic uncertainty assigned to the signal yield fitting procedure (0.05%), which must be repeated following each fiducial selection. As such, no systematic uncertainty is assigned due to fiducial effects.

Table 7.12: The pion candidate fiducial selection (with momentum components in units of MeV).

Detector region	Selection
Beampipe (if $ p_y/p_z  \leq 0.02$ )	$ p_x  \geq (418 - 0.01397 \times p_z)$ $ p_x  \leq (497 + 0.01605 \times p_z)$
Outer region	$ p_x  \leq 0.317 \times (p_z - 2400)$

Table 7.13: The measured asymmetry for various fiducial selections using the MS sample in the  $p$ - $p_T$ - $\phi$  binning scheme (without the LUT correction). The beampipe excluded selection (BPE) requires that the muon and pion candidates have  $|p_y/p_z| > 0.02$ , to remove particles that could traverse the inactive beampipe region.

Fiducial selection	Statistical reduction [%]	Measured asymmetry [%]		
		Magnet down	Magnet up	Mean
Nominal	–	$-0.62 \pm 0.32$	$0.63 \pm 0.38$	$0.01 \pm 0.25$
Muons	1.5	$-0.64 \pm 0.32$	$0.60 \pm 0.38$	$-0.02 \pm 0.25$
Muons+Pions	15.6	$-0.58 \pm 0.35$	$0.50 \pm 0.41$	$-0.04 \pm 0.27$
Muons+Pions+BPE	32.8	$-0.60 \pm 0.39$	$0.70 \pm 0.46$	$0.05 \pm 0.30$

### 7.3.3 HLT2 trigger categories

The muon corrections account for only L0 and HLT1 induced bias. At the HLT2 level the signal data are selected by the logical OR of the inclusive- $\phi$  trigger line and the three topological-muon trigger lines. The topological trigger was discussed in Section 6.5, with potential bias found to be less than  $10^{-3}$  at the 68% confidence level. As approximately half the data is exclusively selected by these triggers, a systematic uncertainty of 0.05% is assigned.

Due to the similar kinematic spectra of  $K^\pm$  (shown in Section 6.3), it is assumed that the inclusive- $\phi$  trigger does not introduce a charge bias. To test this assumption, the data has been analysed in two statistically independent sub-samples which are defined by the HLT2 trigger decisions. The first sample, referred to as ‘‘MuTopo’’, is TOS in one of the topological lines and not-TOS in the inclusive- $\phi$  line. This sample comprises approximately 57% of the total data. The second sample, referred to as ‘‘InclPhi’’, comprises data that is TOS in the inclusive- $\phi$  line. The raw and measured asymmetries in each of these trigger sub-categories are given in Tables 7.14 and 7.15. The results obtained in each sample are statistically compatible with one another, suggesting that there is no significant bias introduced by the HLT2 triggers. Both samples exhibit a negative and positive asymmetry for magnetic field down and up polarity data, as that was observed for the full data sample in Section 7.2.

Table 7.14: The raw asymmetry in each of the HLT2 trigger sub-categories.

Binning scheme	Raw asymmetry [%]					
	HLT2(MuTopo)			HLT2(InclPhi)		
	Magnet down	Magnet up	Mean	Magnet down	Magnet up	Mean
L0 uncorrected						
$p-p_x-p_y$	$-1.29 \pm 0.41$	$1.50 \pm 0.49$	$0.11 \pm 0.32$	$-1.89 \pm 0.48$	$2.18 \pm 0.56$	$0.14 \pm 0.37$
$p-p_T-\phi$	$-1.29 \pm 0.41$	$1.48 \pm 0.47$	$0.10 \pm 0.31$	$-1.90 \pm 0.48$	$2.22 \pm 0.56$	$0.16 \pm 0.37$
L0 corrected						
$p-p_x-p_y$	$-0.34 \pm 0.42$	$0.66 \pm 0.50$	$0.16 \pm 0.33$	$-0.87 \pm 0.49$	$1.27 \pm 0.57$	$0.20 \pm 0.38$
$p-p_T-\phi$	$-0.33 \pm 0.42$	$0.67 \pm 0.50$	$0.17 \pm 0.33$	$-0.88 \pm 0.49$	$1.26 \pm 0.57$	$0.19 \pm 0.38$

Table 7.15: The measured asymmetry in each of the HLT2 trigger sub-categories. The quoted uncertainty is equal to the uncertainty due to signal statistics and muon selection efficiencies added in quadrature.

Binning scheme	Measured asymmetry [%]					
	HLT2(MuTopo)			HLT2(InclPhi)		
	Magnet down	Magnet up	Mean	Magnet down	Magnet up	Mean
L0 uncorrected						
MS: $p-p_x-p_y$	$-0.41 \pm 0.42$	$0.37 \pm 0.50$	$-0.02 \pm 0.33$	$-0.82 \pm 0.49$	$0.94 \pm 0.57$	$0.06 \pm 0.37$
MS: $p-p_T-\phi$	$-0.41 \pm 0.42$	$0.37 \pm 0.50$	$-0.02 \pm 0.33$	$-0.83 \pm 0.48$	$0.97 \pm 0.57$	$0.07 \pm 0.37$
KS: $p-p_x-p_y$	$-0.39 \pm 0.42$	$0.31 \pm 0.51$	$-0.04 \pm 0.33$	$-0.83 \pm 0.49$	$0.89 \pm 0.57$	$0.03 \pm 0.38$
KS: $p-p_T-\phi$	$-0.39 \pm 0.42$	$0.32 \pm 0.51$	$-0.04 \pm 0.33$	$-0.85 \pm 0.49$	$0.95 \pm 0.57$	$0.05 \pm 0.38$
L0 corrected						
KS: $p-p_x-p_y$	$-0.26 \pm 0.43$	$0.33 \pm 0.52$	$0.04 \pm 0.34$	$-0.78 \pm 0.50$	$0.96 \pm 0.59$	$0.09 \pm 0.39$
KS: $p-p_T-\phi$	$-0.28 \pm 0.44$	$0.30 \pm 0.52$	$0.01 \pm 0.34$	$-0.83 \pm 0.50$	$0.89 \pm 0.59$	$0.03 \pm 0.39$

### 7.3.4 Stability over time

The measured asymmetry has been investigated as a function of the time at which the data were collected. Data are collected in ‘‘runs’’, each of which is assigned a unique number. The signal yields are shown as a function of run number in Figure 7.18. Six run ‘‘blocks’’ are defined, corresponding to data collected with each

of the magnetic field polarities at the beginning, middle and end of 2011. The raw and measured asymmetries are shown in Figures 7.19(a) and 7.19(b) for the total data sample (known as “OrHlt2”) and the two HLT2 sub-categories. There is no evidence of a time-dependent bias, with measurements from different run blocks statistically compatible with one another.

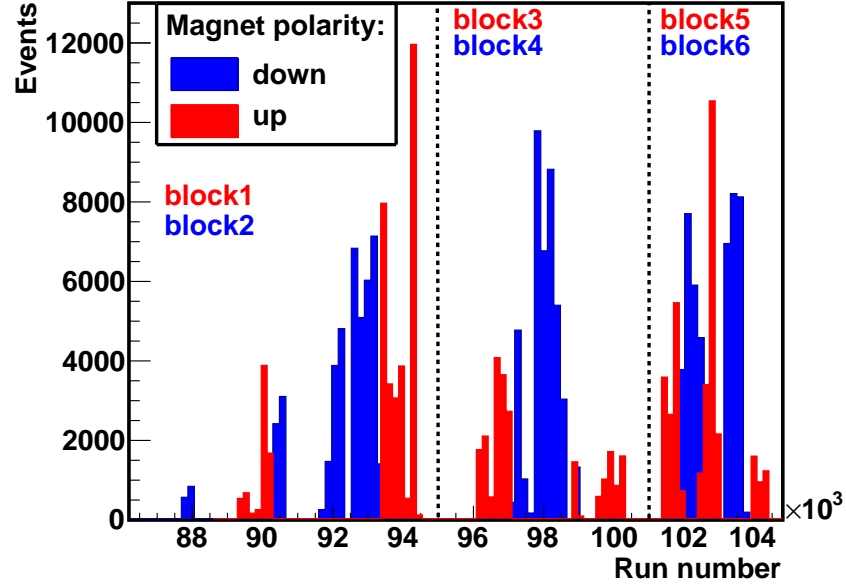


Figure 7.18: The yield of signal data versus run number. The run number block boundaries are divided by the vertical black dashed lines.

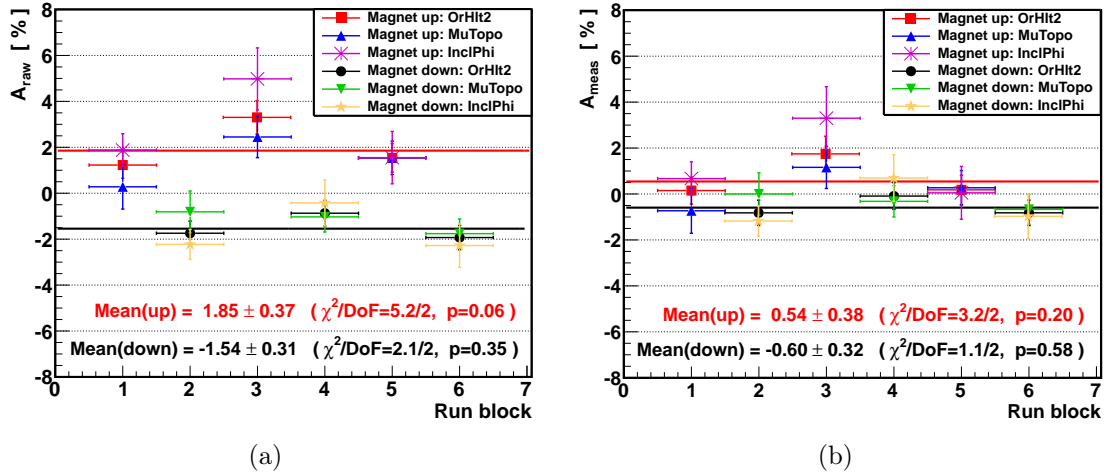


Figure 7.19: The a) raw and b) measured asymmetry as a function of run block.

### 7.3.5 Raw asymmetries

The measured asymmetries from each magnetic field polarity are incompatible with one another at the level of 2.5 standard deviations (see Table 7.10). That the

magnitudes of each asymmetry are approximately equal and of opposite charge is indicative of a residual detector bias. The source of residual bias is further investigated by measuring the raw asymmetry as a function of various event parameters. For the plots shown in this section, the LUT correction has been applied to better observe the raw asymmetries in the absence of the large L0 muon effect.

The raw asymmetry is shown as a function of the SS-kaon and pion kinematics in Figure 7.20. The raw asymmetry has also been found as a function of the  $B_s^\pm$ -candidate ( $D_s^\mp \mu^\pm$ ) kinematics, as shown in Figure 7.21. In the same figure the raw asymmetry is shown as a function of the event multiplicity, which is defined as the total number of long tracks in the event. No obvious source of selection induced bias is apparent from these cross-checks.

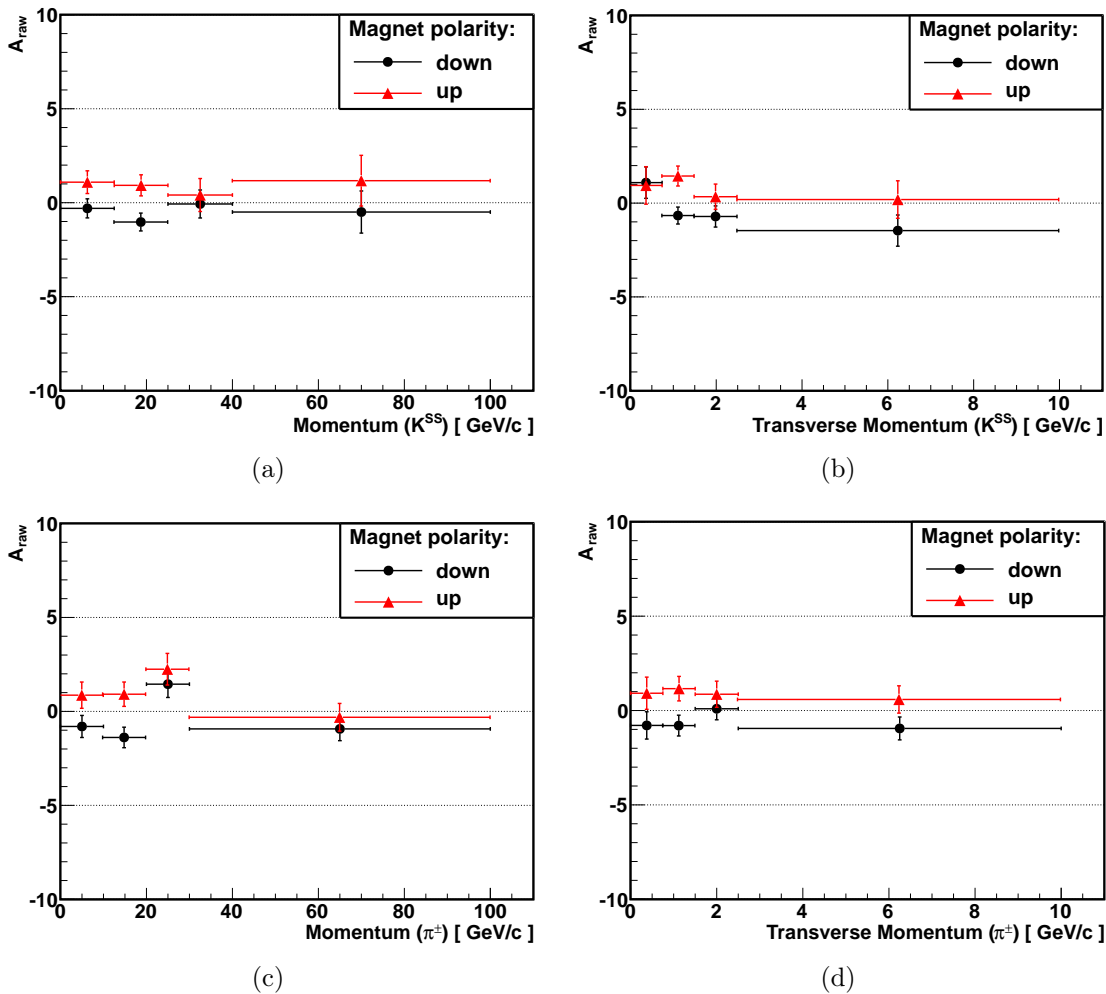


Figure 7.20: The raw asymmetry as a function of the SS kaon a)  $p$  and b)  $p_T$ , and the pion c)  $p$  and d)  $p_T$ .

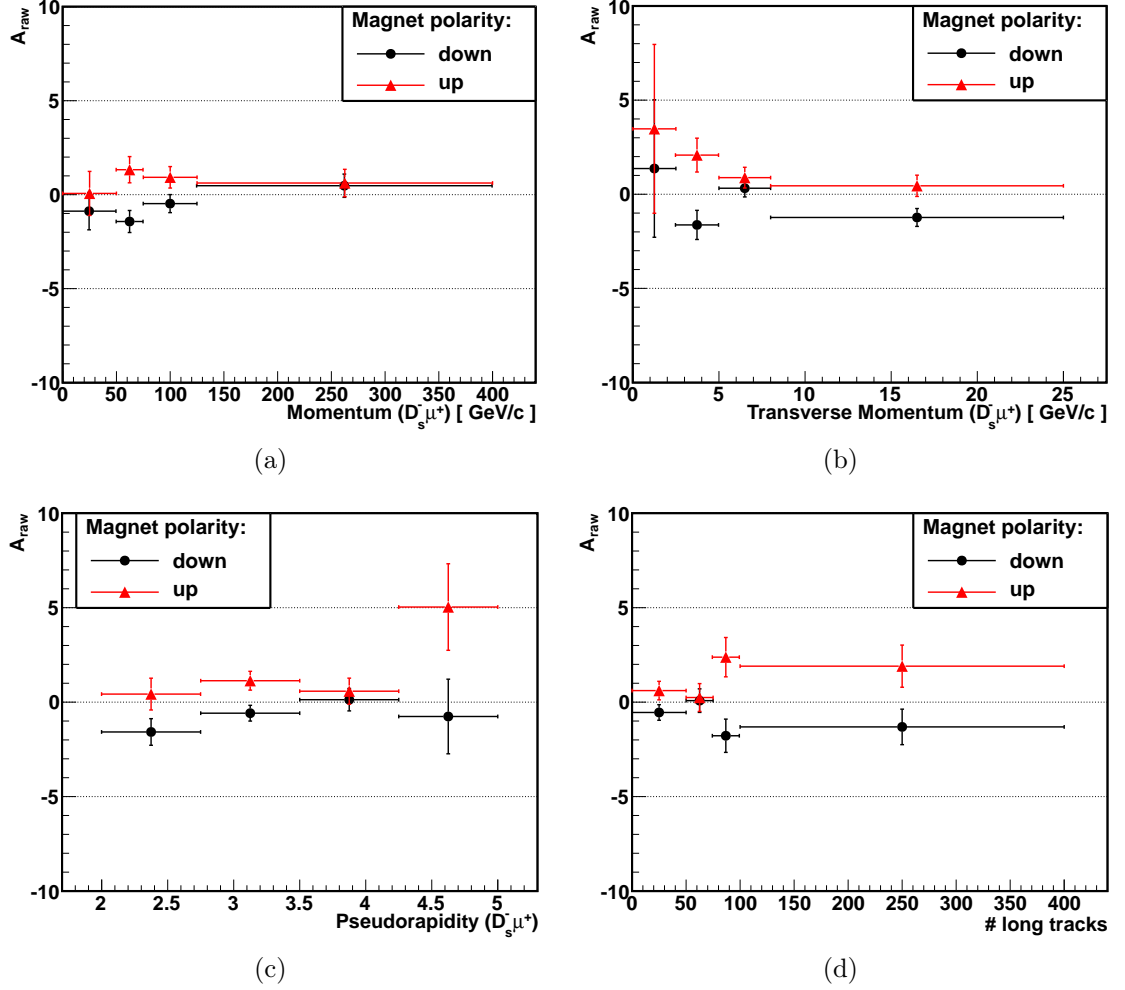


Figure 7.21: The raw asymmetry as a function of the  $B_s^\pm$ -candidate a)  $p$ , b)  $p_T$  and c) pseudorapidity, and d) the total number of long tracks in the event.

### 7.3.6 Background correction

The method used for fitting the Prompt and Detached backgrounds was discussed in Section 7.1. The shape of the Prompt background is determined using  $D_s^+ h^-$  calibration data, which has an enhanced Prompt component with respect to the signal sample. This shape is used to constrain the two-dimensional fit to the signal data, to determine the number of Prompt events. The Prompt induced charge-asymmetry is found to equal  $(0.14 \pm 0.07)\%$  for magnet up,  $(-0.05 \pm 0.05)\%$  for magnet down, and  $(0.04 \pm 0.04)\%$  averaged over magnet polarities. Additional sources of background with very similar or identical final states to the signal candidates have also been investigated [94] and are summarised below.

#### Fake muons associated to $B_s^0 \rightarrow D_s^- X$ decays

Despite the tight muon PID selection used in this analysis, pions and kaons are still sometimes misidentified as muons. This may result in purely hadronic decays

such as  $B_s^0 \rightarrow D_s^- \pi^+$  being mistaken for signal. However, provided that the muon fake-rate is not significantly charge-asymmetric this will not influence the measured asymmetry. The fraction of signal data from this type of background was found to be approximately 1% of the total sample, by study of real  $D_s^- \pi^+$  and  $D_s^- K^+$  decays, and inclusive simulated events (see Table 7.16). The muon fake-rate has been studied using  $D^{*+} \rightarrow \pi^+ D^0 (\rightarrow K^- \pi^+)$  decays. The probability for charged hadrons to be misidentified as muons is shown as a function of  $p$  in Figure 7.22. Misidentification ratios in particular  $p$  bins are less than  $\sim 10\%$  for both kaons and pions, and smaller still when the full momentum range is integrated over. Thus the potential bias from this source is of order  $\sim 10^{-4}$ . This background includes contributions from real muons produced by in-flight kaon decay.

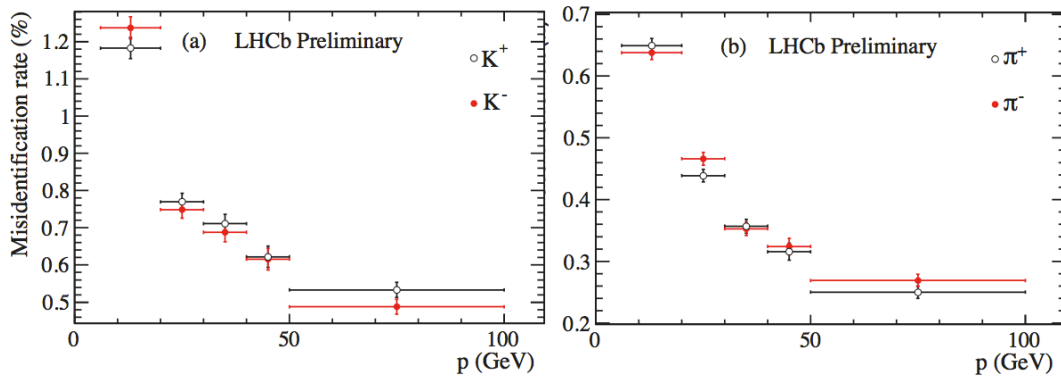


Figure 7.22: The muon misidentification probability as a function of track momentum for a) kaons and b) pions. Figures from Ref. [113].

### $b$ -hadrons to $c$ -hadrons with subsequent semileptonic charm decay

Backgrounds are also considered due to  $D_s^-$  and  $\mu^+$  combinations from  $b \rightarrow c\bar{c}s$  decays, where the virtual  $W^-$  produces a  $D_s^-$  and the muon originates from the semileptonic decay of the other  $D^+$  meson. Alternatively, a  $D_s^-$  and a  $\mu^+$  may be produced from different  $b$  parents. Using inclusive  $B \rightarrow D_s^-$  yields and MC simulation, this background is estimated to be  $(3.5 \pm 0.9)\%$ . Such decays are of opposite sign to the signal and result in a background asymmetry that is proportional to the magnitude of the production asymmetry of the source.

### $B \rightarrow D_s K \mu \bar{\nu}$ semileptonic decays

Semileptonic  $B$ -meson decays in which a kaon is produced in association with a  $D_s$  meson occur at a relatively low rate. The BaBar collaboration measured the exclusive decay branching fraction  $\mathcal{B}(B^- \rightarrow D_s^{(*)+} K^- l^- \bar{\nu}) = (6.1 \pm 1.2) \times 10^{-4}$  [116]. It is assumed (based on isospin invariance) that the same rate is applicable for  $\bar{B}^0$  decays to  $D_s^+ K^0 \mu^- \bar{\nu}$ . Using MC simulations and the  $b$ -hadron fractions measured

at LHCb [103], the fraction of this background in the signal sample is determined to be  $(3.3 \pm 0.9)\%$ . These have the opposite sign to the “ $b$ -hadrons to  $c$ -hadrons” background discussed above. Therefore  $B^-$  and  $\bar{B}^0$  production-asymmetry induced bias between these two sources will partially cancel.

### Background asymmetry correction

The  $B^0$  and  $B^+$  production asymmetries have been measured at LHCb to be  $(-1.0 \pm 1.3)\%$  and  $(-0.18 \pm 0.93)\%$  [117, 118]. Table 7.16 summarises the backgrounds considered in the previous few sections, along with their branching fractions, production asymmetries, and relative efficiency for selection compared to the  $B_s^0 \rightarrow D_s^- \mu^+$  signal. The total asymmetry from  $b$ -type backgrounds is determined to be  $(0.02 \pm 0.02)\%$ . The systematic error includes uncertainties related to the various branching fractions, but is dominated by the large uncertainties in the production asymmetries.

Combined with the  $(0.04 \pm 0.04)\%$  asymmetry associated to Prompt asymmetries, the total background asymmetry is  $A_b = (0.06 \pm 0.05)\%$ . This value is subtracted from the measured asymmetry (from Section 7.2) and a systematic uncertainty of  $0.05\%$  is assigned.

Table 7.16: The branching fractions and selection efficiency ratios for the various  $B \rightarrow DX$  backgrounds considered. Table from Ref.[113].

Mode	Branching fraction	$\varepsilon(\text{signal})/\varepsilon(\text{background})$	Production asymmetry
$B^+ \rightarrow D_s^+ X$	$(7.9 \pm 1.4)\%$	11	$(-0.18 \pm 0.93)\%$
$B^0 \rightarrow D_s^+ D^0 X$	$(5.7 \pm 1.2)\%$	11	$(-1.50 \pm 1.30)\%$
$B^0 \rightarrow D_s^+ D^- X$	$(4.6 \pm 1.0)\%$	18	$(-1.50 \pm 1.30)\%$
$\Lambda_b \rightarrow D_s^+ \Lambda_c X$	$(10 \pm 2)\%$	14	$(-2.0 \pm 2.0)\%$
$B^+ \rightarrow D_s^- K \mu^+$	$(6.1 \pm 1.2) \times 10^{-4}$	2	$(-0.18 \pm 0.93)\%$
$B^0 \rightarrow D_s^- K \mu^+$	$(6.1 \pm 1.2) \times 10^{-4}$	2	$(-1.50 \pm 1.30)\%$

### 7.3.7 Tracking efficiencies

Tracking-induced charge asymmetries may arise due to differences in interaction cross-sections with detector material, or due to acceptance effects that impact one charged particle more than another. A data-driven technique has been developed to determine the charged pion detection efficiency. Fitted yields of partially reconstructed  $D^{*+} \rightarrow D^0 \pi_s^+$  are compared to yields obtained with a full reconstruction. In the partial reconstruction the charm decay  $D^0 \rightarrow K^- \pi^+ \pi^- \pi^+$  is reconstructed with a single pion missing. This channel has sufficient kinematic constraints to be efficiently selected even when one pion is missing. This method has been used in an

independent analysis to measure the  $D_s^\pm$  production asymmetry, and is described in greater detail in the corresponding publication [114].

The  $\pi^\pm$  interaction cross-sections are approximately equal for the pion momentum range used in this analysis. Tracking asymmetries therefore depend mostly upon the detector acceptance. Although the absolute magnitudes of pion and muon tracking efficiencies are expected to differ, acceptance-induced asymmetries are common to both. The tracking efficiency ratio,  $\varepsilon(\pi^+)/\varepsilon(\pi^-)$ , is found to be approximately independent of both the pion  $p$  and  $p_T$ , as shown by Figure 7.23. In selecting both a  $\pi^\pm$  and an oppositely charged  $\mu^\mp$ , tracking-induced bias mostly cancels, as

$$\frac{\varepsilon(\pi^\pm)}{\varepsilon(\pi^\mp)} \times \frac{\varepsilon(\mu^\mp)}{\varepsilon(\mu^\pm)} = 1. \quad (7.4)$$

This statement is only valid to the precision with which the efficiency ratios can be shown to be independent of  $p$  and  $p_T$ , due to kinematic differences between the pions and muons. Figure 7.24 shows that such kinematic differences are significant. The tracking asymmetry  $A_{\mu\pi}^{\text{track}}$  is determined by folding the pion track reconstruction efficiency measurements with the momentum spectra of the pion and muon candidates. The tracking asymmetry is found to be  $A_{\mu\pi}^{\text{track}} = (0.01 \pm 0.13)\%$ . This is treated in an analogous way to the  $b$ -background correction described in the previous section, with the central value subtracted from the measured asymmetry and a systematic uncertainty of 0.13% assigned.

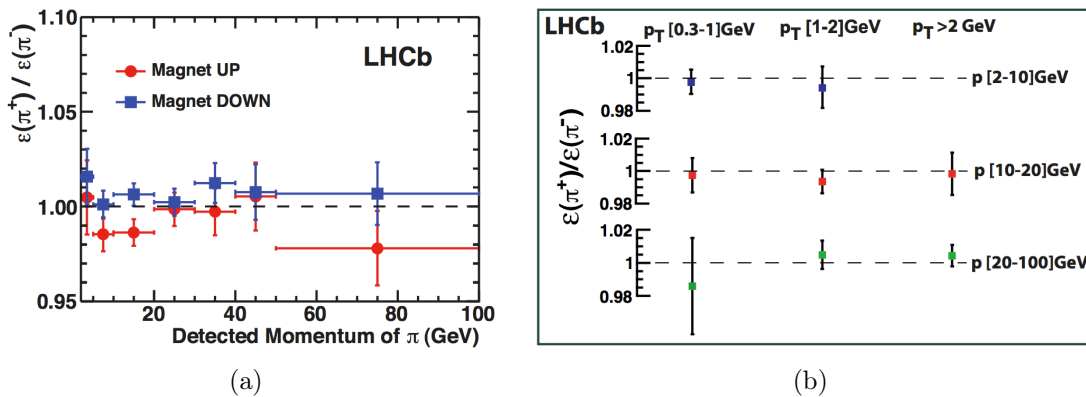


Figure 7.23: **a)** The pion tracking efficiency ratio,  $\varepsilon(\pi^+)/\varepsilon(\pi^-)$ , as a function of pion momentum, for each magnetic field polarity. **b)** The pion tracking efficiency ratio, averaged over both magnet polarities and as a function of the pion  $p$  and  $p_T$ . Figures from Ref. [114].

### 7.3.8 Systematic uncertainties

The various sources of systematic uncertainty are summarised in Table 7.17. Dominant contributions are from pion and muon tracking efficiency measurements (0.13%), muon calibration sample statistics (0.06%), potential HLT2 bias (0.05%),

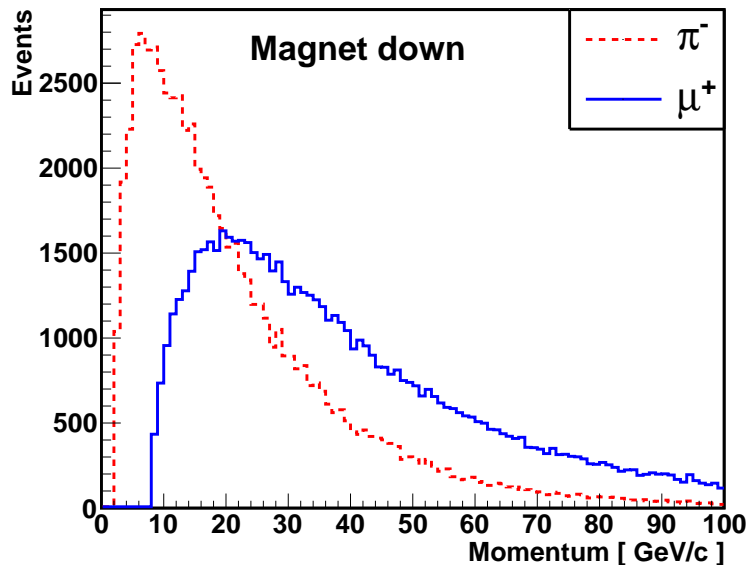


Figure 7.24: The momentum distribution of signal pion and muon candidates.

Table 7.17: A summary of the systematic uncertainties of the corrected asymmetry  $A_{\text{corr}}$ . The sections in which the systematics are discussed are also listed.

Source	Section	$\sigma(A_{\text{corr}})[\%]$
Signal modelling	7.3.1	0.05
Background subtraction	7.3.6	0.05
Track reconstruction	7.3.7	0.13
Kinematic matching between calibration and signal data	7.2	0.04
Muon topological HLT2 trigger	7.3.3	0.05
MS calibration sample statistics	7.2	0.06
<b>Total</b>		<b>0.17</b>

asymmetric backgrounds (0.05%) and signal modelling (0.05%). The total systematic uncertainty is 0.17%, which is approximately two thirds of the statistical uncertainty.

## 7.4 Summary and conclusions

The final result is obtained using the  $p$ - $p_T$ - $\phi$  binning scheme and the MS calibration sample, as this has the smallest statistical uncertainty. The corrected asymmetry,  $A_{\text{corr}} = A_{\text{meas}}(0.01\%) - A_{\mu\pi}^{\text{track}}(0.01\%) - A_b(0.06\%)$  is,

$$A_{\text{corr}} = (-0.06 \pm 0.24 \pm 0.17)\%, \quad (7.5)$$

where the first uncertainty is statistical and the second is systematic (see Table 7.17). The relationship between the corrected asymmetry and  $a_{\text{fs}}^s$  was discussed in Sec-

tion 6.1, with  $A_{\text{corr}} = a_{\text{fs}}^s/2$ . It follows that the flavour-specific asymmetry is,

$$a_{\text{fs}}^s = (-0.12 \pm 0.48 \pm 0.34)\%, \quad (7.6)$$

which is consistent with the Standard Model (SM) prediction of  $a_{\text{fs}}^s = (1.9 \pm 0.3) \times 10^{-5}$  [14] and is the single most precise measurement of  $a_{\text{fs}}^s$  to date.

The measurement is compared to preceding measurements in Figure 7.25. The only measurement that is significantly discrepant from the SM is that of the  $D\bar{O}$  collaboration. They have measured the dimuon asymmetry in 1.96 TeV  $p\bar{p}$  collisions to be  $A_{\text{sl}}^b = (-0.787 \pm 0.172 \pm 0.093)\%$  [17], which is approximately four standard deviations from the SM prediction. The data sample used by the  $D\bar{O}$  experiment contains  $B^0$  and  $B_s^0$  mesons, such that the measured asymmetry can be related to each  $a_{\text{fs}}$  component by the relation,  $A_{\text{sl}}^b = (0.594 \pm 0.022)a_{\text{fs}}^d + (0.406 \pm 0.022)a_{\text{fs}}^s$ . These coefficients depend on both the production rates and mixing frequencies of the  $B$  mesons. Although a greater number of  $B^0$  are produced, the lower mixing frequency of  $B^0$  mesons relative to that of  $B_s^0$  mesons increases the probability of them decaying without oscillating. The two effects approximately cancel, leaving the coefficients for  $B^0$  and  $B_s^0$  approximately equal. By considering several specific cases,

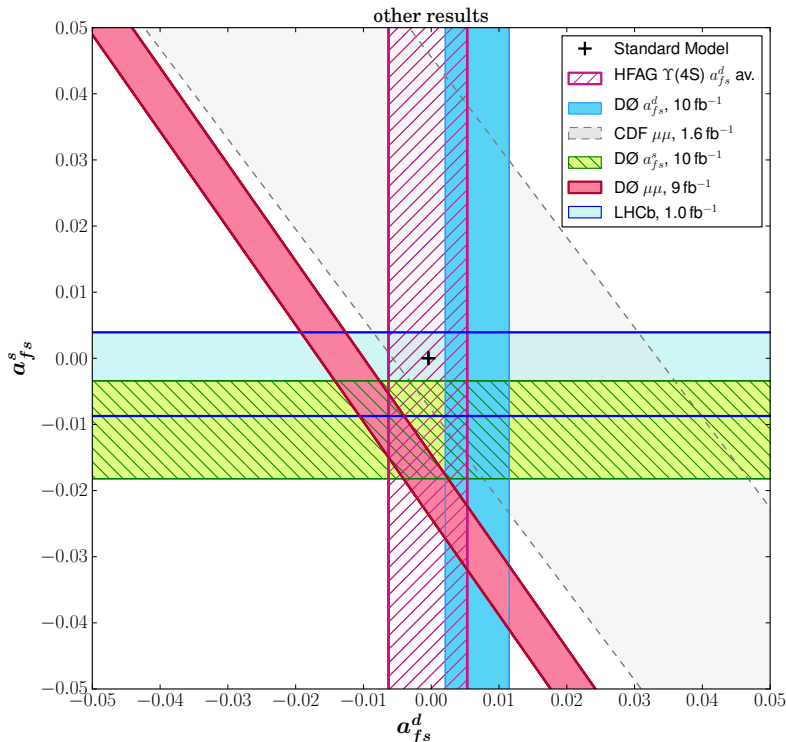


Figure 7.25: The current status of  $a_{\text{fs}}$  in the  $a_{\text{fs}}^d - a_{\text{fs}}^s$  plane. The HFAG averaged  $a_{\text{fs}}^d$  band does not include the most recent measurement from BaBar [98], which changes the HFAG  $\Upsilon(4S)$  average to  $a_{\text{fs}}^d = (0.02 \pm 0.31)\%$ .

this relation can be used to compare the  $D\bar{D}$  measurement with measurements made in other experiments and with the SM predictions. Assuming  $a_{fs}^d = 0$ , the  $D\bar{D}$  measurement becomes  $a_{fs}^s = (-1.94 \pm 0.49)\%$ . This is inconsistent with the result of this analysis at the confidence level of 2.4 standard deviations. In a second case it is assumed that  $a_{fs}^s = 0$ , for which  $D\bar{D}$  measurement becomes  $a_{fs}^d = (-1.32 \pm 0.34)\%$ . This is inconsistent with the Heavy Flavour Averaging Group [101] average from  $\Upsilon(4S)$  measurements of  $a_{fs}^d = (0.02 \pm 0.31)\%$  at the confidence level of 2.9 standard deviations. In a third case it is assumed that each component is equal, in which case the measured  $D\bar{D}$  asymmetry is unchanged and  $a_{fs}^d = a_{fs}^s = (-0.79 \pm 0.20)\%$ . In this case the result is inconsistent with the  $\Upsilon(4S)$  measurements and the result from this analysis at the confidence levels of 2.2 and 1.1 standard deviations, respectively.

The dilepton asymmetry measured by the  $D\bar{D}$  experiment strongly suggests that  $a_{fs}$  is non-zero and negative. The measurement presented in this thesis does not have the precision required to confirm or refute this, and is consistent with both the SM and the anomalous like-sign asymmetry measured by the  $D\bar{D}$  experiment. The result has been obtained using data collected at LHCb from  $1 \text{ fb}^{-1}$  of integrated luminosity in 2011. Following 2012 data taking, an additional  $2 \text{ fb}^{-1}$  of integrated luminosity has been recorded at LHCb. Thus updates to this analysis are expected to have a reduction in the statistical uncertainty by a factor of approximately 2. In addition, it is expected that the dominant systematic uncertainties associated to the calibration sample statistics will be reduced by a similar factor.



## PROJECTED ANGLE

The projected angle is a parameter related to the orientation of a track passing through a silicon sensor. It is related to both the angle of incidence of the track to the sensor plane and the strip orientation within the sensor plane. Figure A.1 is a schematic diagram showing the various angles of a track incident on a sensor region. The projected angle is displayed. The following is an attempt at describing the projected angle, taken from Ref. [33]:

*“The projected angle is the angle between the track and the perpendicular to the sensor, in the plane perpendicular to the sensor and containing the perpendicular to the strip.”*

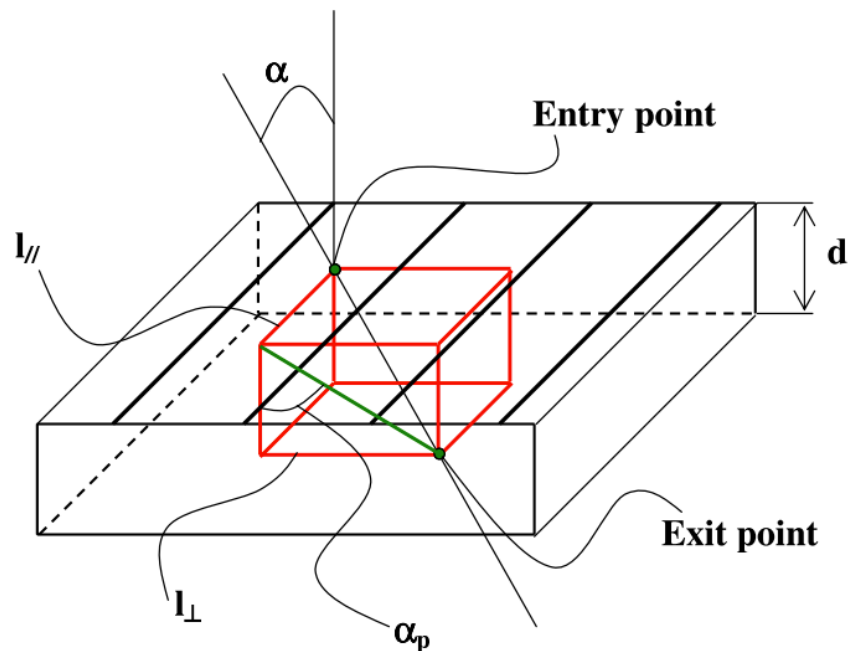


Figure A.1: Geometrical definition of the projected angle.  $\alpha$  and  $\alpha_p$  are the track angle and projected angle respectively.  $l_{\perp}$  and  $l_{//}$  are the track components parallel and perpendicular to the strip. The thickness of the sensor is designated by “d”. Figure and caption from Ref. [119].



## BIBLIOGRAPHY

- [1] I. J. R. Aitchison and A. J. G. Hey, *Gauge Theories in Particle Physics*, vol. 1 of *Graduate Student Series in Physics*, Taylor & Francis, 3rd ed., 2003. 3
- [2] B. R. Martin and G. Shaw, *Particle Physics*, The Manchester Physics Series, John Wiley & Sons, 2nd ed., 2006. 3
- [3] D. H. Perkins, *Introduction to High Energy Physics*, Cambridge University Press, 4th ed., 2000. 3
- [4] RAL Summer School, *Proceedings of the school for experimental high energy physics students*, Tech. Rep. RAL-TR-2010-010, Science & Technology Facilities Council, 2010. 3
- [5] S. A. Thomas, F. B. Abdalla, and O. Lahav, *Upper bound of 0.28 eV on the neutrino masses from the largest photometric redshift survey*, *Phys. Rev. Lett.* **105** (2010) 031301. 4
- [6] Particle Data Group, J. Beringer *et al.*, *Review of particle physics*, *Phys. Rev.* **D86** (2012) 010001. 4, 5, 7
- [7] ATLAS Collaboration, G. Aad *et al.*, *Observation of a new particle in the search for the Standard Model Higgs boson with the ATLAS detector at the LHC*, *Phys. Lett.* **B716** (2012) 1, [arXiv:1207.7214](https://arxiv.org/abs/1207.7214). 7, 10
- [8] CMS Collaboration, S. Chatrchyan *et al.*, *Observation of a new boson at a mass of 125 GeV with the CMS experiment at the LHC*, *Phys. Lett.* **B716** (2012) 30, [arXiv:1207.7235](https://arxiv.org/abs/1207.7235). 7, 10
- [9] I. I. Bigi and A. I. Sanda, *CP Violation*, vol. 2nd, Cambridge University Press, 2009. 10, 12
- [10] G. C. Branco, L. Lavoura, and J. P. Silva, *CP Violation*, vol. 2nd, Clarendon Press, Oxford, 1999. 10

- [11] Particle Data Group, J. Beringer *et al.*, *CP violation (rev.)*, Phys. Rev. **D86** (2012) 010001. 10, 15, 16
- [12] A. Sakharov, *Violation of CP Invariance, C Asymmetry, and Baryon Asymmetry of the Universe*, Pisma Zh. Eksp. Teor. Fiz. **5** (1967) 32. 11
- [13] U. Nierste, *Three Lectures on Meson Mixing and CKM phenomenology*, arXiv:0904.1869. 17, 102
- [14] A. Lenz, *Theoretical update of B-Mixing and Lifetimes*, ArXiv e-prints (2012) arXiv:1205.1444. 19, 101, 164
- [15] A. Lenz and U. Nierste, *Theoretical update of  $B_s - \bar{B}_s$  mixing*, JHEP **0706** (2007) 072, arXiv:hep-ph/0612167. 19
- [16] D0 Collaboration, V. M. Abazov *et al.*, *Evidence for an anomalous like-sign dimuon charge asymmetry*, Phys. Rev. **D82** (2010) 032001, arXiv:1005.2757. 19, 107
- [17] D0 Collaboration, V. M. Abazov *et al.*, *Measurement of the anomalous like-sign dimuon charge asymmetry with  $9 \text{ fb}^{-1}$  of  $p\bar{p}$  collisions*, Phys. Rev. **D84** (2011) 052007, arXiv:1106.6308. 19, 106, 107, 164
- [18] O. S. Brüning *et al.*, *LHC design report: Volume 1, the LHC main ring*, Tech. Rep. CERN-LHC-2004-003-V-1, June, 2004. 21
- [19] O. S. Brüning *et al.*, *LHC design report: Volume 2, the LHC infrastructure and general services*, Tech. Rep. CERN-LHC-2004-003-V-2, June, 2004. 21
- [20] O. S. Brüning *et al.*, *LHC design report: Volume 3, the LHC injector chain*, Tech. Rep. CERN-LHC-2004-003-V-3, June, 2004. 21
- [21] M. Brice, *Aerial View of the CERN taken in 2008.*, July, 2008. 22
- [22] Proton Synchrotron Division, R. Ley, *CERN Accelerators*, 1996. 23
- [23] LHCb collaboration, A. A. Alves Jr. *et al.*, *The LHCb detector at the LHC*, JINST **3** (2008) S08005. 26, 34, 38, 40, 41, 70, 71
- [24] T. Sjöstrand, S. Mrenna, and P. Skands, *PYTHIA 6.4 physics and manual*, JHEP **05** (2006) 026, arXiv:hep-ph/0603175. 26, 42
- [25] LHCb Collaboration, E. Jans, *The LHCb detector*, arXiv:0910.1740. 26
- [26] F. C. D. Metlica, *The LHCb detector and triggers*, Nuclear Physics B - Proc. Supp. **167** (2007) 229. 26

- [27] LHCb collaboration, *Reoptimized Detector Design and Performance*, Tech. Rep. CERN-LHCC-2003-030. LHCb-TDR-9, 2003. 27, 28
- [28] The LHCb Collaboration, *LHCb magnet technical design report*, Tech. Rep. CERN-LHCC-2000-007. LHCb-TDR-1, 2000. 27
- [29] A. A. Affolder, *LHCb VERtEX LOcator (VELO): Module production and performance*, Nucl. Instrum. Meth. **A596** (2008) 25. 29
- [30] S. Köstner and H. Voss, *Long term performance studies of the silicon strip detectors of the LHCb silicon tracker*, Nucl. Instrum. Meth. **A563** (2006), no. 1 259 . 29
- [31] The LHCb Collaboration, *Inner tracker technical design report*, Tech. Rep. CERN-LHCC-2002-029. LHCb-TDR-8, 2002. 29
- [32] P. Koppenburg, *Simulation of the vertex trigger preprocessor: effects of noise on L1 performance*, Tech. Rep. LHCb-99-003, 1999. 30
- [33] LHCb VELO Group, *Performance of the lhcb vertex locator*, To be submitted to JINST (2013). 30, 31, 167
- [34] M. D. Needham, *LHCb silicon tracker operations and performance with first data*, Tech. Rep. LHCb-PROC-2010-034, CERN-LHCb-PROC-2010-034, 2010. 31
- [35] LHCb Silicon Tracker - Material for Publications, <http://www.physik.uzh.ch/groups/lhcb/public/material/>, 2012. 32, 33
- [36] M. Tobin, *Performance of the lhcb silicon tracker in pp collisions at the lhc*, in *Nuclear Science Symposium Conference Record (NSS/MIC), 2010 IEEE*, pp. 935 –938, 2010. doi: 10.1109/NSSMIC.2010.5873899. 32
- [37] B. Stroaci, *The performance of the outer tracker detector at LHCb*, in *13<sup>th</sup> ICATPP Conference on Astroparticle, Particle, Space Physics and Detectors for Physics Applications*, no. LHCb-PROC-2011-058, 2011. 33
- [38] S. Bachmann *et al.*, *Ageing in the LHCb outer tracker: Phenomenon, culprit and effect of oxygen*, Nucl. Instrum. Meth. **A617** (2010) 202. 33
- [39] D. van Eijk *et al.*, *Radiation hardness of the LHCb Outer Tracker*, Nucl. Instrum. Meth. (2012) 62. 34
- [40] LHCb RICH Collaboration, N. Harnew, *Particle identification with the LHCbRICH system*, Nucl. Instrum. Meth. **A563** (2006) 326. 35

- [41] The LHCb RICH Group, *Performance of the LHCbRICH detector at the LHC*, To be submitted to EPJC (2012) [arXiv:1211.6759](#). 36
- [42] F. Ariztizabal *et al.*, *Construction and performance of an iron-scintillator hadron calorimeter with longitudinal tile configuration*, Nucl. Instrum. Meth. **A349** (1994) 384. 38
- [43] The LHCb Collaboration, *LHCb trigger system technical design report*, Tech. Rep. CERN-LHCC-2003-031. LHCb-TDR-10, 2003. 40
- [44] R. Aaij and J. Albrecht, *Muon triggers in the high level trigger of LHCb*, LHCb-PUB-2011-017. 41
- [45] G. Barrand *et al.*, *GAUDI - A software architecture and framework for building HEP data processing applications*, Comput. Phys. Commun. **140** (2001) 45. 42
- [46] G. Corti *et al.*, *Software for the LHCb experiment*, IEEE Trans. Nucl. Sci. **53** (2006) 1323. 42, 43
- [47] M. Clemencic *et al.*, *The LHCb simulation application, GAUSS: design, evolution and experience*, J. of Phys. : Conf. Ser. **331** (2011) 032023. 42
- [48] D. J. Lange, *The EvtGen particle decay simulation package*, Nucl. Instrum. Meth. **A462** (2001) 152. 42
- [49] GEANT4 collaboration, S. Agostinelli *et al.*, *GEANT4: A simulation toolkit*, Nucl. Instrum. Meth. **A506** (2003) 250. 43, 71
- [50] GEANT4 collaboration, J. Allison *et al.*, *Geant4 developments and applications*, IEEE Trans. Nucl. Sci. **53** (2006) 270. 43, 71
- [51] LHCb collaboration, *Framework TDR for the LHCb Upgrade: Technical Design Report*, Tech. Rep. CERN-LHCC-2012-007. LHCb-TDR-12, CERN, Geneva, Apr, 2012. 45, 60
- [52] F. Muheim, *LHCb upgrade plans*, Nucl. Phys. Proc. Suppl. **170** (2007) 317, [arXiv:hep-ex/0703006](#). 45
- [53] V. Coco, M. Kucharczyk, and S. Stone, *Initial studies of the trigger upgrade*, LHCb-INT-2009-008. 45
- [54] J. Gassner, F. Lehner, and S. Steiner, *The mechanical design of the LHCb silicon Trigger Tracker*, CERN-LHCb-2004-110. 46

- [55] M. Needham, *Channel numbering and readout partitioning for the silicon tracker*, CERN-LHCb-2006-033. 46
- [56] M. Needham and O. Steinkamp, *Updated channel numbering and readout partitioning for the silicon tracker*, CERN-LHCb-2007-137. 46
- [57] O. Steinkamp, *Layout and R&D for an All-Silicon TT Station*, CERN-LHCb-2002-056. 49
- [58] O. Callot, M. Kucharczyk, and M. Witek, *VELO-TT track reconstruction*, CERN-LHCb-2007-010. 51
- [59] W. W. Emmett, *The Channels and Water of the Upper Salmon River Area, Idaho*, Geographical Survey Professional Paper **870 A** (1975). 61
- [60] S. M. Sze, *Semiconductor Devices*, John Wiley & Sons, Inc., 2nd ed., 2002. 62
- [61] S. M. Sze, *Physics of Semiconducting Devices*, Wiley, New York, 2nd ed., 1981. 63, 64
- [62] F. Fontanelli, P. Ramella, and S. Vitale, *Charge collection in partially depleted silicon detectors*, Nucl. Instrum. Meth. **A269** (1988), no. 3 603 . 64
- [63] M. Moll, *Radiation Damage in Silicon Particle Detectors*, PhD thesis, Fachbereich Physik der Universität Hamburg, 1999. 64, 67, 68, 69
- [64] M. Needham and T. Ruf, *Estimation of the material budget of the LHCb detector*, CERN-LHCb-2007-025. 65
- [65] Particle Data Group, K. Nakamura *et al.*, *Review of particle physics*, Phys. Rev. **G37** (2010) 075021. 65, 66
- [66] V. A. J. van Lint *et al.*, *Mechanisms of Radiation Effects in Electronic Materials*, John Wiley & Sons, Inc., 1980. 66, 67
- [67] G. Barbottin and A. Vapaille, *Instabilities in Silicon Devices*, Elsevier Science B. V., 1999. 66
- [68] D. K. Schroder, *Semiconductor Material and Device Characterization*, John Wiley & Sons, 1990. 67
- [69] L. Rossi, T. Rohe, P. Fisher, and N. Wermes, *Pixel Detectors*, Springer, 2006. 67, 79
- [70] A. Gureja *et al.*, *Use of IV (current vs voltage) scans to track radiation damage in the LHCb VELO*, LHCb-PUB-2011-020. 68

- [71] A. Hickling *et al.*, *Use of IT (current vs temperature) scans to study radiation damage in the LHCb VELO*, LHCb-PUB-2011-021. 68
- [72] W. Shockley and W. T. Read, *Statistics of the Recombinations of Holes and Electrons*, Physical Review **87** (1952) 835. 68
- [73] The LHCb VELO Group, *VELO approved conference plots*, 2008. 70
- [74] P. R. Turner, *Velo module production - sensor testing*, Tech. Rep. CERN-LHCb-2007-072, Nov, 2007. 71, 81
- [75] M. van Beuzekom, A. Van Lysebetten, and B. Verlaat, *CO<sub>2</sub> cooling experience (LHCb)*, CERN-LHCb-PROC-2007-025. 71
- [76] S. Löchner and M. Schmelling, *The Beetle reference manual - chip version 1.3, 1.4 and 1.5*, CERN-LHCb-2005-105. 73
- [77] G. Haefeli *et al.*, *The LHCb DAQ interface board TELL1*, Nucl. Instrum. Meth. **A560** (2006) 494. 73
- [78] LHCb VELO Group, L. Eklund, *Control and Monitoring of VELO and Pile-Up Level 0 Electronics*, tech. rep., 2005. 73
- [79] A. Papadelis *et al.*, *First study of the VELO detector noise performance at point 8*, LHCb-INT-2009-005. 73
- [80] M. Moll, E. Fretwurst, and G. Linström, *Investigation on the improved radiation hardness of silicon detectors with high oxygen concentration*, NIMPR A **439** (2000) 282 . 74
- [81] G. Lindström *et al.*, *Developments for radiation hard silicon detectors by defect engineering – results by the CERN RD48 (ROSE) collaboration*, NIMPR A **465** (2001) 60. 75
- [82] T. W. Versloot *et al.*, *Positron reconstruction and charge distribution in LHCb VELO silicon sensors*, CERN-LHCb-2007-119. 76, 77
- [83] S. Farry, *A measurement of Z production using tau final states with the LHCb detector*, PhD thesis, University College Dublin, Aug, 2012. 77, 129
- [84] R. Wunstorf *et al.*, *Results on radiation hardness of silicon detectors up to neutron fluences of  $10^{15}$  n/cm<sup>2</sup>*, NIMPR A **315** (1992) 149. 80
- [85] M. Lozano *et al.*, *Comparison of radiation hardness P-in-N, N-in-N, N-in-P silicon pad detectors*, IEEE Trans. Nucl. Sci. **52** (2005) 1468. 80, 84

- 
- [86] F. Lemeilleur *et al.*, *Electrical properties and charge collection efficiency for neutron-irradiated p-type and n-type silicon detectors*, Nuclear Physics B - Proceedings Supplements **32** (1993), no. 0 415. 80, 84
- [87] A. Vasilescu, *The NIEL hypothesis applied to neutron spectra of irradiation facilities and in the ATLAS and CMS SCT*, ROSE/TN/97-2, December, 1999. 81
- [88] LHCb VELO Group, *Radiation damage in the LHCb vertex locator*, To be submitted to JINST (2013). 83, 89, 90
- [89] The CMS Tracker Collaboration, C. Barth, *Evolution of silicon sensor characteristics of the CMS silicon strip tracker*, Nucl. Instrum. Meth. **In Press** (2012) . 90
- [90] ATLAS Pixel Collaboration, L. Tommaso, *Test beam results of ATLAS Pixel sensors*, arXiv:hep-ex/0210045. 95
- [91] T. Rohe *et al.*, *Position Dependence of Charge Collection in Prototype Sensors for the CMS Pixel Detector*, IEEE Trans. Nucl. Sci. **51** (2004) 1150. 95
- [92] U. Nierste, *CP asymmetry in flavour-specific B decays*, arXiv:hep-ph/0406300. 101
- [93] LHCb Collaboration, R. Aaij *et al.*, *Opposite-side flavour tagging of B mesons at the LHCb experiment*, Eur. Phys. J. **C72** (2012) 2022, arXiv:1202.4979. 104
- [94] The LHCb Collaboration, *Measurement of the flavour-specific cp violating asymmetry  $a_{\text{sl}}^s$  in  $B_s$  decays*, LHCb-CONF-2012-022. 105, 136, 159
- [95] E. Norrbin and R. Vogt, *Bottom production asymmetries at the LHC*, arXiv:hep-ph/0003056. 105
- [96] The LHCb Collaboration, *Charmless charged two-body b decays at LHCb with 2011 data*, CERN-LHCb-CONF-2011-042. 105
- [97] Belle Collaboration, E. Nakano *et al.*, *Charge asymmetry of same-sign dileptons in  $B^0 - \bar{B}^0$  mixing*, Phys. Rev. **D73** (2006) 112002, arXiv:hep-ex/0505017. 106
- [98] BaBar Collaboration, M. Margoni,  *$|q/p|$  Measurement from  $B^0 \rightarrow D * l\nu$  Partial Reconstruction*, arXiv:1301.0417. 106, 164

- [99] D0 Collaboration, V. M. Abazov *et al.*, *Measurement of the semileptonic charge asymmetry in  $B^0$  meson mixing with the D0 detector*, Phys. Rev. **D86** (2012) 072009, [arXiv:1208.5813](#). 106
- [100] D0 Collaboration, V. Abazov *et al.*, *Measurement of the semileptonic charge asymmetry using  $B_s^0 \rightarrow D_s \mu X$  decays*, Phys. Rev. Lett. **110** (2013) 011801, [arXiv:1207.1769](#). 106
- [101] Heavy Flavor Averaging Group, Y. Amhis *et al.*, *Averages of  $b$ -hadron,  $c$ -hadron, and tau-lepton properties as of early 2012*, and online update at <http://www.slac.stanford.edu/xorg/hfag>, [arXiv:1207.1158](#). 106, 165
- [102] The LHCb Collaboration, *LHCb public webpage*, 2010. 109
- [103] LHCb Collaboration, R. Aaij *et al.*, *Measurement of  $b$ -hadron production fractions in 7 TeVpp collisions*, Phys. Rev. **D85** (2012) 032008, [arXiv:1111.2357](#). 109, 161
- [104] The LHCb Collaboration, G. Lanfranchi *et al.*, *The muon identification procedure of the LHCb experiment for the first data*, CERN-LHCb-PUB-2009-013. 116
- [105] LHCb Collaboration, R. Aaij *et al.*, *Evidence for CP violation in time-integrated  $D^0 \rightarrow h^- h^+$  decay rates*, Phys. Rev. Lett. **108** (2012) 111602, [arXiv:1112.0938](#). 119
- [106] W. Verkerke and D. Kirkby, *RooFit Users Manual v2.91*, 2008. 121, 135
- [107] T. Skwarnicki, *A study of the radiative cascade transitions between the Upsilon-prime and Upsilon resonances*, PhD thesis, Institute of Nuclear Physics, Krakow, 1986, DESY-F31-86-02. 121
- [108] LHCb Collaboration, R. Aaij *et al.*, *Measurement of  $J/\psi$  production in pp collisions at  $\sqrt{s} = 7$  TeV*, Eur. Phys. J. **C71** (2011) 1645, [arXiv:1103.0423](#). 121, 154
- [109] V. V. Gligorov, *A single track HLT1 trigger*, Tech. Rep. CERN-LHCb-PUB-2011-003, Jan, 2011. 126
- [110] R. Aaij *et al.*, *The LHCb Trigger and its Performance*, [arXiv:1211.3055](#). 127
- [111] J. Van Tilburg and M. Merk, *Track simulation and reconstruction in LHCb.*, PhD thesis, Vrije Univ. Amsterdam, Aug, 2005. 128

- [112] V. Gligorov, C. Thomas, and M. Williams, *The HLT inclusive B triggers*, Tech. Rep. CERN-LHCb-PUB-2011-016, 2011. 133
- [113] M. Artuso *et al.*, *Time integrated measurement of the semileptonic CP violating asymmetry  $a_{sl}^s$* , LHCb-ANA-2012-054. 133, 134, 155, 160, 161
- [114] LHCb Collaboration, R. Aaij *et al.*, *Measurement of the  $Ds^+$  -  $Ds^-$  production asymmetry in  $\gamma$  TeV pp collisions*, Phys. Lett. **B713** (2012) 186, arXiv:1205.0897. 140, 162
- [115] F. Andrianala, T. Bird, and R. Lambert, *2D mass-IP fits in semileptonic decays of neutral B-mesons at LHCb*, CERN-LHCb-INT-2011-019. 141
- [116] BABAR Collaboration, P. del Amo Sanchez *et al.*, *Observation of the Decay  $B^- \rightarrow D_s^{(*)+} K^- \ell^- \bar{\nu}_\ell$* , Phys. Rev. Lett. **107** (2011) 041804, arXiv:1012.4158. 160
- [117] LHCb Collaboration, R. Aaij *et al.*, *First evidence of direct CP violation in charmless two-body decays of Bs mesons*, Phys. Rev. Lett. **108** (2012) 201601, arXiv:1202.6251. 161
- [118] LHCb Collaboration, R. Aaij *et al.*, *Measurements of the branching fractions and CP asymmetries of  $B^+$  to  $J/\psi \pi^+$  and  $B^+$  to  $\psi(2S) \pi^+$  decays*, Phys. Rev. **D85** (2012) 091105, arXiv:1203.3592. 161
- [119] T. Szumlak, C. Parkes, and T. Ruf, *Reconstruction of cluster positions in the LHCb VELO*, Tech. Rep. CERN-LHCb-2007-151, 2007. 167